UNIVERSIDAD COMPLUTENSE DE MADRID
FACULTAD DE CIENCIAS QUIMICAS

TESIS DOCTORAL

Carbon dots: composition, structure and photophysics

Nanopuntos de carbono : composición, estructura y fotofísica

MEMORIA PARA OPTAR AL GRADO DE DOCTOR

PRESENTADA POR

Sergio Ramírez Barroso

Directores

Reinhold Wannemacher
David García Fresnadillo
Nazario Martín León

Madrid

UNIVERSIDAD COMPLUTENSE DE MADRID
FACULTAD DE CIENCIAS QUÍMICAS

TESIS DOCTORAL

Carbon Dots:
Composition, Structure And Photophysics

Nanopuntos de Carbono:
Composición, Estructura y Fotofísica

DOCTORANDO

Sergio Ramírez Barroso

DIRECTORES

Reinhold Wannemacher

David García Fresnadillo

Nazario Martín León

AGRADECIMIENTOS

Por orden cronológico, me siento muy agradecido al CEIP San Juan de la Cruz, y al IES Montes de Toledo (ambos en Gálvez, Toledo), y en particular, quisiera extender mis agradecimientos a todos los profesores que me acompañaron esos años.

Ya en el contexto universitario, concretamente en la Universidad Complutense de Madrid, y más concretamente en el segundo año, me cruce con uno de mis actuales directores de tesis, Nazario. Me impartió la asignatura de química orgánica, y en ese momento paso a ser la asignatura a la que con más ganas dedicaba más tiempo. Este incipiente gusto por la química orgánica definiría una serie de decisiones concatenadas que me han llevado hasta aquí, y este incipiente gusto fue, en parte, culpa de Nazario. Lo que más puedo destacar de mi relación con él, es que siempre he tenido la grata sensación de sentirme muy valorado por su parte, y solo espero haber aprendido y tomado muchas de sus buenas aptitudes en el trabajo.

Un par de años más tarde conocería a otro de mis directores de tesis, David. Fue mi tutor del trabajo final de grado, y su manera de llevarme de la mano en mi primer contacto con la investigación científica me ha hecho llegar hasta aquí. Siendo solo un estudiante confió en mi para ir a Barcelona al laboratorio de Santi Nonell en el IQS (aprovecho para agradecerle a él y a todo su grupo, Roger, Joaquim, Cormac, y muchos otros por cómo me acogieron y me ayudaron), y esto me brindó una gran oportunidad para iniciar posteriormente mi tesis en IMDEA Nanociencia. David ha sido muy importante en todo este proceso, le debo mucho y le estoy enormemente agradecido.

Una vez se cerró la puerta de realizar la tesis en la UCM, busqué una oportunidad fuera de lo que yo hasta entonces conocía y la oferta para realizar la tesis que encontré consistía en preparar nanomateriales de carbono dentro del grupo de fotofísica de IMDEA Nanociencia, parecía hecho a medida. Aquí conocí a otro de mis directores de tesis, Reinhold. Le estoy muy agradecido por la oportunidad que me dio, y por todas las que vinieron después. Es una de las personas más trabajadoras que he conocido, con él he compartido mucho tiempo de trabajo, me ha enseñado mucho y espero haber aprovechado al máximo esta oportunidad.

Agradezco a todas aquellas personas que han participado directamente en el trabajo. Dentro de IMDEA Nanociencia quiero agradecer a Isabel Rodríguez, a Jaime J. Hernández, y a Alejandra Jacobo por todo lo que he aprendido con ellos y por "llevarme" al Sincrotrón ALBA, a Patricia Pedraz por toda su enseñanza y asistencia en el AFM, y a Cristina Navío por las horas de XPS y su excelente trabajo. Dentro del grupo de Materiales Moleculares Orgánicos a Ana Ferruelo y a Mª Ángeles por estar siempre pendientes y dispuestas para ayudar y aclarar las dudas burocráticas, y a todos los que ponen en marcha la maquinaria de los laboratorios y han trabajado de manera directa en la preparación de varios de los compuestos objeto de estudio en la presente tesis,

espero no olvidarme de ninguno ni ahora ni en el futuro: Chus, Paul, Patricia, Manu, Diego, Inés, Eider, Javi Ramos, Alfonso, Andrés y Javi Urieta. Mención especial merecen Antonio José Sánchez, Antonio Ribeiro, y Carlos Agudo, todos ellos han trabajado codo a codo conmigo, me han ayudado y de todos ellos he aprendido algo.

En IMDEA Nanociencia he trabajo durante cuatro años y he tenido muchos compañeros de trabajo que incluso han pasado a ser amigos, Iván, Adri, Gonzalo, Víctor, Alejandra, Joaquim, Patricia Bondia, Patricia Pedraz, Manu, Jaime, Andrea, Maite, Miguel, Sergio Dávila, Ingrid, Gudín, Marina, Juan Carlos, Marzoa, Miguel Ángel, Sergio Revuelta, Jorge, Víctor, Felipe y muchos, muchos otros. Una de las cosas de las que más agradecido me siento es de haber tenido la suerte de poder trabajar con amigos, de poder ir a trabajar con ganas y alegría. Muchas gracias a todos ellos por haber hecho esta etapa tan cómoda y agradable, gracias de verdad.

En estos momentos, en los que tienes que pensar cómo plasmar los agradecimientos de una tesis doctoral, no sabes ni por dónde empezar con tus padres. Lo son todo, les debes todo, y creo que lo único que puedes hacer para corresponderles es quererlos y hacer que se sientan orgullosos, espero estar haciéndolo, y seguir haciéndolo. En esta parte, no puedo olvidar a mi hermano. Es cierto que yo soy el mayor de los dos, el que lleva unos años de ventaja, pero creo que yo le debo más a él que él a mí. Nos entendemos y nos apoyamos a un nivel muy especial, aunque nos hemos ido distanciando es increíble ver cómo nuestra relación cada vez es más altruista y cariñosa.

Me gustaría también dedicar unas líneas de los agradecimientos a algunos cantantes, presentadores, o incluso a mi mascota, porque considero que me han ayudado a distraerme, han cambiado mi estado de ánimo, o simplemente, me han entretenido. Han estado omnipresentes en esta tesis, mientras escribía resultados, analizaba datos, de casa al trabajo y del trabajo a casa, e incluso, mientras estaba en el laboratorio. Y todas esas horas que he pasado con Leiva, Bruno Mars, Bad Bunny, Berto Romero, Buenafuente, Broncano, Jorge Ponce, Javier Santaolalla, Crespo, Jordi Wild e India, estoy seguro de que pueden haber influido en esta tesis.

Por último, y más importante, esta tesis no habría sido posible sin Paula. Me ha acompañado durante todos estos años, me ha apoyado, me ha escuchado, ha sabido siempre qué decirme para que todo llegue a buen puerto y me ha ayudado y aconsejado tanto en lo humano como en lo científico. Mi mayor golpe de suerte es tenerla a mi lado, espero que esto no cambie nunca, y espero seguir viendo cómo seguimos cumpliendo etapas apoyándonos mutuamente. Esta tesis también es tuya. Te quiero.

TABLE OF CONTENTS

List of acronyms

ABF Annular Bright-Field
AFM Atomic Force Microscopy
B-CNDs Blue-Carbon NanoDots
BE Binding Energy
CB Conduction Band
CCD Charge-Coupled Device
CEOS Corrected Electron Optical Systems
CI Chemical Ionization
CL Chemical Luminescence
CNDs, CDs, or C-dots Carbon NanoDots
CNG Curved Nano Graphene
CNPs Carbon Nano Particles
CQDs or C-QDs Carbon Quantum Dots
DG Double Layer Graphene
DLS Dynamic Light Scattering
DSSCs Dye-Sensitised Solar Cells
DWCNTs Double Walled Carbon Nanotubes
ECL Electrochemiluminescence
EDS Energy Dispersive X-ray Spectroscopy
EELS Electron Energy Loss Spectroscopy
EI Electron Ionisation
ESI Electrospray Ionization
ETA Expansion Trajectory Aberration Correction
FA Formic Acid
FCS Fluorescence Correlation Spectroscopy
FEG Field Emission Gun
FG Few Layer Graphene
FRET Föster Resonance Energy Transfer
FTIR Fourier-transform Infrared Spectroscopy
FWHM Full Width at Half Maximum
GIWAXS Grazing-Incidence Wide-Angle X-ray Scattering
GQDs Graphene Quantum Dots
HAADF High-Angle Annular Dark Field
HOPG Highly Oriented Pyrolytic Graphite
HPLC High Performance Liquid Chromatography
HR-TEM High-resolution Transmission Electron Microscopy
IR Infrared
LC-MS Liquid Chromatography – Mass Spectroscopy
LED Light Emitting Diode
MALDI Matrix-Assisted Laser Desorption/Ionization
MS Mass Spectrometry
MWCNTs Multi-Walled Carbon Nanotubes
MWCO Molecular Weight Cut-off
NIR Near-Infrared
PDT Photodynamic Therapy

PL Photoluminescence
PLE Photoluminescence Excitation
PS Photosensitizer
QY Quantum Yield
R-CNDs Red-Carbon Nanodots
SAXS Small-Angle X-ray Scattering
SERS Surface-Enhanced Raman Spectroscopy
SG Single Layer Graphene
siRNA small interfering Ribonucleic Acid
SQDs Semiconductor Quantum Dots
STEM Scanning Transmission Electron Microscope
SWCNTs Single-Walled Carbon Nanotubes
TCSPC Time-Correlated Single-Photon Counting
TRF Time Resolved Fluorescence
UHV Ultra high vacuum
UPLC Ultra High Performance Liquid Chromatography
UPLC-ESI-Q-TOF-MS/MS Ultra High Performance Liquid Chromatography – Electrospray Ionisation – Quadrupole Time-of-Flight – Mass Spectrometry/Mass Spectrometry
UV Ultraviolet
UV-Vis Ultraviolet-visible
VB Valence Band
WAXS Wide Angle X-ray Scattering
XPS X-ray Photoelectron Spectroscopy
XRD X-ray Diffraction

Resumen (Abstract)

RESUMEN

La parte principal de esta tesis se centra en la producción y caracterización de los nanopuntos de carbono. En cuanto a los métodos de producción de los CNDs elegidos en este trabajo, se han estudiado en detalle los CNDs producidos por dos métodos ascendentes claramente diferentes.

Por un lado, se ha utilizado el método solvotérmico. Este método consiste en calentar un líquido, en un recipiente cerrado, por encima de su punto de ebullición, generando una presión superior a la atmosférica, e induciendo así la condensación de los CNDs. Las ventajas evidentes de este método sintético son: es fácil, barato y respetuoso con el medio ambiente (siempre que el disolvente utilizado en el método solvotérmico sea un disolvente respetuoso con el medio ambiente, en nuestro caso hemos utilizado agua y etanol). Todas estas ventajas proporcionaron una gran oportunidad para preparar e investigar fácilmente los CNDs, los cuales, al ser preparados por este método, resultaron tener propiedades prometedoras como la solubilidad en medios acuosos, la biocompatibilidad, la actividad fotocatalítica en heteroestructuras con TiO_2 y propiedades biocidas que pueden ser empleadas para preparar superficies poliméricas biocidas. La combinación de las ventajas propuestas por el método sintético y las prometedoras propiedades de los productos obtenidos han hecho de este método el procedimiento sintético más común para la producción de CNDs.

Lo más habitual en este método de síntesis es trabajar a temperaturas relativamente bajas (< 250 °C), y aunque esto se consideró inicialmente una ventaja respecto al coste energético, pronto se demostró que el rendimiento de producción de los CNDs en sí era muy bajo y que el principal producto de la reacción eran pequeñas moléculas u oligómeros que ocultaban parcialmente las verdaderas propiedades de los nanodots de carbono.

Resaltando los aspectos más relevantes de la caracterización estructural de los nanodots de carbono sintetizados solvotérmicamente, es fundamental destacar la espectrometría de masas acoplada a la cromatografía líquida como técnica clave para entender los resultados de las otras técnicas de caracterización utilizadas, así como las propiedades fotofísicas observadas. La espectrometría de masas nos permitió identificar las pequeñas moléculas orgánicas conjugadas que se producen mayoritariamente durante la síntesis solvotérmica de los nanodots de carbono y que permanecen siempre unidas a las pequeñas estructuras grafíticas que también se producen durante la síntesis, aunque en un rendimiento mucho menor. La formación de estructuras grafíticas en la síntesis solvotérmica no es observable por espectrometría de masas. Sin embargo, hemos demostrado su existencia mediante HR-TEM, GI-WAXS y SERS, además se utilizaron FTIR y XPS para completar la caracterización estructural y dilucidar los grupos funcionales en la superficie.

Las propiedades fotofísicas de las CNDs sintetizadas hidrotermalmente sólo pueden entenderse tras identificar los subproductos moleculares formados, y tras caracterizar las propiedades fotofísicas de estas moléculas de forma aislada y compararlas con las de las CNDs. Hemos demostrado que el rendimiento de producción de las CNDs bajo las condiciones sintéticas típicas empleadas aquí es extremadamente bajo y que el rendimiento cuántico de las CNDs, después de la purificación, es también muy bajo, en contraste con muchos informes en la literatura. La absorción UV-Vis, la fluorescencia y los tiempos de vida de fluorescencia de las CNDs siguen estando dominados por las pequeñas moléculas formadas en la síntesis, así como por sus fotoproductos formados inherentemente (por la exposición a la luz ambiental, en presencia de oxígeno atmosférico a temperatura ambiente). Las pequeñas diferencias entre las propiedades fotofísicas de los CNDs y los productos moleculares aislados pueden atribuirse al hecho de que el entorno de los productos moleculares unidos al núcleo grafítico provoca ligeros desplazamientos en la absorción y la fluorescencia y una pequeña desviación en el tiempo de vida del singlete excitado que causa la fluorescencia. Uno de los principales resultados de la presente tesis es que no hay indicios experimentales de un efecto de tamaño cuántico en los CND estudiados aquí. En cambio, se ha demostrado que la dependencia de la longitud de onda de excitación de la emisión deriva de los fotoproductos producidos por la exposición a la luz y al oxígeno durante la diálisis. Sin embargo, a pesar del bajo rendimiento de producción del pequeño núcleo grafítico, se ha demostrado que son responsables casi exclusivamente de la formación de oxígeno singlete, e incluso se ha demostrado que los subproductos moleculares actúan como barredores de oxígeno singlete, lo que limita el tiempo de vida del singlete.

Por otro lado, también se ha utilizado la síntesis por láser pulsado para la preparación de nanopartículas de carbono. Mientras que la ablación por láser ha sido un enfoque descendente ampliamente explorado para la producción de nanopartículas, el uso de la luz láser para producir CNDs mediante un enfoque ascendente ha sido un método mucho menos explorado. En este caso, la energía láser es parcialmente absorbida por el material y puede reaccionar con él mediante procesos fototérmicos y fotoquímicos. Los procesos fototérmicos suelen predominar cuando el rayo láser está enfocado, donde se pueden superar saltos térmicos de 10^9 K/s; en caso contrario, predominan los procesos fotoquímicos, donde los fotones son lo suficientemente fuertes como para romper enlaces y generar radicales cuya recombinación conduce a la formación de nanoestructuras de carbono.

La principal ventaja de este método es su gran versatilidad, tanto en lo que respecta a las condiciones experimentales (longitud de onda de la irradiación láser, haz láser enfocado o desenfocado, energía por pulso, ...), como en lo que respecta a los precursores potencialmente utilizables (casi cualquier compuesto orgánico, que puede ser disuelto o fundido). Además, el proceso puede llevarse a cabo en presencia

de micropartículas inorgánicas que pueden desempeñar un papel catalizador, de dopaje o actuar como agentes funcionalizadores. En comparación con el método solvotérmico, éste puede ser un método más caro y menos respetuoso con el medio ambiente, pero como hemos mencionado, es versátil y novedoso, permite un control estricto de la composición de las nanopartículas y se pueden conseguir mayores rendimientos de producción de nanopartículas de carbono utilizando reactores de flujo fotoquímicos. Es importante destacar que no se detecta la formación de subproductos moleculares importantes.

Los resultados más destacables de la caracterización estructural de los nanodots de carbono sintetizados por láser pulsado se han obtenido gracias a la microscopía STEM, que ha permitido distinguir dos tipos de familias de CNPs producidos: los de estructura grafítica y los de estructura amorfa. Gracias a la espectroscopia EELS acoplada a STEM, se puede cuantificar la relación Csp^2/Csp^3 (esta información también se ha podido extraer de las áreas bajo la curva de las bandas D y G, características de este tipo de nanoestructuras en sus espectros Raman), así como cuantificar la presencia relativa de otros heteroátomos; y es con esta técnica que se pueden extraer dos conclusiones bastante sorprendentes sobre la síntesis con láser pulsado: la capacidad de modificar la hibridación Csp^2 del precursor para obtener CNPs con proporciones relevantes de Csp^3, así como la ausencia casi total de heteroátomos en las CNPs obtenidos a partir de precursores como la anilina o el clorobenceno. Finalmente, respecto a la estructura conocida de las CNPs sintetizadas por láser pulsado, se han identificado diferentes grupos funcionales superficiales gracias a la espectroscopia infrarroja.

Para discutir las propiedades fotofísicas de las CNPs preparadas con láser pulsado, es necesario considerar la gran variedad de muestras estudiadas, pero a pesar de ello, la mayoría de las propiedades son comunes. Todas ellas muestran una absorción muy fuerte en la región UV que se extiende hacia la región visible de forma decreciente, mostrando en algunos casos una notable absorción incluso a más de 600 nm. Todos las CNPs tienen una emisión más o menos amplia dependiente de la longitud de onda de excitación, es decir, a medida que aumenta la longitud de onda de excitación, el máximo de emisión se desplaza hacia el rojo. Sus rendimientos de fluorescencia a temperatura ambiente son relativamente bajos, entre el 3 y el 9 %, mientras que sus rendimientos de producción de oxígeno singlete a temperatura ambiente no son en absoluto despreciables, alcanzando valores del 37 % en algunos casos.

En relación con la posible aplicación de los sistemas estudiados, también se ha estudiado la capacidad fotocatalítica de los CNDs combinados con nanopartículas de TiO_2. Estas heteroestructuras CND@TiO_2 se prepararon mezclando mecánicamente B-CNDs (sintetizadas hidrotermalmente) y nanopartículas comerciales de TiO_2 y, tras asegurar la formación de estas heteroestructuras mediante la caracterización

estructural por diferentes técnicas (HR-TEM, espectroscopia FT-IR o espectroscopia UV-Vis), se comprobó su capacidad de fotodegradación de diferentes colorantes con diodos LED así como con un láser sintonizable.

La complejidad de la comprensión de las propiedades fotofísicas de las diferentes CNDs radica en que estas propiedades no pueden asociarse a una estructura perfectamente definida. Para entender mejor qué propiedades fotofísicas pueden asociarse a propiedades estructurales específicas, se han estudiado diferentes nanoestructuras de carbono con estructuras perfectamente definidas y de las que se deducen complejas relaciones entre las propiedades fotofísicas observadas y las particularidades estructurales específicas de estas nanoestructuras. El ejemplo relevante que se presenta en esta tesis es el estudio fotofísico de una serie de compuestos moleculares con un sistema π extendido con curvatura negativa y positiva (CNGs). Se observó que pueden mostrar en algunos casos dos mínimos del estado excitado singlete o dos mínimos del estado excitado triplete, lo que les confiere emisiones duales; también presentan TADF en un rango muy estrecho de bajas temperaturas que requieren la población de un estado triplete no emisor, así como la capacidad de producir oxígeno singlete a temperatura ambiente. Lo curioso y conceptualmente útil de estos sistemas es que su fluorescencia se encuentra en una situación intermedia entre un compuesto orgánico pequeño en el que existe un estado básico y un estado excitado perfectamente localizados y los CNDs en los que los defectos superficiales, las moléculas adsorbidas o ciertos grupos funcionales pueden hacer que existan varios estados excitados con, posiblemente, un cierto grado de deslocalización.

ABSTRACT

The main part of this thesis focuses on the production and characterisation of carbon nanodots. Regarding the production methods of the CNDs chosen in this work, CNDs produced by two clearly different bottom-up methods have been studied in detail.

On the one hand, the solvothermal method has been used. This method consists of heating a liquid, in a closed container, above its boiling point, generating a pressure higher than atmospheric pressure, and thus inducing the condensation of CNDs. The obvious advantages of this synthetic method are: it is easy, cheap and environmentally friendly (provided that the solvent used in the solvothermal method is an environmentally friendly solvent, in our case we used water and ethanol). All these advantages provided a great opportunity to easily prepare and investigate CNDs, which, when prepared by this method, were found to have promising properties such as solubility in aqueous media, biocompatibility, photocatalytic activity in heterostructures with TiO_2 and biocidal properties that can be employed to prepare biocidal polymer surfaces. The combination of the advantages proposed by the synthetic method and the promising properties of the products obtained have made this method the most common synthetic procedure for the production of CNDs.

The most common in this method of synthesis is to work at relatively low temperatures (< 250 °C), and although this was initially considered an advantage with respect to energy cost, it was soon shown that the yield of production of CNDs itself was very low and that the main product of the reaction were small molecules or oligomers that partially concealed the true properties of the carbon nanodots.

Highlighting the most relevant aspects of the structural characterisation of the solvothermally synthesised carbon nanodots, it is essential to highlight the mass spectrometry coupled to liquid chromatography as a key technique to understand the results of the other characterisation techniques used, as well as the observed photophysical properties. Mass spectrometry allowed us to identify the small conjugated organic molecules that are mostly produced during the solvothermal synthesis of the carbon nanodots and that always remain attached to the small graphitic structures that are also produced during the synthesis, although in a much lower yield. The formation of graphitic structures in solvothermal synthesis is not observable by mass spectrometry. However, we have demonstrated their existence by HR-TEM, GI-WAXS and SERS, in addition FTIR and XPS were used to complete the structural characterization and elucidate the functional groups on the surface.

The photophysical properties of hydrothermally synthesised CNDs can only be understood after identifying the molecular by-products formed, and after characterising the photophysical properties of these molecules in isolation and comparing them with those of the CNDs. We have shown that the yield of production of CNDs under the typical synthetic conditions employed here is extremely low and that the quantum yield of the CNDs, after

purification, is also very low, in contrast to many reports in the literature. The UV-Vis absorption, fluorescence and fluorescence lifetimes of the CNDs are still dominated by the small molecules formed in the synthesis, as well as by their inherently formed photoproducts (by exposure to ambient light, in the presence of atmospheric oxygen at room temperature). The small differences between the photophysical properties of the CNDs and the isolated molecular products could be attributed to the fact that the environment of the molecular products bound to the graphitic core causes slight shifts in absorption and fluorescence and a small deviation in the lifetime of the excited singlet causing the fluorescence. A main result of the present thesis is that there is no experimental indication for a quantum-size effect in the CNDs studied here. Instead the excitation wavelength dependence of emission has been shown to derive to photoproducts produced by exposure to light and oxygen during dialysis. However, despite the low production yield of the small graphitic core, it has been shown that they are almost exclusively responsible for singlet oxygen formation, and it has even been shown that the molecular by-products act as singlet oxygen scavengers, which limits the singlet lifetime.

On the other hand, pulsed laser synthesis has also been used for the preparation of carbon nanoparticles. While laser ablation has been a widely explored top-down approach for nanoparticle production, the use of laser light to produce CNDs via a bottom-up approach has been a much less explored method. In this case, the laser energy is partly absorbed by the material and can react with it by photothermal and photochemical processes. Photothermal processes usually predominate when the laser beam is focused, where thermal jumps of 10^9 K/s can be overcome; otherwise photochemical processes predominate, where the photons are strong enough to break bonds and generate radicals whose recombination leads to the formation of carbon nanostructures.

The main advantage of this method is its great versatility, both in terms of experimental conditions (wavelength of laser irradiation, focused or unfocused laser beam, energy per pulse, ...), and in terms of potentially usable precursors (almost any organic compound, that can be dissolved or molten). Furthermore, the process may be carried out in the presence of inorganic microparticles that can play catalytic, doping or act as functionalizing agents. Compared to the solvothermal method, this can be a more expensive and less environmentally friendly method, but as we have mentioned, it is versatile and novel, allows strict control of nanoparticle composition and higher production yields of carbon nanoparticles can be achieved by using photochemical flow reactors. Importantly, no major molecular by-product formation is detected.

The most remarkable results of the structural characterisation of carbon nanodots synthesised by pulsed laser are obtained thanks to STEM microscopy, which has allowed us to distinguish two types of CNPs families produced: those with a graphitic structure and those with an amorphous structure. Thanks to EELS spectroscopy coupled to STEM, the Csp^2/Csp^3 ratio can be quantified (this information could also be extracted from the areas under the curve of the D and G bands, characteristic of this type of nanostructures in their

Raman spectra), as well as quantifying the relative presence of other heteroatoms; and it is with this technique that two rather surprising conclusions about pulsed laser synthesis can be drawn: the ability to change the Csp^2 hybridisation of the precursor to obtain CNPs with relevant proportions of Csp^3, as well as the almost total absence of heteroatoms in the CNPs obtained from precursors such as aniline or chlorobenzene. Finally, with respect to the known structure of the CNPs synthesized by pulsed laser, different surface functional groups have been identified thanks to infrared spectroscopy.

To discuss the photophysical properties of pulsed laser-prepared CNPs, it is necessary to consider the wide variety of samples studied, but despite this, most of the properties are common. All of them show a very strong absorption in the UV region that extends towards the visible region in a decreasing way, in some cases showing a remarkable absorption even at more than 600 nm. All CNPs have more or less broad emission depending on the excitation wavelength, i.e. as the excitation wavelength increases, the emission maximum shifts towards the red. Their fluorescence yields at room temperature are relatively low, between 3 and 9 %, while their singlet oxygen production yields at room temperature are not at all negligible, reaching values of 37 % in some cases.

In relation to the potential application of the studied systems, the photocatalytic capacity of CNDs combined with TiO_2 nanoparticles has also been studied. These CND@TiO_2 heterostructures were prepared by mechanically mixing B-CNDs (hydrothermally synthesised) and commercial TiO_2 nanoparticles and, after ensuring the formation of these heterostructures by means of structural characterisation by different techniques (HR-TEM, FT-IR spectroscopy or UV-Vis spectroscopy), their capacity of photodegradation of different dyes was tested with LEDs as well as a tunable laser.

The complexity of understanding the photophysical properties of different CNDs is that these properties cannot be associated with a perfectly defined structure. In order to better understand which photophysical properties can be associated with specific structural properties, different carbon nanostructures with perfectly defined structures have been studied and from which we can deduce complex relationships between the observed photophysical properties and the specific structural particularities of these nanostructures. The relevant example reported in this thesis is the photophysical study of a series of molecular compounds with an extended π system with negative and positive curvature (CNGs). It was observed that they can show in some cases two minima of the singlet excited state or two minima of the triplet excited state, which confers them dual emissions; they also present TADF in a very narrow range of low temperatures that require the population of a non-emitting triplet state, as well as the capacity to produce singlet oxygen at room temperature. What is curious and conceptually useful about these systems is that their fluorescence is in an intermediate situation between a small organic compound where there is a perfectly localised ground state and excited state and CNDs where surface defects, adsorbed molecules or certain functional groups can cause several excited states to exist with possibly a certain degree of delocalisation.

1

General Introduction

1. GENERAL INTRODUCTION

Carbon has undoubtedly played important role throughout human history. The variety of properties exhibited by this natural element provide multiple benefits and biotechnological applications to our society, and the methods for obtaining, characterising and using it have evolved significantly up to the present day.

This consideration of carbon was already evident in prehistoric times, where soot and charcoal began to be used as a dye and fuel, playing a very important role in the evolution of humanity. Also noteworthy is the remote use of charcoal for medicinal purposes to adsorb the odorous vapours of putrefying wounds (recorded in Egyptian papyri around 1500 BC). And we cannot ignore that carbon has been a fundamental part of written communication, being used by the ancient Egyptians in the form of soot for the decoration of their tombs, as a raw material for the production of ink in the Chinese civilization and as graphite powder for pencil tips.

Despite its omnipresence, carbon was not recognised as a chemical element until the end of the 17th century and since then it has been put to countless other uses. Among the most significant milestones in the use of carbon are its use in the production of steel, the process of vulcanising tyres with carbon black, the implementation of carbon switches in computer systems in order to make smaller and lighter computers, and the development of primary batteries, which over the years have evolved into lithium-ion batteries.

These examples show that the versatile properties of elemental carbon, its low cost, its accessibility, the easy processing of various raw materials and the variety of structures obtained (powders, fibres, fabrics, ...) have attracted great economic and industrial interest. As a result of this constant interest, a large amount of valuable research has been carried out in various disciplines. It is essential to mention the works that have awakened new trends in the knowledge of the structure and properties of carbon materials and that have contributed to the benefit of society; such is the case of the discovery and development of conductive polymers (Shirakawa et al. 1977, Nobel Prize in Chemistry in 2000),[1] the synthesis of fullerenes (Kroto, et al. 1985, Nobel Prize in Chemistry in 1996),[2] the discovery of carbon nanotubes (Iijima, 1991, Prince of Asturias Award for Technical and Scientific Research in 2008),[3] or the isolation and studies on graphene (Geim and Novoselov 2007, Nobel Prize in Physics in 2010).[4]

All the above, together with the exponential growth of nanoscience and nanotechnology, mainly in the last decades, has led to a considerable part of scientific research being focused on the production of nanostructured carbon materials. The structural diversity of these nanomaterials (nanodiamonds, fullerenes, nanotubes, nanoclusters, graphene, ...) provide a variety of unique mechanical, electronic, magnetic and optical properties, which when combined with their chemical versatility,

ease of handling, and biocompatibility make them attractive candidates for application in high impact areas.[5-8]

There is no agreed classification of carbon nanostructures. A classification could be made based on the dimensionality of the structures, distinguishing four types of carbon nanostructures: i) zero-dimensional (OD) structures, such as fullerenes, carbon nanodots or finite-sized graphenes; ii) one-dimensional (1D) structures, such as carbon nanotubes, nanobuds and nanoribbons; iii) two-dimensional (2D) structures, such as graphene; and iv) three-dimensional (3D) structures, such as graphite and diamond (Fig. 1.1).[6]

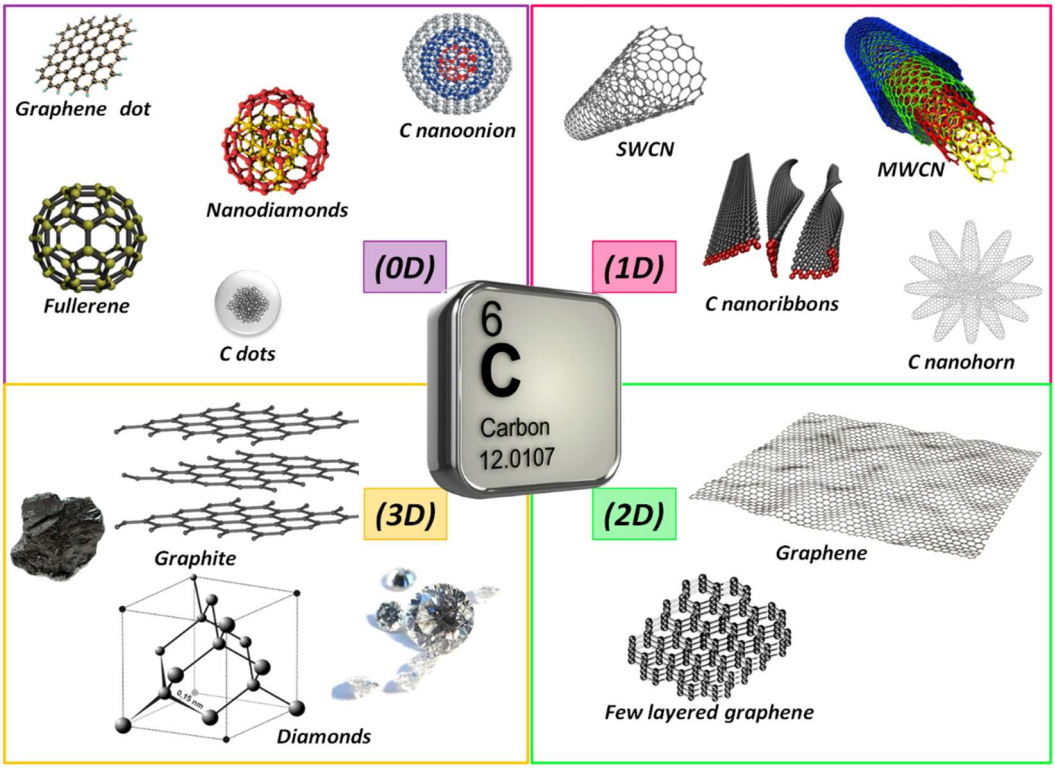

Figure 1.1. Classification of carbon nanostructures based on the dimensionality of the structures.

In particular, carbon nanodots (quasi zero-dimensional carbon allotropes with pseudo-spherical structures of a few nanometres in diameter) have generated significant and growing interest in scientific and technological circles. This interest is reflected in the large number of studies that have been carried out on carbon nanodots in high-impact journals (Fig. 1.2), in which a variety of synthetic approaches have been proposed, their properties have been discussed, and their potential applications (in areas of the greatest impact such as biomedicine, photocatalysis, or energy conversion) have been deeply debated.[9-21]

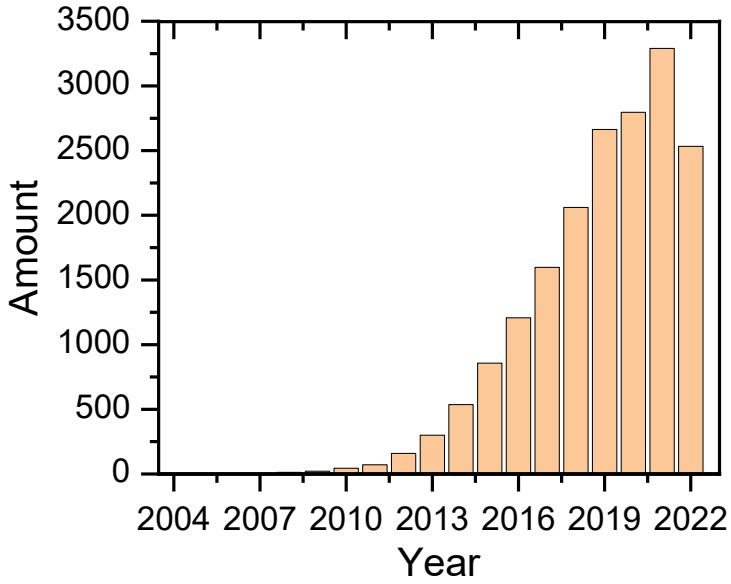

Figure 1.2. Number of publications from 2004 to 2022 found by searching for "carbon dots", "carbon nanodots" or "graphene quantum dots" in Web of Science.

2

Background

2.1. Carbon materials

2.1.1. Carbon, the chemical element

Carbon is the chemical element with symbol C, atomic number six, atomic mass 12.011 uma and electronic configuration in the fundamental state $1s^2\ 2s^2\ 2p^2$. It is the sixth most abundant element in nature and exists mainly in the form of the ^{12}C isotope (98.89 %).[22]

In the elemental state, the carbon atom has two unbound electrons, but can form excited states by transferring an electron from the 2s orbital to the unoccupied 2p orbital, leaving four unbound electrons and thus available for bond formation. In other words, the electronic configuration of carbon in the ground state is $1s^2\ 2s^2\ 2p^2$, and an excited state $1s^2\ 2s^1\ 2p^3$ can be obtained.[23]

To reduce the energy of the excited state, in solid form of carbon, the carbon atom has the ability to modify its atomic orbitals by forming different hybrid orbitals (Fig. 2.1):[23]

- Combining the 2s orbital of the excited state with one of the three 2p orbitals forms two equivalent hybrid orbitals called sp orbitals. These hybrid orbitals have a linear arrangement with an angle of 180°, while the remaining two 2p orbitals are unperturbed.
- In the case where the 2s orbital of the excited state is combined with two 2p orbitals, three equivalent hybrid orbitals called sp^2 orbitals are formed. These hybrid orbitals adopt a triangular geometrical arrangement with an angle of 120°, while the electron remaining in the other 2p orbital is placed perpendicular to the plane formed by the sp^2 orbitals.
- When the 2s orbital of the excited state combines with the three 2p orbitals, it forms four hybrid orbitals called sp^3 orbitals. In this case, the hybrid orbitals are oriented in space in a tetrahedral arrangement at an angle of 109.5°.

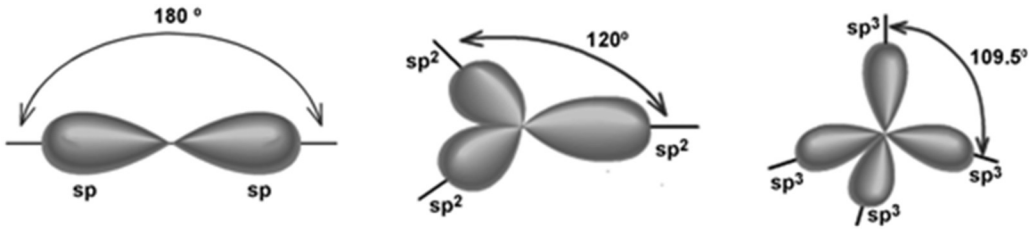

Figure 2.1. Carbon hybrid orbitals.[23]

It is well known that carbon tends to form sigma (σ-type) covalent bonds by head-on interaction between two atomic orbitals, since σ bonds are the strongest type of covalent chemical bond. On the other hand, pi (π-type) covalent bonds are covalent chemical bonds where side-by-side interaction between two p-orbitals occur. A carbon atom has the ability to form four σ-type sp^3 hybridized bonds with an average C–C bond length of 153 pm and bond-dissociation energy at 298 K between 347–377 kJ

mol^{-1}. Carbon atoms are able to form sp^2 hybridized double bonds that arise from combining a σ-bond and a π-bond, which results from the interaction between the electrons in the unhybridised 2p orbitals of two carbon atoms in this configuration. This double bond (σ+π) increases the bond strength so that the C=C length is reduced to 134 pm while the bond-dissociation energy at 298 K increases up to 710 kJ mol^{-1}. Finally, sp-hybridised carbon atoms form triple bonds as a result of combining a σ-bond and two π-bonds (which come from the two unhybridised 2p orbitals that two carbon atoms have in this configuration). This triple bond (σ+2π) is even stronger so that the C≡C bond distance decreases to 120 pm and the bond-dissociation energy at 298 K reaches 960 kJ mol^{-1}.[23]

2.1.2. Macroscopic allotropic forms of carbon

Carbon's ability to modify its atomic orbitals to form different types of hybrid orbitals allows the existence of allotropic forms (Fig. 2.2). The literature lists various macroscopic and nanoscopic allotropes for elemental carbon, of which cubic diamond and graphite are the most common and best known macroscopic structures.

In graphite, the carbon atoms have sp^2 hybridization and are located at the vertices of regular hexagons forming sheets which are arranged in parallel layers separated by a distance of 0.3354 nm, a value that corresponds to twice the van der Waals radius of the carbon atom. Depending on its packing, from a crystallographic point of view, graphite can be classified into two structural types: hexagonal and rhombohedral, but only hexagonal graphite is thermodynamically stable below 2600 K and 6 GPa.[24] The lattice is made up of very stable layers that are weakly bound together, resulting in a large anisotropy in properties. For example, in the case of electrical conductivity, electrons can move within each layer (due to the existence of an energy band partially occupied by the delocalised electrons of the unhybridised 2p orbitals) but cannot move from one layer to another.[25]

The tetrahedral arrangement of sp^3-hybridised carbon atoms generates the three-dimensional structure that gives rise to diamond. In diamond, each carbon atom is surrounded by four neighbouring atoms at an equal distance of 0.1544 nm. Depending on the packing of the carbon atoms, two structural types can be distinguished: cubic and hexagonal.[24] Although the hardness of diamond is its most characteristic feature, the presence of impurities (such as boron or nitrogen) within the structure induces changes in its electrical, optical and thermal properties which are of great importance for its industrial applications.[26] In contrast to sp^2 hybridized carbon sp^3 hybridized carbon are semiconductors, in the case of diamond with a very large bandgap, making it an electric insulator at room temperature.

Besides graphite and diamond, which are crystalline allotropes of carbon, amorphous carbon is the term usually used for carbon lacking any macroscopic crystalline structure. However, although there is no long-range pattern concerning the

atomic positions, some short-range order can be observed in amorphous carbon, and most amorphous carbon actually can contain microscopic crystals of graphite-like or even diamond-like carbon. Coal and soot or carbon black are informally called amorphous carbon, however, they are formed by the action of heat, which does not produce true amorphous carbon under normal conditions. It often contains carbon nanodots, fullerenes or carbon nanotubes.

Finally, the nature of a linear acetylenic carbon chain formed by sp-hybridised carbon atoms has been a matter of controversy since its discovery by a group of Russian scientists in the 1960s who named it carbyne.[27] In these chains of sp-hybridised carbon atoms, the bonds can be arranged in two possible configurations: alternating single and triple bonds (polyyne) and repeating of double bonds (polycumulene).[28]

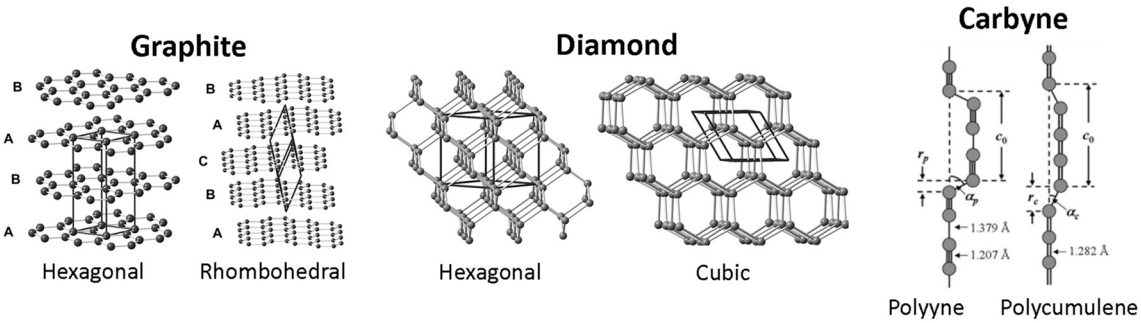

Figure 2.2. Structural representation of the allotropic forms of graphite, diamond and carbyne.[24, 28]

2.1.3. Classification of carbon nanostructures

Carbon nanostructures can be defined as carbon materials that are produced in such a way that their size is controlled on the nanometre scale (0.1 -100 nm) in at least one dimension.

Among the possible classifications of carbon nanostructures (see Fig.1.1), the type of hybridization present in carbon atoms is one of them.[27] According to this concept, two main types can be considered:

- Mixed carbon forms composed of carbon atoms with different states of hybridization, for example: diamond-like carbon, glassy carbon, carbon black or hypothetical structures such as "superdiamonds".
- Intermediate forms of carbon with an intermediate order of hybridization (sp^n). The subgroup with $1<n<2$ includes monocyclic carbon structures, while for $2<n<3$ it includes closed nanostructures such as fullerenes, nano-onions or nanotubes.

Figure 2.3 shows a classification of carbon nanostructures based on both the type of hybridization and the characteristic size of the nanostructures. In a first group, in the inner circle, are molecular fragments (requiring at least some hydrogen termination), which by extension give rise to fullerenes, nanotubes, finite-sized

graphenes and nanodiamonds, located at a second level. The next structural level considers structural units that arise by increasing in size from simple forms, e.g. multi-walled carbon nanotubes (MWCNTs), nano-onions, or architecturally more complicated forms such as carbon black. Finally, at the outermost level, there are materials with micro/macroscopic dimensions such as diamond, graphite, fullerite and the recently described macroscopically sized single-walled carbon nanotubes (SWCNTs).[6]

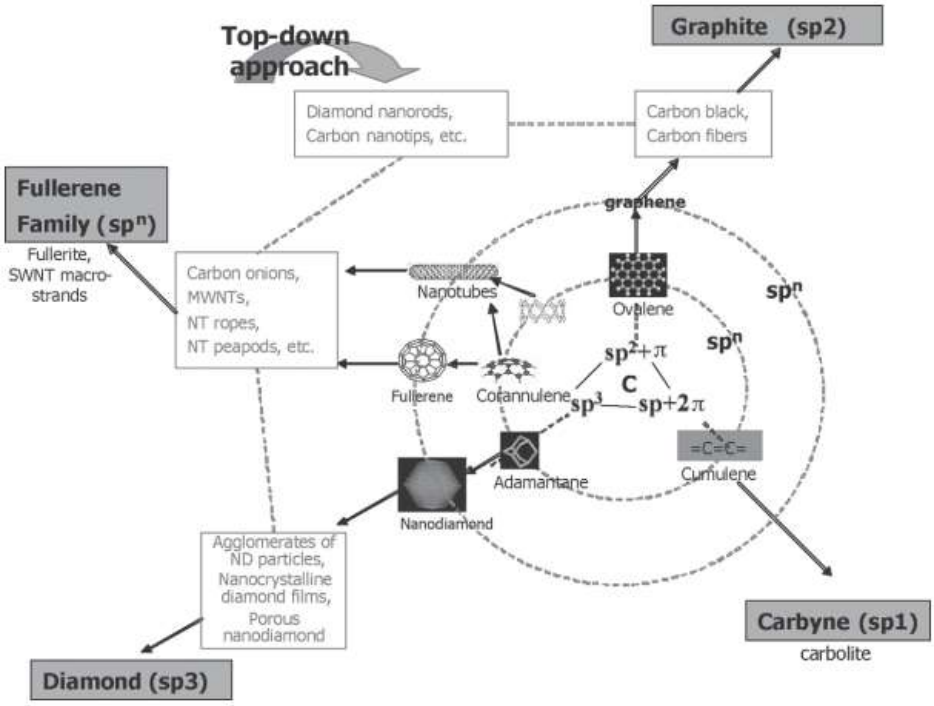

Figure 2.3. Mixed classification of carbon nanostructures based on the hybridization of the atomic orbitals (integers sp^1, sp^2, $sp^3$and fractional sp^n) and the size of the structure increasing from the centre to the outside of the rings.[6]

2.1.4. Most relevant carbon nanostructures

2.1.4.1. Graphene

Graphene is a two-dimensional (2D) one-atom-thick material composed of hexagons with sp^2-hybridised carbon atoms at the vertices. It can be considered to be a single sheet of graphite and also a structural precursor to other carbon structures: it can be rolled into a cylindrical shape to form SWCNTs or MWCNTs if several graphenes are rolled together. If the graphene is defective in a certain proportion (pentagons instead of hexagons), it can be wrapped into a spherical or ellipsoid shape, as is the case with fullerenes and nano-onions. Or it can be stacked into the three-dimensional shape graphite (Fig. 2.4).[4]

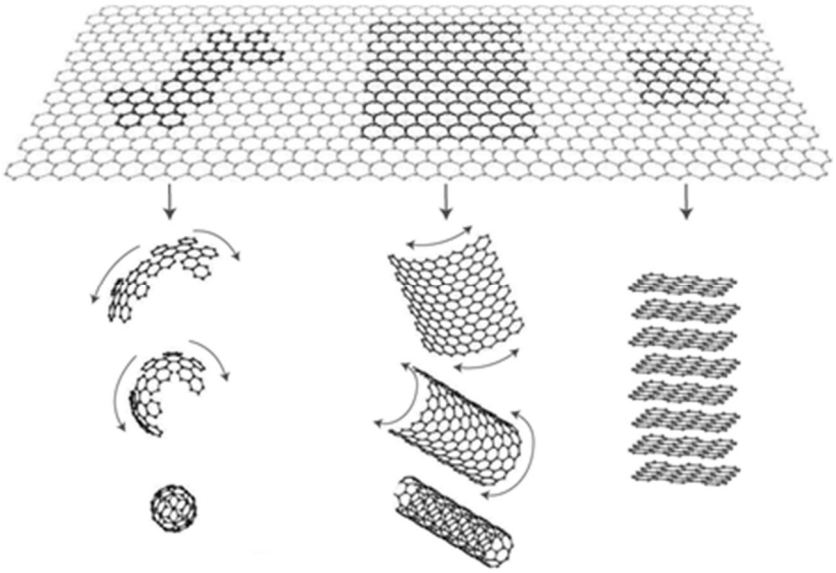

Figure 2.4. Graphene as structural precursor of the various forms of graphitic carbon.[4]

Although graphene is the name given to a single sheet of carbon atoms, there are single layer graphene (SG), double layer graphene (DG) and few layers graphene (FG, with a number of layers ≤ 10).[29]

Graphene properties are truly exceptional, in short: the valence and conduction bands of graphene overlap slightly, which makes this material a zero-bandgap semiconductor with high electronic mobility at room temperature (> $1.5 \cdot 10^4$ cm^2 V^{-1} s^{-1}); its magnetic behaviour is atypical and very interesting, since it exhibits a quantum Hall effect even at room temperature; it has a high thermal conductivity ($5 \cdot 10^3$ W m^{-1} K^{-1}); it absorbs a relatively high fraction of light (about 2.3 %) with little dependence on its wavelength in the visible spectrum; and it has a high mechanical strength. The main limitations of graphene in view of applications are its poor dispersion in solvents and its strong trend to self-aggregation.[29]

The potential applications of graphene are very interesting due to its exceptional properties. Therefore, a large number of applied research studies have been initiated in the last few years aiming to the use of graphene in gas sensors, transistors, ultracapacitor components, integrated circuit components, etc.[29]

Excitons (electron-hole pairs attracted by the electrostatic Coulomb force) in graphene have large Bohr diameter, therefore, graphene fragments termed as graphene quantum dots, GQDs, can give rise to exciton confinement as well as quantum size effects which are still under study. Unlike graphene, graphene fragments have a bandgap greater than zero that can be tuned by modifying the size and chemistry of their surface, which causes them to luminesce when excited. Their properties and peculiarities, as well as the synthesis methods used to prepare these GQDs, will be discussed below.[30]

2.1.4.2. Carbon nanotubes

The discovery of carbon nanotubes is attributed to S. Iijima in 1991, found as a by-product of the synthesis of fullerenes.[3] Carbon nanotubes can be described as cylinders (diameter 0.3-100 nm and length 10 nm-µm) that can be closed at the ends by a hemi-fullerene. In carbon nanotubes, the carbon atoms are in an intermediate state of hybridization between sp^2 and sp^3, although they are closer to sp^2.

There are many types of nanotubes and they can be classified according to different criteria (Fig. 2.5):[31]

- According to the number of nanotube walls, there are single-walled (SWCNTs), double-walled (DWCNTs) and multi-walled (MWCNTs) nanotubes.
- Depending on the way the graphene sheet is bound, if it is connected parallel to the tube axis, a "zig-zag" configuration is obtained, if it is attached perpendicular to the tube axis, an "armchair" configuration is obtained. A third possibility for rolling up a graphene sheet is to rotate it at a certain angle before closing it. In this configuration, the carbon atoms are arranged helically around the axis of the tube in a chiral configuration.

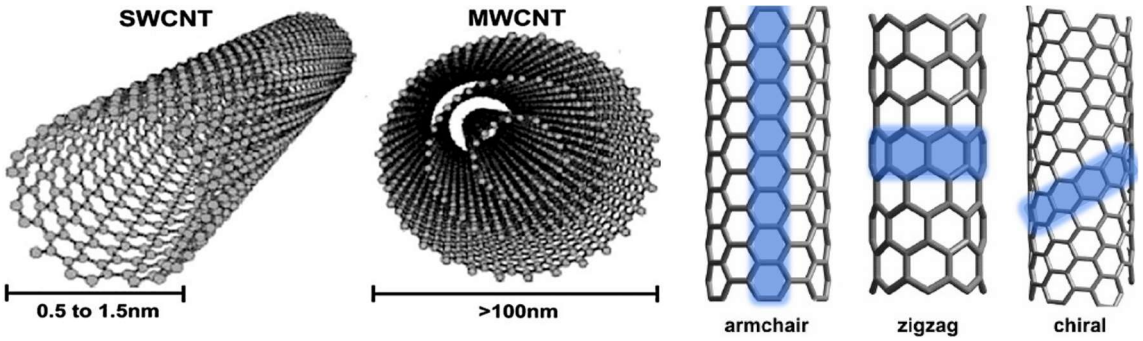

Figure 2.5. Different types of carbon nanotubes depending on the number of layers and the roll-up of the graphene.

Considering that the properties of carbon nanotubes depend critically on the type of nanotube, its dimensions, chirality, etc., its most relevant characteristics are: its high mechanical strength (about 1000 times more than in a steel fibre), its high chemical stability, and its high conductivity (~10^6 times more than metallic copper). Carbon nanotubes can be electrically conductive or semiconducting depending on whether the carbon atoms are in an armchair (metallic), zig-zag or chiral (semiconducting) arrangement, respectively.[31]

Their exceptional properties have catapulted carbon nanotubes into the field of technological applications such as batteries, reinforced materials, electrochemical transducers and sensors. Importantly, open-tipped carbon nanotubes have a potential application for reversible hydrogen storage, providing an important role in a future economy based on harnessing hydrogen as an energy source.[32]

2.1.4.3. Fullerene

Fullerenes are a family of materials consisting of a hollow cluster formed by a number of carbon atoms. The most common of the fullerenes is the C_{60} structure called "buckminster fullerene-C_{60}" (Fig. 2.6).[2] It is a very small molecule (van der Waals diameter = 10.34 Å) where the sixty carbon atoms are located at the vertices of a regular truncated icosahedron (giving it icosahedral symmetry with all carbon atoms chemically equivalent). The average distance between the carbon atoms is 0.144 nm, although two different bond distances of 0.137 nm and 0.145 nm can be distinguished. The truncated icosahedron is formed by twenty regular hexagons and twelve pentagons and therefore satisfies Euler's rule. This theorem states that a closed structure consisting of hexagons and pentagons must contain twelve pentagons and an arbitrary number of hexagons.[33]

According to Euler's theorem, the smallest possible fullerene is the C_{20} consisting of twelve pentagonal faces, however, this structure is energetically unstable according to the isolated pentagon rule (to minimise local curvature the pentagons must be separated from each other). The addition of a hexagon brings two carbon atoms so that the rest of the C_n fullerene series can be predicted. Other prominent members of the fullerene family are C_{70}, C_{80}, C_{240}, C_{320}, or C_{960}.[33]

Among the properties of fullerenes, it is necessary to mention that:[33]

- Fullerenes are stable, but not totally inert. The carbon atoms must bend to form a sphere, which produces an angular tension that enhances reactivity. The most characteristic reaction is the electrophilic addition to the double bonds, which reduces the angular tension and contributes to the stability of the fullerene molecule.
- The solubility of fullerenes is poor in most solvents. The most commonly used solvents are those consisting of aromatic organic compounds such as benzene and toluene, and carbon disulphide derivatives. Their solubility in water is extremely low ($1.3 \cdot 10^{-11}$ mg/mL).
- With regard to toxicity, there is little evidence of harmful effects of C_{60} fullerene.

Fullerene molecules have not had a major practical impact but have recently started to be used in medicine as antibiotic carriers and as light-activated antimicrobiological agents.[33.]

Like multi-walled carbon nanotubes, when several layers of fullerenes are arranged concentrically, carbon nano-onions emerge (Fig 2.6.). Predictably, carbon nano-onions are highly insoluble, and their reactivity is moderately low, which makes them similar to graphite concerning its chemical inertness.[34] Both MWCNTs and nano-onions show a larger interplanar distance than graphite (0.3354 nm), which can reach up to 0.42 nm.[35]

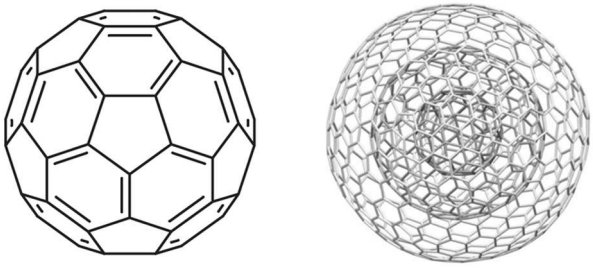

Figure 2.6. Structure of [60]fullerene (left) and structure of the nano-onions (right).

2.1.4.4. Carbon materials with disordered structure

IUPAC suggests the expression carbon materials for those solids with high elemental carbon content and structurally in a non-graphitic state. A first classification for carbon materials arising from pyrolysis of various organic materials was proposed in 1951 (Fig. 2.7):[36]

- Graphitizable carbon materials: they arise from precursors with a high hydrogen content and consist of small crystallites that have a high tendency to be arranged in parallel.
- Non-graphitizable carbon materials: these come from substances with little hydrogen or a lot of oxygen, and consists of small randomly oriented crystallites.

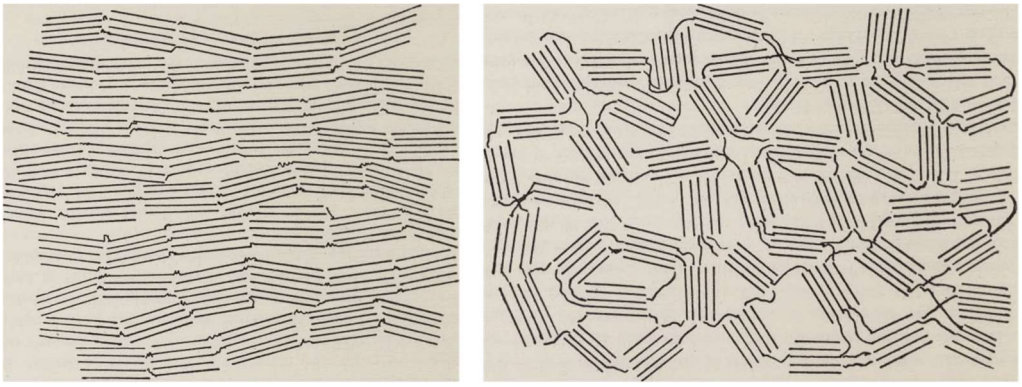

Figure 2.7. Schematic representation of the structure of graphitizable (left) and non-graphitizable (right) carbon materials.[36]

Carbon materials with a disordered structure include (Fig. 2.8):

- Carbon black: has a characteristic morphology in the form of loose, aggregated or fused spheres in a size range from 10 nm to 1 µm. Carbon black is a combination of disordered carbon units and small concentrically arranged graphite-like conglomerates.[37]
- Glass-like carbon: the most recent studies suggest that it is formed by small curved sheets of carbon, in which the atoms forming pentagons and heptagons in the hexagonal lattices produce the curvature.[38]
- Carbon fibres: are formed by a weave of carbon filaments (diameter 5 - 10 µm), where the carbon atoms are found forming sheets more or less aligned parallel

to the longitudinal axis of the fibre. In graphite the sheets are flat and have an orderly stacking, whereas in carbon fibres the sheets are bent and randomly arranged.[39]

- Activated carbon: this is composed of graphene-like sheets called basal planes, which are irregularly stacked and are joined together randomly, giving rise to highly porous structures.[40]

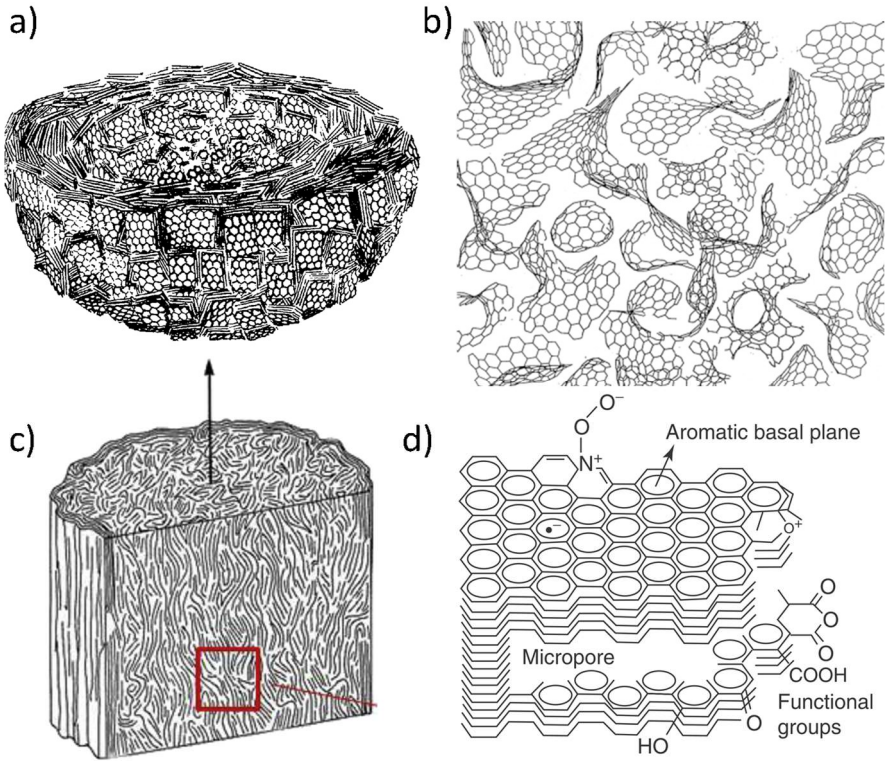

Figure 2.8. Structural models of carbon black a), glass-like carbon b), carbon fibre c), and activated carbon d).[37-40]

2.1.4.5. Carbon nanodots

First of all, in nanoscience the term "nanodot" refers to structures or particles of nanometric size, whose interest lies in the fact that they exhibit properties that cannot be observed in either molecules or macroscopic materials. On the other hand, the term "quantum dot" refers to nanostructures that confine the motion in all three spatial directions of conduction band electrons and valence band holes or excitons (electron and electron-hole pair attracted by the electrostatic Coulomb force). The term implies the existence of quantum size effects as in semiconductor quantum dots.

So-called "carbon quantum dots" or "carbon nanodots" refer to carbon nanostructures that are typically smaller than 20 nm in size and often exhibit unique optical characteristics (excitation wavelength-dependent fluorescence, modulated emission and high photostability) that are not observed in other carbon nanostructures. In addition, unlike inorganic semiconducting quantum dots (SQDs), carbon nanodots generally exhibit low toxicity and good solubility in various solvents

(including water), making them much easier to handle and much more desirable for many applications.

The different types of carbon nanodots could be classified into three main categories based on their structure and whether or not they exhibit quantum confinement (Fig. 2.9):[20]

- Carbon NanoDots (CNDs): these are quasi-spherical (< 10 nm) amorphous carbon nanodots, consisting mainly of Csp^3, which lack quantum confinement. They have been given different names in the literature, such as carbon nanoclusters, polymer dots, carbon dots or carbogenic dots.
- Carbon Quantum Dots (CQDs): refers to quasi-spherical carbon nanodots (< 10 nm) consisting predominantly of graphene nanoflakes combined with amorphous carbon, which exhibit quantum confinement. Such carbon nanodots have been proposed conceptually by previous authors but the evidence that they exist and that the properties attributed to them actually correspond to carbon nanodots themselves is a matter of great controversy.
- Graphene Quantum Dots (GQDs): refers to carbon nanodots based on a fragment of a single graphene sheet (< 20 nm) that exhibit quantum confinement.[30]

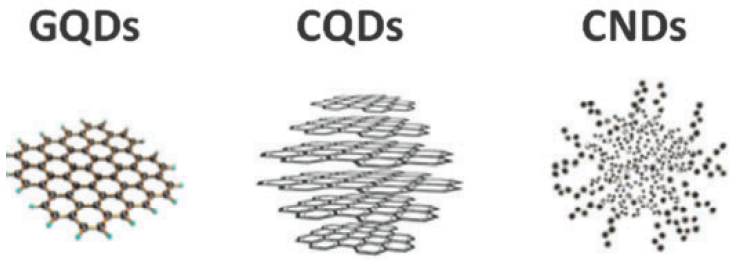

Figure 2.9. Classification of carbon nanodots: GQDs (Graphene Quantum Dots), CQDs (Carbon Quantum Dots) and CNDs (Carbon NanoDots).[20]

2.1.4.5.1. Methods for the synthesis of carbon nanodots

Since the accidental discovery of fluorescent carbon nanoparticles as a by-product in the synthesis of carbon nanotubes and the realisation that these contained novel carbon nanostructures, there has been a growing interest in the development of specific synthetic methods for carbon nanodots.

The first proposed synthesis processes consisted of fragmentation of macroscopic carbon sources (top-down methods, Fig. 2.10) where the aim was to induce or retain the crystalline organisation of the carbon cores of these fragments and to functionalise their surface.

Shortly after the first methods for the production of carbon nanodots appeared in the literature, it was shown that their synthesis could be carried out using readily

available precursors (organic solvents, saccharides, amino acids, proteins, ...) that are assembled to produce the carbon nanostructure (bottom-up methods, Fig. 2.10).

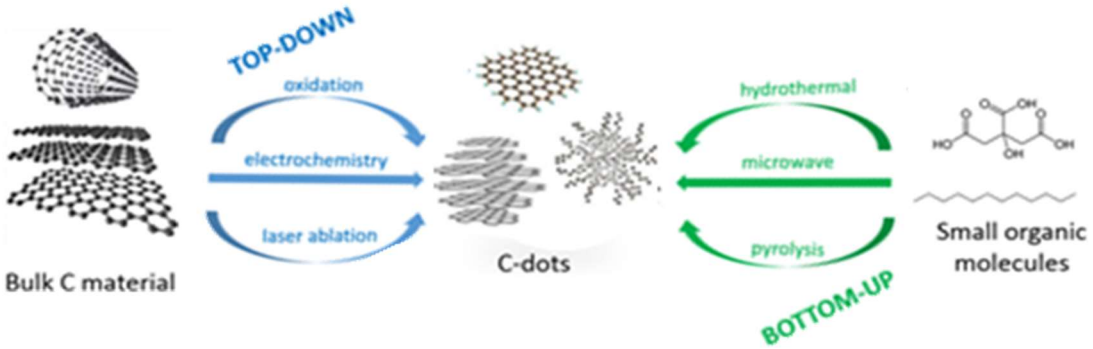

Figure 2.10. Top-down and bottom-up approaches most relevant to the production of carbon nanodots.

A first representative example of a top-down approach to building carbon nanodots is laser ablation (Fig. 2.11). It is well known that the high energy delivered by the laser beam causes ablation, or removal of particles from inorganic solid substrates, and it has been observed that the substances thus removed appear at the nanoscale. This phenomenon also occurred in one of the first demonstrations of carbon nanodots production by applying laser ablation (using an Nd-YAG laser) on graphite powder;[41] and since then this method has been widely explored in the literature using different precursors such as amorphous or graphitic carbon or in large carbon nanomaterials such as nanotubes, nanoclusters or even molecular entities such as [60]fullerene.[42-46]

More recently, it was also shown that laser synthesis could be used in a bottom-up approach, starting from readily available precursors such as organic solvents. Therefore, pulsed laser synthesis has generated endless possibilities since it is possible to use laser irradiation of different wavelengths, of different power and with or without focusing systems.[42, 47-51]

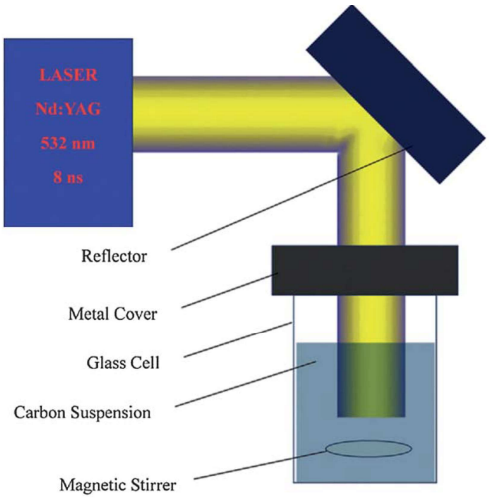

Figure 2.11. Schematic illustration of laser ablation experimental setup.[43]

Electrochemical methodologies have also been used for the synthesis of carbon nanodots (Fig. 2.12). Generally, electrodes (cathode and/or anode) made of carbon, typically graphite, are introduced into an electrolytic solution where the passage of current causes the graphite to splinter, generating the nanodots. This method has been widely used, as the technique is easy to carry out and the product yield is usually high. However, an apparent limitation is the wide distribution of sizes and morphologies of the carbon nanodots obtained, necessitating further separation and purification steps.[52]

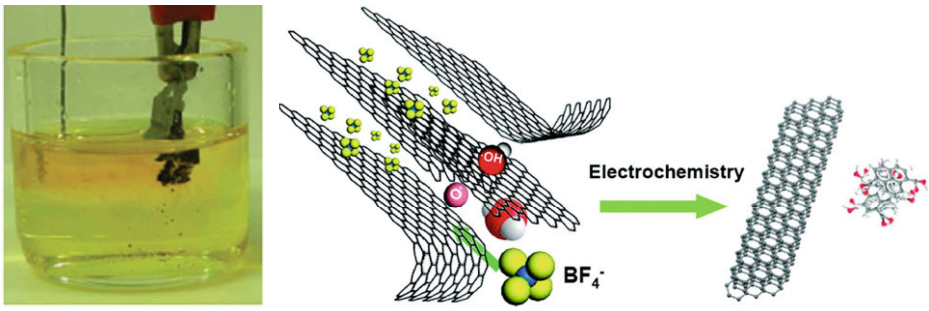

Figure 2.12. Production of carbon nanodots through exfoliation of graphite in ionic liquids. The photograph shows that the graphite anode is placed in an electrolyte solution comprising the ionic liquid. In the illustration of the proposed mechanism, the ions penetrate between the graphite sheets, generating carbon nanotubes and carbon nanodots.[52]

Numerous other synthetic routes have used "wet chemistry" to produce carbon nanodots. It was observed that by treating carbon precursors with a strong oxidising acid (such as nitric acid), they fragmented and small nanoparticles were produced (Fig. 2.13). The oxidation properties of the acid play a crucial role in the production of surface defects containing oxygen and nitrogen, thus defining their photoluminescence. These methods demonstrated that carbon nanoparticles could be produced in large quantities from readily available reagents, by easily applicable synthetic schemes and without the need for sophisticated and/or expensive instrumentation.[53-55.]

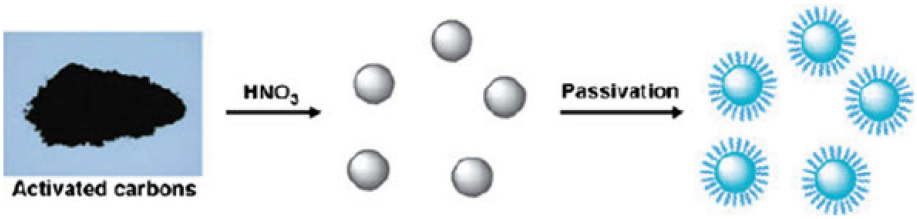

Figure 2.13. Synthesis of carbon nanodots from activated carbon.[55]

In parallel to the proliferation of chemical oxidation techniques for the production of carbon nanodots, methods such as hydrothermal treatment were developed (Fig. 2.14). This method has probably become the most common procedure for the production of carbon nanodots, due to a series of important advantages such as simplicity, versatility, low cost, ecological use of biomass (products or wastes), etc. The key of the hydrothermal synthesis of carbon nanodots is that the use of temperatures above the boiling point of water in closed systems increases the pressure inside the

reactor, which induces condensation of the carbonaceous building blocks and crystallisation of the graphitic core. Another important feature of hydrothermal synthesis schemes has been the observation that synthetic by-products are retained on the surface of graphitic cores giving them varied and chemically controllable functionalities and optical properties. Numerous carbon precursors have been used in hydrothermal methods, such as sugars, proteins, citrates, food residues, biomass, human hair, urine, etc. This type of synthesis has been carried out in solvents other than water (solvothermal treatment) and microwave-assisted hydrothermal synthetic schemes have also been designed, aiming at a faster and more homogeneous heating that would lead to much more uniform particle sizes.[56-66]

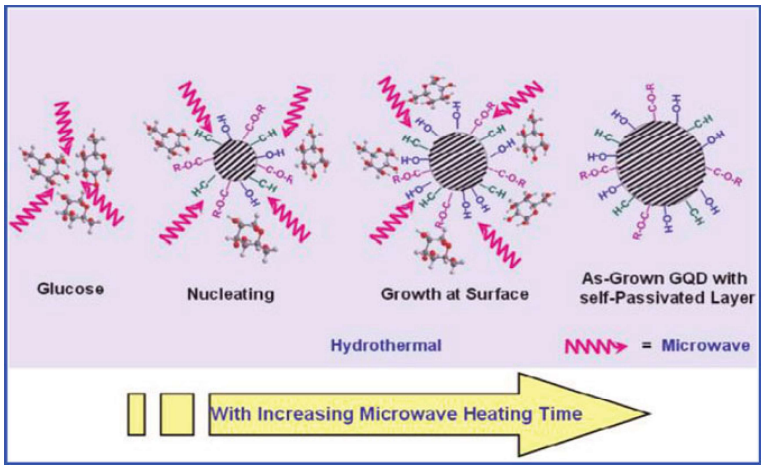

Figure 2.14. Hydrothermal synthesis of carbon nanodots using glucose a carbon source. A model for nucleation and growth of carbon nanodots induced by microwave heating of glucose solution.[63]

In general, the methods proposed so far involve a certain high energy, and there is no precise control of the morphology of the product obtained or of the size distribution. It should be noted that other methods allowing precise control over the morphology of carbon nanodots were also explored, either top-down such as electron beam nanolithography,[67] or bottom-up such as stepwise organic synthesis,[68] but these processes are often complex or require very specialised equipment, and generally lead to very low yields.

Despite the wide range of synthetic methods proposed to produce carbon nanodots, a primary obstacle to progress is insufficient purification. Relatively recent studies suggest that fluorescence can originate significantly from organic by-products generated alongside carbon nanodots. In the future, standardised purification procedures that take these findings into account will have to be implemented, and in cases where purification is inadequate, unsubstantiated or non-existent, corresponding studies need to be carried out to assess the veracity of proposed claims about the structure of carbon nanodots and the origin of their emission.[69] This requires at least a comparison of the properties of the small molecule fraction (which so far generally has been simply discarded) to the properties of the CNDs.

2.1.4.5.2. Photophysics of carbon nanodots

Carbon nanodots typically show absorption in the UV region, with a tail extending into the visible region. However, the absorption capacity of carbon nanodots could increase and move to a longer wavelength after functionalization (passivation) of the surface.[10]

Although most authors do not delve into the mechanism of photoluminescence (PL) of carbon nanodots, a thorough understanding of the origins of the photoemission of these nanomaterials is one of the most important topics in the current debate. So far, several mechanisms have been proposed to explain the fluorescence of carbon nanodots.[18,70-72] We summarise here the three possible origins of photoluminescence, highlighting their particular characteristics (Fig. 2.15).[20]

In semiconductor quantum dots, photoluminescence arises after absorption of a photon (with energy higher than the bandgap energy) which causes an electron in the valence band to be promoted to the conduction band. The subsequent recombination results in the emission of photons in a narrow spectral range (Full Width at Half Maximum (FWHM) < 40 nm) that depends on the size of the quantum dot and is independent of the excitation wavelength. This is the origin of the photoluminescence of inorganic semiconducting quantum dots (SQDs), regardless of their composition and synthetic method.

On the other hand, trap states may arise in the bandgap due to different causes such as surface defects, the presence of atomic impurities or functional groups, or adsorbed molecules, etc. In this case, the photoexcited electron and/or hole can be trapped, and their recombination generates an emission of photons at lower energy. The photoluminescence observed in the case of trap states results in broad emission bands whose position is systematically shifted towards longer wavelengths as the excitation wavelength increases. The photoluminescence of most CQDs and GQDs has been conceptually explained by considering both the size of the core and the presence of trap states.

On the other hand, the photoluminescence observed in CNDs cannot be explained by quantum confinement and must result from the superposition of several individual emitting centres (molecular fluorophores or emitting functional groups located on the surface of the nanoparticles). In this case, very broad emission bands are observed, the position of the emission maximum depending on which emitting centre is being excited most efficiently.

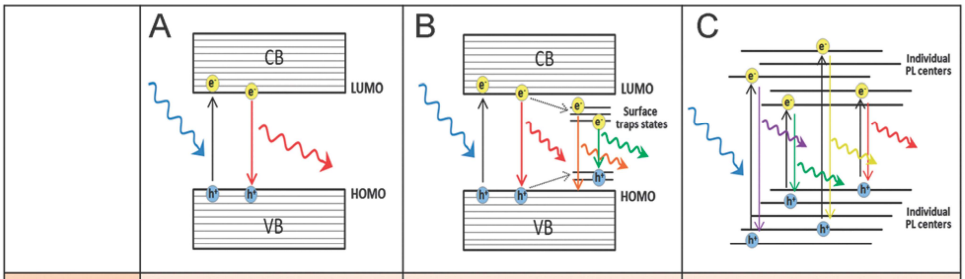

PL scheme	I	II	III
Nanodot Type	SQDs	CQDs / GQDs	CNDs
Characteristics	Quantum confinement	Quantum confinement	No quantum confinement
	Size-dependent PL	Size-dependent PL (no clear)	Size-independent PL
	Excitation-independent PL	Excitation-dependent PL	Excitation-dependent PL
	Narrow PL band	Broad PL band	Very broad PL band
	Long lifetimes	Medium lifetimes	Short lifetimes

Figure 2.15. Diagram of the different photoluminescence mechanisms of carbon nanodots and their properties.[20]

In many cases, synthetic methods produced carbon nanodots that did not exhibit photoluminescence, but passivation of the surface with different molecular components such as hydrocarbon chains made them photoluminescent. This indicates that, in many cases, the photoluminescent properties of carbon nanodots are inherent to the trap states present in the bandgap, like surface defects, functional groups, adsorbed molecules, etc. In fact, surface passivation has played a very important role in the proliferation of studies of carbon nanodots, as in addition to making them luminescent, it could make them water-soluble and available for biological applications.

The fluorescence quantum yield (QY) of carbon nanodots is highly dependent on the fabrication method and the passivation of the surface involved. Generally, carbon nanodots have low fluorescence quantum yields, which may or may not depend on the excitation wavelength. Surface passivation has been reported to significantly increase QY, but this is highly questionable and would require extensive studies and the application of purification methods to clarify why surface passivation has this effect.[41, 73-76] Another important feature of carbon nanodots is that they have shown high photostability in studies to date.[76-79] It has also been observed that the fluorescence decay of carbon nanodots is often multi-exponential, suggesting that different emission sites are present.[79-80]

Various phenomena related to the luminescence of carbon nanodots have been investigated. For example, electrochemiluminescence (ECL) processes, in which electrochemically generated electrons and holes give rise to excited states that subsequently relax to their ground states upon light emission.[80-83] They have also been used in chemical luminescence (CL) systems, in which excitation of carbon nanodots occurs through chemical reactions and the resulting luminescence allows the detection of various analytes through their participation in oxidation/reduction reactions (Fig. 2.16).[84]

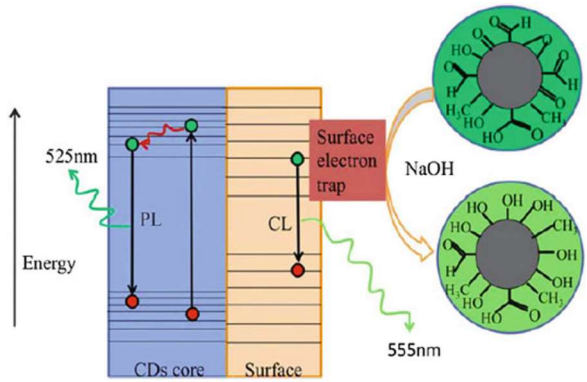

Figure 2.16. Chemiluminescence of carbon nanodots in strongly alkaline solutions. Proposed mechanism of the CL associated with surface states of the carbon nanodots generated upon reaction with NaOH. A photoluminescence (PL) generated from the carbon cores of the carbon nanodots is also illustrated.[84]

Förster resonance energy transfer (FRET) is a widely studied fluorescence phenomenon that has also been reported in carbon nanodots. FRET constitutes a non-radiative energy transfer between two fluorophores, a fluorescence donor and acceptor, which are physically adjacent. Carbon nanodots could in principle be excellent candidates to function as donors and acceptors in FRET experiments, as they have a wide excitation/emission wavelength range. This property implies that a single Carbon-Dot species can serve as energy donor for different acceptors, simply by using a different excitation wavelength. Likewise, carbon nanodots can constitute a FRET acceptor for different donors (Fig. 2.17).[85-89]

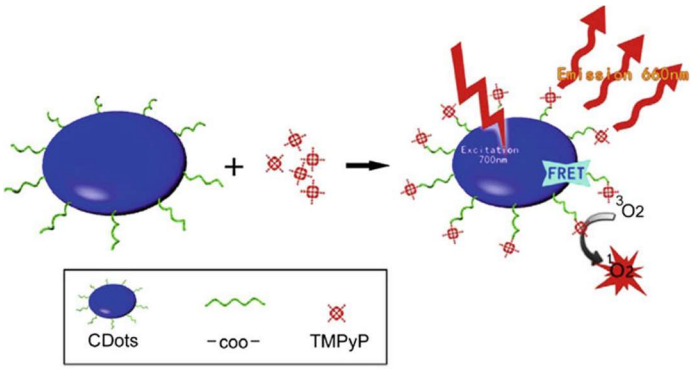

Figure 2.17. Carbon nanodots for photodynamic therapy (PDT). The Carbon nanodots were coupled to TMPyP (the phtosensitizer). The spectral properties of the Carbon-dots and TMPyP reveal overlap between the carbon nanodots' emission and TMPyP excitation, enabling energy transfer from the carbon nanodots, irradiated with NIR light to the TMPyP.[88]

Up-conversion fluorescence materials have recently attracted much attention for their promising applications, especially in the field of biomedical imaging and photocatalysis by visible light. Carbon nanodots capable of absorbing two long wavelength photons (near infrared) and emitting one photon of a shorter wavelength (visible region) have been reported.[77, 90-92]

2.1.4.5.3. Applications of carbon nanodots

This section will outline the potential applications for which carbon nanodots have been postulated as interesting candidates to date. But in light of our results, and the results of many other recent reports, many of the papers cited in this section (which attribute to carbon nanodots properties such as high fluorescence quantum yields or quantum size effects) would require revision and in some cases may even be invalidated.

Biological applications

As carbon nanodots are biocompatible and easily functionalised, they have attracted great interest for biological applications, especially in biomarking applications due to their remarkable apparent fluorescence properties.

In this context, carbon nanodots seem to present very promising properties for cellular imaging such as high quantum yield and excitation-dependent emission, which allows the selection of different excitation wavelengths in fluorescence microscopy experiments. Furthermore, carbon nanodots also showed applicability as *in vivo* bioimaging agents, since, in addition to all of the above, they can fluoresce for relatively long periods of time in physiological environments and can have a longer wavelength (red) emission that is less absorbed by human tissues (Fig. 2.18). Another advantage of using carbon nanodots is that their surface is easily functionalised, allowing the attachment of different cellular recognition elements. But it has been observed that by using the recognition elements as a carbon source in the synthesis of carbon nanodots, further functionalisation processes can be avoided as they appear to retain their structural and chemical identity, which still allows their use for attachment to cellular and tissue targets.[60, 62, 85, 89, 93-96]

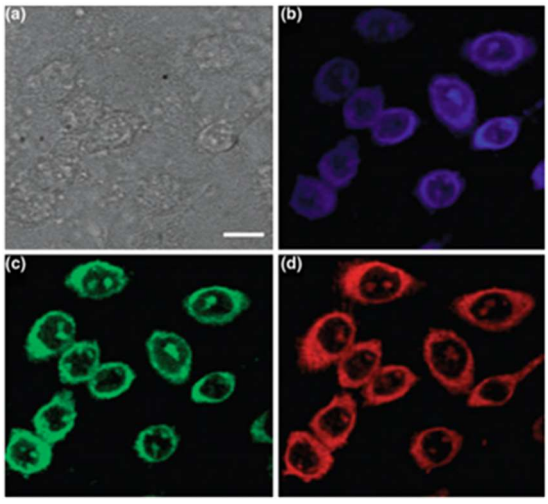

Figure 2.18. Images of cells incubated with carbon nanodots. Brightfield image (a) and confocal fluorescence microscopy images with 405 nm excitation (b); 488 nm excitation (c); and 561 nm excitation.[81]

In addition to biomarking applications, carbon nanodots have been evaluated in other biological applications, and although there are still many unresolved unknowns,

there are already several reports of their potential application as therapeutic agents for different diseases. Their potential as gene and drug carriers has been studied, and it has been shown that carbon nanodots could be easily internalised into cells. They have even been used for intracellular delivery of small interfering RNA (siRNA, also known as silencing RNA), whose transport across the cell membrane is one of the challenges to overcome before using siRNA to turn off the expression of target genes. An important advantage of carbon nanodots as a cell delivery vehicle is the possibility of luminescence imaging, which allows assessment of transport efficiency.[97-103]

Photodynamic therapy (PDT) has also been proposed as a potential application for carbon nanodots. PDT is based on administering a photosensitiser (PS) that releases singlet oxygen through light excitation of the PS, destroying tumour cells or bacteria in its environment. The main challenge of PDT is the absorption of light by the PS, as human tissues absorb light in the visible region, which restricts the available excitation window of the PS. Systems have been developed for PDT where carbon nanodots are responsible for absorbing light in the near-IR range and their emission coincides with the excitation of the covalently coupled PS (Föster resonance energy transfer process, FRET) allowing the release of singlet oxygen. And systems have also been developed where carbon nanodots could generate singlet oxygen by themselves presumably involving a triplet excited state. Again, their photoluminescent properties can be used simultaneously to more effectively target the carbon nanodots to the cells and tissues where photodynamic therapy is to be applied (therapeutic and diagnostic or theragnostics systems) (Fig. 2.19).[88, 104]

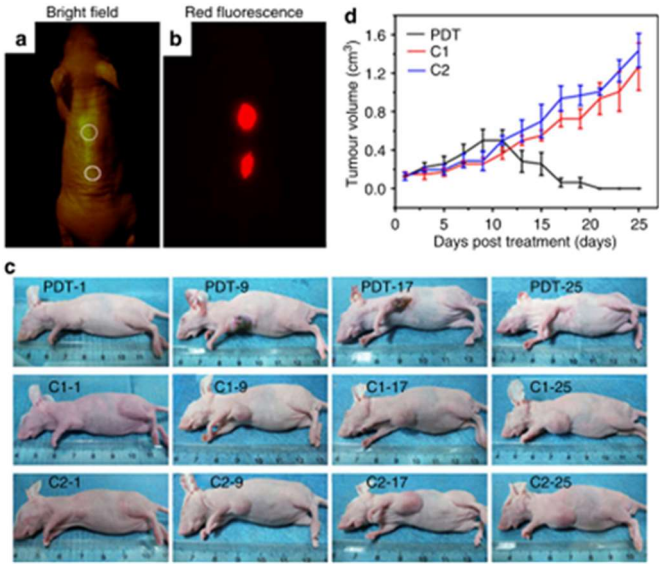

Figure 2.19. (a) Bright-field image and (b) red-fluorescence image after subcutaneous injection of GQDs in different areas. The excitation wavelength was 502–540 nm, and the collected fluorescence channel was 695–775 nm. (c) Photographs of mice after various treatments on the 1st, 9th, 17th and 25th day. (PDT: GQDs + light irradiation; C1: GQDs only; C2: light irradiation only.) (d) Time-dependent tumour growth curves (n = 5) after different treatments. $P < 0.05$ for each group.[104]

It has also been shown that some carbon nanodots can exhibit selective antibacterial activities in which their effect is attributed to bacterial wall disruption.[105] Both photodynamic therapy and cell surface disruption are bactericidal treatments that provide a viable alternative to antibiotic treatment and thus alleviate one of the greatest public health challenges of antibiotic resistance.

Detection applications

The properties observed in carbon nanodots, in particular the processes involved in their fluorescence, such as energy transfer, fluorescence quenching and the sensitivity of fluorescence spectra in molecular environments, point to broad applications in biodetection and chemodetection.

Most sensing applications of carbon nanodots have focused on altering surface environments, modulating surface energy states accordingly and thus affecting fluorescence emission, either in intensity and/or position.

One of the most powerful features of carbon nanodots as sensors is the possibility of endowing them with molecular recognition elements simply by using synthetic building blocks containing such binding units. This approach simplifies the process as no post-synthesis docking is required.

Carbon nanodots have been proposed as sensors for the detection of biomolecules, particularly proteins and enzymes, radicals, bacteria or gases, but the detection of metal ions has probably been the most widespread detection application (Fig. 2.20). The detection of metal ions can have applications in relevant fields such as the food industry or environmental monitoring, allowing the quality of water or food to be assessed.[58, 87, 90, 106-121]

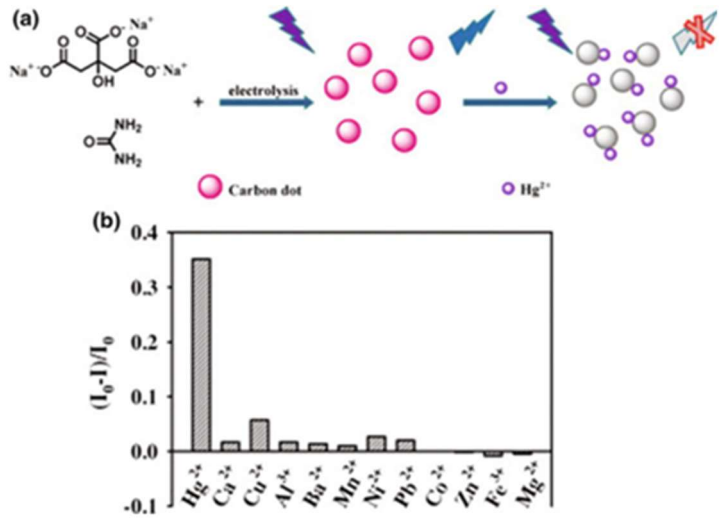

Figure 2.20. Hg^{2+} sensing by carbon nanodots. (a) Scheme showing the synthesis of carbon nanodots through electrolysis of sodium citrate/urea mixture and quenching of the carbon nanodots' fluorescence following binding to Hg^{2+} ions; (b) selectivity of the assay — significantly more pronounced fluorescence quenching induced by mercury ions as compared to other metal ions.[117]

Energy-related applications

The wide excitation/emission range and high quantum yields reported in many cases in carbon nanodots have attracted interest for their use in solar energy applications. Primarily, carbon nanodots have been proposed as sensitisers in dye-sensitised solar cells (DSSCs). TiO_2 has become the semiconductor of choice in these solar cells, the problem is that it has a wide bandgap capable of absorbing only photons in the UV region. To overcome this limitation, TiO_2 doping has been proposed using sensitisers, such as carbon nanodots, with a lower energy bandgap (able to absorb light in the visible or infrared regions), capable of transferring the photoexcited electrons to the conduction band of TiO_2.[122-123]

In addition to serving as light converters, as illustrated in the application mentioned above, carbon nanodots have also been used as light sources in LED configurations (Fig. 2.21). However, these uses have faced significant challenges due to the need to employ the carbon nanodots in the solid state, and when immobilised or deposited they tend to aggregate and/or lose their luminescence properties. Despite this, there are already several reports presenting innovative strategies to overcome the quenching/aggregation obstacles.[62, 124-128]

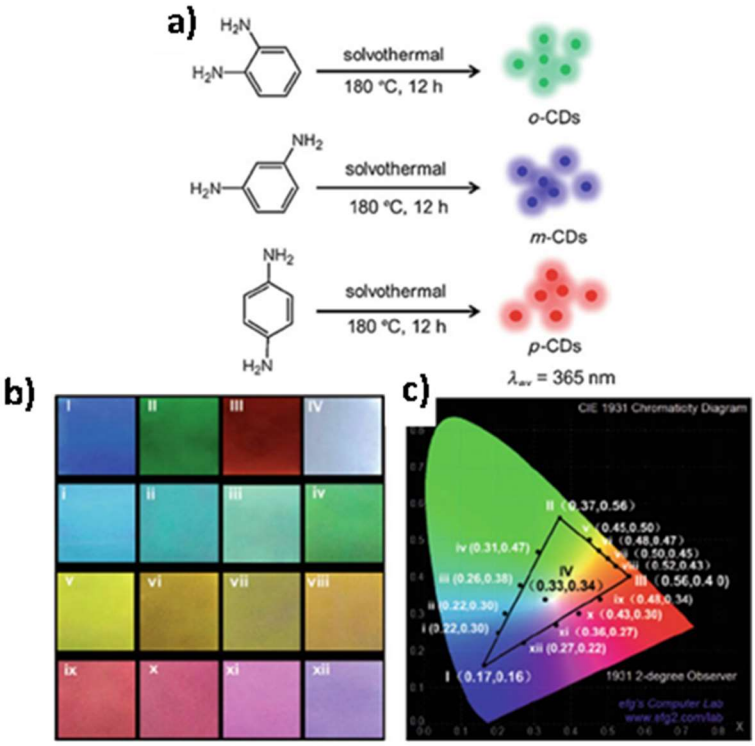

Figure 2.21. Coloured light-emitting films embedding carbon nanodots prepared from phenylenediamine isomers in transparent polymer matrixes. a) The three phenylenediamine isomers and corresponding carbon nanodots exhibiting different colours (upon excitation at 365 nm); b) photographs of carbon nanodot/polymer films comprising carbon nanodots produced from different mixtures of the phenylenediamine isomers; c) light emission coordinates of the films shown on a CIE 1931 chromaticity map.[62]

Photocatalysis-related applications

The light absorption properties of carbon nanodots have also been exploited as a means to enhance photocatalysis, in particular under visible light illumination. Photocatalysis reactions have mostly been studied using metal oxides, such as titanium oxide, zinc oxide, or silicon oxide, especially in nanoparticle configuration to increase the surface area available. Again, the main impediment to using metal oxides as photocatalysts is their large bandgap, which results in inefficient absorption of sunlight. Consequently, the usual methods to improve the photocatalytic activity of metal oxides have been to couple them with dyes, or carbon nanodots, which either absorb visible light by transferring the photoexcited electrons to the semiconducting particles, or by accepting the photoexcited electrons from the semiconductor, thus minimising electron-hole recombination and broadening the catalytic activity. Several reports have shown that carbon nanodots exhibit photocatalytic activity in their own right, where the photoexcited electrons and corresponding holes can be harnessed to induce various catalytic reactions (Fig. 2.22).[19, 77, 91, 129-132]

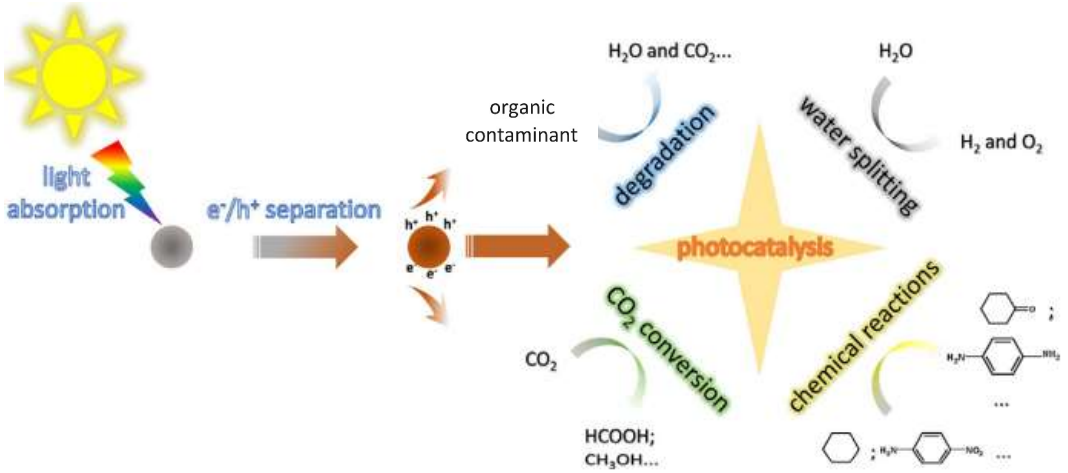

Figure 2.22. The photocatalytic process of CDs-based photocatalysts (the solid circles represent CDs-based photocatalysts).[132]

2.1.5. Techniques for characterization of carbon nanomaterials

As new members of carbon nanostructures, carbon nanodots have been extensively characterised in order to elucidate their structure and consequently elucidate the mechanisms responsible for the photophysical phenomena they exhibit. The following sections briefly describe the fundamentals of the study techniques used to obtain information on the structure and composition of these materials.

Electron microscopy:

Conventional electron microscopy allows direct images to be obtained that show the morphology of these materials in detail. It also offers the possibility of studying the arrangement of carbon atoms, the degree of hybridization, the degree of aggregation and the crystalline organization. In electron microscopy, electrons act as a

source of ionising radiation which, when incident on the sample, have the ability to produce a series of interactions that produce secondary signals that can be detected and subsequently used analytically to provide semi-quantitative chemical information and other characteristic features of the sample.[133]

The following is a brief description of the electron microscopy and associated techniques used for the structural characterization of carbon nanodots presented in this work.

- High-resolution transmission electron microscopy (HR-TEM): allows the study and interpretation of micrographs obtained by electrons passing through the sample with an interpretable resolution between 0.1 and 0.2 nm (Fig. 2.23). Recently, the resolution of electron microscopes has been improved through the application of holography, the use of correctors for the aberrations of the microscope lenses and the reconstruction of the phase of the emerging wave.[134]

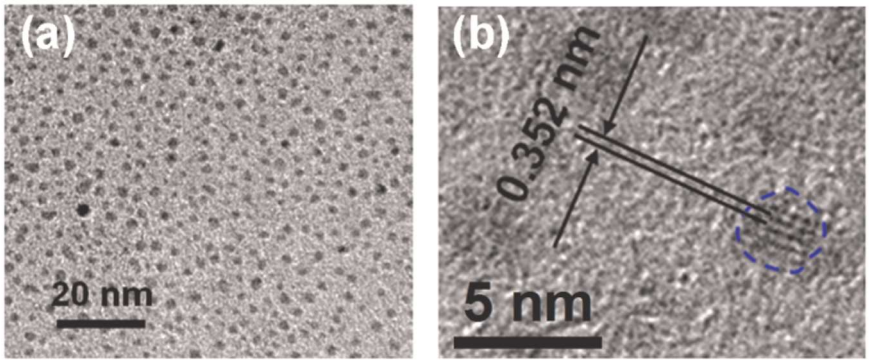

Figure 2.23. (a) TEM image of GQDs assembled on Cu grid coated with ultrathin amorphous carbon film; (b) the HRTEM image of the GQDs.[86]

- Scanning Transmission Electron Microscopy (STEM): the sample is scanned by a finely focused electron beam. Imaging by STEM on a high-angle angular dark field detector (HAADF) allows the variations of the intensity of the image to be related to the atomic number of the elements in the sample (Fig. 2.24).[135]

Since the development of Analytical Electron Microscopy in the late 1970s, information on the chemical composition of a sample can be obtained with the implementation of techniques associated or coupled to the microscope, the most common being:[136]

- X-ray Energy Dispersive Spectroscopy (EDS): when the electron beam is incident on a region of the sample, X-rays characteristic of each element are produced. With the use of internal standards, it can be quantitative with a margin of error of 1-5 % (Fig. 2.24).
- Electron energy loss spectroscopy (EELS): measures the kinetic energy loss of electrons interacting inelastically with the sample, which is characteristic of each of the elements present in a study region. The EELS technique can be considered complementary to EDS, since it is more sensitive for light elements ($Z < 10$), while EDS is more sensitive for elements with $Z > 10$ (Fig. 2.24).

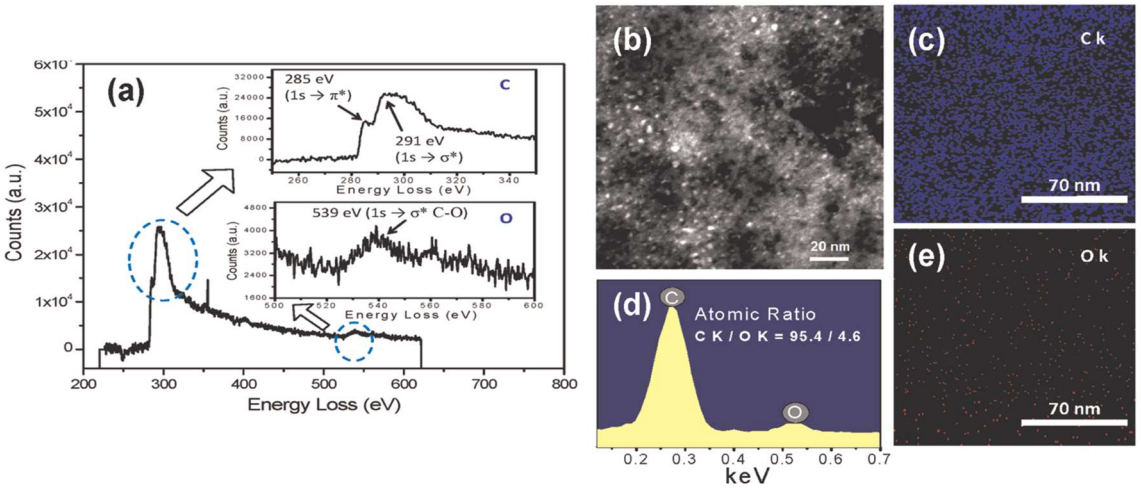

Figure 2.24. EELS spectra, STEM image and EDS analysis of GQDs. (a) EELS spectrum of the GQDs; the insets show the EELS spectra of C K-edge and O K-edge of the GQDs; (b) STEM image of the GQDs assembled on Cu grid coated with ultrathin amorphous carbon film; (c) Elemental C mapping (in blue) of the image shown in panel b; (d) EDS spectrum of the GQDs; (e) elemental O mapping (in red) of the image shown in panel b.[86]

X-Ray Diffraction (XRD) / Small and Wide Angle X-ray Scattering (SAXS-WAXS)

The fundamental application of this technique is the identification of the structure of a crystalline sample. When an X-ray beam is incident on a crystal, some of the rays pass through the crystal and some are scattered by the electrons of the atoms in the crystal. Of all the scattered electrons, some may exit, in phase, in certain directions, which depend on the orientation of the crystal planes relative to the X-ray source. As a result, their waves are strengthened and give rise to a diffracted X-ray beam. The set of beams diffracted by a crystal constitutes its diffraction pattern. In the case of carbon materials, this technique makes it possible to determine the degree of crystallinity of the different samples (Fig. 2.25).[137]

SAXS is one of the most versatile tools to analyse dimensions and nanoscale structures of a variety of sample types (liquids, powders, solids, gels...). Samples can be amorphous, crystalline or semi-crystalline. Typical samples that can be investigated with SAXS include colloidal dispersions, surfactants, polymers, biomacromolecules, membranes, nanocomposites, Nano powders and porous materials. The orientation of anisotropic nanoscale structures can be investigated by measuring 2D SAXS patterns.[137]

Based on the measured scattering pattern at wide angles (WAXS), the crystalline phases present in a given sample can be identified and quantified, and the size of nanocrystallites can be calculated. The crystal lattice orientation in anisotropic structures, e.g. in polymers, can be deduced from 2D WAXS patterns.[137]

Generally speaking, the WAXS technique is used to obtain structural information on scales of the order of 1 nm or smaller, whereas SAXS is used for orders of 1 to 1000 nm.[137]

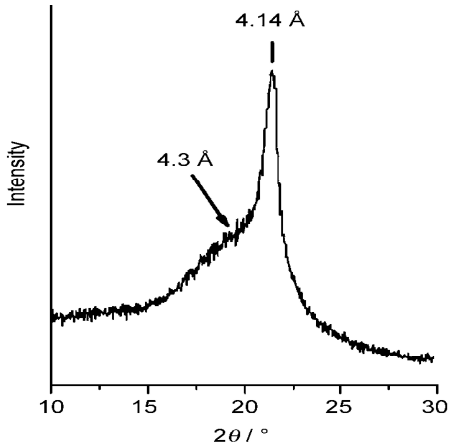

Figure 2.25. XRD pattern of octadecyl-functionalised carbon nanodots. The XRD peak points to a lattice spacing greater than graphite (0.35 nm), indicating certain amorphous character of the synthesised carbon nanodots.[138]

Atomic Force Microscope (AFM)

An atomic force microscopy is a scanning microscope which probes a sample's surface. It consists in a tip positioned at the end of a cantilever and an optical system using a laser to detect the tip's deflections. When the tips is brought into contact with the sample and moved along its surface, the laser deviation allows to measure the sample's profile. The AFM allows to visualize the topography of the surface down to atomic resolution. One often uses the so-called "tapping mode". Here, the tip is driven to oscillate up and down during its displacement and the amplitude of the oscillation is detected which will be reduced in vicinity of the sample surface. This technique causes less damage during scanning because of fewer and lighter contacts. Furthermore, the detection of these periodic oscillations and their modification along the surface results in more accurate topographic measurements (Fig. 2.26).[139]

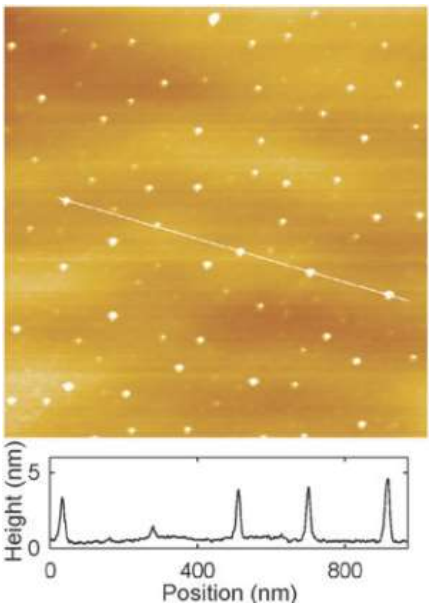

Figure 2.26. AFM image of carbon nanodots. The AFM specimen was prepared by depositing a few drops of a diluted carbon dot solution on a mica surface.[140]

Dynamic Light Scattering (DLS)

Dynamic light scattering (DLS) is a physical technique that can be used to determine the size distribution of small particles in suspension or polymers in solution.

DLS measures Brownian motion and relates it to particle size. Brownian motion is the random movement of particles due to bombardment by surrounding solvent molecules. The larger the particle, the slower the Brownian motion and the smaller the particles the faster they are moving and the further are they "kicked" away by the solvent molecules. Particles in a dispersion are in a constant, random, Brownian motion causing the intensity of scattered light to fluctuate as a function of time. For a large number of monodisperse particles in Brownian motion, the correlation function is an exponentially decaying function of the correlator time delay, the pre-exponential factor being proportional to the diffusion coefficient of the particles and the refractive index of the solvent. From the correlation function using various algorithms, the mean hydrodynamic size (z-average diameter) or Stokes radius of the particles and an estimate of the width of the distribution (polydispersity index) can be obtained (Fig. 2.27) employing the Stokes-Einstein relation $D = k_B T/(6\pi\eta r_{Stokes})$ where k_B is the Boltzmann constant, T the temperature of the solvent and η the dynamic viscosity. [141] For the derivation of the Stokes radius therefore the refractive index and the viscosity of the solvent must be known, which in turn requires the temperature to be stabilized.

The size distribution obtained is a plot of the relative intensity of light scattered by particles in various size intervals and is therefore known as an intensity size distribution. If the distribution by intensity is a single fairly smooth peak, then there is little point in doing the conversion to a volume distribution using the Mie theory. If the optical parameters are correct, this will just provide a slightly different shaped peak. However, if the plot shows a substantial tail, or more than one peak, then Mie theory can make use of the input parameter of sample refractive index to convert the intensity distribution to a volume distribution. This will then give a more realistic view of the importance of the tail or second peak present. In general terms it will be seen that: d(intensity) > d(volume) > d(number).

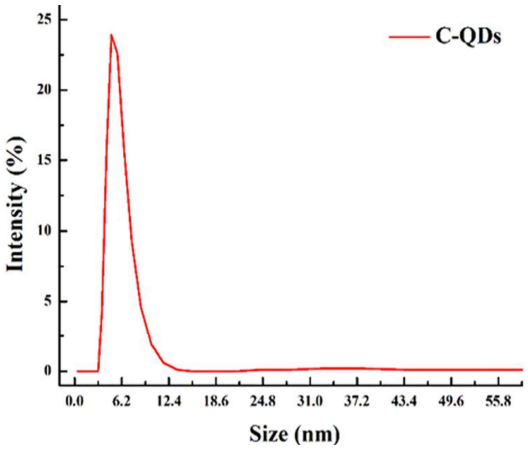

Figure 2.27.Dynamic light scattering (DLS) size distribution curve of carbon nanodots dispersed in water.[142]

Fluorescence Correlation Spectroscopy (FCS)

Fluorescence correlation spectroscopy is, in a sense, the fluorescent counterpart of dynamic light scattering (DLS). FCS provides quantitative information about fluorescent particles in suspension, in particular their diffusion coefficients, hydrodynamic radii or average concentrations, among others.

The typical FCS configuration consists of a pulsed or continuous wave laser that is focused by a high numerical aperture lens to a femtoliter volume into the sample containing fluorescent particles in suspension at such a high dilution that only a few are within the focal spot. When the particles cross the focal volume, due to Brownian motion, they emit fluorescence, which reaches a detector. The fluorescence intensity fluctuates as the fluorescent particles move in and out of the focal volume and is analysed by temporal autocorrelation. To extract the information, it is necessary to calibrate parameters by performing FCS on a species with known diffusion coefficient and concentration and then fit the autocorrelation data using appropriate models (Fig. 2.28).[143]

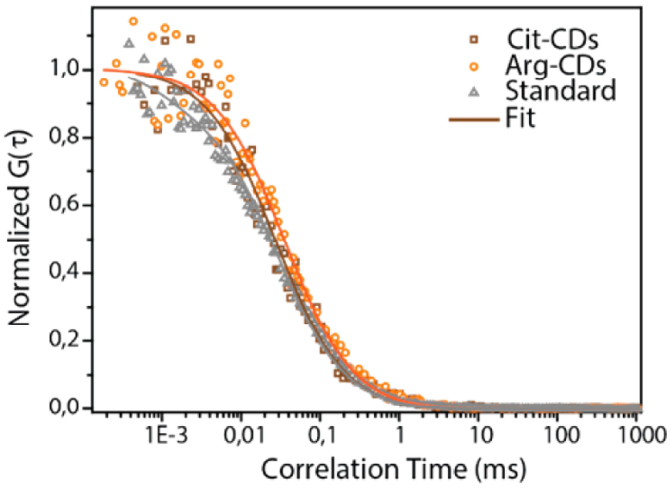

Figure 2.28. Normalised FCS curves for different carbon nanodots and Coumarin 153 (Standard). FCS curves are fitted (solid lines) to the translational diffusion model.[144]

Raman spectroscopy and Surface-Enhanced Raman Spectroscopy (SERS)

When a beam of monochromatic light is incident on a sample, some of the light is transmitted, some is absorbed, and the rest is scattered. Most of the scattered light has the same wavelength as the incident beam, however, a small fraction of the scattered light is spectrally shifted, by molecular vibrations and rotations (inelastic scattering or Raman scattering).[145]

Raman spectroscopy plays an important role in the study of carbon materials. It provides valuable information such as the size of the existing sp^2 domains, the presence of sp^2 - sp^3 hybridization, the presence of chemical impurities, defects, or the degree of order and disorder, among others.[146]

In the Raman spectrum of carbon materials with sp^2 hybridization, two characteristic signals can be identified: the G-band located in the range 1540 - 1600 cm^{-1} and the D-band located between 1340 - 1400 cm^{-1}. The G-band is associated with the elongation of the in-plane C-C bonds and the vibrations arising from the relative motion of the sp^2-hybridised carbon atoms. As a result of the loss of symmetry in the crystal structure of the material, the D band appears. The ratio of intensities between the D and G bands (I_D/I_G) can be used to determine the relative abundance of graphitic carbon atoms versus disordered carbon atoms.[146]

Surface-enhanced Raman spectroscopy (SERS) is a surface-sensitive technique that enhances the Raman scattering of molecules adsorbed on rough metal surfaces or metal nanostructures. The enhancement factor in the case of coinage metals like silver or gold can be as high as 10^{10} to 10^{11}, which means that the technique can detect single molecules. The exact mechanism of the SERS enhancement effect is still under debate in the literature, with the most supported theory stating that the increase in Raman signal intensity for adsorbates on certain surfaces occurs due to an increase in the electric field caused by surface plasmon polaritons on the metal surface excited by the incident light. The increase in intensity is not the same for all frequencies. For those frequencies where the Raman signal deviates only slightly from the incident light, both the incident laser light and the Raman signal can be close to resonance with the surface plasmon resonant frequency, leading to a maximum increase in intensity. When the frequency deviation is large, the incident light and the Raman signal cannot simultaneously be in resonance with the plasmon frequency, so the total enhancement is limited.[147-149]

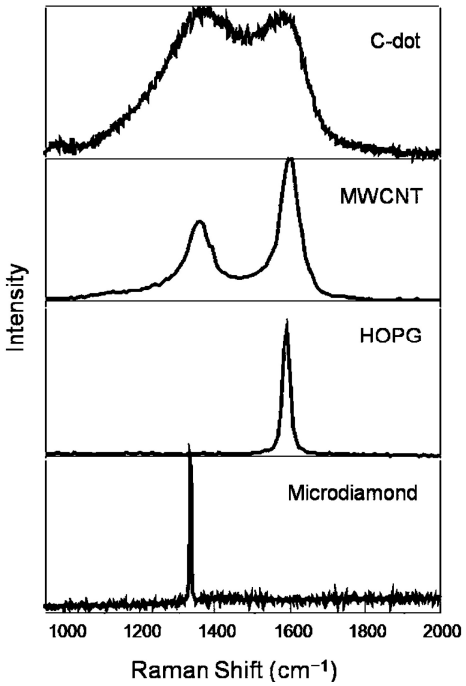

Figure 2.29. Raman spectra of carbon nanodots, multi-walled carbon nanotubes (MWCNTs), highly ordered pyrolytic graphite (HOPG), and microdiamond powder.[150]

Fourier-transform infrared spectroscopy (FTIR)

The infrared region lies between the visible and microwave regions of the electromagnetic spectrum and infrared (IR) spectroscopy is one of the best tools for solving problems related to molecular structure and chemical identification, because polar vibrations of individual covalent bonds or of functional groups couple to infrared light and therefore appear in the infrared spectrum. In this work, the infrared spectra of the samples have been measured in the mid-infrared range (400-4000 cm^{-1}), which is the range that has the greatest analytical application.[151]

Since IR spectroscopy is based on the fact that molecules rotate and vibrate as a result of their interaction with IR radiation, the implementation of this technique allows, in the case of carbon nanodots, to perform identification of surface functional groups such as carboxyl groups, phenols, carbonyls, amines, amides, etc., as well as the identification of molecular species.

The particular technique of infrared spectroscopy called Fourier transform spectroscopy registers the intensity modulations at the output of a scanning Michelson interferometer after passing the infrared light through the sample. The technique has significant advantages over dispersive infrared spectroscopy in terms of light-gathering efficiency. The spectral resolution is determined by the travel of the scanning interferometer.

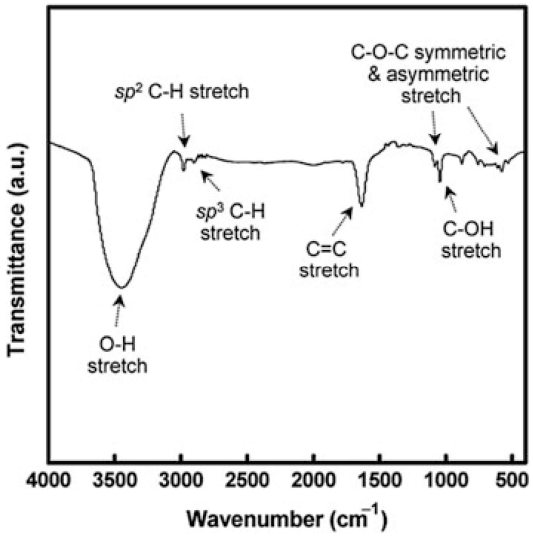

Figure 2.30. Fourier-transform infrared (FTIR) spectrum of carbon-dot sample. Distinct vibration bands corresponding to carbon nanodots' surface units are indicated.[21]

X-ray Photoelectron Spectroscopy (XPS)

X-ray spectroscopy is a technique with low spatial resolution and sensitive to the surface (up to a depth of 6-8 nm) that allows the identification of the chemical elements present, as well as the elements to which they are bound.

The technique basically consists of the excitation by an X-ray beam of the innermost levels of atoms, causing the emission of photoelectrons, and since the energy of the X-ray photon beam used is known and the kinetic energies of the emitted electrons are measured, the characteristic binding energy (BE) of each element can be determined thanks to the principle of conservation of energy. A typical XPS spectrum is a plot of the number of electrons detected at a specific binding energy. Each element produces a set of XPS peaks corresponding to the electronic configuration, e.g. 1s, 2s, 2p, etc. In addition, the number of electrons detected in each peak is directly related to the amount of that element in the sample.[152]

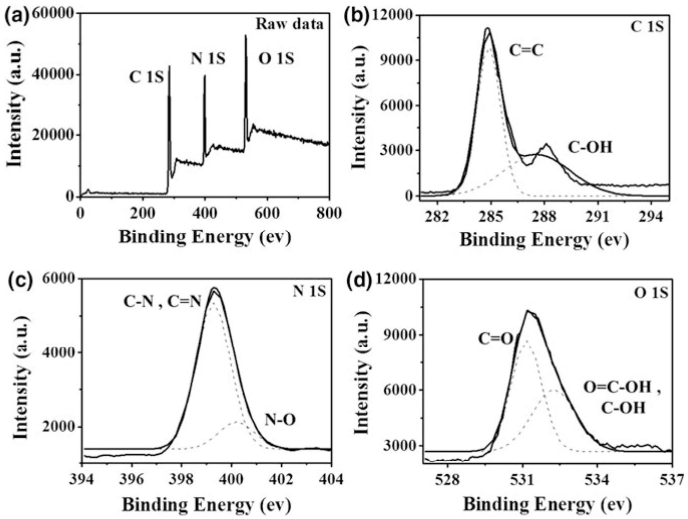

Figure 2.31. X-ray photoelectron spectra (XPS) of carbon nanodots. The spectra reveals distinct functional groups corresponding to different atoms present upon the carbon nanodots' surface.[21]

Mass Spectrometry (MS)

However, all the techniques mentioned above are unable to determine the chemical structure of the sample. In order to identify possible by-products of synthesis such as small organic molecules or oligomers generated with the carbon nanodots, mass spectrometry (MS) can be used.[153-154]

In mass spectrometry, basically, the sample is ionised, which can cause the sample molecules to break into charged fragments or simply become charged without fragmenting. These ions are separated according to their mass-to-charge ratio by subjecting them to a magnetic or electric field. The results are shown as signal intensity spectra of the detected ions as a function of mass-to-charge ratio.[155]

Ionisation techniques have been key in determining which types of samples can be analysed by mass spectrometry. Several ion sources are available and could be divided into hard and soft ionisation techniques. The most common example of hard ionisation is electron ionisation (EI) which gives a high degree of fragmentation, however it is not suitable for coupling to high performance liquid chromatography (HPLC), as at atmospheric pressure, the filaments used to generate electrons burn quickly. On the other hand, soft ionisation refers to processes that involve little residual energy to the molecule and result in little fragmentation. Representative examples could be: electrospray ionisation (ESI), chemical ionisation (CI) or matrix assisted laser desorption/ionisation (MALDI).[155]

Of particular note is the possibility of using tandem mass spectrometry capable of performing multiple rounds of mass spectrometry, usually separated by some form of molecule fragmentation. Another important improvement in the resolving power of mass spectrometry is its use in conjunction with chromatography that separates compounds before they are introduced into the ion source.[155]

2.1.6. Future perspectives

In this introduction, recent advances in carbon nanodots research have been described so far. It is clear that carbon nanodots have attracted enormous attention due to their apparent attractive properties, including biocompatibility, unique optical properties (excitation-dependent emission, high photostability or modulatable emission) and relative ease of functionalisation.

These interesting properties and the abundance and inexpensive availability of precursors have promoted a large number of synthetic methods, and this has provided immense scope for tailoring the chemical and surface nature of carbon nanodots as desired for specific purposes.

The infinite possibilities of producing different carbon nanodots have led to inconsistency in their classification and nomenclature. According to the recommendation of Cayuela et al.,[20] all carbon nanodots can be classified into three subgroups (GQDs, CQDs and CNDs) according to their structure and the mechanism that gives rise to their photoluminescence.

Naturally, research on carbon nanodots continues to face challenges, both conceptual and technical, that need to be solved before they can be applied in the various proposed fields. One of the main challenges is to synthesize carbon nanodots with structural uniformity on a large scale. The precise physical mechanisms responsible for the unique spectroscopic properties of carbon nanodots have not sufficiently been elucidated yet. Although significant progress has been made, future experimental and theoretical work should shed more light on the effect of factors such as size or surface and core nature. Other more technical challenges involving optical properties are the optimization of luminescence quantum yield, as well as modulating the excitation range of the emission.

In general, the methods proposed to date are not capable of producing carbon nanodots on a large scale and with a well-defined structure and composition. In general, methods involving high energy on carbon materials lack control over the morphology and size distribution of the resulting nanoparticles. Furthermore, the synthetic methods that would allow this control are often inefficient. On the other hand, carbon nanodots exhibit interesting optical properties; however, the underlying photophysical phenomena still remain a matter of debate and are not yet fully rationalised.

References

1. Shirakawa, H.; Louis, E. J.; MacDiarmid, A. G.; Chiang C. K.; Heeger, A. J. Synthesis of Electrically Conducting Polymers: Halogen Derivatives of Polyacetylene, (CH)x. *J. Chem. Soc., Chem. Commun.,* **1977**, *16*, 578-580.

2. Kroto, H. W.; Heath, J. R.; O´Brien, S. C.; Curl, R. F.; Smalley, R. E.; C_{60}: Buckminsterfullerene. *Nature,* **1985**, *318*, 162-163.

3. Iijima, S. Helical Microtubules of Graphitic Carbon. *Nature,* **1991**, *354*, 56-58.

4. Geim, A. K.; Novoselov, K. S. The Rise of Graphene. *Nat. Mater.,* **2007**, *6*, 183-191.

5. Inagaki, M. *New Carbons: Control of Structure and Functions.* Elsevier Science: Amsterdam, 2000.

6. Shenderova, O. A.; Zhirnov, V. V.; Brenner, D. W. Carbon Nanostructures. *Crit. Rev. Sol. State and Mat. Sci*., **2002**, *27*, 227-356.

7. Dai, L., ed. *Carbon Nanotechnology: Recent Developments in Chemistry, Physics, Material Science and Device Applications*. Elsevier: Amsterdam, 2006.

8. Delgado, J. L.; Herranz, M. A.; Martín, N. The Nano-Forms of Carbon. *J. Mater. Chem.* **2008**, *18*, 1417-1426.

9. Esteves da Silva, J. C. G.; Gonçalves, H. M. R. Analytical and Bioanalytical Applications of Carbon Dots. *TrAC, Trends Anal. Chem.* **2011**, *30*, 1327-1336.

10. Li, H.; Kang, Z.; Liu, Y.; Lee, S-T. Carbon Nanodots: Synthesis, Properties and Applications. *J. Mater. Chem*. **2012**, *22*, 24230-24253.

11. Shen, J.; Zhu, Y.; Yang, X.; Li, C. Graphene Quantum Dots: Emergent Nanolights for Bioimaging, Sensors, Catalysis and Photovoltaic Devices. *Chem. Commun*. **2012**, *48*, 3686–3699.

12. Luo, P. G.; Sahu, S.; Yang, S-T.; Sonkar, S. K.; Wang, J.; Wang, H.; LeCroy, G. E.; Cao, L.; Sun, Y-P.; Carbon "Quantum" Dots for Optical Bioimaging. *J. Mater. Chem. B.* **2013**, *1*, 2116-2127.

13. Hola, K.; Zhang, Y.; Wang, Y.; Giannelis, E. P.; Zboril, R.; Rogach, A. L. Carbon Dots: Emerging Light Emitters for Bioimaging, Cancer Therapy and Optoelectronics. *Nano Today.* **2014**, *9*, 590–603.

14. Georgakilas, V.; Perman, J. A.; Tucek, J.; Zboril, R. Broad Family of Carbon Nanoallotropes: Classification, Chemistry, and Applications of Fullerenes, Carbon Dots, Nanotubes, Graphene, Nanodiamonds, and Combined Superstructures. *Chem. Rev*. **2015**, *115*, 4744–4822.

15. Lim, S. Y.; Shen, W.; Gao, Z. Carbon Quantum Dots and their Applications. *Chem. Soc. Rev*. **2015**, *44*, 362–381

16. Zhao, A.; Chen, Z.; Zhao, C.; Gao, N.; Ren, J.; Qu, X. Recent Advances in Bioapplications of C-dots. *Carbon.* **2015**, *85*, 309–327.

17. Baptista, F. R.; Belhout, S. A.; Giordani, S.; Quinn, S. J. Recent Developments in Carbon Nanomaterials Sensors. *Chem. Soc. Rev*. **2015**, *44*, 4433–4453.

18. Zhu, S.; Song, Y.; Zhao, X.; Shao, J.; Zhang, J.; Yang, B. The Photoluminescence Mechanism in Carbon Dots (Graphene Quantum Dots, Carbon Nanodots, and Polymer Dots): Current State and Future Perspective. *Nano. Res*. **2015**, *8*, 355-381.

19. Fernando, K. A. S.; Sahu, S.; Liu, Y.; Lewis, W. K.; Guliants, E. A.; Jafariya, A.; Wang, P.; Bunker, C. E.; Sun, Y-P. Carbon Quantum Dots and Applications in Photocatalytic Energy Conversion. *ACS Appl. Mater. Interfaces*. **2015**, *7*, 8363-8376.

20. Cayuela, A.; Soriano, M. L.; Carrillo-Carrion, C.; Valcarcel, M. Semiconductor and Carbon-Based Fluorescent Nanodots: The Need for Consistency. *Chem. Commun*. **2016**, *52*,1311–1326.

21. Jelinek, R. *Carbon Quantum Dots: Synthesis, Properties and Applications.* Springer International Publishing: Switzerland, 2017.

22. Cotton, F. A.; Wilkinson, G. *Química Inorgánica Avanzada.* Traducción de la obra publicada en inglés *Advanced Inorganic Chemistry.* Chap. 11, 4th ed.; Limusa: México D.F., 2005.

23. Wade, L. G. *Organic Chemistry.* Chap. 1-2, 5th ed.; Pearson Education Inc.: UK, 2004.

24. Greenwood, N. N.; Earnshaw, A. *Chemistry of the Elements*. Chap. 8, 1st ed.; Pergamon Press.: Oxford, 1984.

25. Harris, P. J. F. *Carbon Nanotubes and Related Structures.* Cambridge University. Chap. 4, Press.: Cambridge, UK, 1999.

26. Dresselhaus, M. S.; Dresselhaus, G.; Eklund, P. C. *Science of Fullerenes and Carbon Nanotubes.* Chap. 2, Elsevier Ltd.: Oxford, UK, 1996.

27. Heimann, R. B.; Evsyukov, S. E.; Koga, Y. Carbon Allotropes: A Suggested Classification Scheme Based on Valence Orbital Hybridization. *Carbon*. **1997**, *35*, 1654-1658.

28. Luo, W.; Windl, W. First Principles Study of the Structure and Stability of Carbines. *Carbon*. **2009**, *47*, 367-383.

29. Rao, C. N. R.; Sood, A. K.; Subrahmanyam, K. S.; Govindaraj, A. Graphene: The New Two-dimensional Material. *Angew. Chem.* **2009**, *48*, 7752-7777.

30. Bacon, M.; Bradley, S. J.; Nann, T. Graphene Quantum Dots. *Part. Part. Syst. Charact.* **2013**, *31*, 415-428.

31. Fisher, J.E. Carbon Nanotubes: Structure and Properties. In *Nanomaterials handbook*. Gogotsi, Y. CRC Press: Boca Raton, Fl., 2006.

32. Rayner-Canham, G.; Overton, T. *Descriptive Inorganic Chemistry.* Chap. 14, 4th ed.; Freeman and Co.: New York, USA, 2003.

33. Dresselhaus, M. S.; Dresselhaus, G.; Eklund, P. C. *Science of Fullerenes and Carbon Nanotubes.* Chap. 3, 5, 10, and 20, Elsevier Ltd.: Oxford, UK, 1996.

34. Ugarte, D. Curling and Closure of Graphitic Networks Under Electron-Beam Irradiation. *Nature,* **1992**, *359*, 707-709.

35. Kharissova, O. V.; Kharisov, B. I. Variations of Interlayer Spacing in Carbon Nanotubes. *RCS. Adv.,* **2014**, *4*, 30807-30815.

36. Franklin, R. E. Crystallite Growth in Graphitizing and Non-Graphitizing Carbons. *Proc. Royal. Soc. A.* **1951,** *209,* 196-218.

37. Heidenreich, R. D.; Hess, W. M.; Ban, L. L. A Test Object and Criteria for High Resolution Electron Microscopy. *J. Appl. Crystallogr.* **1968**, *1,* 1-19.

38. Harris, P. J. F. Fullerene-Related Structure of Commercial Glassy Carbons. *Philosophical Magazine,* **2004***, 84*, 3159-3167.

39. Donnet, J. B.; Wang, T. K.; Rebouillat, S.; Peng, J. C. M. *Carbon Fibres.* 3rd ed. Marcel Dekker: New York, 1998.

40. Boppart, S.; Ingle, L.; Potwora, R. J. Understanding Activated Carbons. *Chem. Proc.* **1996***,* 79-85.

41. Sun, Y-P.; Zhou, B.; Lin, Y.; Wang, W.; Fernando, K. A. S.; Pathak, P.; Meziani, M. J.; Harruff, B. A.; Wang, X.; Wang, H.; Luo, P. G.; Yang. H.; Kose, M. E.; Chen, B.; Veca, L. M.; Xie, S-Y. Quantum-Sized Carbon Dots for Bright and Colorful Photoluminescence. *J. Am. Chem. Soc*., **2006**, *128*, 7756–7757.

42. Habiba, K.; Makarov, V. I.; Weiner, B. R.; Morell, G. Fabrication of Nanomaterials by Pulsed Laser Synthesis. In Manufacturing Nanostructures. Waqar, A.; Ali, N., One Central Press (OCN): UK, 2014.

43. Li, X.; Wang, H.; Shimizu, Y.; Pyatenko, A.; Kawaguchi, K.; Koshizaki, N. Preparation of Carbon Quantum Dots with Tunable Photoluminescence by Rapid Laser Passivation of ordinary Organic solvents. *Chem. Commun.,* **2011**, *47*, 932-934.

44. Isnaeni, M.; Yusrul Hanna, M.; Pambudi, A. A.; Murdaka, F. H. Influence of Ablation Wavelength and Time on Optical Properties of Laser Ablated Carbon Dots. *AIP Conference Proceedings,* **2017***, 1801.*

45. Kazemizadeh, F.; Malekfar, R.; Parvin, P. Pulsed Laser Ablation Synthesis of Carbon Nanoparticles in Vacuum. *J. Phys. Chem. Sol.,* **2017***, 104*, 252-256.

46. Hang, S. H.; Mhin, S.; Han, H.; Kim, K. M.; Jones, J. L.; Ryu, J. H.; Kang, J. S.; Kim, S. H.; Shim, K. B. Ultrafast Method for Selective Design of Graphene Quantum Dots with Highly Efficient Blue Emission. *Sci. Rep.,* **2016***, 6,* 38423-38429.

47. Gokhale, R.; Singh, P. Blue Luminescent Graphene Quantum Dots by Photochemical Stitching of Small Aromatic Molecules Fluorescent Nanoprobes in Cellular Imaging. *Part. Part. Syst. Charact.,* **2014***, 31,* 433-438.

48. Zhu, Z.; Wang, S.; Chang, Y.; Yu, D.; Jiang, Y. Direct Photodissociation of Toluene Molecules to Photoluminescent Carbon Dots Under Pulsed Laser Irradiation. *Carbon,* **2016**, *105*, 416-423.

49. Gokhale, R.R.; Thakare, V. P.; Warule, S.; Lefez, B.; Hannoyer, B.; Jog, J. P.; Ogale, S. B. From Small Aromatic Molecules to Functional Nanostructured Carbon by Pulsed Laser-Induced Photochemical Stitching. *AIP Advances,* **2012**, *2.*

50. Habiba, K.; Makarov, V. I.; Avalos, J.; Guinel M. J. F.; Weiner, B. R.; Morell, G. Luminescent Graphene Quantum Dots Fabricated by Pulsed Laser Synthesis. *Carbon,* **2013***, 64*, 341-350.

51. Yu, H.; Li, X.; Zeng, X.; Lu, Y. Preparation of Carbon Dots by Non-Focusing Pulsed Laser Irradiation in Toluene. *Chem. Commun.,* **2016***, 52,* 819-822.

52. Lu, J.; Yang, J-X.; Wang, J.; Lim, A.; Wang, S.; Loh, K. P. One-Pot Synthesis of Fluorescent Carbon Nanoribbons, Nanoparticles, and Graphene by the Exfoliation of Graphite in Ionic Liquids. *ACS Nano,* **2009**, *3*, 2367-2375.

53. Liu, R.; Wu, D.; Liu, S.; Koynov, K.; Knoll, W.; Li, Q. An Aqueous Route to Multicolor Photoluminescent Carbon Dots Using Silica Spheres as Carriers. *Angew. Chem. Int. Ed.,* **2009***, 48*, 4598-4601.

54. Ray, S. C.; Saha, A.; Jana, N. R.; Sarkar, R. Fluorescent Carbon Nanoparticles: Synthesis, Characterization, and Bioimaging Application *J. Phys. Chem. C.,* **2009***, 113,* 18546-18551.

55. Qiao, Z. A.; Wang, Y.; Gao, Y.; Li, H.; Dai, T.; Liu, Y.; Huo, Q. Commercially Activated Carbon as the Source for Producing Multicolor Photoluminescent Carbon Dots by Chemical Oxidation. *Chem. Commun.,* **2010**, *46,* 8812-8814.

56. Xu, M.; He, G.; Li, Z.; He, F.; Gao, F.; Su, Y.; Zhang, L.; Yang, Z.; Zhang, Y. A Green Heterogeneous Synthesis of N-Doped Carbon Dots and Their Photoluminescence Applications in Solid and Aqueous States. *Nanoscale,* **2014***, 6,* 10307-10315.

57. Wang , F.; Pang, S.; Wang, L.; Li, Q.; Kreiter, M.; Liu, C. Y. One-Step Synthesis of Highly Luminescent Carbon Dots in Noncoordinating Solvents. *Chem. Mater.,* **2010***, 22,* 4528-4530.

58. Jiang, K.; Sun, S.; Zhang, L.; Wang, Y.; Cai, C.; Lin, H. Bright-Yellow-Emissive N-Doped Carbon Dots: Preparation, Cellular Imaging, and Bifunctional Sensing. *ACS Appl. Mater. Interfaces,* **2015**, *7,* 23231-23238.

59. Zhang, Z.; Hao, J.; Zhang, J.; Zhang, B.; Tang, J. Protein as the Source for Synthesizing Fluorescent Carbon Dots by a One-Pot Hydrothermal Route. *RCS Adv.,* **2012**, *2*, 8599-8601

60. Bhunia, S. K.; Maity, A. R.; Nandi, S.; Stepensky, D.; Jelinek, R. Imaging Cancer Cells Expressing the Folate Receptor with Carbon Dots Produced from the Folic Acid. *ChemBioChem.,***2016**, *17*, 614-619.

61. Kozák, O.; Datta, K. K. R.; Greplová, M.; Ranc, V.; Kaslik, J.; Zboril, R. Surfactant-Derived Amphiphilic Carbon Dots with Tunable Photoluminescence. *J. Phys. Chem. C.,* **2013**, *117,*24991-24996.

62. Jiang, K.; Sun, S.; Zhang, L.; Lu, Y.; Wu, A.; Cai, C.; Lin, H. Red, Green, and Blue Luminescence by Carbon Dots: Full-Color Emission Tuning and Multicolor Cellular Imaging. *Angew. Chem. Int.,* **2015**, *54*, 5360-5363.

63. Tang, L.; Ji, R.; Cao, X.; Lin, J.; Jiang, H.; Li, X; Teng, K. S.; Luk, C. M.; Zeng, S.; Hao, J.; Lau, S. P. Deep Ultraviolet Photoluminescence of Water-Soluble Self-Passivated Graphene Quantum Dots. *ACS Nano,* **2012***, 6,* 5102-5110.

64. Song, Y.; Zhu, S.; Zhang, S.; Fu, Y.; Wang, L.; Zhao, X.; Yang, B. Investigation from Chemical Structure to Photoluminescent Mechanism: A Type of Carbon Dots from the Pyrolysis of Citric acid and Amine. *J. Mater. Chem. C.,***2015**, *3,* 5976-5984.

65. Sharma, A.; Gadly, T.; Neogy, S.; Ghosh, S. K.; Kumbhakar, M. Molecular Origin and Self-Assembly of Fluorescent Carbon Nanodots in Polar Solvents. *J. Phys. Chem. Lett.,* **2017**, *8,* 1044-1052.

66. Ehrat, F.; Bhattacharyya, S.; Schneider, J.; Löf, A.; Wyrwich, R.; Rogach, A. L.; Stolarczyk, J. K.; Urban, A. S.; Feldmann, J. Tracking the Source of Carbon Dot Photoluminescence: Aromatic Domains Versus Molecular Fluorophores. *Nano Lett.*, **2017***, 17,* 7710-7716.

67. Ponomarenko, L. A.; Schedin, F.; Katsnelson, M. I.; Yang, R.; Hill, E. W.; Novoselov, K. S.; Geim, A. K. Chaotic Dirac Billiard in Graphene Quantum Dots. *Science,* **2008***, 320,* 356-358.

68. Yan, X.; Cui, X.; Li, L.S. Synthesis of Large, Stable Colloidal Graphene Quantum Dots with Tunable Size. *J. Am. Chem. Soc.,* **2010**, *132,* 5944-5945.

69. Essner, J. B.; Kist, J. A.; Polo-Parada, L.; Baker, G. A. Artifacts and Errors Associated with the Ubiquitous Presence of Fluorescent Impurities in Carbon Nanodots. *Chem. Mater.,* **2018***, 30,* 1878-1887.

70. Krysmann, M. J.; Kelarakis, A.; Dallas, P.; Giannelis, E. P. Formation Mechanism of Carbogenic Nanoparticles with Dual Photoluminescence Emission. *J. Am. Chem. Soc.,* **2011***, 134,* 747-750.

71. Li, X.; Zhang, S.; Kulinich, A.; Liu, Y.; Zeng, H. Engineering Surface States of Carbon Dots to Achieve Controllable Luminescence for Solid-Luminescent Composites and Sensitive Be^{2+} Detection. *Sci. Rep.,* **2014**, *4,* 4976-4984*.*

72. Dekaliuk, M. O.; Viagin, O.; Malyukin, V.; Demchenko, A. P. Fluorescent Carbon Nanomaterials: "Quantum Dots" or Nanoclusters? *Phys. Chem. Chem. Phys.,* **2014**, *16*, 16075-16084.

73. Sun Y-P.; Wang, X.; Lu, F.; Cao, L.; Meziani, M. J.; Luo, P. G.; Gu, L.; Veca, L. M. Doped Carbon Nanoparticles as a New Platform for Highly Photoluminescent Dots. *J. Phys. Chem. C.,* **2008,** *112,* 18295-18298.

74. Tian, L.; Ghosh, D.; Chen, W.; Pradhan, S.; Chang, X.; Chen, S. Nanosized Carbon Particles From Natural Gas Soot. *Chem. Matter,* **2009***, 21,* 2803-2809.

75. Hu, S-L.; Niu, K-Y.; Sun, J.; Yang, J.; Zhao, N-Q.; Du, X-W. One-Step Synthesis of Fluorescent Carbon Nanoparticles by Laser Irradiation. *J. Mater. Chem.,* **2009***, 19,* 484-488.

76. Peng, H.; Travas-Sejdic, J.; Simple Aqueous Solution Route to Luminescent Carbogenic Dots from Carbohydrates. *Chem. Mater.,* **2009**, *21,* 5563-5565.

77. Li, H.; He, X.; Kang, Z.; Liu, Y.; Liu, J.; Lian, S.; Tsang, C. H. A.; Yang, X. B.; Lee, S-T.; Huang, H. Water-Soluble Fluorescent Carbon Quantum Dots and Photocatalyst Design. *Angew. Chem. Int. Ed.,* **2010**, *49,* 4430-4434.

78. Zhao, Q-L.; Zhang, Z-L.; Huang, B-H.; Peng, J.; Zhang, M.; Pang, D-W. Facile Preparation of Low Cytotoxicity Fluorescent Carbon Nanocrystals by Electrooxidation of Graphite. *Chem. Commun.,* **2008***,* 5116-5118.

79. Li, H.; Ming, H.; Liu, Y.; Yu, H.; He, X.; Huang, H.; Pan, K.; Kang, Z.; Lee, S-T. Fluorescent Carbon Nanoparticles: Electrochemical Synthesis and their pH Sensitive Photoluminescence Properties. *New J. Chem.,* **2011***, 35,* 2666-2670.

80. Zhu, H.; Wang, X. L.; Li, L.; Wang, Z. J.; Yang, F.; Yang, X. R. Microwave Synthesis of Fluorescent Carbon Nanoparticles with Electroluminescence Properties. *Chem. Commun.,* **2009***,* 5118-5120*.*

81. Zheng, L.; Chi, Y. Dong, Y.; Lin, J.; Wang, B. Electrochemiluminescence of Water-Soluble Carbon Nanocrystals Released Electrochemically from Graphite. *J. Am. Chem. Soc.,* **2009**, *131,* 4564-4565.

82. Li, L. L.; Ji, J.; Fei, R.; Wang, C. Z.; Lu, Q.; Zhang, J. R.; Jiang, L. P.; Zhu, J. J. A Facile Microwave Avenue to Electrochemiluminescent Two-Color Graphene Quantum Dots. *Adv. Funct. Mater,* **2012**, *22,* 2971-2979.

83. Zhang, P.; Xue, Z.; Luo, D.; Yu, W.; Guo, Z.; Wang, T. Dual-Peak Electrogenerated Chemiluminescence of Carbon Dots for Iron Ions Detection. *Anal. Chem.,* **2014***, 86,* 5620-5623.

84. Zhao, L.; Di, F.; Wang, D.; Guo, L. H.; Yang, Y.; Wan, B.; Zhang, H. Chemiluminescence of Carbon Dots Under Strong Alkaline Solutions: A Novel Insight into Carbon Dot Optical Properties. *Nanoscale,* **2013***, 5,* 2655-2658.

85. Nandi, S.; Malishev, R.; Parambath Kootery, K.; Mirsky, Y.; Kolusheva, S.; Jelinek, R. Membrane Analysis with Amphiphilic Carbon Dots. *Chem. Commun.,* **2014**, *50,* 10299-10302.

86. Feng. L.; Zhao, A.; Ren, J.; Qu, X.; Lighting up Left-Handed Z-DNA: Photoluminescent Carbon Dots Induce DNA B to Z Transition and Perform DNA Logic Operations. *Nucleic Acids Res.,* **2013**, *41,* 7987-7996.

87. Yu, C.; Li, X.; Zeng, F.; Zheng, F.; Wu, S. Carbon-Dot-Based Ratiometric Fluorescent Sensor for Detecting Hydrogen Sulfide in Aqueous Media and Inside Live Cells. *Chem. Commun.,* **2013**, *49*, 403-405.

88. Wang, J.; Zhang, Z.; Zha, S.; Zhu, Y.; Wu, P.; Ehrenberg, B.; Chen, J-Y. Carbon Nanodots Featuring Efficient FRET for Two-Photon Photodynamic Cancer Therapy with a Low fs Laser Power Density. *Biomaterials,* **2014***, 35,* 9372-93817

89. Tang, J.; Kong, B.; Wu, H.; Xu, M.; Wang, Y.; Wang, Y.; Zhao, D.; Zheng, G. Carbon Nanodots Featuring Efficient FRET for Real-Time Monitoring of Drug Delivery and Two-Photon Imaging. *Adv. Mater.,* **2013**, *25*, 6569-6574.

90. Kong, B.; Zhu, A.; Ding, C.; Zhao, X.; Li, B.; Tian, Y. Carbon Dot-Based Inorganic-Organic Nanosystem for Two-Photon Imaging and Biosensing of pH Variations in Living Cells and Tissues. *Adv. Mater.,* **2012***, 24,* 5844-5848.

91. Zhuo, S.; Shao, M.; Lee, S. T. Upconversion and Downconversion Fluorescent Graphene Quantum Dots: Ultrasonic Preparation and Photocatalysis. *ACS Nano,* **2012***, 6,* 1059-1064.

92. Shen, J.; Zhu, Y.; Chen, C.; Yang, X.; Li, C. Facile Preparation and Upconversion Luminescence of Graphene Quantum Dots. *Chem. Commun.,* **2011**, *47*, 2580-2582.

93. Bhunia, S. K.; Saha, A.; Maity, A. R.; Ray, S. C.; Jana, N. R. Carbon Nanoparticle-Based Fluorescent Bioimaging Probes. *Sci. Rep*., **2013**, 3, 1473

94. Yang, S. T.; Cao, L.; Luo, P. G.; Lu, F.; Wang, X.; Wang, H.; Meziani, M. J.; Liu, Y.; Qi, G.; Sun, Y. P. Carbon Dots for Optical Imaging In Vivo. *J. Am. Chem. Soc*., **2009**, *131*, 11308-11309.

95. Zheng, M.; Ruan, S.; Liu, S.; Sun, T.; Qu, D.; Zhao, H.; Xie, Z.; Gao, H.; Jing, X.; Sun, Z. Self-Targeting Fluorescent Carbon Dots for Diagnosis of Brain Cancer Cells. *ACS Nano*, **2015**, *9*, 11455-11461.

96. Bourlinos, A. B.; Bakandritsos, A.; Kouloumpis, A.; Gournis, D.; Krysmann, M.; Giannelis, E. P.; Polakova, K.; Safarova, K.; Hola, K.; Zboril, R. Gd(II)-Doped Carbon Dots as a Dual Fluorescent-MRI Probe. *J. Mater. Chem.,* **2012**, *22*, 23327-23300.

97. Shereema, R. M.; Sruthi, T. V.; Kumar, V. B. S.; Rao, T. P.; Shankar, S. S. Angiogenic Profiling of Synthesized Carbon Quantum Dots. *Biochemistry,* **2015***, 54,* 6352-6356.

98. Liu, C.; Zhang, P.; Zhai, X.; Tian, F.; Li, W.; Yang, J.; Liu, Y.; Wang, H.; Wang, W.; Liu, W. Nano-Carrier for Gene Delivery and Bioimaging Based on Carbon Dots with PEI-Passivation Enhanced Fluorescence. *Biomaterials,* **2012***, 33,* 3604-3613.

99. Ding, H.; Du, F.; Liu, P.; Chen, Z.; Shen, J. DNA-Carbon Dots Function as Fluorescent Vehicles for Drug Delivery. *ACS Appl. Mater. Interfaces*, **2015**, *7*, 6889-6897.

100. Wang, Q.; Zhang, C.; Shen, G.; Liu, H.; Fu, H.; Cui, D. Fluorescent Carbon Dots as an Efficient siRNA Nanocarriers for its Interference Therapy in Gastric Cancer Cells. *J. Nanobiotechnol,* **2014***, 12*, 58.

101. Xu, J.; Zeng, F.; Wu, H.; Hu, C.; Yu, C.; Wu, S. Preparation of a Mitochondria-Targeted and NO-Releasing Nanoplatform and its Enhanced Pro-Apoptotic Effect on Cancer Cells. *Small*, **2014**, *10*, 3750-3760.

102. Wang, Q.; Huang , X.; Long, Y.; Wang, X.; Zhang, H.; Zhu, R.; Liang, L.; Teng, P.; Zheng, H. Hollow Luminescent Carbon Dots for Drug Delivery. *Carbon,* **2013**, *59,* 192-199.

103. Krishna, A. S.; Radhakumary, C.; Antony, M.; Sreenivasan, K. Functionalized Carbon Dots Enable Simultaneous Bone Crack Detection and Drug Deposition *J. Mater. Chem. B.,* **2014**, *2,* 8626-8632.

104. Ge, J.; Lan, M.; Zhou, B.; Liu, W.; Guo, L.; Wang, H.; Jia, Q.; Niu, G.; Huang, X.; Zhou, H.; Meng, X.; Wang, P.; Lee, C. S.; Zhang, W.; Han, X. A Graphene Quantum Dot Photodynamic Therapy Agent with High Singlet Oxygen Generation. *Nat. Commun.,* **2014,** *5,* 4596.

105. Hui, L.; Huang, J.; Chen, G.; Zhu, Y.; Yang, L. Antibacterial Property of Graphene Quantum Dots (Both Source Material and Bacterial Shape Matter). *ACS Appl. Mater Interfaces*, **2016**, *8,* 20-25.

106. Shao, X.; Gu, H.; Wang, Z.; Chai, X.; Tian, Y.; Shi, G. Highly Selective Electrochemical Strategy for Monitoring of Cerebral Cu^{2+} Based on a Carbon Dot-TPEA Hybridized Surface. *Anal. Chem*., **2013**, *85*, 418-425.

107. Costas-Mora, I.; Romero, V.; Lavilla, I.; Bendicho, C. In Situ Building of a Nanoprobe Based on Fluorescent Carbon Dots for Methylmercury Detection. A*nal. Chem*., **2014**, *86*, 4536-4543.

108. Lin, Y.; Wang , C.; Li, L.; Wang, K.; Liu, K.; Wang, K.; Li, B. Tunable Fluorescent Silica-Coated Carbon Dots: A Synergistic Effect for Enhancing the Fluorescence Sensing of Extracellular Cu^{2+} in Rat Brain. *ACS Appl. Mater. Interfaces*, **2015**, *7*, 27262-27270.

109. Ma, N.; Jiang, W.; Li, T.; Zhang, Z.; Qi, H.; Yang, M. Fluorescence Aggregation Assay for the Protein Biomaker Mucin 1 Using Carbon Dot-Labeled Antibodies and Aptamers. *Microchim. Acta*, **2015**, *182*, 443-447.

110. Deng, J.; Lu, Q.; Hou, Y.; Liu, M.; Li, H.; Zhang, Y.; Yao, S. Nanosensor Composed of Nitrogen-Doped Carbon Dots and Gold Nanoparticles for Highly Selective Detection of Cysteine with Multiple Signals. *Anal. Chem*., **2015**, *87*, 2195-2203.

111. Chai, L.; Zhou, J.; Feng, H.; Tang, C.; Huang, Y.; Qian, Z. Functionalized Carbon Quantum Dots with Dopamine for Tyrosinase Activity Monitoring and Inhibitor Screening: In Vitro and Intracellular Investigation. *ACS Appl. Mater. Interfaces,* **2015**, *7*, 23564-23574.

112. Lin, F.; Pei, D.; He, W.; Huang, Z.; Huang, Y.; Guo, X. Electron Transfer Quenching by Nitroxide Radicals of the Fluorescence of Carbon Dots. *J. Mater. Chem*., **2012**, *22*, 11801-11807.

113. Gao, X.; Ding, C.; Zhu, A.; Tian, Y. Carbon-Dot-Based Ratiometric Fluorescence Probe for Imaging and Biosensing of Superoxide Anion in Live Cells. *Anal. Chem*., **2014**, *86*, 7071-7078.

114. Shen, P.; Xia, Y. Synthesis-Modification Integration: One-Step Fabrication of Boronic Acid Functionalized Carbon Dots for Fluorescent Blood Sugar Sensing. *Anal. Chem*., **2014**, *86*, 5323-5329.

115. Nandi, S.; Ritenberg, M.; Jelinek, R. Bacterial Detection with Amphiphilic Carbon Dots. *Analyst*, **2015**, *140*, 4232-4237.

116. Wang, R.; Xu, Y.; Zhang, T.; Jiang, Y. Rapid and Sensitive Detection of Salmonella Typhimurium Using Aptamer-Conjugated Carbon Dots as Fluorescence Probe. *Anal. Methods*, 2015, 7, 1701-1706.

117. Hou, Y.; Lu, Q.; Deng, J.; Li, H.; Zhang, Y. One-Pot Electrochemical Synthesis of Functionalized Fluorescent Carbon Dots and Their Selective Sensing for Mercury Ion. *Anal. Chim. Acta*, **2015**, *866*, 69-74.

118. Zhu, S.; Meng, Q.; Wang, L.; Zhang, J.; Song, Y.; Jin, H.; Zhang, K.; Sun, H.; Wang, H.; Yang, B.; Highly Photoluminescent Carbon Dots for Multicolor Pattering, Sensors and Bioimaging. *Angew. Chem. Int. Ed*., **2013**, *52*, 3953-3957.

119. Pan, L.; Sun, S.; Zhang, A.; Jiang, K.; Zhang, L.; Dong, C.; Huang, Q.; Wu, A.; Lin, H. Truly Fluorescent Excitation-Dependent Carbon Dots and their Applications in Multicolor Cellular Imaging and Multidimensional Sensing. *Adv. Mater*., **2015**, *27*, 7782-7787.

120. Wang, R.; Li, G.; Dong, Y.; Chi, Y.; Chen, G. Carbon Quantum Dot-Functionalized Aerogels for NO_2 Gas Sensing. *Anal. Chem*., **2013**, *85*, 8065-8069

121. Chen, P. C.; Chen, Y. N.; Hsu, P. C.; Shih, C. C.; Chang, H. T. Photoluminescent Organosilane-Functionalized Carbon Dots as Temperature Probes. *Chem. Commun*., **2013**, *49*, 1639-1641.

122. Yan, X.; Cui, X.; Li, B.; Li, L. S. Large, Solution-Processable Graphene Quantum Dots as Light Absorbers for Photovoltaics. *Nano Lett.,* **2010**, *10*, 1869-1873.

123. Kim, J. K.; Park, M. J.; Kim, S. J.; Wang, D. H.; Cho, S. P. Bae, S.; Park, J. H.; Hong, B. H. Balancing Light Absorptivity and Carrier Conductivity of Graphene Quantum Dots for High-Efficiency Bulk Heterojunction Solar Cells. *ACS Nano*, **2013**, *7*, 7207-7212.

124. Chen, B.; Feng, J. White-Light-Emitting Polymer Composite Film Based on Carbon Dots and Lanthanide Complexes. *J. Phys. Chem. C*., **2015**, *119*, 7865-7872.

125. Kim, T. H.; Wang, F.; McCormick, P.; Wang, L.; Brown, C.; Li, Q. Salt-Embedded Carbon Nanodots as a UV and Thermal Stable Fluorophore for Light-Emitting Diodes. *J. Lumin,* **2014**, *154*, 1-7.

126. Wang, Y.; Kalytchuk, S.; Zhang, Y.; Shi, H.; Kershaw, S. V.; Rogach, A. L. Thickness-Dependent Full-Color Emission Tunability in a Flexible Carbon Dot Ionogel. *J. Phys. Chem. Lett*., **2014**, *5*, 1412-1420.

127. Zhang, X.; Zhang, Y.; Wang, Y.; Kalytchuk, S.; Kershaw, S. V.; Wang, Y.; Wang, P.; Zhang, T.; Zhao, Y.; Zhang, H.; Cui, T.; Wang, Y.; Zhao, J.; Yu, W. W.; Rogach, A. L. Color-Switchable Electroluminescence of Carbon Dot Light-Emitting Diodes. *ACS Nano,* **2013**, *7*, 11234-11241.

128. Bhunia, S. K.; Nandi, S.; Shikler, R.; Jelinek, R. Tuneable Light-Emitting Carbon-Dot/Polymer Flexible Films Prepared Through One-Pot Synthesis. *Nanoscale*, **2016**, *8*, 3400-3406.

129. Liu, R.; Liu, J.; Kong, W.; Huang, H.; Han, X.; Zhang, X.; Liu, Y.; Kang, Z. Adsorption Dominant Catalytic Activity of a Carbon Dots Stabilized Gold Nanoparticles System. *Dalton Trans*., **2014**, *43*, 10920-10929.

130. Zhang, H.; Ming, H.; Lian, S.; Huang, H.; Li, H.; Zhang, L.; Liu, Y.; Kang, Z.; Lee, S. T. Fe_2O_3/Carbon Quantum Dots Complex Photocatalysts and Their Enhanced Photocatalytic Activity Under Visible Light. *Dalton Trans*., **2011**, *40*, 10822-10825.

131. Xie, S.; Su, Hua, Wei, W.; Li, M.; Tong, Y.; Mao, Z. Remarkable Photoelectrochemical Performance of Carbon Dots Sensitized TiO_2 Under Visible Light Irradiation. *J. Mater. Chem. A,* **2014**, *2*, 16365-16368.

132. Han, M.; Zhu, S.; Lu, S.; Song, Y.; Feng, T.; Tao, S.; Liu, J.; Yang, B. Recent Progress on the Photocatalysis of Carbon Dots: Classification, Mechanism and Applications. *Nano Today*, **2018**, *19*, 201-218.

133. González, R.; Pareja, R.; Ballesteros, C. *Microscopía Electrónica.* EUDEMA: Madrid, 1991.

134. Kirkland, A. I.; Chang, S. L. Y.; Hutchison, J. L. Atomic Resolution Transmission Electron Microscopy. In *Science of Microscopy;* Hawkes, P. W.; Spence, J. C. H.; Springer: N.Y., 2007.

135. Nellist, P. D. Scanning Transmission Electron Microscopy. In *Science of Microscopy;* Hawkes, P. W.; Spence, J. C. H.; Springer: N.Y., 2007.

136. Botton, G. Analytical Electron Microscopy. In *Science of Microscopy;* Hawkes, P. W.; Spence, J. C. H.; Springer: N.Y., 2007.

137. Venkateshaiah, A.; Nutenki, R.; Kattimuttathu, S. X-ray Diffraction Spectroscopy of Polymer Nanocomposites. In *Spectroscopy of Polymer Nanocomposites.* Sabu, T.; Didier, R.; Deepalekshmi, P. William Andrew Publishing: NY, 2016

138. Bourlinos, A. B.; Stassinopoulos, D.; Anglos, D.; Zboril, R.; Karakassides, M.; Giannelis, E. P. Surface Functionalized Carbogenic Quantum Dots. *Small,* **2008**, *4*, 455-458.

139. Jalili, N.; Laxminarayana K. A Review of Atomic Force Microscopy Imaging Systems: Applications to Molecular Metrology and Biological Sciences. *Mechatronics,* **2004***, 14*, 907-945.

140. Wang, X.; Cao, L.; Lu, F.; Meziani, M. J. Li, H.; Qi, G.; Zhou, B.; Harruff. B. A.; Kermarrec, F.; Sun, Y. P. Photoinduced Electrons transfers with Carbon Dots. *Chem. Commun.,* **2009**, 3774-3776.

141. Stetefeld, J.; Mckenna, S. A.; Patel, T. R. Dynamic Light Scattering : A Practical Guide and Applications in Biomedical Sciences. *Biophys. Rev.,* **2016***, 8*, 409-427.

142. Dager, A.; Uchida, T.; Maekawa, T.; Tachibana, M. Synthesis and Characterization of Mono-Disperse Carbo Quantum Dots from Fennel Seeds: Photoluminescence Analysis Using Machine Learning. *Scientific Reports*, **2019**, *9*, 14004-14015.

143. Schwille, P.; Ries, J. Principles and Applications of Fluorescence Correlation Spectroscopy (FCS). In *Biophotonics: Spectroscopy, Imaging, Sensing and Manipulation.* Bartolo, B. D.; Collins, J. Springer Science: The Netherlands, 2011

144. Righetto, M.; Privitera, A.; Fortunati, I.; Mosconi, D.; Zerbetto, M.; Curri, M. L.; Corricelli, M.; Moretto, A.; Agnoli, S.; Franco, L.; Bozio, R.; Ferrante, C. Spectroscopic Insights Into Carbon Dot System. J. Phys. Chem. Lett., **2017***, 8*, 2236-2242.

145. Pelletier, M. J. *Analytical Applications of Raman Spectroscopy.* Chap. 1, Blackwell Science Ltd: Oxford, U.K., 1999.

146. Wang, Y.; Alsmeyer, D. C.; McCreery, R. L. Raman Spectroscopy of Carbon Materials: Structural Basis of Observed Spectra. *Chem. Mater.,* **1990**, *2*, 557-563.

147. Fan, Y.; Cheng, H.; Zhou, C.; Xie, X.; Liu, Y.; Dai, L.; Zhang, J.; Qu, L. Honeycomb Architecture of Carbon Quantum Dots: A new Efficient Substrate to Support Gold for Stronger SERS. *Nanoscale,* **2012**, *4*, 1776-1781.

148. Zhang, Y.; Xing, C.; Jiang, D.; Chen, M. Facile Synthesis of Core-Shell-Satellite Ag/C/Ag Nanocomposites Using Carbon Nanodots as Reductant and Their SERS Properties. *CrystEngComm.,* **2013***, 15*, 6305-6310.

149. Duley, W. W.; Hu, A. The 217.5 nm Band, Infrared Absorption, and Infrared Emission Features in Hydrogenated Amorphous Carbon Nanoparticles. *Astrophys. J.,* **2012***, 761*, 115-130.

150. Zhou, J. G.; Booker, C.; Li, R. Y. Zhou, X. T.; Sham, T. K.; Sun, X. L. Ding, F. An Electrochemical Avenue to Blue Luminescent Nanocrystals from Multiwalled Carbon Nanotubes (MWCNTs). *J. Am. Chem. Soc.,* **2007**, *129*, 744-745.

151. Olsen, E. D. *Métodos Ópticos de Análisis.* Reverte: Barcelona, España, 1990.

152. Moulder, J. F.; Stickle, W. F.; Sobol, P. E.; Bomben, K. D. *Handbook of X-ray Photoelectron Spectroscopy.* Perkin-Elmer Corp.: MN, USA, 1992.

153. Gong, X.; Paau, M. C.; Hu, Q.; Shuang, S.; Dong, C.; Choi, M. M. F. UHPLC Combined with Mass Spectrometric Study of As-Synthesized Carbon Dots Samples. *Talanta,* **2016***, 146,* 340-350.

154. Hu, Q.; Meng, X.; Choi, M. M. F.; Gong, X.; Chan, W. Elucidating the Structural of Carbon Nanoparticles by Ultra-Performance Liquid Chromatography Coupled with Electrospray Ionisation Quadrupole Time-of-Flight Tandem Mass Spectrometry. *Analytica Chimica Acta,* **2016**, *911,* 100-107.

155. Hoffmann, E.; Stroobant, V.; *Mass Spectrometry: Principles and Applications.* John Wiley & Sons Ltd: England, 2001.

3

Objectives

3. OBJECTIVES

According to the background and context of the research plan, the aim of this work is the synthesis and the structural and photophysical characterisation of unprecedented carbon nanostructures, as well as the analysis of their applicability in different scientific-technological fields.

Specific objectives of chapter 1 and chapter 2

- Carbon nanodots will be prepared by solvothermal and pulsed laser synthesis and it will be assessed how the relevant chemical and instrumental parameters are affected by the synthetic routes

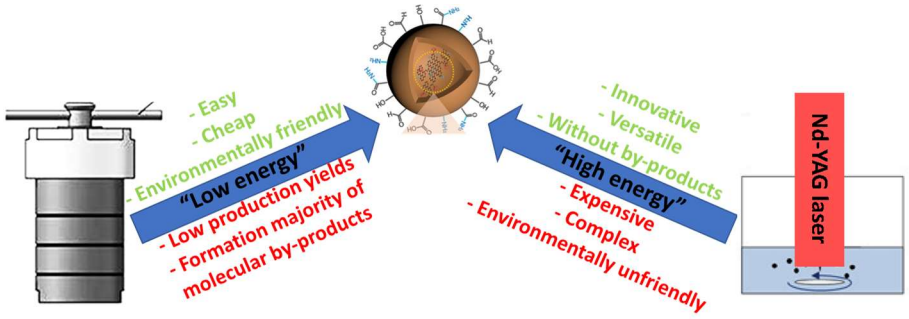

Figure 3.1. Schematic representation of the synthetic methods used in this work to prepare CNDs with their main advantages and disadvantages

- The morphology and structure of the synthesized carbon nanodots will be characterized by techniques such as: NMR, FTIR, MS, Raman spectroscopy, SERS, ATG, XPS, FCS, TEM, STEM combined with EELS and EDS, DLS, AFM, XRD, SAXS and GI-WAXS.
- The photophysics of the prepared carbon nanodots will be studied by absorption and photoluminescence spectroscopy with and without time resolution at variable temperature. Photoluminescence quantum yields will be determined and charge and/or energy transfer processes will be investigated, and their kinetic parameters and quantum yields, will be determined.
- The role of small molecule by-products of solvothermal synthesis will be determined and critically assessed.

Specific objectives of chapter 3

- The CNDs prepared in chapter 1 will be hybridized with TiO_2 nanoparticles affording new CND@TiO_2 heterostructures whose morphological and photophysical properties will be determined.
- The photocatalytic activity of the CND@TiO_2 heterostructures under illumination by visible light will be studied, in particular taking into account

photocatalytic action spectra and experiments with scavenger of radicals and reactive oxygen species. Resonant and non-resonant contributions and interactions between the contaminants and TiO_2 nanoparticles as well as the CND component in the heterostructures will be discussed.

- The possibility of up-conversion processes taking part in the photocatalytic reactions will be determined.

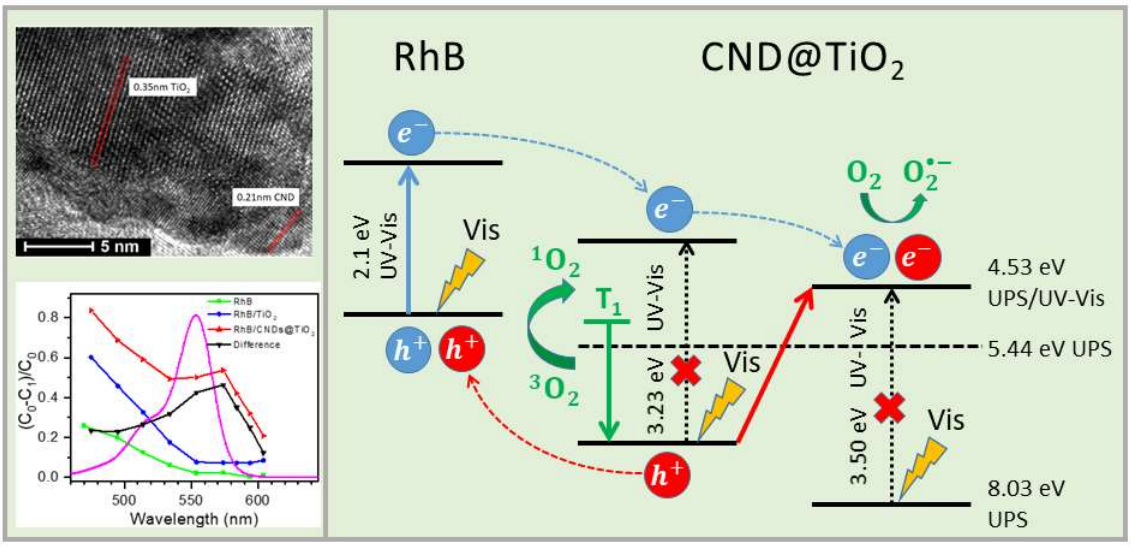

Figure 3.2. Figure composed of: HR-TEM image of the CND@TiO_2 heterostructure; the excitation wavelength-dependent degradation of RhB in the absence or presence of TiO_2, CNDs and CNDs@TiO_2; and schematic representation of the band alignments of the CNDs@TiO_2 heterostructure and RhB and the processes taking place in the RhB photodegradation mechanism.

Specific objectives of chapter 4

- A series of structurally well-defined curved molecular nanographenes previously synthesized by a bottom-up approach, will be photophysically characterized.
- The photophysics of the nanographenes will be studied by photoluminescence spectroscopy at variable temperature with and without time resolution, with the intention to obtain detailed information on the emitting electronic states.
- Temperature-dependent non-radiative decay of the electronically excited states will be studied.
- Quantum chemical calculations by density functional theory (DFT) will provide a better understanding of the experimentally observed photophysical processes.

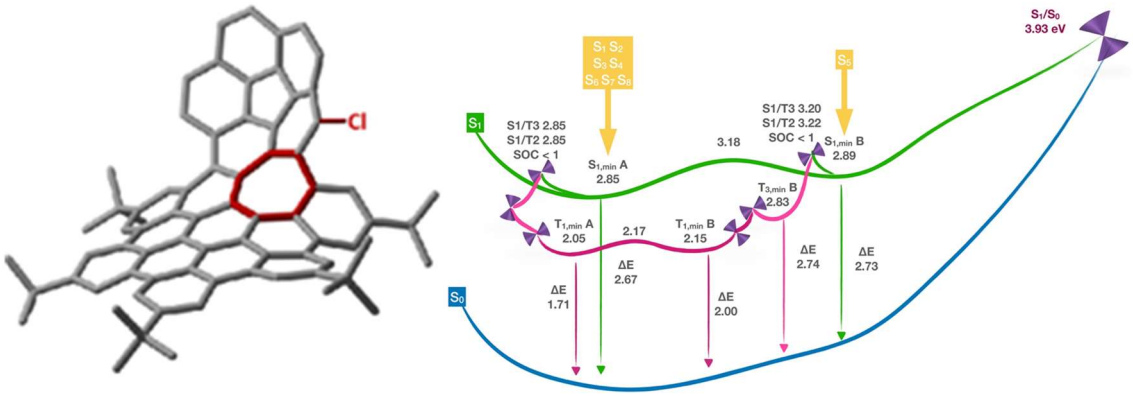

Figure 3.3. Structure of CNG 7 with the schematic representation of its potential energy surface showing two S_1 minima, two T_1 minima and a non-emitting T_3 minimum, responsible for fluorescence, phosphorescence and TADF, respectively.

4

Results and discussion

Chapter 1:

Solvothermally Synthesized Carbon Nanodots

The results presented in this chapter have been published in:

S. Ramírez-Barroso, A. Jacobo-Martín, I. Navarro-Baena, J. J. Hernández, C. Navio, I. Rodríguez, R. Wannemacher. "On the nature of solvothermally synthesized carbon nanodots" *J. Mater. Chem. C.,* **2021**, *9,* 16935-16944.

Selected for the "Hot paper collection" of J. Mater. Chem. C

Chapter 1: Solvothermally Synthesized Carbon Nanodots

4.1.1. Introduction

Solvothermally synthesized carbon nanodots (CNDs) have received tremendous attention because of their significant advantages in terms of their easy, cheap and green metal-free synthesis, excellent biocompatibility, low cytotoxicity and apparent outstanding photophysical properties, such as high fluorescence quantum yield and high photostability.[1-8] Such desirable combination of properties suggests opportunities for replacing conventional fluorescent materials in various fields of applications, ranging from optoelectronics, photovoltaics or photocatalysis to biomedicine.[9-20] This interest has led to an almost exponential growth in the number of scientific articles published on the subject, but, on the other hand, this rapid pace has been accompanied by a host of misconceptions that have hindered the elucidation of the true nature of carbon dots. The characterization of the structure and photophysics of solvothermally synthesized CNDs is complicated by the fact that it is masked by the presence of molecular and oligomeric products partially attached to the CNDs. For this reason, it is essential to carefully purify the synthesized materials, to know all the major reaction products generated during the synthesis and to compare the properties of the fractions separated in the purification step.[21-22] Related to this problem, there is still controversy about the photophysical properties of CNDs. Part of the recent studies ascribe the fluorescence of one of the CNDs studied in the present work actually to conjugated small molecules, such as IPCA (imidazo[1,2,α]pyridine-7-carboxilic acid, 1,2,3,5-tetrahydro-5oxo)[23], or similar structures[24-27]. Recent reports on fluorescence or phosphorescence from non-conjugated polymer dots[28-32] also do not appear to fully exclude the presence of small conjugated molecules as the origin of those emissions. In line with the results presented below mass spectrometry of the synthesized products at m/z < 1500, extensive dialysis and comparison of the PL of dialysate and retentate, respectively, are indispensable for this purpose. In general, the published work still does not sufficiently characterize the complex products that arise from solvothermal synthesis of CNDs. The present work attempts to contribute to this task. To this end we have synthesized solvothermal CNDs (a) from citric acid and ethylenediamine as sources of carbon and nitrogen, respectively (blue carbon dots, B-CNDs), one of the most frequently studied types of solvothermal carbon dots, and (b) from p-phenylenediamine as precursors (red carbon dots, R-CNDs).[33-35]

4.1.2. Experimental Section

Synthesis and purification of CNDs

Citric acid (Sigma Aldrich, 99 %), ethylenediamine (Fluka Analytical, 99,5 %), p-phenylenediamine (Sigma Aldrich, 98 %) and absolute ethanol (Merck, 99.5 %) were used to synthesize the carbon dots. Its purification was done with dialysis tubing

cellulose (Merck) of different pore size (1, 14 and 25 kDa molecular weight cut-off MWCO) in the dark, as well as under ambient illumination. Purification was also carried out by size exclusion chromatography (SEC) using Sephadex G25-80.

Characterization of CNDs

Ultra-performance liquid chromatography coupled with electrospray ionization quadrupole time-of-flight tandem mass spectrometry (UPLC-ESI-Q-TOF-MS/MS) was carried out using an ACQUITY UPLC system coupled with high resolution mass spectrometer MAXIX II Bruker. Chromatography was performed using a Waters UPLC C18 column (2.1 mm × 5 cm) packed with 1.7 µm octadecyl (C_{18}) bonded silica. The mobile phase contains 0.1 % formic acid (FA) in water (pH 2.8) as eluent A and MeOH or acetonitrile as eluent B for the B-CNDs or R-CNDs, respectively. The flow rate was 0.1 mL/min, whose composition by volume was 98 % A and 2 % B. Unless otherwise stated, the optimized source conditions were set as follows: capillary voltage, 3.5 kV; desolvation temperature, 300 ^{o}C; and desolvation gas (N_2) flow rate, 8 L/min. The MS range was scanned from 20 Da to 3000 Da and centroided during acquisition using an internal reference (lock spray). Data processing was carried out with Bruker Compass DataAnalysis 4.4 software.

High-resolution transmission electron microscopy (HR-TEM) was carried out using the JEM GRAND ARM300cF with ETA (Expansion Trajectory Aberration Correction) consisting of dodeca-poles (JEOL) on the objective lens and a FEG. The electron accelerating voltage used was 60 kV. Scanning Transmission Electron Microscopy (STEM) was carried out using the JEOL JEM ARM200Cf with CEOS aberration corrector on the field effect emission condenser (cold FEG) lens and HAADF imaging with a JEOL detector and Gatan ABF and HAADF detectors. In this case, the electron acceleration voltage used was 80 kV.

Grazing incidence wide angle X-ray scattering (GIWAXS) measurements was performed at the BL-11 NCD-SWEET beamline of the ALBA synchrotron at Barcelona, Spain. The X-ray patterns were recorded with a WAXS LX255-HS detector from Rayonix (pixel size 80x80µm^2). The norm of the reciprocal space q-vector ($q=4\pi\sin\theta/\lambda$, where θ is the Bragg angle and λ is the wavelength) was calibrated using a chromium oxide (Cr_2O_3) standard. Temperature dependence measurements were performed by using a Linkam heating plate coupled to a precision stage with vertical, horizontal and rotational motions.

Atomic force microscopy (AFM) was carried out on a NT-MDT NTEGRA instrument in dynamic mode. The hydrodynamic size of the CNDs was measured by dynamic light scattering (DLS) from a dilute suspension of the sample in water at pH 7 in a standard cuvette, using a Zetasizer NanoZS device (Malvern Instruments).

Surface-enhanced micro-Raman spectroscopy (SERS) was carried out using an inverted Nikon Eclipse Ti microscope (objective lens 100x/0.8 NA) coupled to a Shamrock SR303i spectrograph equipped with a Peltier-cooled CCD camera (Andor Newton). The home-built set-up allowed excitation of the Raman signals by a helium-neon laser operating at 632.8 nm. The laser was attenuated in order to avoid graphitization of the sample by the excitation. To produce the SERS effect, a commercial gold electrode was used, the surface of which was nano-roughened by cycling in 0.1 M KCl. Absence of the formation of Au oxides was confirmed by cyclic voltammetry. Samples of the B-CDs, R-CNDs and the dialysate, respectively, were drop-cast on the nano-roughened gold surface and allowed to dry.

Attenuated total internal reflection Fourier-transform infrared spectroscopy (ATR-FTIR) was carried out using a Bruker Alpha spectrometer. XPS (X-ray Photoelectron Spectroscopy) measurements were performed under Ultra High Vacuum conditions (UHV, with a base pressure of 5×10^{-10} mbar), using a monochromatic Al K α line as exciting photon source for core level analysis (hv = 1486.7 eV). The emitted photoelectrons were collected in a hemispherical energy analyzer (SPHERA-U7, pass energy set to 20 eV for the XPS measurements to have a resolution of 0.6 eV) and to compensate the charge built up on the sample surface the use of a Flood Gun (FG-500, Specs) was employed, with low energy electrons of 3 eV and 40 μ A. Binding energy was corrected using the Si $2p_{3/2}$ level at 99.3 eV.

UV-Vis absorption spectra were recorded on a UV-Vis spectrophotometer (Varian Cary 50) using 1 cm quartz cuvette (Suprasil). Room-temperature PL and PLE spectra were acquired on a spectrofluorimeter (Horiba FluoroLog 3) equipped with a high-pressure Xenon lamp and a Hamamatsu R928P photomultiplier tube; the PLE and PL spectra were corrected for the characteristics of the lamp source and of the detection system, respectively. The quantum yields of B-CNDs and their dialyzed material were obtained by a relative method using quinine sulphate (QY = 55 % in 0.5 M H_2SO_4), adjusting the optical absorbance to 0.1 at 350 nm and integrating the fluorescence intensity between 370 and 600 nm. Fluorescence quantum yields of the R-CNDs and their dialyzed material were determined by a relative method using rhodamine B (QY = 56 % in ethanol). To obtain reliable results the optical absorbance was adjusted to 0.1 at 510 nm and the fluorescence intensity was integrated between 580 and 610 nm.

PL lifetimes (τ_F) were measuring via time-correlated single photon counting (TCSPC) employing an Acton SP2500 spectrometer equipped with a PMA 06 photomultiplier (PicoQuant) and a HydraHarp-400 TCSPC event timer with 1 ps time resolution. The excitation source was a 405 nm picosecond pulsed diode laser (LDH-D-C-405, PicoQuant) driven by a PDL828 driver (PicoQuant) with FWHM < 70ps. Fluorescence decays were analyzed using PicoQuant Fluofit v4.6.5 data analysis software.

Time-resolved detection of phosphorescence $^1O_2$ was performed using a customized Fluotime 200 fluorescence lifetime system (PicoQuant, Germany) described elsewhere. Briefly, for $^1O_2$ phosphorescence measurements, an AO-Z-473 solid state AOM Q-switched laser (Changchun New Industries Optoelectronics Technology Co., Changchun, China) working at a 4 kHz repetition rate (<1.5 mW average power) was used for excitation at 473 nm. In order to remove any residual component of its fundamental emission in the NIR region, a 1064-nm rugate notch filter (Edmund Optics, U.K.) and an uncoated SKG-5 filter (CVI Laser Corporation) were placed at the exit port of the laser. The NIR luminescence exiting from the side of the sample was filtered by a long-pass filter of 1000 nm and a narrow bandpass filter at 1270 nm. In this way any scattered laser radiation was removed and the NIR emission from singlet oxygen was isolated. A thermoelectrically cooled Hamamatsu NIR sensitive photomultiplier tube assembly (H9170-45, Hamamatsu, Japan) coupled to a multichannel scaler (Nanoharp 250, PicoQuant) was used for single photon counting detection. The time-dependent $^1O_2$ phosphorescence signal S(t) was analyzed using the GraphPad Prism 7 software to fit the data to eq 1, in which τ_T and τ_Δ are the lifetimes of the photosensitizer triplet state and of $^1O_2$ respectively, and S(0) is a pre-exponential parameter proportional to Φ_Δ.

$$S_{1270}(t) = S_{1270}(0) \times \frac{\tau_\Delta}{\tau_\Delta - \tau_T} \times \left(e^{-t/\tau_\Delta} - e^{-t/\tau_T}\right) \quad \text{eq. 1}$$

The Φ_Δ values of the different samples were obtained by comparison of the slopes of S(0) vs. absorbed-laser-energy plots obtained at different sample and reference concentrations (eq. 2).

$$\Phi_{\Delta,sample} = \Phi_{\Delta,ref} \times \frac{Slope_{sample}}{Slope_{ref}} \quad \text{eq. 2}$$

Flavin mononucleotide (Chemodex Ltd. Switzerland) was used as reference (ϕ_Δ = 0.56 ± 0.05).

Fluorescence correlation spectroscopy was performed using an Olympus Ix83 inverted microscope, coupled to a confocal system Olympus FV1200, with 3 confocal detectors (two of them spectral) and one transmitted light, 7 lines of laser, of which 405 and 458 nm were used. The latter is equipped with a motorized stage, an autofocus system (ZDC) and temperature control. The fitting model used was pure diffusion: this assumes that exclusively diffusion contributions are present in the FCS curve (as opposed to contributions from, e.g., triplet states or blinking). The equations used were:

$$G(t) = \sum_{i=0}^{n_{Diff}-1} \frac{\rho[i]}{\left[1 + \frac{t}{\tau_{Diff}[i]}\right]\left[1 + \frac{t}{\tau_{Diff}[i]\,\kappa^2}\right]^{0.5}} \quad \text{eq. 3}$$

$$N = \left[\sum_{i=0}^{n_{Diff}-1} \rho[i]\right]^{-1} \quad \text{eq. 4}$$

$$C = \frac{N}{V_{Eff}\, N_A} \quad \text{eq. 5}$$

$$w_0 = \left[\frac{V_{Eff}}{\kappa}\right]^{\frac{1}{3}} - 0.5 \quad \text{eq. 6}$$

$$z_0 = \kappa\, w_0 \quad \text{eq. 7}$$

$$D[k] = \frac{w_0^2}{4\, \tau_{Diff}\, [k]} \quad \text{eq. 8}$$

$$R_H = \frac{4\, k_B\, T\, \tau_{Diff}}{6\, \pi\, \eta\, w_0^2} \quad \text{eq. 9}$$

4.1.3. Results and discussion

Synthetic procedures of B-CNDs

Different hydrothermal treatments of citric acid and ethylenediamine were explored to synthesize CNDs. The definitive hydrothermal synthesis conditions were chosen based on optimum fluorescence quantum yield of the final product and these conditions are: citric acid (6,5 mmol) and ethylenediamine (12 mmol) were dissolved in 30 mL of water in a Teflon liner. The Teflon liner was placed in a stainless-steel autoclave and held at 200 °C for 5 hours.

After the autoclave was cooled to room temperature, the reaction products were subjected to dialysis with cellulose dialysis tubing of different pore size (1, 14 and 25 kDa molecular weight cut-off, MWCO) for one week, changing the water containing the dialysate outside the dialysis bag every day. In case of dialysis with a 1 kDa MWCO membrane for one week, the dry mass content of the retained material is approximately 20 mg, resulting in a mass yield of ≈ 1%. Although this is a low yield, when characterizing this retained material, it is observed by the different structural and photophysical characterization techniques that there are still a large number of small molecules masking the graphitic structures. On the other hand, in the case of dialysis with 25 kDa MWCO membranes for the same time span, the retained material was insufficient to be fully characterized. Finally, dialysis with 14 kDa MWCO membrane allowed to obtain sufficient retained material (labeled in the following as B-CNDs) for analysis (≈ 5 mg, mass yield ≈ 0.25%), but minimizing as much as possible by dialysis the interference of dissolved molecular and oligomeric compounds. Alternatively, size-exclusion chromatography (SEC) was performed to separate fractions.

Morphological and structural characterization of B-CNDs

The retentate material from the dialysis was separated by UPLC into thirteen fractions within 12 min where it should be evident that only small molecules can be

detected by this technique, not the CNDs themselves. On the other hand, the dialyzed material revealed a very complex mixture with more than 40 kinds of chemical species, but, surprisingly, even after prolonged dialysis, small molecules are still observed in the B-CNDs and are the same as those found in the dialysate (Fig. 1). The high-accuracy mass spectra of the most representative fractions of the B-CNDs sample are displayed in Fig. 1. Fraction 10 is the main one and contains a compound with a mass of 181.0610, which corresponds to a chemical species with formula $C_8H_9N_2O_3$ resulting from the four-fold dehydrated product of the union of a molecule of citric acid and a molecule of ethylenediamine. This molecule has already been reported as imidazo[1,2,α]pyridine-7-carboxilic acid, 1,2,3,5-tetrahydro-5oxo, IPCA.[23] The next most relevant fraction is fraction 8, which reveals a compound with mass of 223.1187, corresponding to a chemical formula $C_{10}H_{15}N_4O_2$, a molecule arising from the union of a molecule of citric acid, two molecules of ethylenediamine and subsequent five-fold dehydration. This molecule (N-(2-aminoethyl)-5-oxo- 1,2,3,5 tetrahydroimidazol [1,2,α]pyridine-7-carboxamide, IPCA-EDA) is another fluorescent molecule found in the B-CNDs. Other relevant fractions are fractions 3, 4, 5, 7 and 9, which reveal chemical species with formulae $C_8H_{13}N_2O_5$, $C_7H_{13}N_2O_3$, $C_{10}H_{17}N_4O_3$, $C_{10}H_{19}N_4O_4$, and $C_8H_{15}N_2O_6$, respectively. All these molecular formulae correspond to molecules that occur in the scheme of synthesis of IPCA and IPCA-EDA, but these are not yet sufficiently conjugated to act as molecular fluorophores (compare Scheme 1). Also noteworthy are the fractions 6 and 13 which reveal the presence of chemical species with the formulae $C_{13}H_{21}N_2O_{10}$ and $C_{13}H_{13}N_2O_6$. Those molecules result from the union of a molecule of ethylenediamine and two molecules of citric acid, once decarboxylated and two or six times dehydrated, respectively. The molecule with the highest molecular weight 379.1248 is found in fraction 11 and corresponds to a molecular formula of $C_{16}H_{19}N_4O_7$. It derives from the union of two molecules of citric acid and two molecules of ethylenediamine after seven-fold dehydration. The mass spectra of fractions 1, 2 and 12 (Fig. 2) arise from the eluent and can be seen in the blank (Fig. 3). In addition, the mass spectra of some of the minority fractions, besides containing peaks corresponding to molecular products of the reaction, also show peaks coming from the eluent or instrument noise. All the identified molecules are much smaller than the pore size of dialysis tubes, the only possible explanation for finding them in the retentate is that they are bound through non-covalent forces to the graphitic cores and partially released after the dialysis.

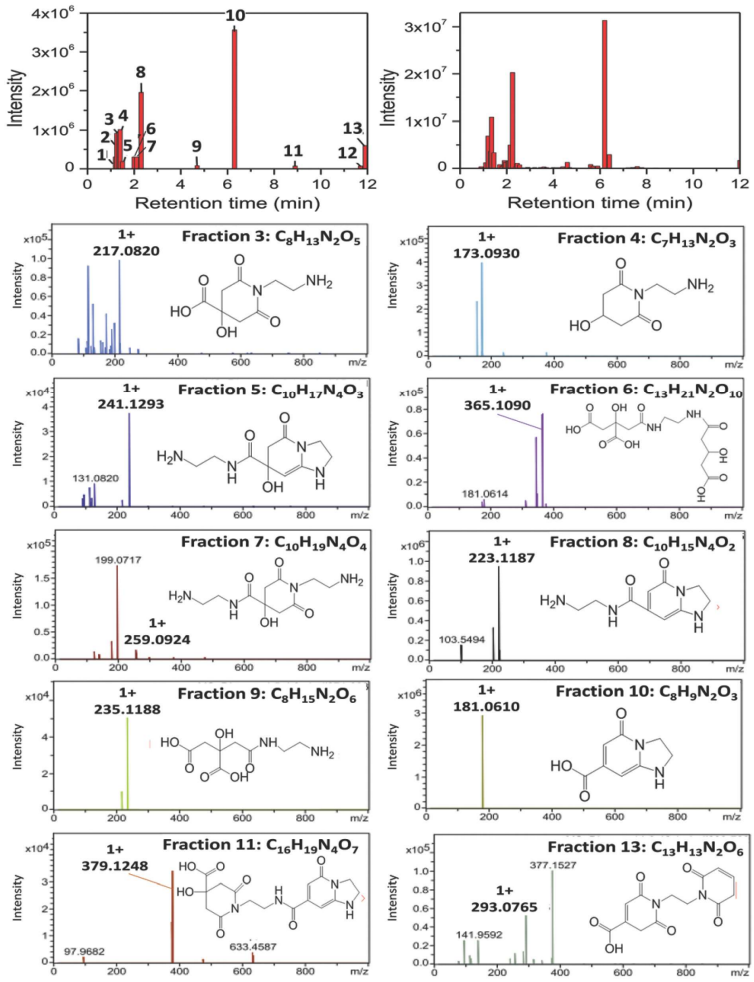

Figure 1. Gradient elution of B-CNDs (left-hand side) and dialyzed material (right-hand side). The chromatograms are monitored with ESI-Q-TOF MS/MS and only the mass spectra of the main molecules observed in the B-CNDs are shown. These main molecules are identical to those found in the dialysate.

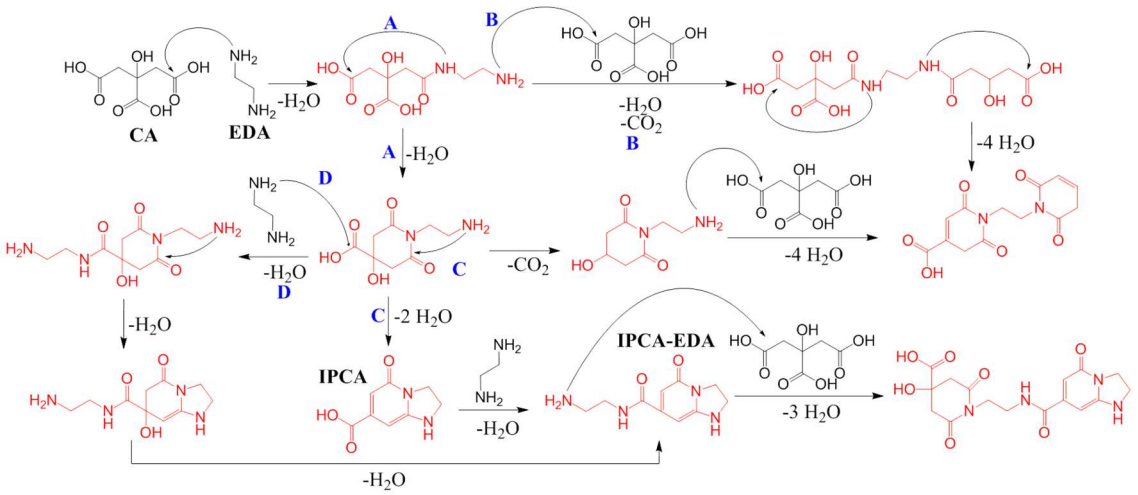

Scheme 1. Process of forming the molecules present in B-CNDs from citric acid (CA) and ethylene diamine (EDA). Molecules in red are those identified by UPLC-MS.

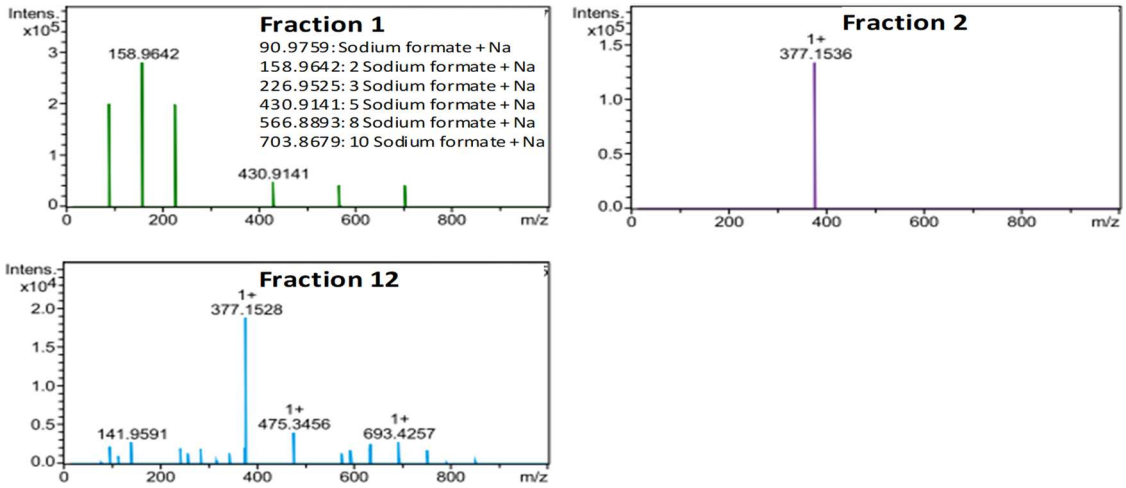

Figure 2. MS spectra of the fractions observed in B-CNDs coming from the blank.

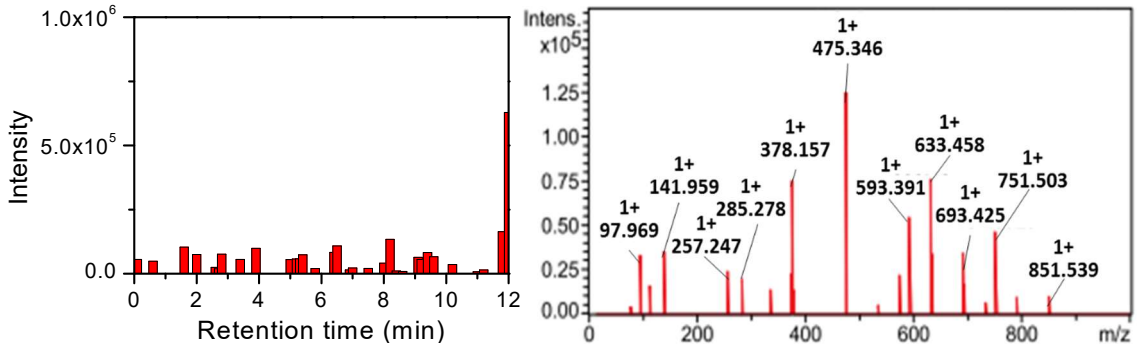

Figure 3. Gradient elution of the blank sample. The chromatograms are monitored with ESI-Q-TOF MS/MS detection and representative MS spectra.

AFM images of the B-CNDs deposited on a mica substrate reveal heights of also approximately 3 nm, suggesting that the B-CNDs have a near spherical shape and typically consist of 8-9 graphene layers (Fig. 4).

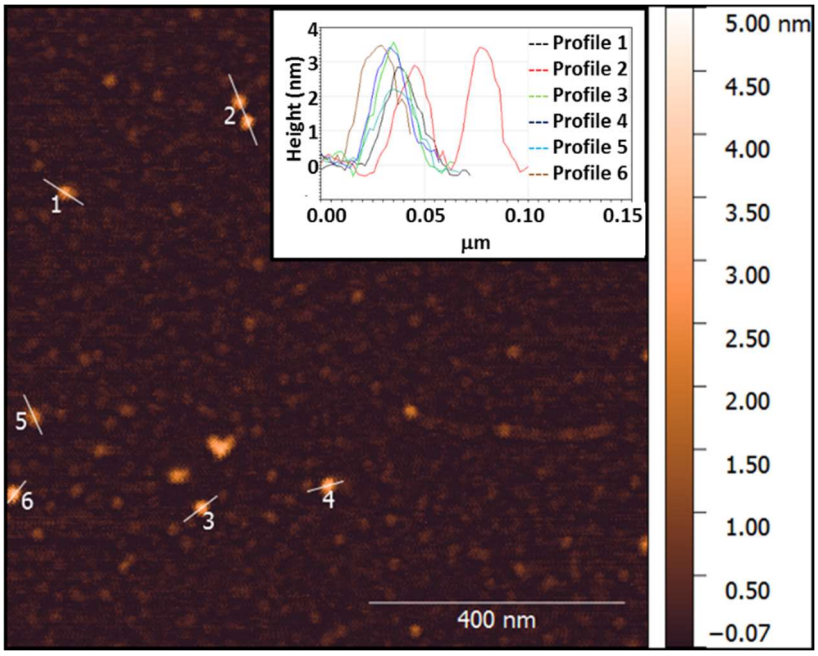

Figure 4. Representative AFM images and height profiles of B-CNDs.

HR-TEM images could only be obtained on single layer graphene TEM supports. Graphene offers a support that is more conductive and also much thinner than the average amorphous carbon supports, and although it is a crystalline support, its contribution to signal formation is relatively low (Figure 5). These images show that the collected B-CNDs are fairly monodisperse and have a uniform size of about 3 nm (Fig. 6). HR-TEM measurements of B-CNDs revealed lattice spacings of 0.12, 0.16, 0.21 and 0.32 nm, respectively, which is consistent with the (110), (004), (100) and (002) diffraction planes of sp^2 graphitic carbon and another lattice spacing of 0.26 nm, which cannot be assigned to graphitic carbon (Fig. 6).

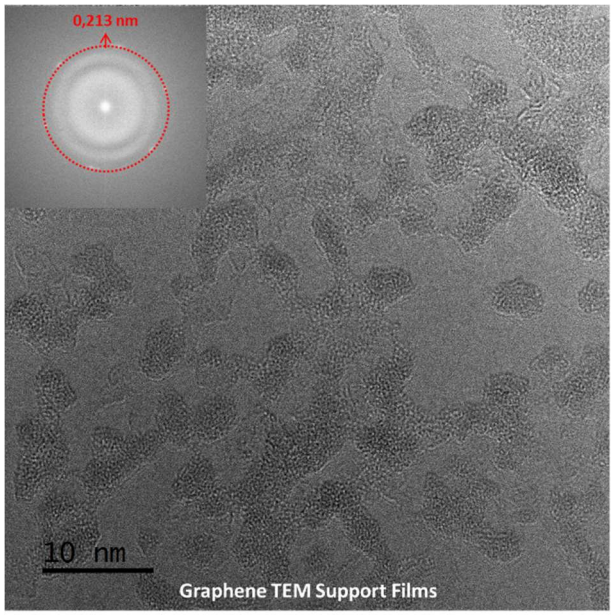

Figure 5. Representative HR-TEM images and fast Fourier transform (FFT) diffraction patterns of graphene TEM Support films.

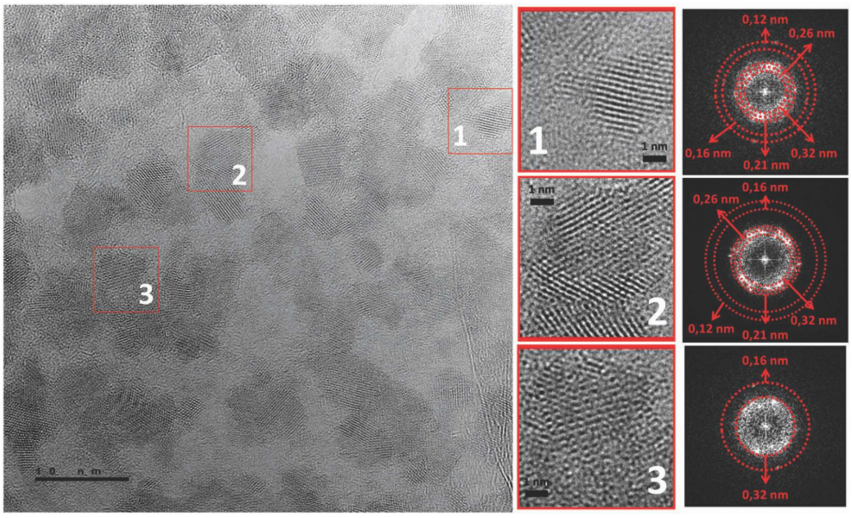

Figure 6. Representative HR-TEM images and fast Fourier transform (FFT) diffractions patterns of B-CNDs.

The HR-TEM images do not show the molecular products identified by mass spectrometry, but the 0.26 nm lattice spacings observed in these images that cannot be associated with graphitic structures could be due to aggregates of these molecular products. To solve this conflict, we resort to grazing incidence wide angle X-ray scattering (GI-WAXS). The GI-WAXS spectrum of the B-CNDs at room temperature shows many signals corresponding to lattice spacings of 0.36, 0.32, 0.30, 0.22, 0.21, 0.18, 0.17 nm, respectively, but upon heating to 200 ^{o}C in air most of the signals disappear or are noticeably reduced leaving only two dominant signals corresponding to 0.30 and 0.21 nm (Fig. 7). These results indicate that the majority of the signals observed in the GIWAXS spectrum of B-CNDs at room temperature correspond to molecular products that degrade at a high temperature, leaving only the signals corresponding to the graphitic structures (0.30 and 0.21 nm, associated with the (002) and (100) diffraction planes of the sp^2 graphitic carbon, respectively), which are stable up to at least 200 ^{o}C in air. The same experiments were performed also for the dialyzed material, resulting in a GIWAXS spectrum at 200 ^{o}C showing no remarkable signal. All other peaks observed at room temperature for the dialysate therefore likely arise from molecular aggregates which are destroyed at 200 ^{o}C (Fig. 7).

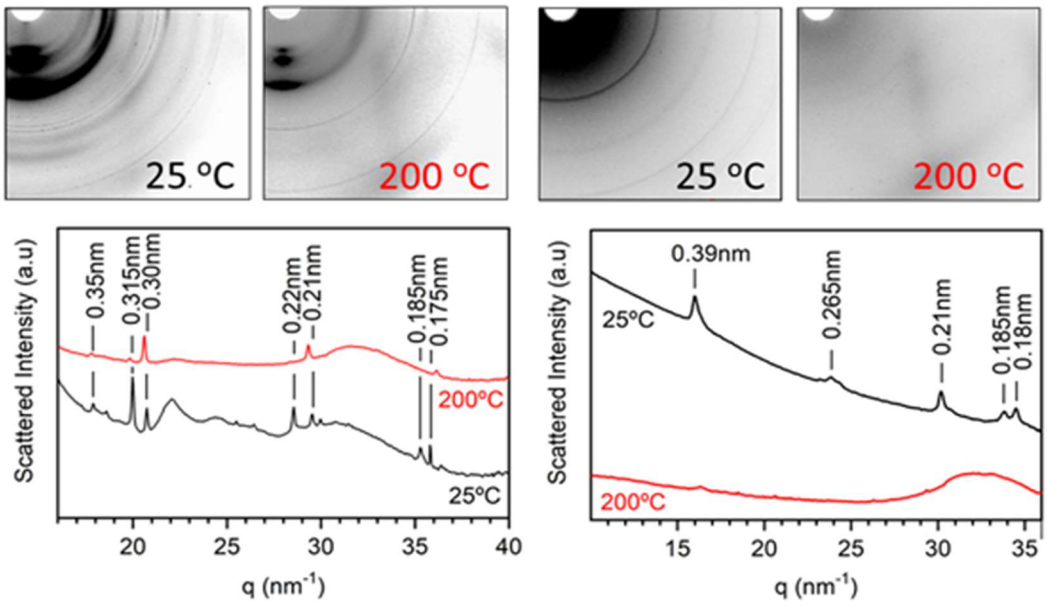

Figure 7. 2D GI-WAXS spectra and radially integrated scattered intensity obtained at 25 and 200 °C of B-CNDs (left) and dialyzed material (right). Numbers mark lattice spacings of the B-CNDs.

Whereas the AFM and HR-TEM measurements reveal monodisperse graphitic cores of about 3 nm in diameter on a dry surface, dynamic light scattering (DLS) measurements are able to produce the hydrodynamic size distribution in aqueous suspension. DLS in Milli-Q® water at a pH of 7.4 of the B-CNDs (Fig. 8) reveal two main populations, one of them with an average size of 42 ± 2 nm (which represents 10% in intensity, 54% in volume and 97% in number) and the other population with an average size of 133 ± 9 nm (which represents 90% in intensity, 46% in volume and 3% in number). This shows that in aqueous suspension the graphitic cores, despite some solubility thanks to the presence of functional groups or molecular products on their surface, tend to form large aggregates.

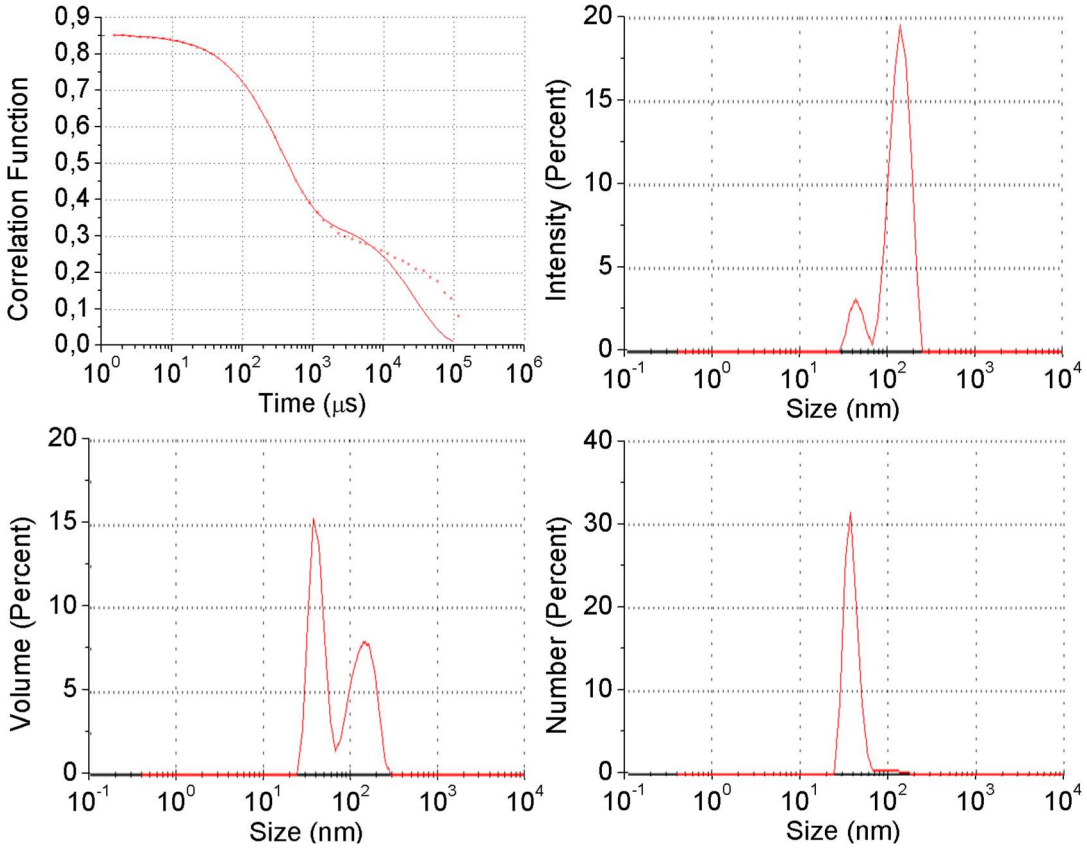

Figure 8. Correlogram and size distribution analysis by DLS by intensity, volume or number of B-CNDs in water at pH 7.4.

The results presented above were complemented by micro-SERS experiments which are able to reveal the chemical identity of the products (Fig. 9). These spectra are locally strongly enhanced in "hot spots" due to the electromagnetic fields of the nano-roughened gold surface. SERS spectra of the B-CNDs exhibit the well-known D and G bands (characteristics of graphitic structures) with a relatively weak, but non-negligible influence of the bands of functional groups of the molecular compounds. SERS spectra of the dialysate, on the other hand, show a series of much narrower Raman lines. A calculation of the Raman spectra of the major fraction of the molecular products, corresponding to the molecule IPCA, by density functional theory (marked in blue in Fig. 9) describes in fact the majority of the Raman lines of the dialysate. Comparing the calculated and experimentally observed intensities it must be kept in mind that SERS spectra often deviate intensity considerably from conventional Raman spectra.

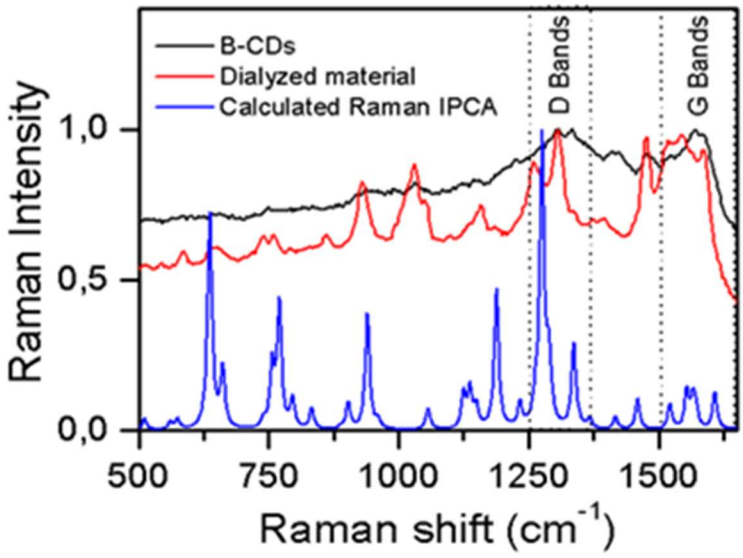

Figure 9. Surface-enhanced micro-Raman spectra (SERS) of B-CNDs and dialyzed material on nano-rough gold surface and calculated Raman spectrum of IPCA (λ_{exc} = 633 nm).

Fourier Transform Infrared Spectroscopy (FTIR) and X-ray Photoelectron Spectroscopy (XPS) enables the elucidation of the functional groups on the surface of B-CNDs. The FTIR spectra (Fig. 10) of the B-CNDs are found to differ from those of the dialysate mainly in a significantly higher intensity of the vibration bands corresponding to the alkoxy C-O stretch and vibrations of the methyl group. Those are therefore ascribed to surface functional groups of the graphitic cores, whereas the otherwise almost identical FTIR spectra of B-CNDs and the dialysate, respectively, prove that molecular fractions are bound to the B-CNDs, considering also that graphitic cores without functional groups cannot produce any signals in the IR spectrum.

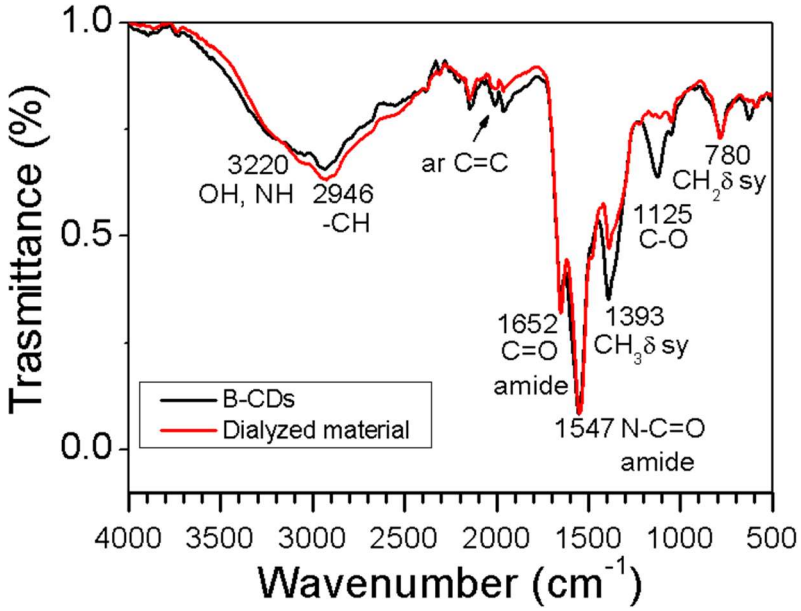

Figure 10. Attenuated total reflection Fourier-transform infrared (ATR-FTIR) spectra of dialyzed material and B-CNDs. Distinct vibration bands corresponding to B-CNDs surface groups are indicated.

XPS spectroscopy is employed to complement the results of FTIR spectroscopy. Comparing the XPS spectra obtained from the dialyzed material and the B-CNDs, respectively (Fig. 11), a decrease in signal intensity due to the presence of nitrogen and an increase in signal intensity due to the presence of oxygen is observed for B-CNDs, relative to the dialysate. This higher oxygen content again evidences the presence of functional groups such as OH or COOH on the surface of the graphitic cores. On the other hand, the enhanced presence of C=C bonds in the fitted spectra of the B-CNDs relative to the signals ascribed to C-H and C=O bonds, when compared to the dialysate, is in accordance with expectation for the graphitic cores.

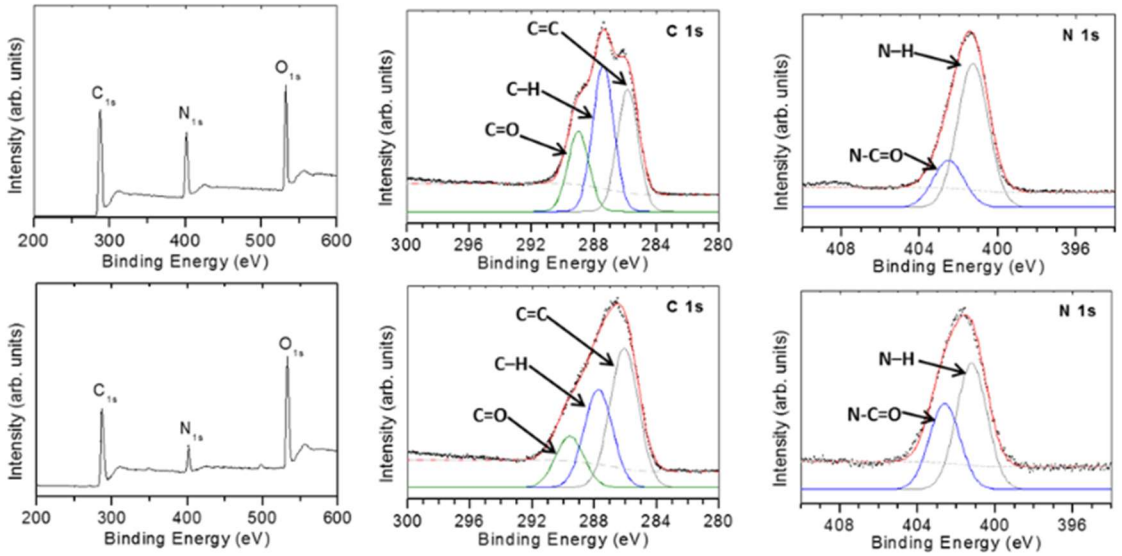

Figure 11. XPS spectra of dialyzed material (upper row of figures) and B-CNDs (lower row).

Photophysical characterization of the B-CNDs

The fluorescence quantum yields differ drastically for the dialysate (84%) and the B-CNDs (0.79%), a result relevant for the interpretation of the outcome of the fluorescence correlation experiments to be discussed below. It was observed, however, that the initially almost colorless aqueous solutions of the dialyzed material gradually changed under daylight, at room temperature and in the presence of atmospheric oxygen to maroon, then orange and finally becoming practically colorless again (Fig. 12a). More quantitatively, the evolution of dialyzed material under ambient illumination was monitored through emission-excitation maps and UV-Vis absorption. Figures 12b,c,d,e displays the normalized emission-excitation maps, on a logarithmic scale, of dialyzed material collected after 5 hours of dialysis in the dark, B-CNDs after 1 week of dialysis in the dark, dialyzed material after 14 days under ambient illumination and B-CNDs after 14 days under ambient illumination, respectively. The main features in the maps of Figures 12b and 12c, respectively, are very similar, which suggests that the same fluorophores are responsible for the emission of the retentate (B-CNDs) and the dialysate. As shown previously[23] and confirmed above the large

majority of those fluorophores corresponds to IPCA. Small differences in the shapes of the main feature in Figures 12b and 12c can be ascribed to the modification of the spectra of the fluorophores due to their binding to the graphitic cores. In both, the dialysate and the retentate the formation of a satellite is observed after illumination (Figures 12d and 12e, respectively). In the case of the dialysate the satellite is centered at 538 /450 nm in emission/excitation, respectively. At the same time the intensity of the main emission centered at 440 nm is decreasing. In the case of the retentate a shoulder appears centered at 496/418 nm in emission/excitation, respectively. Both satellites are weakly present already in the maps of Figures 12b and 12c, but, in particular in the case of the retentate, their shape is similar to the one observed after 14 days of illumination, such that their appearance must be ascribed to the dose of light received, in particular in the ultraviolet region of the spectrum, during acquisition of the maps. The obvious conclusion is that there are photoreactions in both the dialysate and the retentate, but they result in photoproducts with red-shifted, but somewhat different excitation and emission spectra. Emission spectra dependent on the excitation wavelength were extracted from the maps (see Figure 13). In both cases the emission spectra depend on the excitation wavelength as already evident from the maps, but in the case of the dialysate the emission is bimodal, whereas for the B-CNDs the spectra shift more gradually, most likely due to the inhomogeneity of the surroundings of the fluorophores bound to the graphitic cores. Interestingly, there is also a dark reaction as evidenced by differential emission/excitation maps of material kept in the dark (Fig. 14). This dark reaction appears to be different for the dialysate and the retentate.

Fig. 12f shows the ultraviolet-visible (UV-Vis) absorption spectra of dialyzed material with and without exposure to ambient light and B-CNDs dialyzed with and without ambient light. Aqueous suspensions of B-CNDs dialyzed without light show an absorption spectrum virtually identical to the starting dialysate material, which demonstrates that the absorption of the B-CNDs is completely dominated by the small molecules produced in the synthesis. B-CNDs dialyzed under ambient light, on the other hand, show an absorption spectrum more similar to that of the dialysate material after exposure to light. This implies again that it is the photoproducts which cause the difference in the properties of the retentate and dialysate when the dialysis is carried out under ambient illumination. The monotonic development of the UV-VIS spectra of the dialysate under ambient illumination is demonstrated in Figure 15. The absorption maximum at 240 nm of the pristine material was found to decrease progressively until it becomes a shoulder, the minimum of absorption found at 290 nm and the absorption tail that extends to the red region of the visible spectrum suffer a hyperchromic effect, and finally the maximum absorption found at 350 nm suffer a slight bathochromic shift that positions the maximum absorption at 340 nm.

The fluorescence of the material outside of the dialysis bag (dialysate), containing the molecular by-products, and extracted after 5h of dialysis in the dark, exhibits a biexponential PL decay with time constants of 15.6 ns (intensity-weighted amplitude 98%) and 3.6 ns (amplitude 2%), which possibly corresponds to two different molecular fluorophores, such as IPCA and IPCA-EDA. (Fig. 12g, black line). The fluorescence decay of the same dialysate after exposure to ambient light for 14 days can be fitted to a tetraexponential function with time constants of 15.4, 3.7, 0.6 and 0.27 ns with intensity-weighted amplitudes of 38%, 46%, 19% and 7%, respectively (Fig. 12g, red line). The fluorescence of B-CNDs dialyzed in the dark, on the other hand, exhibit decays that are fitted with a tetraexponential function with time constants of 12.0, 4.7, 1.5 and 0.29 ns with intensity-weighted amplitudes of 27%, 41%, 26% and 6%, respectively (Fig. 12g, green line), whereas the fluorescence decays of B-CNDs dialyzed under ambient light are fitted to a tetraexponential function with time constants of 13.3, 4.0, 0.7 and 31 ns with intensity-weighted amplitudes of 48%, 36%, 9% and 7%, respectively (Fig. 12g, blue line). Because the fluorescence decays of B-CNDs dialyzed in the dark and of the dialysate not exposed to ambient light on the one hand and of B-CNDs dialyzed in ambient light and of the dialysate exposed to light on the other hand are quite similar to each other, we can conclude that it is the creation of the photoproduct that causes most of the difference in the decay dynamics of B-CNDs and the dialysate.

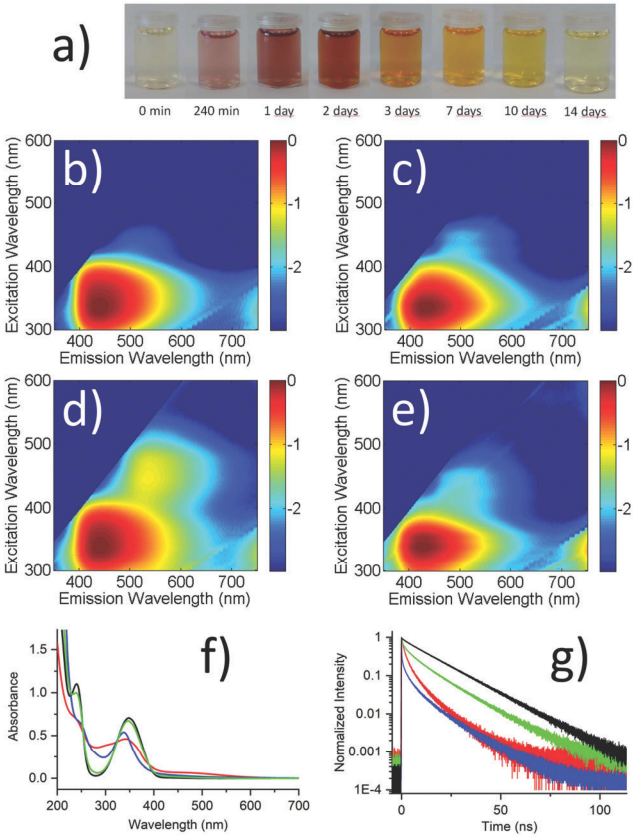

Figure 12. Photophysical characterization of dialyzed material and B-CNDs in H2O, (a) Evolution of the material dialyzed in the dark under ambient illumination. Normalized emission-excitation maps, on a logarithmic intensity scale, of (b) dialyzed material collected after 5 hours of dialysis in the dark, (c) B-CNDs immediately after dialysis during one week in the dark, (d) dialyzed material after additional 14 days under ambient illumination and (e) B-CNDs after additional 14 days under ambient illumination, respectively, (f) UV-Vis absorption spectra of dialyzed material after dialysis in the dark (black) and after dialysis under ambient light (red) and B-CNDs dialyzed in the dark (green) and dialyzed under ambient light (blue), and (g) Fluorescence decays (λ_{exc} = 405 nm, λ_{det} = 615 nm) of the material outside of the dialysis bag (dialysate), dialyzed without (black) and with (red) exposure to ambient light and B-CNDs dialyzed in the dark (green) and exposed to ambient light (blue).

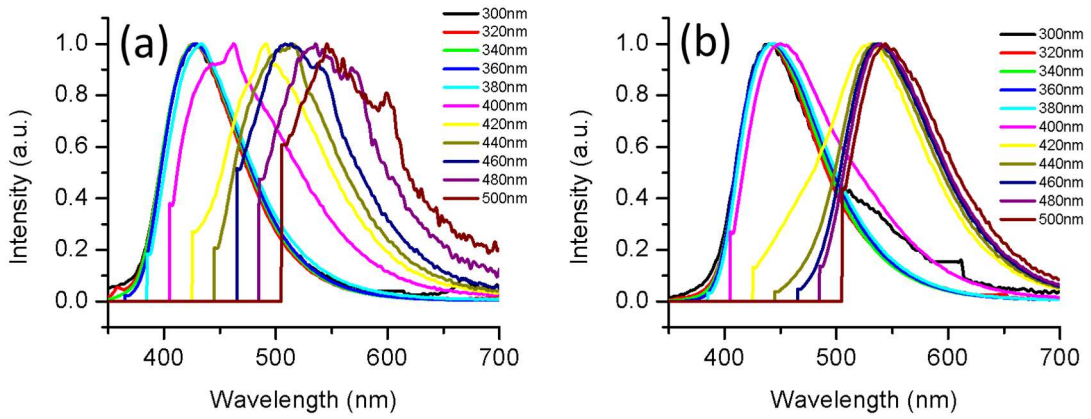

Figure 13. PL spectra of the B-CNDs (a) and the dialysate after 14 days under ambient illumination. Small peaks in the spectra correspond to Raman signals of the water.

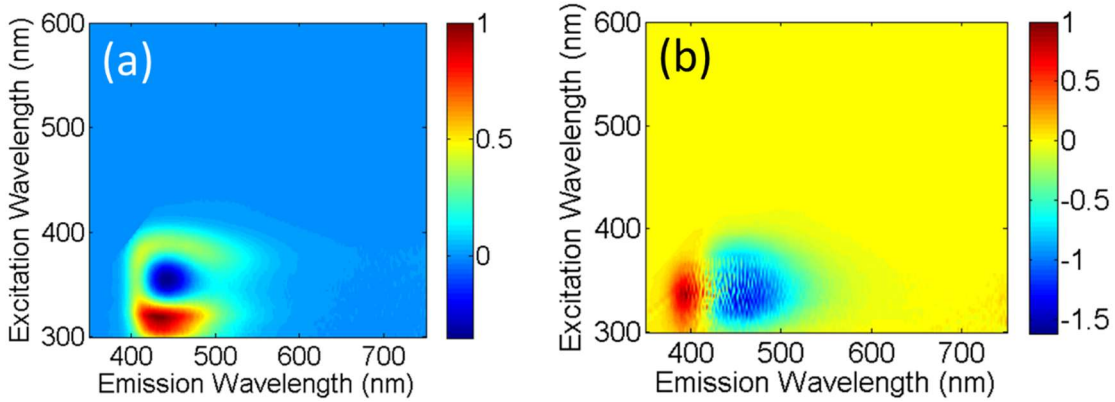

Figure 14. Differential excitation-emission map of the dialysate Figure a) and the retentate (B-CNDs, Figure b) after 14 days in the dark and immediately after collection / dialysis in the dark, respectively.

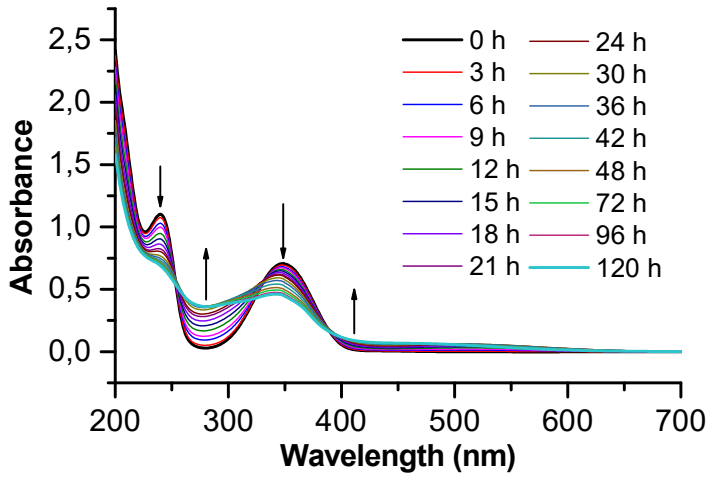

Figure 15. Evolution of the UV-Vis absorption of the dialyzed material when exposed to ambient light for 120 hours.

Fluorescence correlation spectroscopy (FCS) of the B-CNDs was also performed and indicates that the emission properties of B-CNDs are strongly dominated neither by the graphitic cores nor by molecular species linked to them, but rather by free molecules released by them. Fig. 16 shows the normalized FCS curves of the standards used (Atto-488 and Alexa-405), B-CNDs and the dialysate material. A fit of the correlations of B-CNDs reveals a hydrodynamic radius of (0.98 + 0.08) nm and (0.48 + 0.04) nm for excitation wavelengths of 405 and 488 nm, respectively, and the dialysate material shows a hydrodynamic radius of (1.1 + 0.1) nm, and (0.45 + 0.02) nm for excitation wavelengths of 405 and 488 nm, respectively. This difference in the hydrodynamic radius observed for excitation wavelengths of 405 and 488 nm can be justified by the presence of different molecular fluorophores such as IPCA and IPCA-EDA, or the photoproducts studied, but in any case, the unexpectedly small hydrodynamic radius shows that the emission of the retentate when excited in the 405-480 nm range is dominated by free molecular entities and not by the graphitic cores. This is in agreement with the low QY observed for the retentate. It may be of interest to note that no phosphorescence was observed in the case of the B-CNDs even after cooling to 1.5 K indicating a very low intersystem crossing yield and/or low phosphorescence quantum yield.

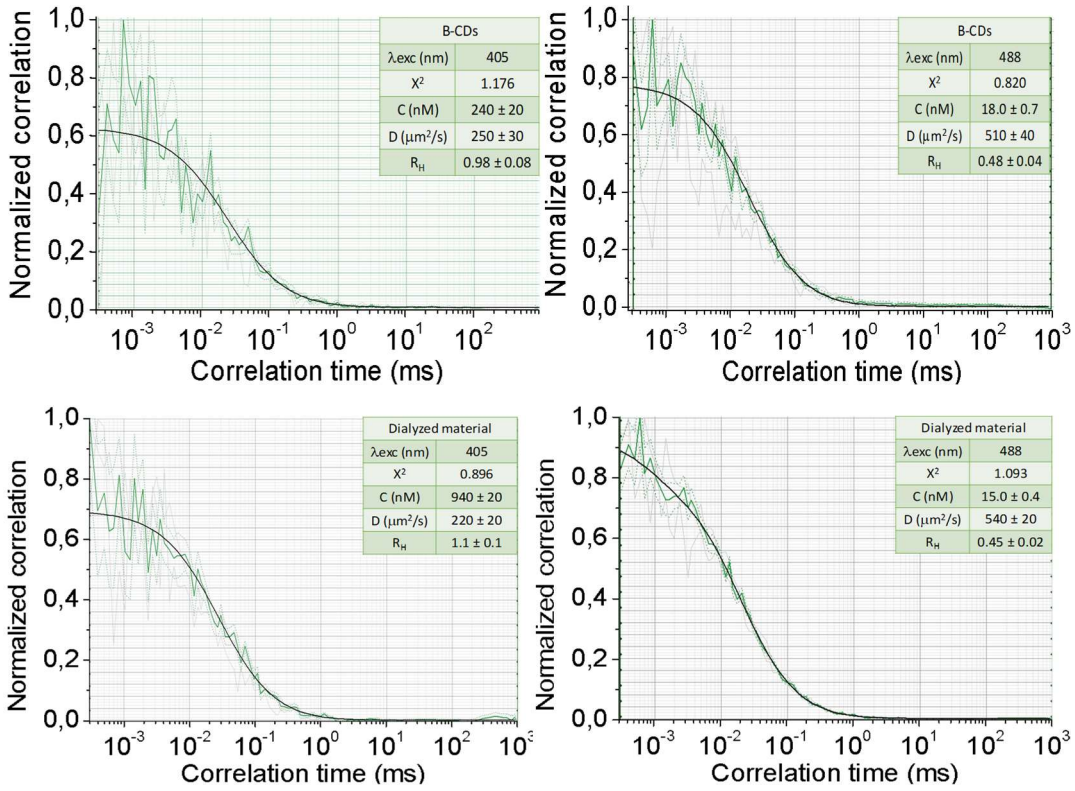

Figure 16. Normalized FCS curves for the standards used (up), B-CNDs (middle) and the dialysate material (down), under 405 and 488 nm excitation (left and right, respectively).

The capacity of B-CNDs and dialyzed material, respectively, to photosensitize $^1O_2$ was assessed in D_2O by time-resolved detection of the near-infrared $^1O_2$ phosphorescence at 1275 nm. The luminescence observed is assigned to $^1O_2$ because

the transient is completely quenched in presence of sodium azide (NaN_3, a well-known $^1O_2$ quencher; 25 mM). As shown in Fig. 17, B-CNDs indeed generate $^1O_2$ with quantum yield ΦΔ = 0.42, but the dialyzed material does not have this capacity. It is noteworthy that the lifetime of the singlet oxygen in D_2O should be 64 µs, as observed for flavin mononucleotide (reference photosensitizer), but in the presence of the CNDs this time is shortened to 10 µs, which implies that the B-CNDs also quench $^1O_2$.

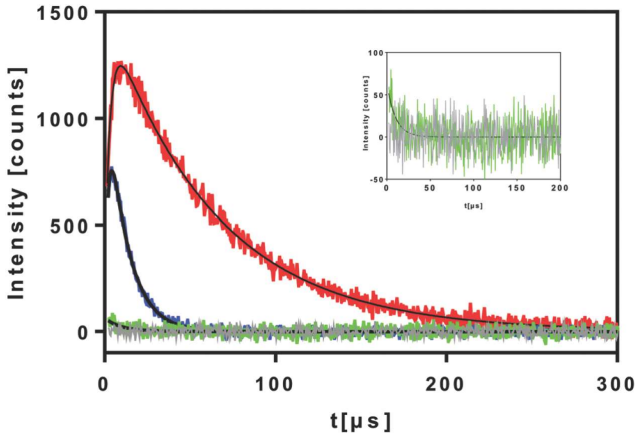

Figure 17. Singlet oxygen phosphorescence kinetics at 1275 nm in D_2O solutions of B-CNDs (blue), dialyzed material (green), reference photosensitizers (red) and B-CNDs in presence of NaN_3 (grey) (λ_{exc} = 473 nm).

In order to evaluate if the quenching of singlet oxygen is related to the molecular products, an experiment was made using phenalene-1-one as singlet oxygen photosensitizer and 1,3-diphenylisobenzofuran as singlet oxygen trap whose bleaching can be monitored by its absorbance at 410 nm and a UV light emitting diode was used as the light source (λ_C = 365 nm) (Fig. 18). The illumination intensity at the sample was set to the same value in these experiments (12.9 W/cm^2).

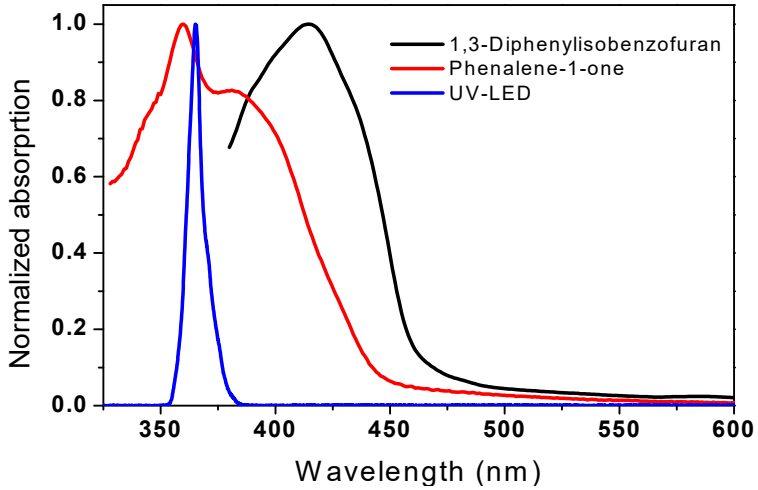

Figure 18. UV-Vis absorption spectra of phenalene-1-one as singlet oxygen photosensitizer, 1,3-diphenylisobenzofuran as singlet oxygen trap and the emission of a UV LED (l_c = 365 nm) used for illumination.

As can be seen in Fig. 19, the absorption of 1,3-diphenylisobenzofuran decreases in the presence of phenalene-1-one under visible light with a constant of 0.014 min^{-1} and when a small amount of the dialyzed material solution is added (the concentration of dialyzed material was adjusted to an absorbance value 10 times lower than that of phenolene-1-one at λ_{exc} = 365 nm) the absorption of 1,3-diphenylisobenzofuran decreases with a time constant of 0.002 min^{-1}, 7 times smaller than in the absence of the dialysate. This result shows that the dialysate indeed acts as a singlet oxygen deactivator, which limits the lifetime of singlet oxygen generated by B-CNDs. This result, of course, should also apply to the same molecular products attached to the surface of the B-CNDs.

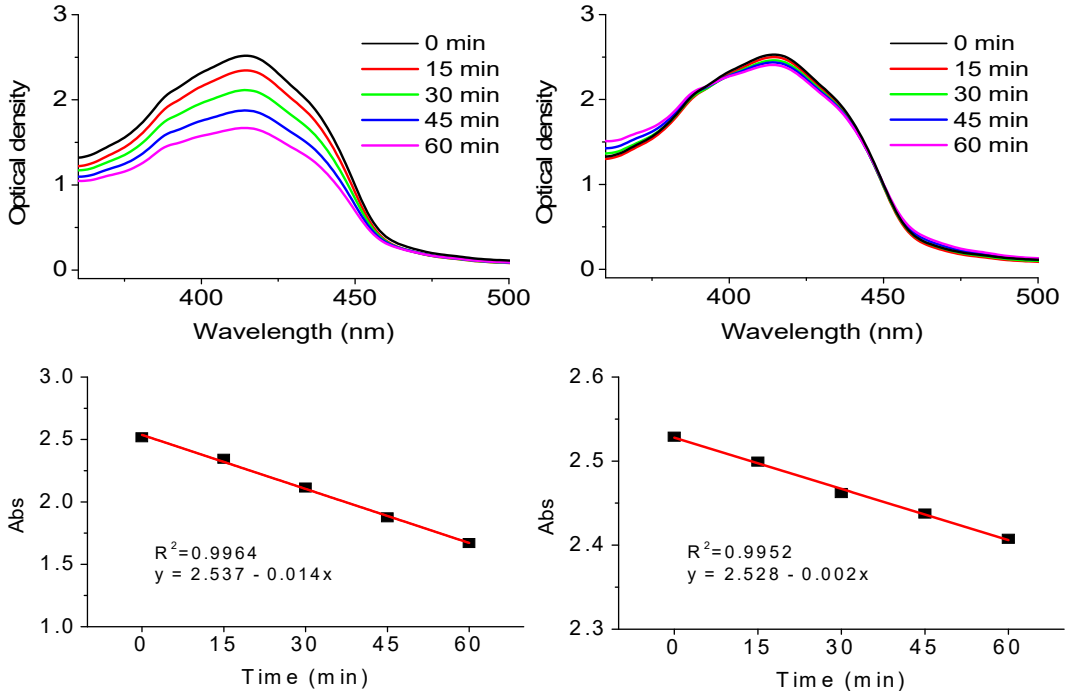

Figure 19. Photodegradation of 1,3-Diphenylisobenzofuran in the presence of phenalene-1-one only (left) or in the presence of phenalene-1-one and dialyzed material (right) under UV-LED.

Synthetic procedures of R-CNDs

In order to compare some of the findings discussed above with results obtained on a different kind of CNDs we have prepared red-emitting CNDs.[33-35] 2.8 mmol of p-phenylenediamine (p-PDA) was first dissolved in 30 mL absolute ethanol and then the solution was transferred to a Teflon liner and the latter to a stainless-steel autoclave. After heating at 180 °C in an oven for 12 h and allowing to cool down to room temperature, a dark-red suspension was obtained. The crude products were subjected to dialysis with a membrane MWCO of 14 kDa against an aqueous ethanol solution (15 % v/v) for one week. After dialysis, approximately 12 mg R-CNDs were obtained, representing a 4 % yield by mass.

Morphological and structural characterization of the R-CNDs

By using UPLC separation, the R-CNDs were well separated into approximately 40 fractions in less than 12 min. For its part, the dialyzed material revealed a very similar and complex mixture with more than 50 kinds of chemical species, but the most relevant molecules are the same as the one observed in the R-CNDs (Fig. 20). The high-accuracy MS analyses mass and mass/mass spectra of the most representative fractions of the R-CNDs sample are displayed in Fig. 20.

The first fraction (approx. 3 % of separated material) contains a compound with a mass of 321.1818, which revealed a chemical species with formula $C_{18}H_{20}N_6$ resulting from the union of three molecules of p-phenylenediamine. To know which structural isomer is formed by the union of three p-phenylenediamine molecules and gives rise to the chemical species $C_{18}H_{20}N_6$ we use tandem mass spectrometry (Fig. 21); this allows us to identify some molecular fragments of a single molecule (Tri-pPDA). The following fraction (approx. 48% of separated material) reveals a compound with a mass of 369.1819 corresponding to a chemical formula $C_{22}H_{21}N_6$, in this case the molecule arises from the union of four molecules of p-phenylenediamine and two losses of HCN (Tetra-pPDA), which can result in more than 20 different structural isomers practically indistinguishable by mass spectrometry (two of which are shown in Fig. 20). The third fraction (approx. 12% of separated materials) reveals a compound with mass of 211.0976 corresponding to a chemical formula $C_{12}H_{11}N_4$, in this case the molecule arises from the union of two molecules of p-phenylenediamine and an additional dehydrogenation (Bi-pPDA-1). The fourth fraction (approx. 6% of separated materials) reveals a compound with mass of 419.1729 corresponding to a chemical formula $C_{24}H_{19}N_8$ that arises from the union of four molecules of p-phenylenediamine, but the tandem mass spectrometry does not allow us to distinguish between two possible structural isomers (Tetra-p-PDA). The tenth fraction (approx. 26% of separated material) reveals a compound with a mass of 213.1130 corresponding to a chemical formula $C_{12}H_{13}N_4$. In this case the molecule arises from the union of two molecules of p-phenylenediamine (Bi-pPDA). All these molecules identified by UPLC-MS appear in the synthetic scheme 2. It should be noted that the fractions separated by UPLC for both the dialysate material and the R-CNDs that elute between 7 and 8 min and at 10 min, at least in part derive from the eluent and can also be seen in the blank. (Fig. 22).

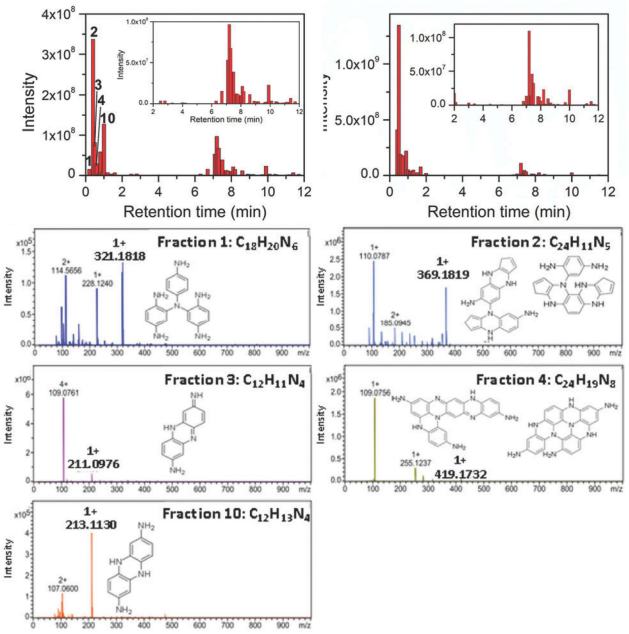

Figure 20. Gradient elution of R-CNDs (left) and dialyzed material (right). The chromatograms are monitored with ESI-Q-TOF MS/MS and the mass spectra of the main molecules observed in the R-CNDs are observed, which are the same as those identified in the dialysate.

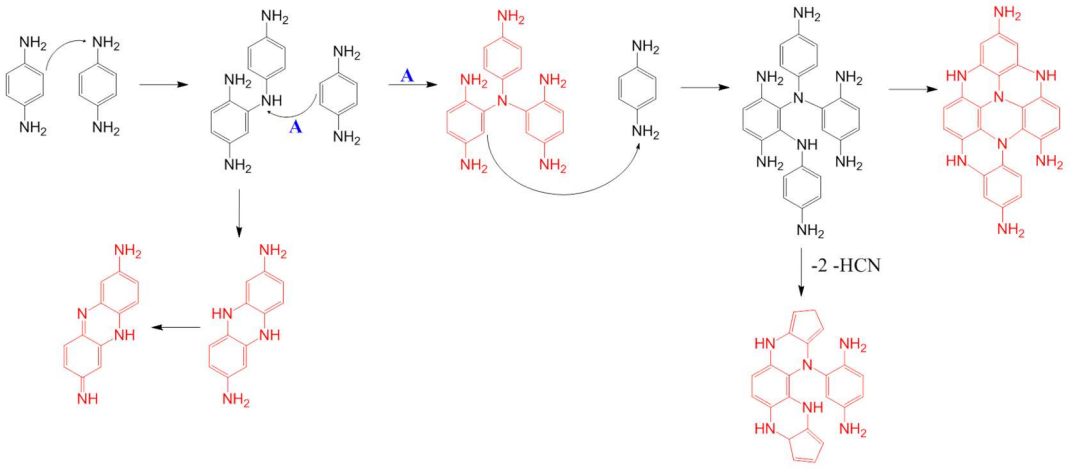

Scheme 2. Process of forming the molecules present in R-CNDs from p-Phenylenediamine. Molecules in red are those identified by UPLC-MS.

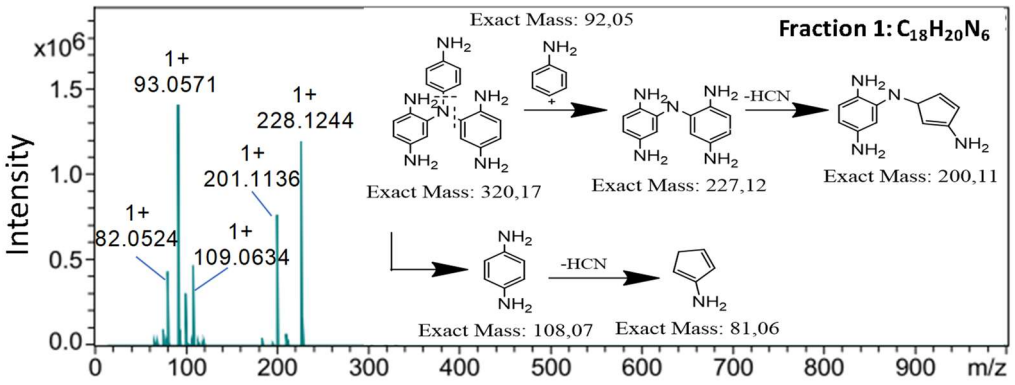

Figure 21. MS/MS spectrum of fraction 1 of R-CNDs to elucidate the structural isomer present.

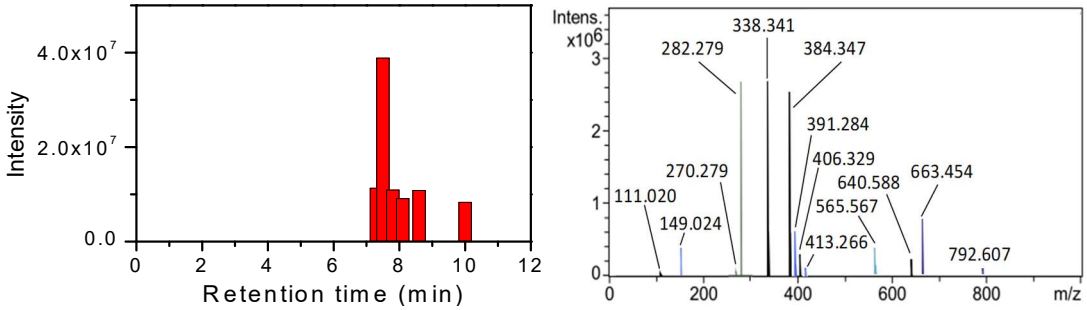

Figure 22. Gradient elution of the blank sample. The chromatograms are monitored with ESI-Q-TOF MS/MS detection and representative MS spectra.

STEM images could only be obtained on TEM graphene support films, these images show that the R-CNDs contain two types of particles: particles of an average size of 15.5 nm that are polycrystalline or amorphous and particles of an average size of 2.9 nm crystalline with lattice spacings of 0.22 nm which coincides with the diffraction plane (100) of graphitic carbon sp^2 (Fig. 23). Although on the surface we could see monodisperse graphitic cores of about 3 nm in size, we were also interested in knowing the hydrodynamic size. For this purpose, we carried out dynamic light scattering (DLS) measurements in Milli-Q® water at a pH of 7.4 of the R-CNDs. (Fig. 24). It can be observed that the R-CNDs show a very broad distribution of hydrodynamic diameters with a mean diameter of (260 ± 80) nm. This indicates that R-CNDs have a strong tendency to form aggregates of various sizes.

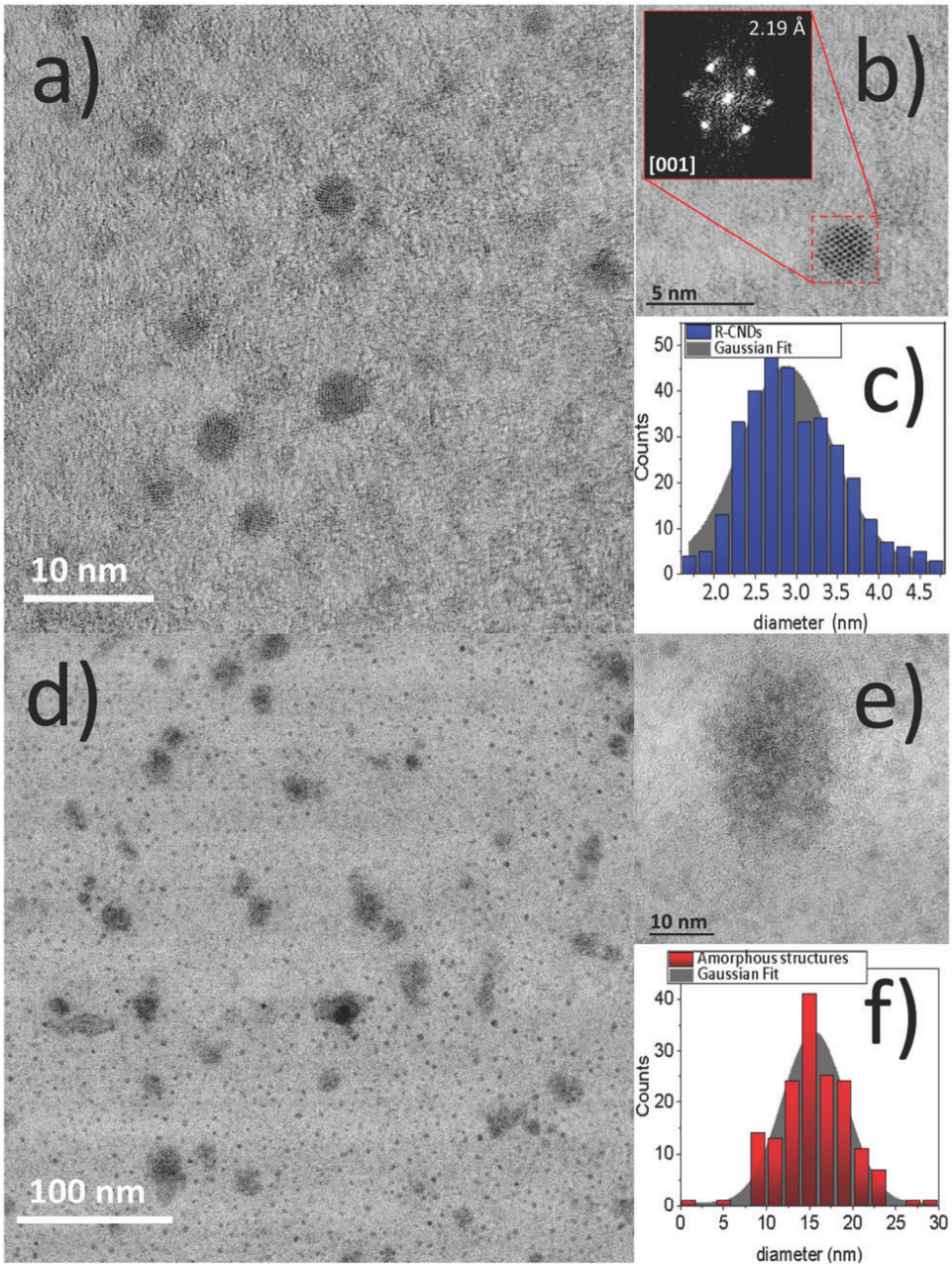

Figure 23. Representative STEM images of R-CNDs. The images are characterized by small crystalline particles of average size 2.9 nm and larger polycrystalline or amorphous particles of average size 15.5 nm. Images (a and d) are representative for both fractions, respectively. Images (b and e) show typical examples of the two kinds of particles and, in the case of the small crystalline particles, the fast Fourier transform of the image. The size distributions of the two fractions, as obtained from images covering a large area, are reproduced in figures (c and f).

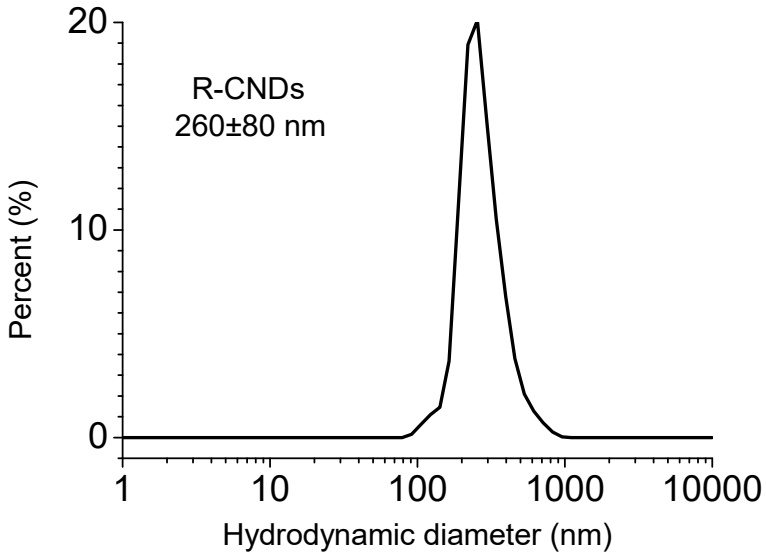

Figure 24. Correlogram and size distribution analysis by DLS of R-CNDs in water at pH 7.4.

Surface-enhanced micro-Raman spectroscopy of the R-CNDs indicates the coexistence of the molecules identified by mass spectrometry and the graphitic cores observed by HR-TEM. Raman spectra of the R-CNDs show D and G bands (characteristics of the graphitic structures). On the other hand, the Raman spectra of the dialyzed material show narrower Raman bands characteristic of molecular products. (Fig. 25).

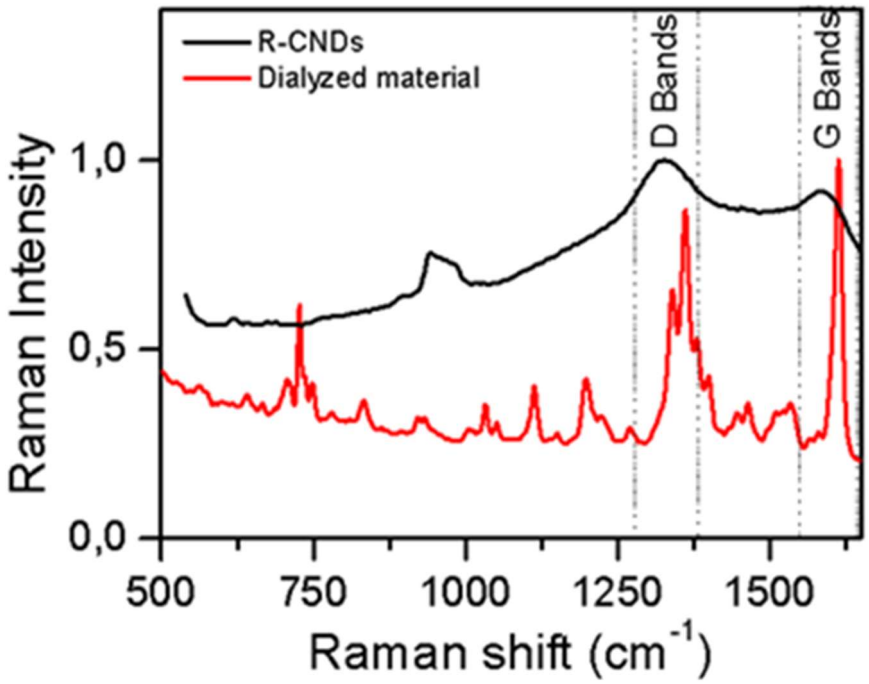

Figure 25. Surface-enhanced micro-Raman spectra (SERS) of R-CNDs, dialyzed material on nano-rough gold surface (λ_{exc} = 633 nm).

The functional groups on the surface of R-CNDs are identified by Fourier Transform Infrared Spectroscopy (FTIR). The corresponding spectra (Fig. 26) are very similar for the dialysate and the R-CNDs confirming that the FTIR spectrum of the R-

CNDs essentially reveals the molecular products attached to the surface of the R-CDNs. Three FTIR bands of the R-CNDs that are not observed in the dialysate occur at 649, 835 and 1505 cm^{-1}, respectively, and are marked in blue in Fig. 26, whereas a single band that is observed in the dialysate, but not in the R-CNDs, is marked in red. The former three bands should be ascribed to functional groups of the graphitic cores of the R-CNDs, in particular to aromatic azo groups (1505 cm^{-1}), vinyl ether groups (835 cm^{-1}) and saturated aliphatic nitro compounds (649 cm^{-1}).

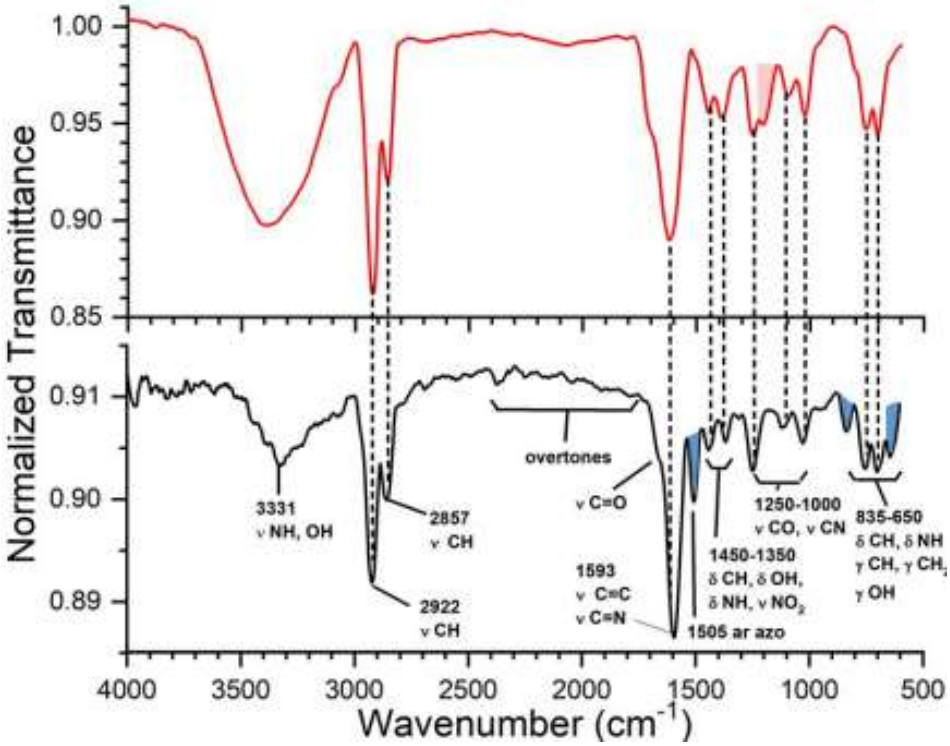

Figure 26. Normalized attenuated total reflection Fourier-transform infrared (ATR-FTIR) spectra of dialysate (red, top graph) and R-CNDs (black, bottom graph). Vibration bands corresponding to R-CNDs surface groups are indicated as blue-shaded areas. A single band occurring in the dialysate, but not in the R-CNDs, is marked in red.

Photophysical characterization of the R-CNDs

The ultraviolet-visible (UV-Vis) absorption spectra of R-CNDs, the dialyzed material and p-phenylenediamine are shown in Fig. 27C. A solution of p-phenylenediamine in EtOH is characterized by two intense absorption peaks around 243 and 309 nm. The dialyzed material approximately maintains one of the absorption maxima observed in the synthesis precursor, now at 248 nm, suggesting that it contains unreacted p-phenylenediamine. In addition, the UV-Vis absorption spectrum of the dialyzed material shows another absorption maximum at 278 nm and a wide absorption band ranging from 370 to 740 nm with a maximum at 489 nm. On the other hand, R-CNDs, similar to the dialyzed material, show a maximum absorption at 279 nm

and a wide absorption band ranging from 388 to 740 nm with a maximum absorption at 497 nm. That is, R-CNDs exhibit a UV-Vis absorption spectrum similar to that of the dialyzed material, without the absorption corresponding to the presence of unreacted p-phenylenediamine.

The emission-excitation map of dialyzed material (Fig. 27A) reveals an emission maximum centered at 394 nm for excitation wavelengths between 300 and 350 nm corresponding to the unreacted p-phenylenediamine, and two other emission maxima centered at 594 nm for excitation wavelengths between 335 and 375 nm as well as between 430 and 580 nm. The emission-excitation map of R-CNDs (Fig. 27B), on the other hand, reveals a weak emission centered at 394 nm, corresponding to the p-phenylenediamine remaining unreacted in the R-CNDs, but shows the other two emission maxima in a similar way as the dialyzed material. In this case the emission is almost 50 nm wider and is centered at 595 nm for excitation wavelengths between 360 and 395 nm and between 400 and 590 nm. Similar to the B-CNDs, this seems to indicate that the emission of the R-CNDs is related to fluorophores attached to the graphitic cores during dialysis and constantly released into the liquid thereafter. In contrast to the B-CNDs, however, we did not observe any photoproducts of those fluorophores. The PL QYs determined were 28% and 1.6% for the dialyzed material and R-CNDs, respectively.

The fluorescence of the dialyzed material exhibits a triexponential decay with time constants of 4.5, 2.3 and 0.31 ns with intensity-weighted amplitudes of 61%, 22% and 17%, respectively, which likely corresponds to different molecular fluorophores. For R-CNDs the fluorescence decays were fitted with a triexponential function with time constants of 7.0, 1.9 and 0.48 ns with amplitudes of 45%, 25% and 30 %, respectively. (Fig. 27D). As with the B-CNDs, the PL decay times observed for R-CNDs are similar to those of the dialyzed material but show a faster decay at short times, which should be attributed to quenching by the graphitic cores to which the molecules are attached in the case of the R-CNDs. It may be of interest in this context to note that a recent study,[36] of red-emitting CNDs produced from citric acid and urea also came to the conclusion, but based on a method of orthogonal solvents, that the absorption and emission of the reaction product were produced by small conjugated molecules, without identifying the latter, however, and without investigating the graphitic cores produced in the synthesis.

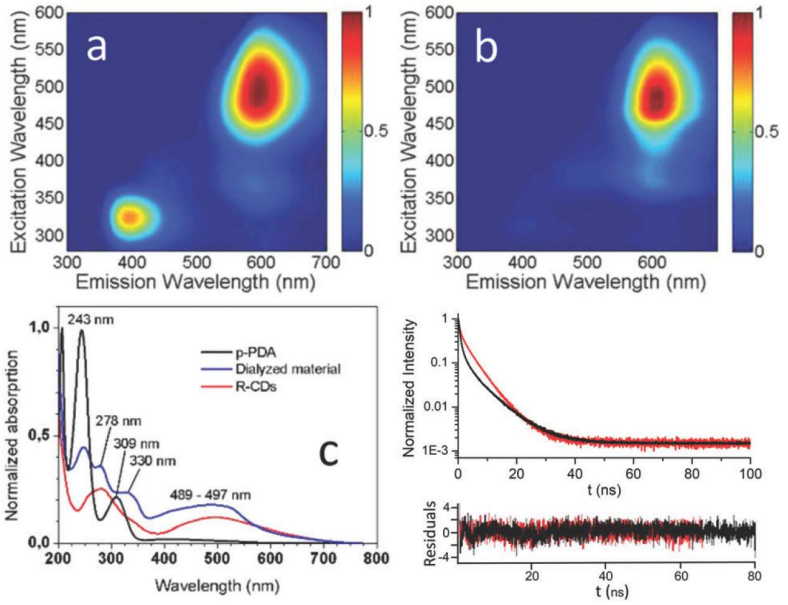

Figure 27. Photophysical characterization of dialyzed material and R-CNDs in EtOH, A), B) Normalized emission-excitation maps of dialyzed material and R-CNDs, respectively, on a linear intensity scale, C) UV-Vis absorption spectra of dialyzed material, R-CNDs and p-phenylenediamine (p-PDA) and D) Time resolved fluorescence (TRF) decays (λ_{exc} = 405 nm, λ_{det} = 615 nm) of R-CNDs (black) and dialysate (red), respectively.

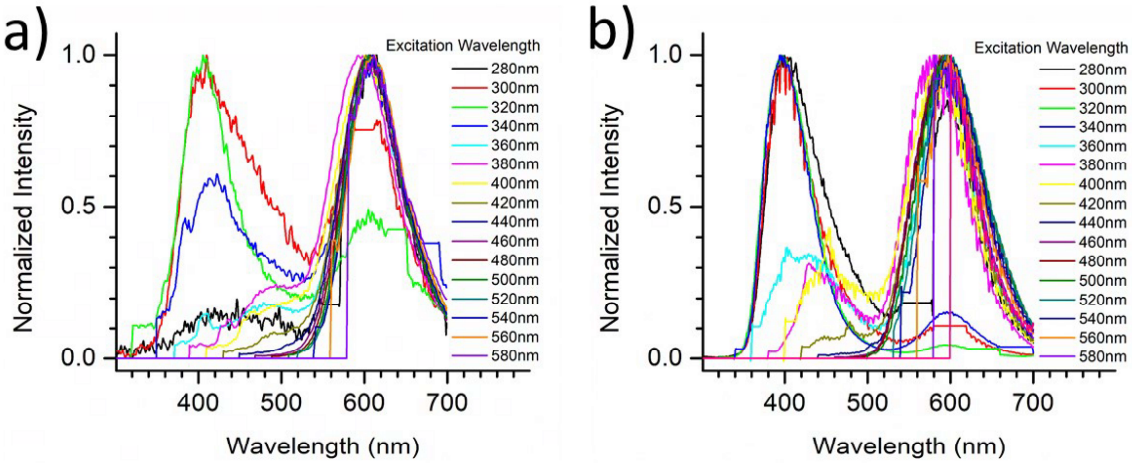

Figure 28. Selected normalized PL spectra, corresponding to the maps of Figure 27, of (a) R-CNDs and (b) the dialyzed material as a function of the excitation wavelength. Sharp peaks correspond to Raman signals from the water. Plateaus are caused by the aromatic protection electronics of the photomultiplier in order to avoid saturation due to the second order of the excitation.

4.1.4. Conclusions

Hydrothermal or, in general, solvothermal treatments have become the most common procedure for production of CNDs due to their environmental friendliness, simplicity and versatility, generating CNDs from the condensation of carbonaceous blocks and the crystallization of the graphitic cores induced by high temperature and/or pressure. We have collected rather convincing evidence, however, that the UV-VIS, PL and PL excitation spectra and PL decays of the products of solvothermal synthesis of the B-CNDs, as well as the R-CNDs studied here are dominated by small molecules, some of which we have identified through UPLC-ESI-Q-TOF-MS/MS, and, in the case of the B-CNDs, their photoproducts. Comparison and careful analysis of the optical and structural properties of the low molecular weight products that are dialyzed and of the CNDs proves that the molecular fluorophores observed in the dialysate still appear in the retentate, even after prolonged dialysis, suggesting that those compounds are attached to the graphitic cores and/or amorphous aggregates and constantly being released into the liquid surrounding. This may indeed confer varied and chemically controllable functionalities and photo-physical properties useful for applications to the CNDs. It demonstrates, however, that even extended dialysis cannot guarantee the absence of small conjugated fluorophores. No photophysical characteristics of sp^2 domains in the graphitic cores have been identified in the present work, contrary to previous assignments and contrary to the concept of "carbon quantum dots", which, in analogy to semiconductor quantum dots, suggests optical properties dominated by coherent size effects. In the case of our B-CNDs photoproducts, previously ignored, have been shown in the present study to dominate the photophysical properties of the retentate, when the dialysis is not carried out in the dark, and readily explain photophysical differences between dialysate and retentate, which were previously ascribed to the sp^2 domains of the graphitic cores. A recent study[37] on the formation of CNDs employing small angle x-ray scattering (SAXS) and optical spectroscopy suggests a core-shell structure of their CNDs with aromatic groups within the core of the CNDs. This model may also be applicable to the CNDs investigated here, explaining the escape of the aromatic molecules from the CNDs on an extended time scale, but implying that the aromatic molecules are not covalently bound to the cores.

At the moderate temperatures employed by us in the solvothermal synthesis graphitic cores, on the other hand, are produced in a very low yield, but are identified by HR-TEM, GI-WAXS and SERS. HR-TEM analysis reveals the presence of amorphous aggregates, presumably consisting of non-conjugated molecules, which we detected and partially identified via UPLC-ESI-Q-TOF-MS/MS, and non-conjugated polymers. In spite of the low yield of graphitic CNDs we have shown that the latter are almost exclusively responsible for the generation of singlet oxygen, which we partly ascribe to the low intersystem crossing yield of the fluorophores. The exact mechanism of

formation of singlet oxygen at the graphitic cores, however, remains to be explored. It may also be worth noting that the B-CNDs were previously confirmed to be able to anchor nucleic acids,[20] in contrast to the dialysate material, constituting another example where the graphitic cores confer unique functionalities, in spite of the overwhelming presence of small molecules in the product of solvothermal synthesis.

References

1. X. Cui, L. Zhu, J. Wu, Y. Hou, P. Wang, Z. Wang and M. Yang, *Biosens. Bioelectron.*, 2015, **63**, 506-512.

2. Y-C. Chen, C-Y. Nien, K. Albert, C-C. Wen, Y-Z. Hsieh and H-Y. Hsu, *RSC Adv.*, 2016, **6**, 44024-44028.

3. S. Zhu, Q. Meng, L. Wang, J. Zhang, Y. Song, H. Jin, K. Zhang, H. Sun, H. Wang and B. Yang, *Angew. Chem. Int. Ed.,* 2013, **52**, 3953-3957.

4. S. Do, W. Kwon and S-W. Rhee, *J. Mater. Chem. C.*, 2014, **2**, 4221-4226.

5. S. Pei, J. Zhang, M. Gao, D. Wu, Y. Yang and R. Liu, *J. Colloid Interface Sci.,* 2015, **439**, 129-133.

6. J. Bian, C. Huang, L. Wang, T. Hung, W-A. Daoud and R. Zhang, *ACS Appl. Mater. Interfaces,* 2014, **6**, 4883-4890.

7. Y. Song, S. Zhu, S. Xiang, X. Zhao, J. Zhang, H. Zhang, Y. Fu and B. Yang, *Nanoscale*, 2014, **6**, 4676-4682.

8. P-C. Hsu and H-T. Chang, *Chem. Commun.*, 2012, **48**, 3984-3986.

9. R. Jelinek, *Carbon Quantum Dots: Synthesis, Properties and Applications*, Springer International Publishing, Switzerland, 2017.

10. A. Gulzar, P. Yang, F. He, J. Xu, D. Yang, L. Xu, and M-O. Jan, *Chem. Biol. Interact.*, 2017, **262**, 69-89.

11. J. Shen, Y. Zhu, X. Yang and C. Li, *Chem. Commun.*, 2012, **48**, 3686-3699.

12. H. Li, Z. Kang, Y. Liu, and S-T. Lee, *J. Mater. Chem.* 2012, **22**, 24230-24253.

13. Z. Zhang, J. Zhang, N. Chen and L. Qu, *Energy Environ. Sci.,* 2012, **5**, 8869-8890.

14. S-N. Baker and G-A. Baker, *Angew. Chem. Int. Ed.*, 2010, **49**, 6726-6744.

15. M. Han, S. Zhu, S. Lu, Y. Song, T. Feng, S. Tao, J. Liu and B. Yang, *Nano Today*, 2018, **19**, 201-218.

16. R. Ma, Y. Zhou, P. Li, Y. Chen, J. Wang and Q. Liu, *Electrochim. Acta*, 2016, **216**, 347-354.

17. D-M. Wang, K-L. Lin and C-Z. Huang, *Luminescence*, 2019, **34**, 4-22.

18. J. Ge, M. Lan, B. Zhou, W. Liu, L. Guo, H. Wang, Q. Jia, G. Niu, X. Huang, H. Zhou, X. Meng, P. Wang, C-S. Lee, W. Zhang and X. Han, *Nat. Commun.*, 2014, **5**, 4596.

19. T. García-Mendiola, I. Bravo, J-M. López-Moreno, F. Pariente, R. Wannemacher, K. Weber, J. Popp and E. Lorenzo. *Sensors and Actuators B: Chemical*, 2018, **256**, 226-233.

20. T. García-Mendiola, C-G. Elosegui, I. Bravo, F. Pariente, A. Jacobo-Martín, C. Navio, I. Rodríguez, R. Wannemacher, K. Weber, J. Popp and E. Lorenzo, *Microchimica Acta*, 2019, **186**, DOI: 10.1007/s00604-019-3386-9.

21. A. Cayuela, M-L. Soriano, C. Carrillo-Carrión and M. Valcárcel, *Chem. Commun.*, 2016, **52**, 1311-1326.

22. J-B. Essner, J-A. Kist, L. Polo-Parada and G-A. Baker, *Chem. Mater.*, 2018, **30**, 1878-1887.

23. Y. Song, S. Zhu, S. Zhang, Y. Fu, L. Wang, X. Zhao and B. Yang, *J. Mater. Chem. C.*, 2015, **3**, 5976.

24. J. Schneider, C-J. Reckmeir, Y. Xiong, M. von Seckendorff, A-S. Susha, P. Kasák and A-L. Rogach, *J. Phys. Chem. C.*, 2017, **121**, 2014-2022.

25. L. Shi, J-H. Yang, H-B. Zeng, Y-M. Chen, S-C. Yang, C. Wu, H. Zeng, O. Yoshihito and Q. Zhang, *Nanoscale*, 2016, **8**, 14374-14378.

26. F. Ehart, S. Bhattacharyya, J. Schneider, A. Löf, R. Wyrwich, A-L. Rogach, J-K. Stolarczyk, A-S. Urban and J. Feldmann, *Nano Lett.*, 2017, **17**, 7710-7716.

27. A. Sharma, T. Gadly, S. Neogy, S-K. Ghosh and M. Kumbhakar, *J. Phys. Chem. Lett.*, 2017, **8**, 1044-1052.

28. S. Zhu, Y. Song, J. Shao, X. Zhao and B. Yang, *Ang. Chem. Int. Ed.*, 2015, **54**, 14626-14637.

29. B. Sun, B. Zhao, D. Wang, Y. Wang, Q. Tang, S. Zhu, B. Yang and H. Sun, *Nanoscale*, 2016, **8**, 9837-9841.

30. S. Tao, S. Zhu, T. Feng, C. Xia, Y. Song and B. Yang, *Mater. Today Chem.*, 2017, **6**, 13-25.

31. S. Tao, Y. Song, S. Zhu, J. Shao and B. Yang, *Polymer*, 2017, **116**, 472-478.

32. L. Vallan, E. P. Urriolabeitia, F. Ruipérez, J. M. Matxain, R. Canton-Vitoria, N. Tagmatarchis, A. M. Benito, W. K. Maser *J. Am. Chem. Soc.,* 2018, **140**, 12862-12869.

33. K. Jiang, S. Sun, L. Zhang, Y. Lu, A. Wu, C. Cai and H. Lin, *Angew. Chem. Int. Ed*., 2015, **54**, 5360-5363.

34. J. Yue, K. Zhang, H. Yu, L. Yu, T. Hou, X. Chen, H. Ge, T. Hayat, A. Alsaedi, S. Wang. *J. Mater. Sci.*, 2019, **54**, 6140-6150

35. C. Liu, D. Ning, C. Zhang, Z. Liu, R. Zhang, J. Zhao, T. Zhao, B. Liu, Z. Zhang, *ACS Appl. Mater. Interfaces* 2017, **9**, 18897−18903

36. W. Liang, P. Wang, M. J. Meziani, L. Ge, L. Yang, A. K. Patel, S. O. Morgan, Y. P. Sun, *Nanoscale Adv.*, 2021, **3**, 4186 – 4195.

37. F. Rigodanza, M. Burian, F. Arcudi, L. Dordević, H. Amenithsh,M. Prato, Nat.Commun., 2021, 12, 2640.

-

Chapter 2:

Carbon Nanoparticles by Pulsed Laser Synthesis

Chapter 2: Carbon Nanoparticles by Pulsed Laser Synthesis

4.2.1. Introduction

Carbon nanoparticles (CNPs) have recently attracted great interest due to their unique structure, high specific surface area and outstanding physicochemical, optoelectronic and biological properties,[1] including relatively low toxicity,[2] reasonable photochemical and thermal stability,[3] and most importantly, good dispersibility in different solvents and functionalization or immobilization capability for the preparation of high added-value nanomaterials (e.g., (bio)conjugates, nanocomposites or polymer-scaffolded supported nanostructures).[4] In addition, their special characteristics in terms of electronic and optical properties,[5] as well as some specific features such as their size- and excitation wavelength-dependent fluorescence,[6] make them carbon nanostructures suitable for a wide variety of applications in different fields such as bioimaging and nanomedicine,[7] sensors and probes,[8] energy conversion and storage,[9] light emitting devices,[10] microscopy,[11] water treatment,[12] carbon dioxide valorization,[13] (photo/electro)catalysis,[14] information encryption,[15] and as electromagnetic wave or electrochemical barriers.[16]

Among the different types of carbon nanoparticles that may de synthesized (e.g., graphene quantum dots (GQDs), carbon quantum dots (CQDs), carbon nanodots (CNDs) and carbonized polymer dots (CPDs), following one of the most recent classification schemes),[17] two main preparation strategies may be used for their synthesis, the so-called top-down and bottom-up approaches. In general, many of the top-down or bottom-up methods have several drawbacks, including the low yield of the target product, soot formation, and production of CNPs with heterogeneous composition and morphology. Therefore, the search for efficient methods to synthesize and isolate highly homogeneous nanoparticles is of great importance.

In the top-down methods, CNPs are fabricated by oxidation cutting of macroscopic carbon substrates such as carbon rods, polymers or raw natural materials, carbon black, candle soot; graphite, graphene and their oxides, and even carbon nanostructures such as carbon nanotubes. The top-down synthetic approach involves the widely used pyrolysis and chemical oxidation of carbon precursors (under acidic conditions), and the electrochemical, hydrothermal and solvothermal oxidation methods working under strong electric fields, pressures and temperatures, as well as the intercalation of metals within graphite. Alternatively, other top-down physical procedures such as arc discharge between high purity graphite electrodes, laser ablation of macroscopic carbon precursor targets, and nanolithography via reactive ion etching have also been used.[1c,1e-i,5c]

Although the size of the particles does not strictly depend on the synthetic approach (top-down or bottom-up), size control of the resulting CNPs in the top-down methods is particularly difficult since the fragmentation of the carbon precursor tends to occur in a nonuniform way. Therefore, thermal synthesis of carbon nanoparticles

inside the pores of inorganic matrices, that serve as a template to control the size of the nanomaterial obtained, has also been explored with porous silica and zeolites as the nanoreactors. However, bottom-up methods are commonly believed to be more convenient for the synthesis of particles with homogeneous morphology.

Concerning the bottom-up approach to prepare CNPs starting from a wide variety of organic molecular precursors, pyrolysis in inert atmospheres, thermal or chemical oxidation, hydrothermal and microwave heating have been the most studied methods; whereas electrochemical processes or the irradiation of molecular precursors in solution with laser beams have been barely explored.[1c,1e-h,5c18] Additionally, those methods aiming to the preparation of larger carbon nanostructures (nanoparticles and nanoobjects) via organic synthesis of molecular nanographene building blocks, by their thermolysis or by disruptive on-site methods, are of particular interest, provided they are cost-effective, due to the homogeneity of the nanometric-sized building blocks, and the uniform chemical composition and morphology of the achieved carbon nanomaterials.[19]

Regarding the laser irradiation methods to synthesize CNPs, following both approaches, top-down and bottom-up; pulsed laser ablation has been the most successful top-down process, making use of focused laser beams targeting macroscopic amorphous/graphitic carbon substrates or, alternatively, carbon powder suspensions and even nanomaterials such as carbon nanotubes.[1f,5b,c,20] UV/vis/NIR laser beams with pulse durations in the fs–ns range have been employed, and the role played by irradiation parameters and experimental conditions as well as the mechanism of nanoparticle formation under pulsed laser ablation methods have been described in detail.[21] Conversely, bottom-up approaches using laser light and small organic molecules as building blocks for the preparation of larger carbon nanostructures have been considerably less explored. These methods can be classified according to the different experimental conditions used: i) laser excitation at specific wavelengths (usually UV) absorbed by the organic substrates, or ii) laser irradiation at wavelengths not absorbed by the reaction medium (i.e., organic compounds which are transparent to vis-NIR incident light). Furthermore, focused or nonfocused laser beams may be used in the latter category, resulting in different configurations of the experimental setup and reaction medium.

In relation to those experiments where the laser light photons have a suitable wavelength to be absorbed by the organic substrates, the corresponding photochemical processes are triggered (i.e., C–X bond fission) resulting in the formation of radical species that collide and, subsequently, self-assemble producing carbon nanoparticles (e.g., photodissociation and photochemical stitching).[22]

Concerning those experimental setups making use of a focusing system for concentrating the laser energy in a tiny microvolume inside the bulk solution, the extremely high power achieved, regardless of the wavelength used, produces a plasma

state causing the fragmentation of the molecular substrates in separated organic radicals, ions and electrons, whose recombination leads to the formation of carbon nanostructures. Inert inorganic substrates or microparticles can be added to the reaction medium, serving as catalysts for the production of CNPs under focused irradiation.[21b,23] On the other hand, experiments carried out focusing the laser beam in different positions of biphasic liquid systems have also been reported.[24]

Finally, experiments carried out with nonfocused laser beams and at wavelengths where the organic substrates do not absorb the incident radiation are, by far, much less common, and only one literature reference reports on this specific method for the preparation of carbon nanoparticles.[25]

We report herein several examples of the until now little explored synthesis, purification, structural and photophysical characterization, as well as kinetic studies regarding the formation of carbon nanodots by nonfocused pulsed laser synthesis, devising some of their potential applications. The role played by the surface of the reaction container, medium viscosity, light wavelength and power, and the influence of the starting organic substrates are discussed as well.

4.2.2. Experimental Section

Synthesis and purifications of CNPs

The organic precursors used in the pulsed laser synthesis experiments are benzene (HPLC grade, ≥ 99.8 %, Fisher Chemical), toluene (HPLC grade, ≥ 99.8 %, Fisher Chemical), aniline (99 %, PanReac), chlorobenzene (99+ %, Acros) and naphthalene (99 %, Sigma-Aldrich). aniline was distilled over KOH.[26] The solvents used to purify and characterize the carbon nanoparticles were distilled and deionized water, diethyl ether (99.7 %, Panreac) and HPLC-grade methanol, 2-propanol (≥ 99.5 %, Carlo Erba), acetone and dichloromethane (HPLC grade, ≥ 99.8 %, Fisher Chemical), chloroform (for spectroscopy, ≥ 99.0 %, Merck) and dimethyl sulfoxide (≥ 99.7 %, HPLC, Sigma-Aldrich).

A Nd-YAG (Continuum Surelite, 10 Hz, 6 ns pulse width and 6 mm beam diameter) providing laser radiation either of 1064 or 532 nm (2nd harmonic) was used in the pulsed laser experiments to synthesize the carbon nanoparticles. The nonfocused laser beam was appropriately guided with a suitable combination of mirrors to irradiate the air-equilibrated samples from their top side. Some preliminary experiments where the kinetics of carbon nanoparticle formation was studied in detail were performed in a standard 1 × 1 cm quartz cell for spectrofluorimetry filled with 3 mL toluene at 25 ± 2 ^{o}C, while the rest of pulsed laser synthesis experiments were carried out with a home-made photochemical reactor at 25 ± 2 ^{o}C or at the melting temperature of naphthalene (80 ± 2 ^{o}C). Nickel(II) oxide green powder (NiO, 400 mesh, Alfa Aesar, mp 1984 ^{o}C) was used in a control experiment with toluene,[23a,c] in order to evaluate how its presence

could affect the formation of carbon nanoparticles compared to the experiments performed with no additive in the colorless and transparent quartz or borosilicate 3.3 glass vessels used as the reactant containers (mp 1715 ^{o}C and 1648 ^{o}C for quartz and borosilicate 3.3 glass, respectively).

The home-made reactor consists of a metal structure that comprises three parts: i) a cylinder-shaped aluminum container lined with aluminum foil inside, where a borosilicate 3.3 glass vessel (5 cm outer diameter, 4 cm height) is placed; ii) a stainless-steel lid, with two holes each covered by a rubber septum where a temperature probe, gas purge or sampling system can be fitted, and a replaceable pyrex glass window (90% transmittance in the range 2000–350 nm) that allows the laser beam to irradiate the reaction mixture; and iii) a stainless-steel clamp to fit the container with the lid. The mixture was left to reach the desired temperature while magnetically stirred with a Teflon-coated magnet (600 rpm for liquid samples or 1200 rpm for NiO experiments) and, once the photoreactor was sealed, the system was irradiated for 6 hours with the laser beam eccentric to the magnetic stirring axis in order to avoid any damage of the magnetic stirrer by the laser beam. Yellowish to brownish reaction crudes were obtained from the experiments performed with organic precursors which are liquid at 25 ^{o}C, while the gray colored reaction crude was obtained in the experiments performed with naphthalene. In addition, in the latter experiment with naphthalene, a volatile nanoparticle fraction (v-CNPs) recovered from the reactor lid and a non-volatile fraction (nv-CNPs) that was isolated from the reaction vessel were obtained.

As for the purification of the carbon nanoparticles obtained, different procedures were implemented depending on the characteristics of the starting organic precursors. The nanoparticles from experiments carried out with benzene, toluene and chlorobenzene precursors at room temperature were purified by rotavaporation of the starting liquid. FTIR analysis evidenced the different nature of the isolated nanomaterial and complete removal of the organic precursor. In the control experiment with toluene in the presence of NiO, filtration with a 0.2 μm pore filter (Fluoropore, Millipore) allowed removal of the nickel(II) oxide microparticles (< 37 μm diameter) and rotavaporation of the organic solvent afforded the corresponding nanomaterial. Nanomaterials prepared from aniline at room temperature were purified by rotavaporation of the organic precursor to dryness and the solid product was suspended in diethyl ether followed by centrifugation (3× 10 min., 6000 rpm) to remove any impurity soluble in diethyl ether, finally, the nanomaterial was recovered by rotavaporation of the remaining solvent. When naphthalene was used as the organic precursor, the carbon nanoparticles were isolated by removing the remaining naphthalene by sublimation. Experiments of pulsed laser synthesis of carbon nanoparticles were performed by triplicate at least, and 10–100 mg of isolated nanomaterial was typically obtained. Once purified, the carbon nanoparticles were finally dissolved in 2-propanol, toluene, dimethyl sulfoxide or chloroform for further characterization.

Structural characterization of CNPs

The hydrodynamic size of the CNPs was measured by dynamic light scattering (DLS) from a dilute suspension of the sample in 2-propanol and toluene in a standard cuvette, using a Zetasizer NanoZS device (Malvern Instruments).

Atomic force microscopy (AFM) measurements were carried out in a commercial AFM system (Ntegra Prima, NT-MDT) in semicontact (dynamic) mode using scanning by sample configuration in ambient conditions. Rectangular aluminium coated cantilevers HQ:NSC15/Al BS (Mikromash) were used with a tip radius < 8 nm. Their nominal spring constant is 40 N/m and its resonance frequency is around 325 kHz. The samples were prepared by spin coating in DMSO:H_2O on a mica support.

Scanning Transmission Electron Microscopy (STEM) combined with electron energy loss spectroscopy (EELS spectrometer, Quantum GIF) and energy dispersive X-ray spectroscopy (EDS spectrometer, Oxford) was carried out using the JEOL JEM ARM200Cf with CEOS (Corrected Electron Optical Systems) aberration corrector on the field effect emission condenser (cold FEG) lens and HAADF (High-Angle Annular Dark-Field) imaging with a JEOL detector and Gatan ABF (Annular Bright Field) and HAADF detectors. In this case, the electron acceleration voltage used was 80 kV. HR-STEM images were obtained using holey carbon grids. Electron microscopy was carried out at the ICTS-CNME at the University Complutense of Madrid campus.

Raman spectroscopy measurements were performed with a Senterra II Raman microscope (Bruker), which combines a Raman spectrometer equipped with 532, 633 and 785 nm laser lines and a confocal microscope module (Olympus BX51). Data analysis was done with OPUS software. The Fourier transform infrared (FTIR) spectra were obtained using a JASCO FT/IR-410 equipped with an attenuated total reflection (ATR) accessory. Acquisition was made either from samples dispersed in volatile organic solvents such as methanol or acetone deposited on the ATR prop or, when necessary for quality reasons, from KBr pellets. Data analysis was done with OPUS software.

Photophysical characterization of CNPs

UV-Vis absorption spectra were recorded on UV-Vis spectrophotometers (Varian Cary 5000) using 1 cm path length quartz cuvettes (Suprasil). The optical density was corrected for Rayleigh scattering due to the tendency of the carbon nanoparticles to strongly interact forming aggregates. Correction of the absorption spectra was performed with the correction function shown in Equation 1: :[27]

$$A = \log\left[\frac{1}{1 - c\,\lambda^4}\right] \quad \text{eq. } 1$$

where, A is the absorbance, c is a proportionality constant (10^9) and λ is the wavelength of light in the UV-vis region used for recording the spectra (200–800 nm,

with negligible light absorption by the samples in the 700–800 nm interval). The correction function was subtracted from the experimental optical density and this spectral correction allowed the determination of several features (peaks or shoulders) in the UV end of the spectra below 360 nm.

Room-temperature photoluminescence (PL) and photoluminescence excitation (PLE) spectra were acquired on a spectrofluorometer (Horiba FluoroLog 3) equipped with a high-pressure Xenon lamp and a Hamamatsu R928P photomultiplier tube; the PLE and PL spectra were corrected for the characteristics of the lamp source and of the detection system, respectively.

The fluorescence quantum yields of the samples (Φ_{fluo}) were determined at room temperature (25 ± 2 °C) using different excitation wavelengths (375 and 457 nm) relative to quinine sulfate in 0.5 m H_2SO_4 (Φ_{fluo} = 0.55 ± 0.05)[28] and riboflavin in methanol (Φ_{fluo} = 0.30 ± 0.03)[29] respectively. Identical emission wavelength ranges were used for all the samples in order to determine the areas under the spectral curves. The optical density (≤ 0.1 at λ_{exc}) of each solution was checked before and after collection of the corresponding emission spectrum. In these conditions, the unknown Φ_{fluo} values were calculated by using Equation 2:

$$\Phi_{fluo} = \Phi_{fluo\,Ref} \frac{I}{I_{Ref}} \frac{A_{Ref}}{A} \frac{n^2}{n_{Ref^2}} \quad \text{eq. 2}$$

where I is the integrated area of the emission intensity under the spectral curve, A is the absorbance at the excitation wavelength, and n is the refractive index of the solvent (1.333 for water, 1.329 for methanol and 1.3756 for 2-propanol),[30] and Ref stands for the corresponding values of the reference standard.

Time-resolved fluorescence experiments (TRF) were performed with a custom-made PicoQuant Fluotime 200 fluorescence lifetime system. Fluorescence was excited at 290, 405, 457 and 502 nm by a pulsed LED, at 375 nm by a pulsed laser working at a repetition rate of 10 MHz and at 405 nm picosecond pulsed diode laser (LDH-D-C-405, PicoQuant). Emission maxima were observed by keeping the count frequency below 1 %. In the cases of fluorescence excitation at 375, 405 and 457 nm, measurements were made under argon and at different oxygen concentrations (air equilibrated and oxygen saturated). For all other excitation wavelengths, measurements were made only under air-equilibrated conditions. Fluorescence decays were analyzed using PicoQuant Fluofit v4.6.5 data analysis software. The decay of the excited singlet is adjusted by Equation 3.

$$I(t) = \int_{-\infty}^{t} IRF(t') \sum_{i=1}^{n} A_i \, e^{-\frac{t-t'}{\tau_i}} \, dt' \quad \text{eq. 3}$$

where I(t) stands for the fluorescence intensity at time t, IRF(t') is the instrumental response time function, t' takes a value of 0.08 due to the instrumental

time delay, Ai are the pre-exponential factors, and τ_i are the discrete components of the multi-exponential fitting life of the decay curve.

Triplet state lifetimes were determined for Ar-purged samples by laser flash photolysis experiments with a Q-switched Nd-YAG laser (Surelite I-10, Continuum) at 355 nm for excitation and a Xe lamp (PTI, 75 W) at right-angle geometry for analysis. The white-light probe beam passed through a grating monochromator (mod. 101, PTI) observing at 600 nm, and was detected by a photomultiplier (R928, Hamamatsu) whose output was finally fed to a Lecroy Wavesurfer 454 oscilloscope.

Time-resolved phosphorescence detection of $^1O_2$ emission at 1270 nm was performed using a customized Fluotime 200 fluorescence lifetime system (PicoQuant, Germany) described elsewhere.[31] Briefly, a diode-pumped Q-switched Nd-YAG laser (FTSS355-Q, Crystal Laser, Berlin, Germany) was used to excite samples at 355 nm (1 kHz repetition rate, 0.5 µJ per pulse, 1 ns pulse-width). In order to remove any residual component of its fundamental emission in the NIR region, a 1064-nm rugate notch filter (Edmund Optics, U.K.) and an uncoated SKG-5 filter (CVI Laser Corporation) were placed at the exit port of the laser. The NIR luminescence exiting from the side of the sample was filtered by a long-pass filter of 1000 nm and a narrow bandpass filter at 1270 nm. In this way any scattered laser radiation was removed and the NIR emission from singlet oxygen was isolated. A thermoelectrically-cooled Hamamatsu NIR sensitive photomultiplier tube assembly (H9170-45, Hamamatsu, Japan) coupled to a multichannel scaler (Nanoharp 250, PicoQuant) was used for single photon counting detection. The time-dependent $^1O_2$ phosphorescence signal S(t) was analyzed using the GraphPad Prism 7 software to fit the data to Equation 4, in which τ_T and τ_Δ are the lifetimes of the photosensitizer triplet state and of $^1O_2$ respectively, and S(0) is the phosphorescence signal at zero time, just after pulsed excitation, which is proportional to Φ_Δ.

$$S_{1270}(t) = S_{1270}(0) \times \frac{\tau_\Delta}{\tau_\Delta - \tau_T} \times \left(e^{-t/\tau_\Delta} - e^{-t/\tau_T}\right) \quad \text{eq. 4}$$

The Φ_Δ values of the different samples were obtained by comparison of the slopes of $S_{1270}(0)$ vs. absorbed-laser-energy plots obtained at different sample and reference concentrations following Equation 5.

$$\Phi_{\Delta,\text{sample}} = \Phi_{\Delta,\text{ref}} \times \frac{\text{Slope}_{\text{sample}}}{\text{Slope}_{\text{ref}}} \quad \text{eq. 5}$$

Phenalen-1-one (Φ_Δ = 1.00 ± 0.05, in 2-propanol)[32] and Bengal rose (Φ_Δ = 0.75 ± 0.05, in 2-propanol)[32] references were used for the excitation wavelengths of 355 and 473 nm, respectively.

In addition, singlet oxygen scavenging experiments with 1,3-diphenylisobenzofuran (DPBF) were carried out to evaluate singlet oxygen production of some carbon nanoparticle batches dispersed in chloroform. A medium-pressure

mercury UV lamp (PL-UV, 7 W, 230 V, Mod 60.281 Electro DH) was used as the light source (λ = 365 nm). The concentration of each solution was adjusted at an absorbance value of ~0.10 at 365 nm in order to ensure that an equal number of photons were absorbed per time unit in all experiments. Bleaching of DPBF by singlet oxygen was monitored by following the changes in its characteristic absorbance peak at 412 nm. The observed rate constants (k_{obs}) were obtained by a linear least-squares fit of the plot of absorbance vs. time. The values of singlet oxygen quantum yields (Φ_Δ) were calculated with respect to phenalen-1-one reference standard (Φ_Δ = 0.98 ± 0.15 in chloroform) by using Equation 6.[34]

$$\Phi_\Delta^{PS} = \frac{\Phi_\Delta^{Ref} k_{obs}^{PS} Abs_0^{Ref}}{k_{obs}^{Ref} Abs_0^{PS}} \quad \text{eq. 6}$$

where Φ_Δ is the singlet oxygen production quantum yield of the sample or reference, respectively, k_{obs} is the rate constants from the linear least-squares fit of the absorbance vs time plot, and A_{365} is the initial absorbance of each photosensitizer at 365 nm.[35]

4.2.3. Results and discussion

Synthesis of CNPs

To obtain information about the relationship between the generation conditions and the nanoparticles obtained and about the chemical kinetics of their generation in real time, the configuration shown in Figure 1 was used. In this configuration, 3 mL of toluene in quartz cuvette (40 x 10 x 10 mm) were used using a magnetic stirrer and a spherical magnet to maintain a homogeneous agitation during irradiation. A Nd-YAG non focused pulsed laser beam with a wavelength 1064 and 532 nm and a laser power density adjusted to 2.3 and 3.5 W/cm^2 was used to irradiate the liquid phase and a solution fluorescence monitoring system with real-time detection was used to follow the CNPs production, which uses a 443 nm continuous laser as the excitation source, and a CCD detector spectrometer focused on the cuvette through a fiber optic cable to collect the emission signal.

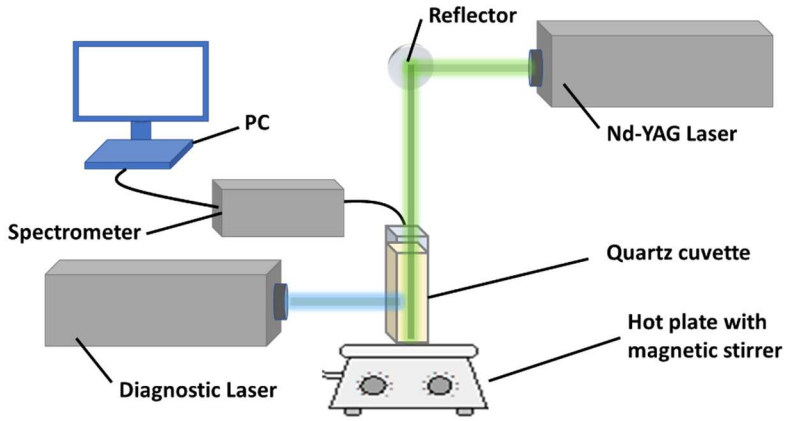

Figure 1. Detailed schematic illustration of the experimental setup for the preparation of CNPs.

The real-time fluorescence detection system allows us to follow the formation of CNPs and evaluate parameters such as the wavelength of irradiation and the power density of the laser in situ. For this purpose, experiments were performed with irradiation wavelengths of 532 and 1064 nm and evaluated at the same laser power adjusted to 2.3 W/cm^2, similarly, experiments were performed varying the laser power at 2.3 and 3.5 W/cm^2 and evaluated at the same irradiation with wavelength 532 nm. As can be seen in Figure 2, for the same laser power of 2.3 W/cm^2, an irradiation wavelength of 532 nm causes a CNPs formation in 20 minutes with an emission intensity in 510 nm 10 times higher than the emission intensity of the CNPs generated during one hour with an irradiation wavelength of 1064 nm. On the other hand, Figure 3 shows the dependence of the emission intensity of the nanoparticles on laser power for an irradiation wavelength of 532 nm, since it has been seen that for this wavelength CNPs with greater intensity of fluorescent emission are produced. In this case, a laser power of 3.5 W/cm^2 implies almost double the fluorescence intensity of the CNPs obtained at 510 nm than a laser power of 2.3 W/cm^2 for the same time of laser irradiation.

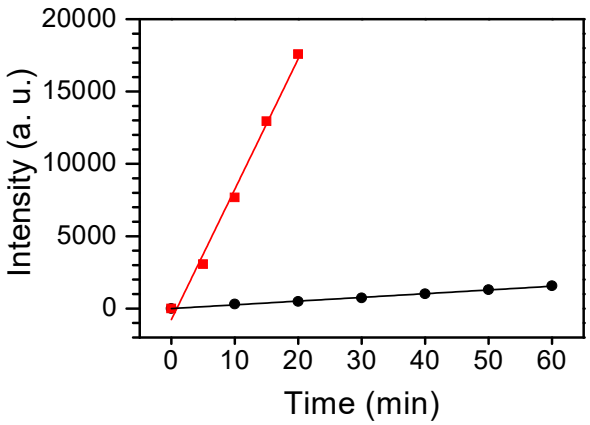

Figure 2. Increased intensity of real-time fluorescent emission of CNPs generated from toluene during laser radiation of 532 nm (red) and 1064 nm (black). λ_{exc} = 443 nm, λ_{det} = 510 nm, P = 2.3 W/cm^2.

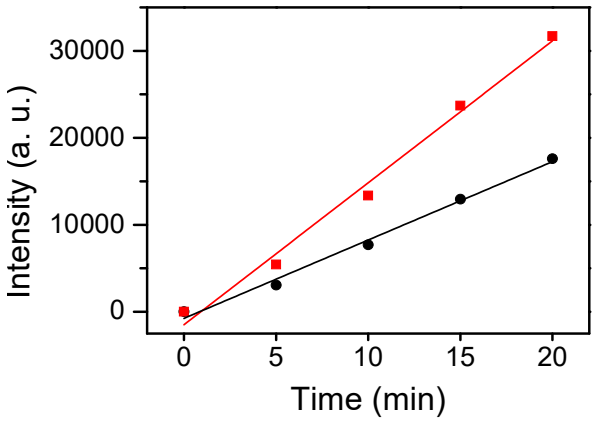

Figure 3. Increased intensity of real-time fluorescent emission of CNPs generated from toluene during laser radiation of 532 nm at a power of 3.5 W/cm^2 (red) and 2.3 W/cm^2 (black). λ_{exc} = 443 nm, λ_{det} = 510 nm.

During the first experiments, it was observed that if the 443 nm diagnostic laser of the real-time fluorescence detection system was used continuously, there was a decrease in the photoluminescent emission of the CNPs, compared to the samples that were not illuminated with the diagnostic laser during the whole experiment, but only every 5 min to record the emission spectrum. This novel effect of photochemical suppression or slowing down of the CNPs formation reaction can be seen in Figures 4a and 4b. Furthermore, when comparing these figures with each other, it can be seen how when applying an irradiation wavelength of 532 nm, in the case of Figure 4b, as opposed to 1064 nm in the case of Figure 4a, the difference in slope between the lines is less, i.e., the slowdown that occurs is less. This effect is attributed to the excitation, by an intense laser source, of the intermediate species in the CNPs formation, so that their corresponding excited states would have an energy barrier big enough to not allow the CNPs formation as a final product. This mechanism is schematized in Figure 5.

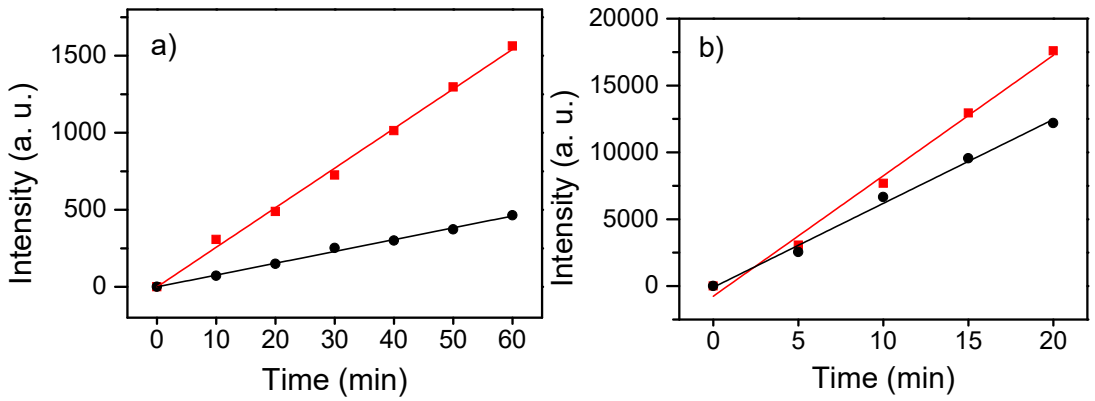

Figure 4. Increased intensity of real-time fluorescent emission of CNPs generated from toluene during laser radiation of 1064 nm a), and 532 nm b), with the real-time fluorescence detection system continuously (black) or every five minutes (red). λ_{exc} = 443 nm, λ_{det} = 510 nm, P = 2.3 W/cm^2.

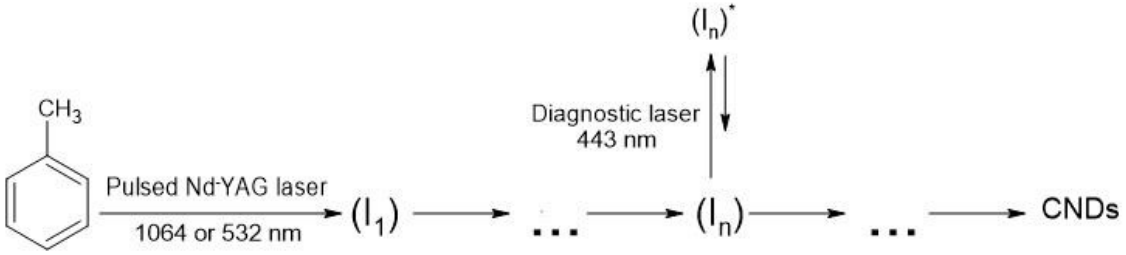

Figure 5. Mechanistic scheme of the pulsed laser synthesis of CNPs through the successive formation of intermediate species (I_1 ... I_n, where I_n is the first intermediate that absorbs visible light), and the role of the excited states $(I_n)^*$ slowing down the formation of CNPs.

Once the parameters involved in pulsed laser synthesis have been studied, and in order to increase production and use different precursors as building blocks, the configuration shown in Figure 6 was used. In a generic experiment, 20–50 mL of the organic aromatic precursor was put for irradiation into a borosilicate glass reaction vessel inside an aluminum container provided with a stainless steel lid with a gas/vacuum connection, two septum capped ports for reactants addition/aliquots extraction and thermocouple-assisted temperature monitoring, and a pyrex glass window. A Nd-YAG non focused pulsed laser beam with a wavelength 532 nm and a laser power density adjusted to 3.5 W/cm^2 was used to irradiate the liquid phase within the reaction vessel through the pyrex glass window. During irradiation (typical period of 5–6 hours), a magnetic stirrer was used to homogenize the irradiated crude. In addition, aliquots were regularly drawn (every 15–30 min) to analyze the fluorescence emission spectra of the reaction crude, in order to evaluate the chemical reaction kinetics governing the formation of the nanoparticles. Table 1 shows the different CNPs produced from the different precursors and how they were purified.

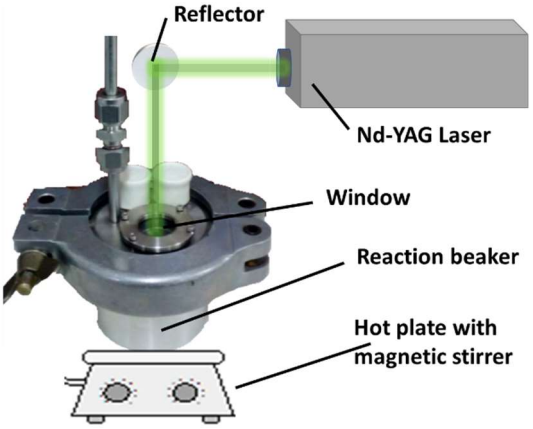

Figure 6. Detailed schematic illustration of the experimental setup for the preparation of CNPs.

Table 1. CNPs produced from the different precursors.

Experiment	Precursor
CNPs-1	Toluene
CNPs-2	Benzene
CNPs-3	Aniline
CNPs-4	Chlorobenzene
CNPs-5*	Naphtalene
CNPs-6	Toluene / NiO (0.255 % p/p)

* two fractions are obtained: volatile fraction (v) and non-volatile (nv).

Formation of the CNPs was monitored by following the onset of the sample's fluorescence and the increased emission during laser irradiation, as can be seen in Figure 7, different behaviors are observed when representing the intensity of the emission maximum against the reaction time. The formation of CNPs 1, 2, and 3 requires an initial induction period of 60-150 min, which could be associated to the formation of nonfluorescent reaction intermediates, before the generation of fluorescent nanoparticles, after this induction time a linear dependence between fluorescence intensity and irradiation time is observed. On the other hand, the formation of CNPs 4 and 6 shows that no induction time is required, and a linear dependence is always observed. In particular, the sample CNPs-4, where the lability of the C–Cl bond could favour the fast formation of nanoparticles, shows the highest rate of CNPs formation, while in the case of CNPs-6 where the experiment is conducted in the presence of nickel oxide microparticles that may behave as a catalyst,[20, 21] a similar slope is observed and the change of slope suggest a saturation behavior that would justify the kinetic slowdown observed at long reaction times. In the case of CNPs obtained from solid precursors, fluorescence monitoring is not technically feasible.

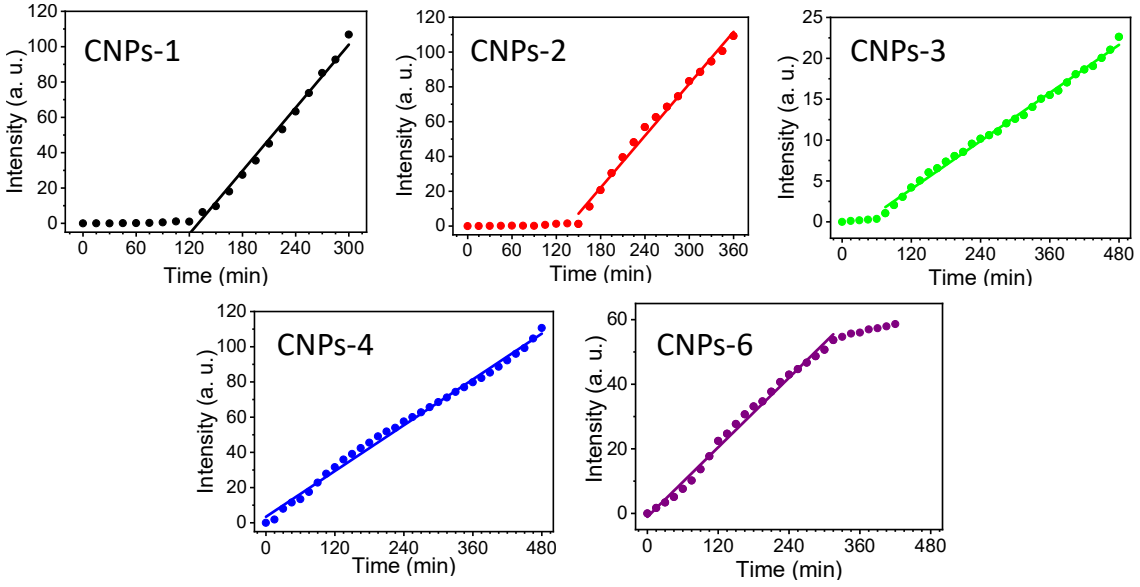

Figure 7. Increased intensity of fluorescent emission of different CNPs (λ_{exc} = 400 nm and λ_{det} = 510 nm).

Assuming that the observed fluorescence in the visible region is proportional to the population or concentration of excited states of the CNPs (no self-quenching effect or quenching by any reaction intermediate acting as quencher may also be assumed, due to high dilution in the reaction crude), regular increments of fluorescence intensity against time have been observed in all cases (straight lines in Figures 2, 3, 4 and 7), which would point to the existence of zero-order kinetics along the pulsed laser synthesis of CNPs. In the case of zero-order kinetics, where the reaction rate is constant, the rate is independent of the concentration of reactant so long as some is present and, since in these experiments the concentration of organic precursors is always in the 8.5–14.4 M interval, and laser radiation with homogeneous fluence is continuously delivered to the reaction system, it seems likely that the previous assumptions might hold. Moreover, zero-order reactions imply that a small fraction of the reactant is in a location or state in which it can react (typical of light-induced reactions), this fraction being continuously replenished. Furthermore, zero-order rate laws are typical of heterogeneous reactions and, in particular, of surface-catalyzed processes and, therefore, it is plausible that the irradiated surface of the reaction vessel (or any solid particles added to the reactor in the case of experiments performed in the presence of NiO microparticles) might play a role as a catalyst. Therefore, it can be assumed that the pulsed laser synthesis of the CNPs follows zero-order kinetics, probably catalyzed by the surface of the reaction vessel.

Morphological and structural characterization of CNPs

The CNPs were morphologically and structurally characterized by dynamic light scattering (DLS), atomic force microscopy (AFM), scanning transmission electron microscopy (STEM) combined with electron energy loss spectroscopy (EELS) and energy dispersive X-ray spectroscopy (EDS), as well as Raman and FTIR spectroscopies.

DLS measurements allowed the determination of the size distribution profiles of the CNPs in suspension. DLS results in 2-propanol show wide distributions and a hydrodynamic diameter of hundreds of nm (Figure 8), revealing the strong tendency exhibited by these nanoparticles to form aggregates with much larger sizes in a protic and relatively polar solvent. On the other hand, when the carbon nanoparticles are dispersed in hydrophobic toluene, CNPs display much narrower size distribution (Figure 9). However, although the hydrodynamic diameter decreases in toluene with respect to 2-propanol suspensions by 2-5 times, it remains high except for CNPs 6 prepared from toluene/NiO where a 1.7 nm size distribution was found (Table 2). Overall, these results show that CNPs in toluene also form aggregates but much smaller and with narrower distributions than 2-propanol. Time-dependent DLS measurements also evidenced that these nanomaterials tend to form larger aggregates and to produce sediments over time.

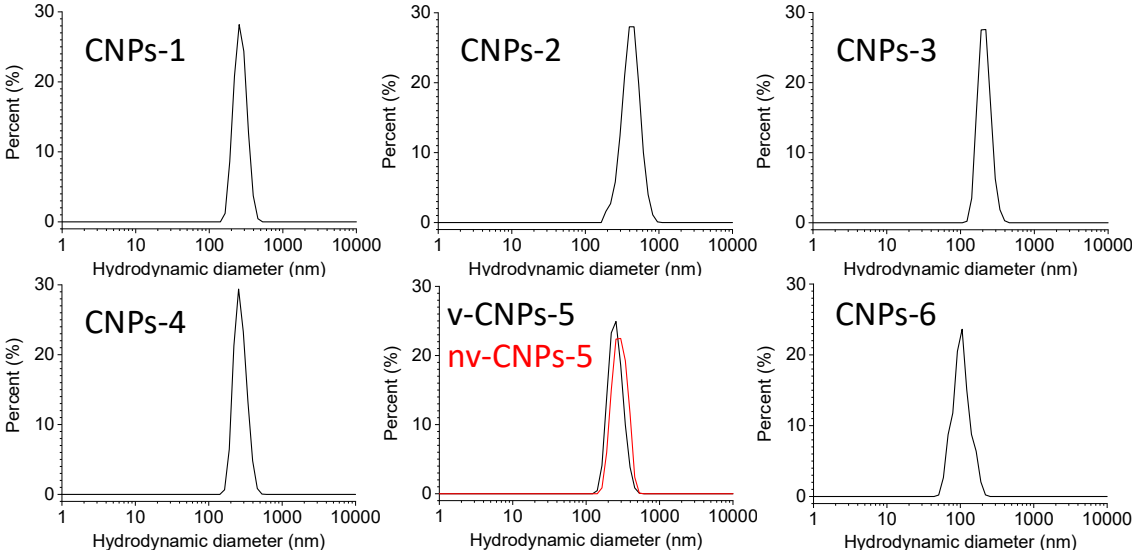

Figure 8. Dynamic light-scattering (DLS) spectra of different CNPs in 2-propanol.

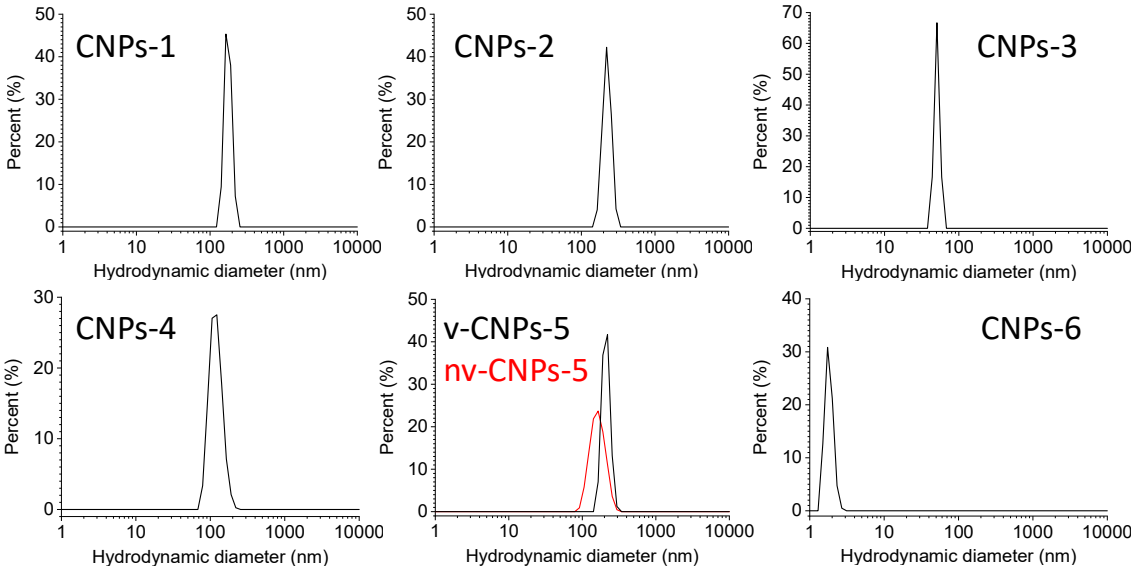

Figure 9. Dynamic light-scattering (DLS) spectra of different CNPs in toluene.

Table 2. Hydrodynamic diameter of CNPs in 2-propanol and toluene.

Sample	CNPs 1	CNPs 2	CNPs 3	CNPs 4	nv-CNPs 5	v-CNPs 5	CNPs 6
2-PrOH (nm)	270 ± 70	400 ± 100	200 ± 50	260 ± 70	290 ±70	260 ± 70	100 ± 50
Toluene (nm)	160 ± 20	220 ± 30	51 ± 5	120 ± 30	160 ± 40	260 ± 20	1.7 ±0.3

AFM images allowed us to observe the carbon nanoparticles individually. Average heights of between 1.1 and 11.2 nm were observed for populations of between 350 and 6500 individual nanoobjects (Table 3). In general, narrow population distributions were obtained, which explains the excellent agreement between the peak of the fitted Gaussian or Lorentzian distribution and the slightly larger mean size values, within the experimental error of the technique. Surprisingly, experiments performed from naphthalene resulted in volatile fractions with larger CNPs. AFM images of CNPs with their size distribution histograms and Gaussian/Lorentzian fittings are shown in Figure 10.

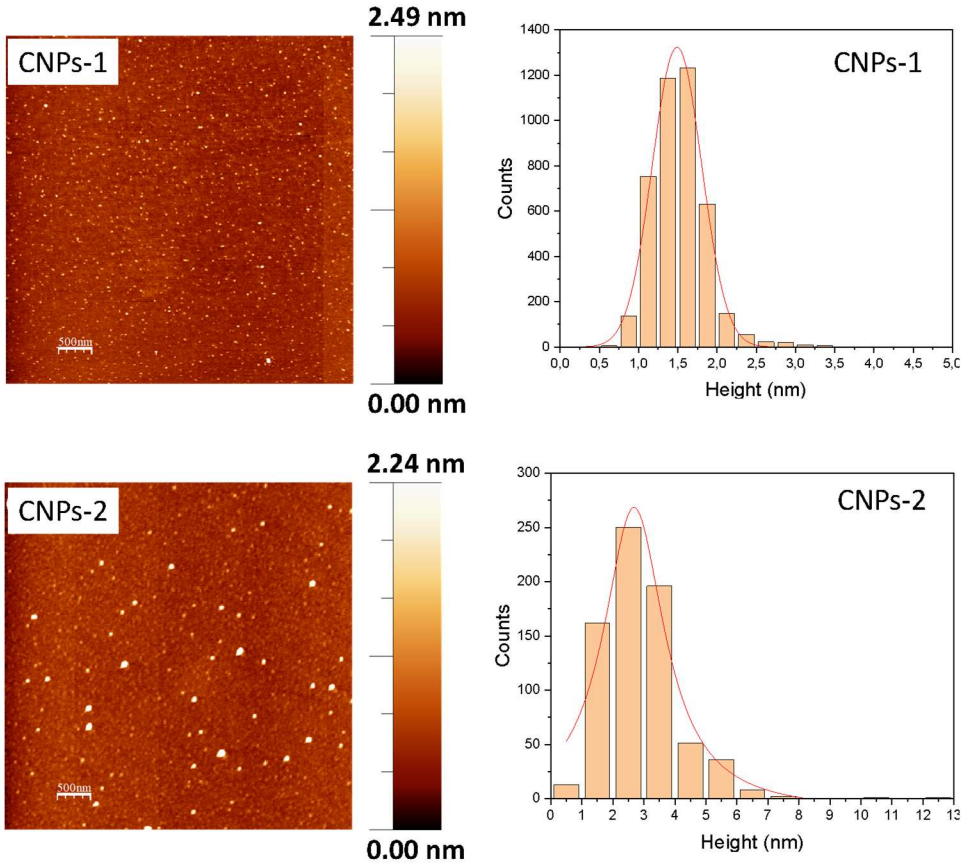

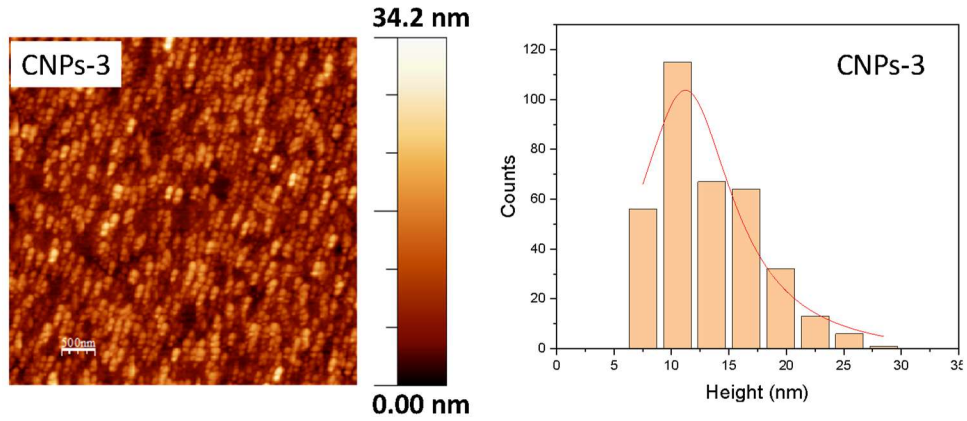
CNPs-3
300nm
34.2 nm
0.00 nm
CNPs-3
Counts
Height (nm)

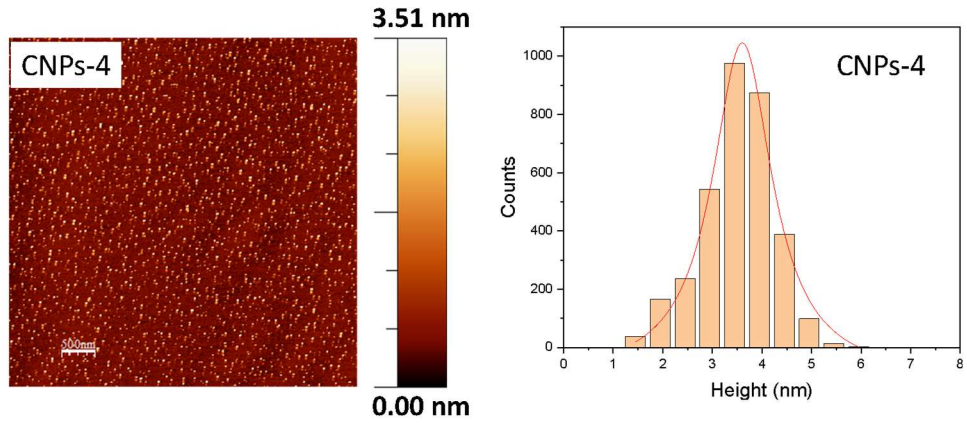
CNPs-4
500nm
3.51 nm
0.00 nm
CNPs-4
Counts
Height (nm)

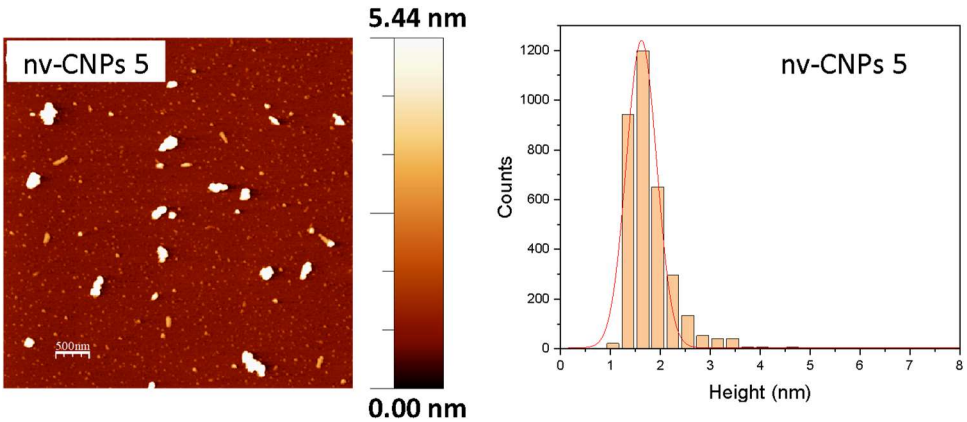
nv-CNPs 5
500nm
5.44 nm
0.00 nm
nv-CNPs 5
Counts
Height (nm)

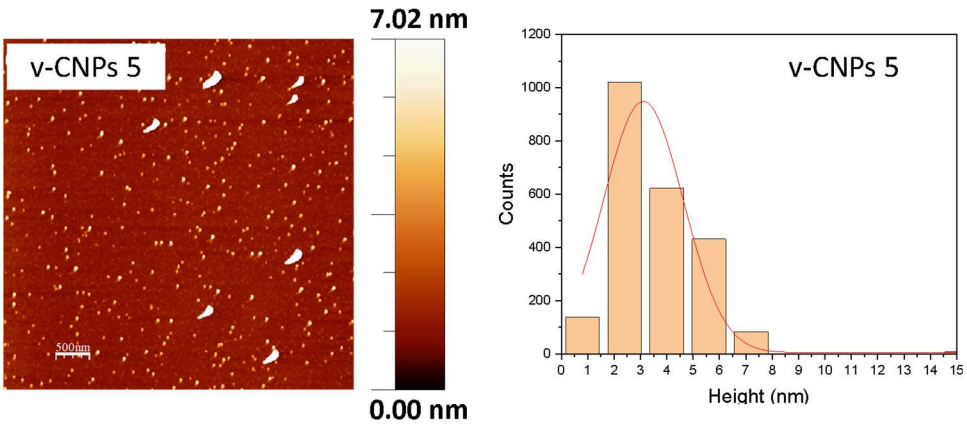
v-CNPs 5
500nm
7.02 nm
0.00 nm
v-CNPs 5
Counts
Height (nm)

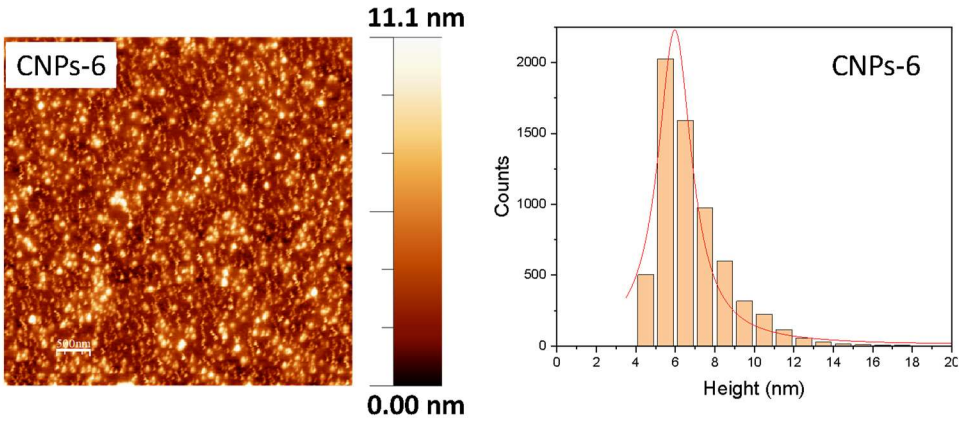

Figure 10. AFM images of CNPs with their size distribution histograms and Gaussian/Lorentzian fits.

Table 3. Parameters and statistical data obtained from atomic force microscopy images.

Sample	CNPs 1	CNPs 2	CNPs 3	CNPs 4	nv-CNPs 5	v-CNPs 5	CNPs 6
Model	Gauss	Lorentz	Lorentz	Lorentz	Gauss	Gauss	Lorentz
Fit centre (nm)	1.5	2.7	11.2	3.6	1.6	3.1	6.0
σ (nm)	0.3	1.2	5.0	0.7	0.3	1.5	1.0
FWHM (nm)	0.74	2.41	10.1	1.48	0.71	3.57	2.10
N total	4214	720	354	3338	3468	2327	6484
Mean (nm)	1.5	2.8	13.3	3.5	1.9	3.6	6.9
σ (nm)	0.4	1.3	4.3	0.7	1.1	2.9	1.9
Minimum (nm)	0.72	0.98	7.9	1.33	1.13	1.43	3.90
Median (nm)	1.50	2.92	12.3	3.56	1.66	3.21	6.40
Maximum (nm)	12.1	12.1	27.7	5.82	20.67	39.03	23.14

Scanning electron transmission microscopy was performed to observe the CNPs with atomic resolution. Figure 11 shows low magnification and high-resolution images of the samples. As can be observed in low magnification images, the nanoparticles tend to aggregate in globular structures of hundreds of nanometers as a result of the deposition process on the carbon grids from sample dispersions in 2-propanol after 5 min sonication. Interestingly, the presence of CNPs aggregates spanning the edges of the carbon grid holes, with no carbon background, allowed a precise determination of the amount of Csp^2 vs. Csp^3 and of the C/O ratio in the CNPs by STEM-EELS technique. Table 4 collects results from STEM and EELS data obtained from the electron microscopy characterization.

Strikingly, high-resolution images reveal the presence of graphitic stripes or disrupted onion-like fragments forming the carbon matrix in both the volatile and nonvolatile fraction of those samples obtained from benzene and naphthalene, (CNPs

2, v-CNPs 5 and nv-CNPs 5), precursors which lack Csp^3 carbon and do not have Cl or N heteroatoms. The interplanar distances of the observed onion-like carbon structures were measured from different images. Same mean values were obtained for all the samples, with a median value of 3.6 Å (different from the interlayer distance of 3.34 Å typically observed in graphite). On the other hand, samples as CNPs 1, CNPs 3, CNPs 4 and CNPs 6, prepared from toluene, aniline, and chlorobenzene, show a markedly different amorphous structure. These nanomaterials were highly sensitive under the electron beam and, in addition, were prone to contamination, since EDS results showed the presence of undesired impurities which made very difficult their observation and analysis.

Characterization by electron energy loss spectroscopy was used in a GIF Quantum Dual EELS system to measure the Csp^2 content by the signatures of the π* and σ* bonds at 282-288 eV and 290-320 eV, respectively.[35] An important decrease was observed in the amount of Csp^2 in the CNPs, from 100 % in almost all the organic precursors to 40–70 %. In toluene, a variation from 86 % to 67 % Csp^2 was also observed. EELS technique allowed the semiquantitative analysis of the C/O ratio as well. Some oxygen atoms were incorporated to the CNPs, likely from the SiO_2 of the reactor walls, although less than 7 % O was detected in all the CNPs except those prepared from toluene/NiO (18 % O), suggesting that the use of inorganic microparticles such as NiO plays a role regarding the elemental composition of the CNPs, via transference of oxygen atoms in this case. On the other hand, no significant evidence concerning the incorporation of other heteroatoms such as N and Cl (or even Si) was observed by STEM-EELS or STEM-EDS.

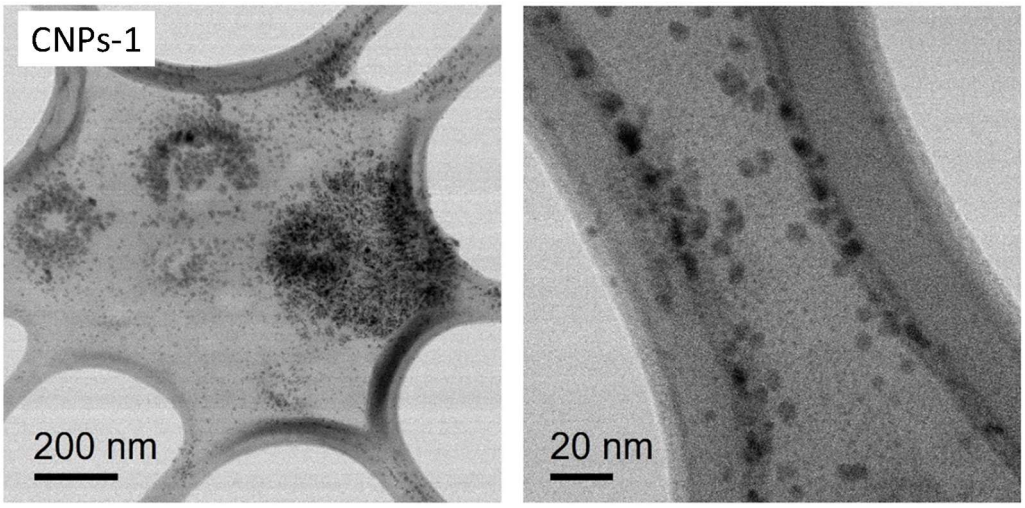

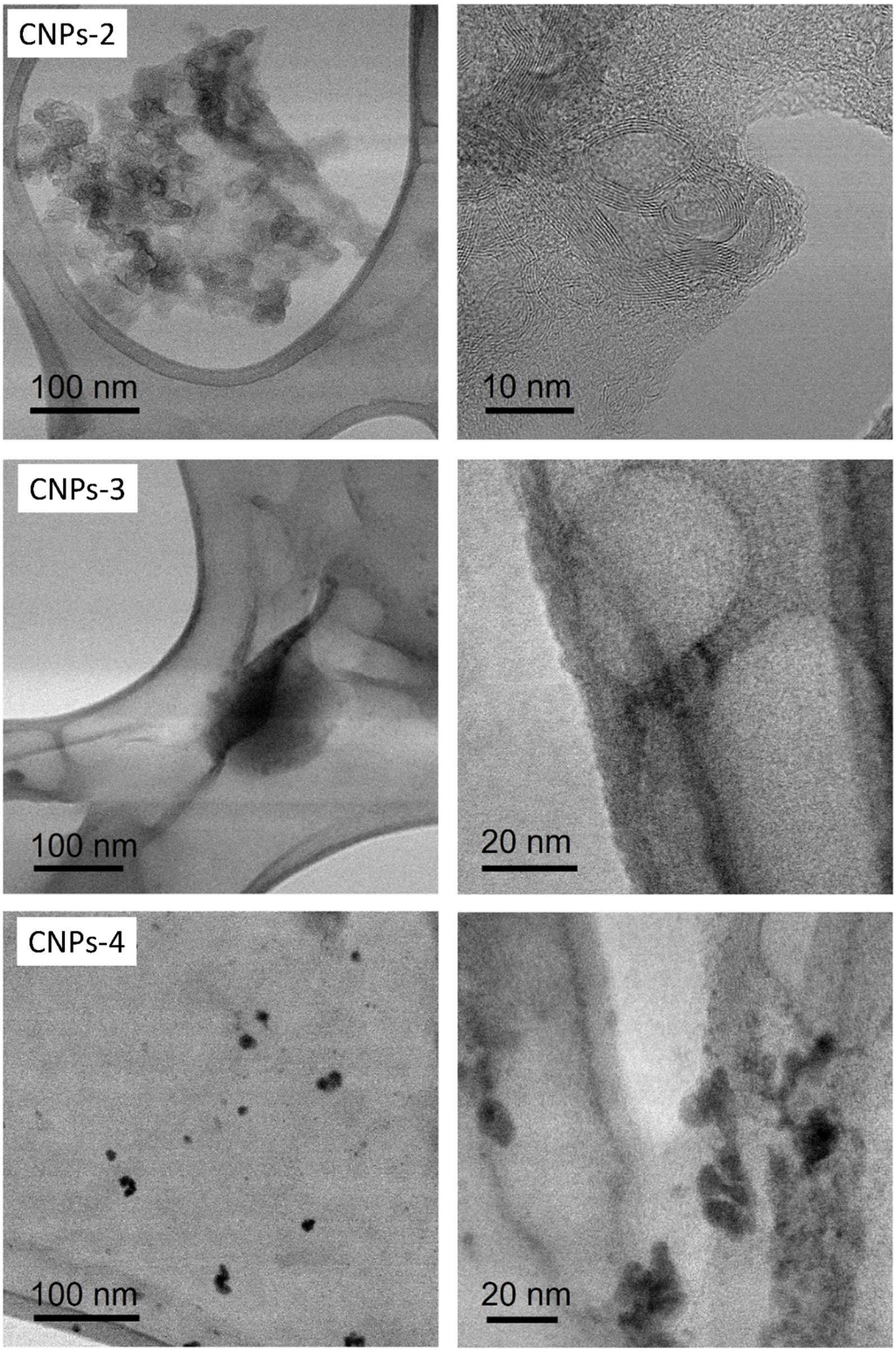
CNPs-2
100 nm
10 nm
CNPs-3
100 nm
20 nm
CNPs-4
100 nm
20 nm

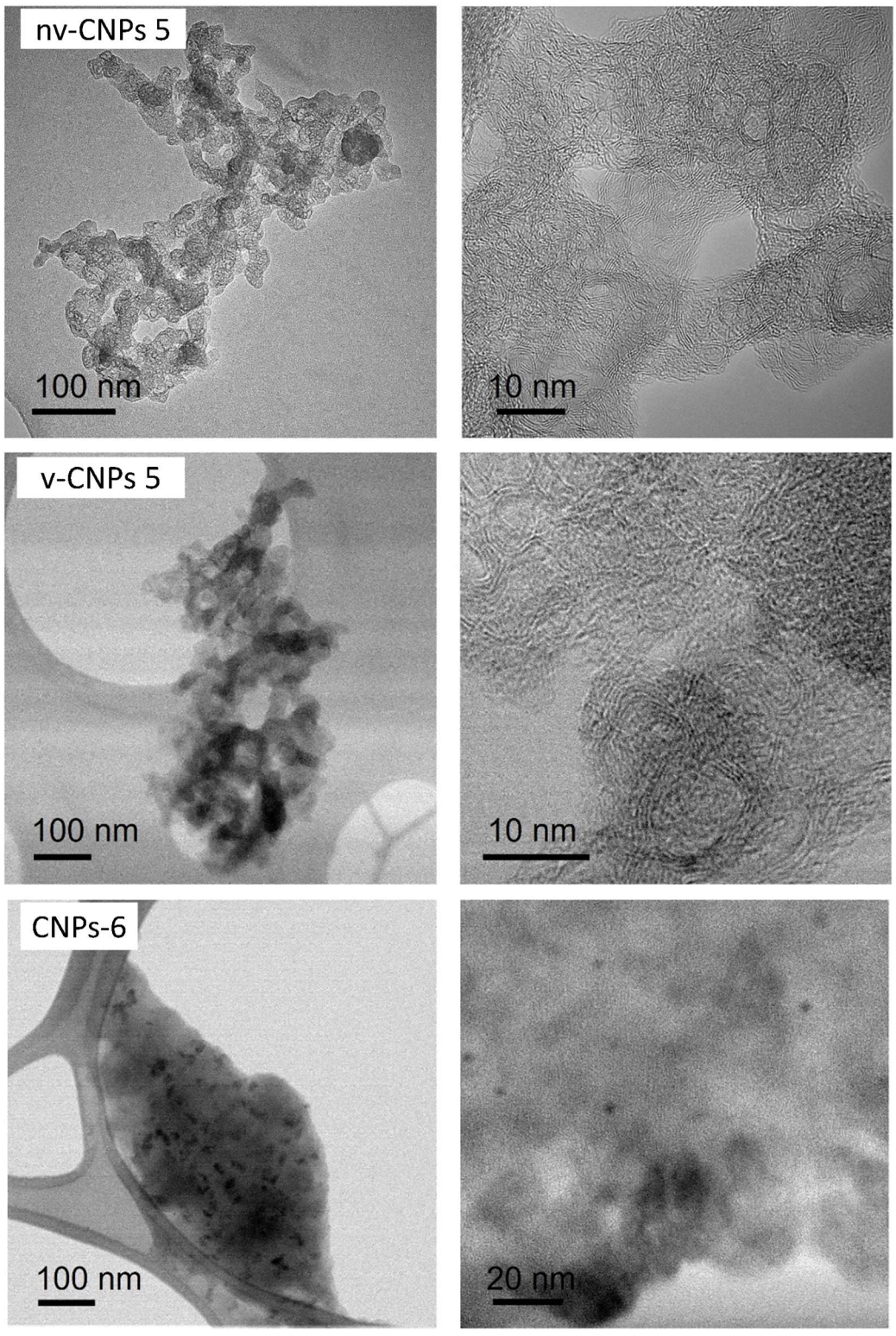

Figure 11. Low magnification (left) and high resolution (right) ABF-STEM images of the CNPs.

Table 4. Characterization of the carbon nanoparticles from STEM and EELS data obtained from STEM measurements. Csp^2 content was also determined from Raman measurements.

Sample	Mean intershell distance (Å)	N total	sp^2 fraction (Raman)	Semiquantitative C/O content (at. %)
CNPs-1	Amorphous carbon	-	67 ± 1 (52 ± 6)	97/3 %
CNPs-2	3.6	115	68 ± 12 (52 ± 5)	93/7 %
CNPs-3	Amorphous carbon	-	Beam damage (58 ± 6)	100/0 %
CNPs-4	Amorphous carbon	-	40 ±3 (49 ± 5)	94/7 %
nv-CNPs-5	3.5	86	64 ± 20 (46 ± 5)	100/0 %
v-CNPs-5	3.5	60	50 ± 1 (43 ± 6)	98/2 %
CNPs-6	Amorphous carbon	-	Beam damage (54 ± 6)	82/18 %

Raman spectroscopy of the CNPs (Figure 12) reveals the bonded carbon G (≈1550 cm^{-1}) and D (≈1350 cm^{-1}) bands of Csp^2 (graphitic) and Csp^3 (defects), respectively. It is worth mentioning the almost total absence of vibrations related to hydrogen or hydroxyl around 3000 cm^{-1} that the band appearing below 1000 cm-1 belongs to the silicon support. The intensities ratio of the characteristic Raman bands (I_D/I_G) can be used to characterize the degree of disorder in the graphitic structure. To determine this ratio, the area under the bands was taken after subtraction of the large background signal, therefore, the detected % of Csp^2, which is 5–19% below the % Csp^2 detected by STEM-EELS microscopy, can only be considered as the lower limit of % Csp^2 (between 58% and 43 %, depending on the sample).

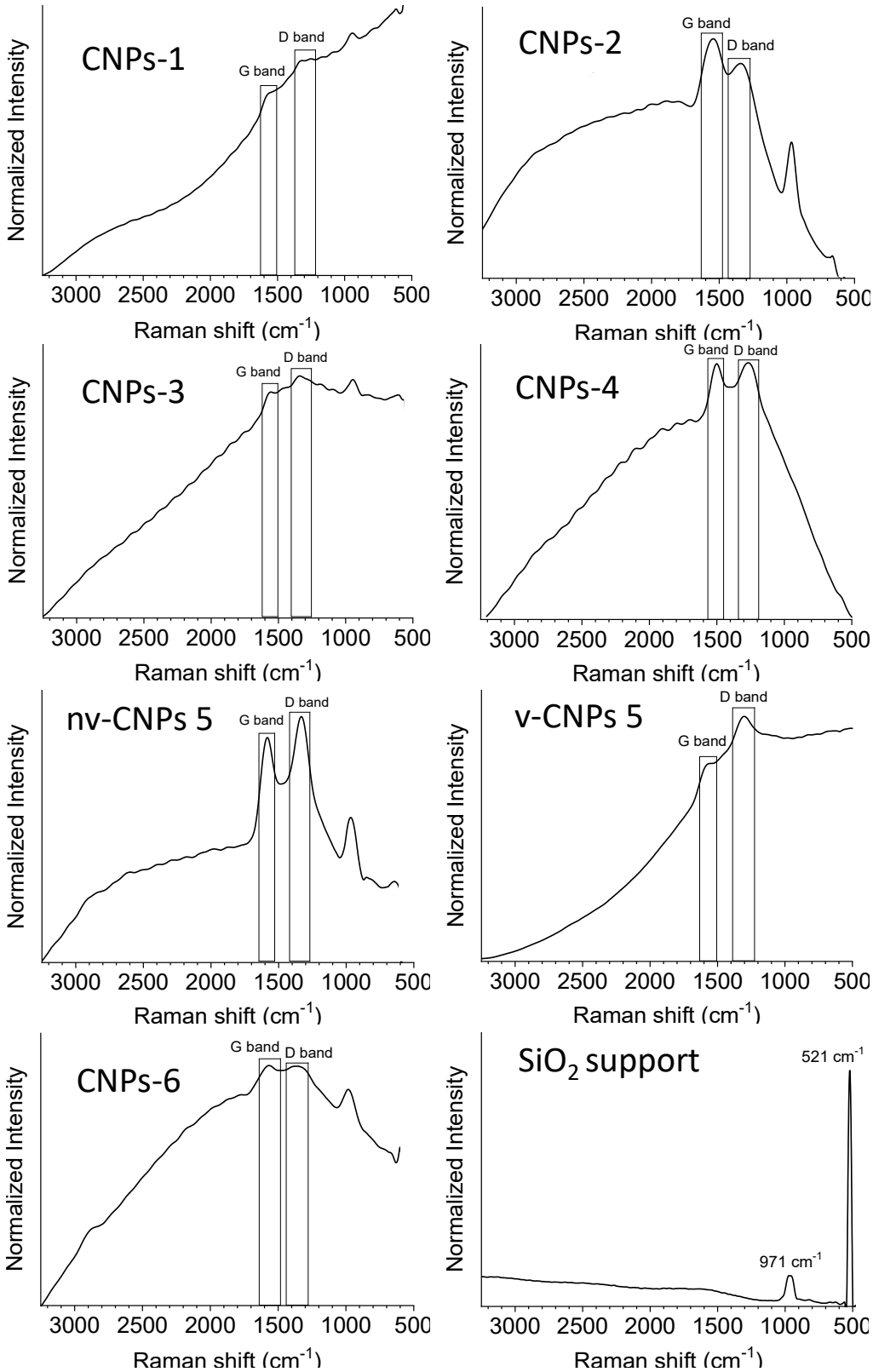

Figure 12. Raman spectra of different CNPs (λ_{exc} = 633 nm).

FTIR spectroscopy reveals different functional groups on the surfaces of CNPs by recording typical vibration bands. It is usual to see, for the different CNPs, O-H or N-H (if the precursor used contains nitrogen) stretching bands (3300 – 3400 cm^{-1}). C-H

stretching bands can also be observed, being more easily observable the band due to Csp^3-H stretching (2957, 2924 and 2854 cm^{-1}) than the band due to Csp^2-H stretching (3030 cm^{-1}), which indicates that the surface is richer in Csp^3 and the Csp^2 of the core is only appreciable in some cases. C=O stretch bands are also observed, although sometimes this band is only revealed as a shoulder in the C=C stretch band (1750 – 1660 cm^{-1}). In the region below 1500 cm^{-1}, several bands can be observed that are difficult to assign unequivocally, but among them are probably the C-O, C-N or C-Cl stretching bands (if the precursor contains nitrogen or chlorine respectively), the C-H bending band or bands due to C-Si or Si-O stretching, if this assignment of the bands observed by FTIR spectroscopy is correct, the Si must come from the borosilicate container used in the synthesis.

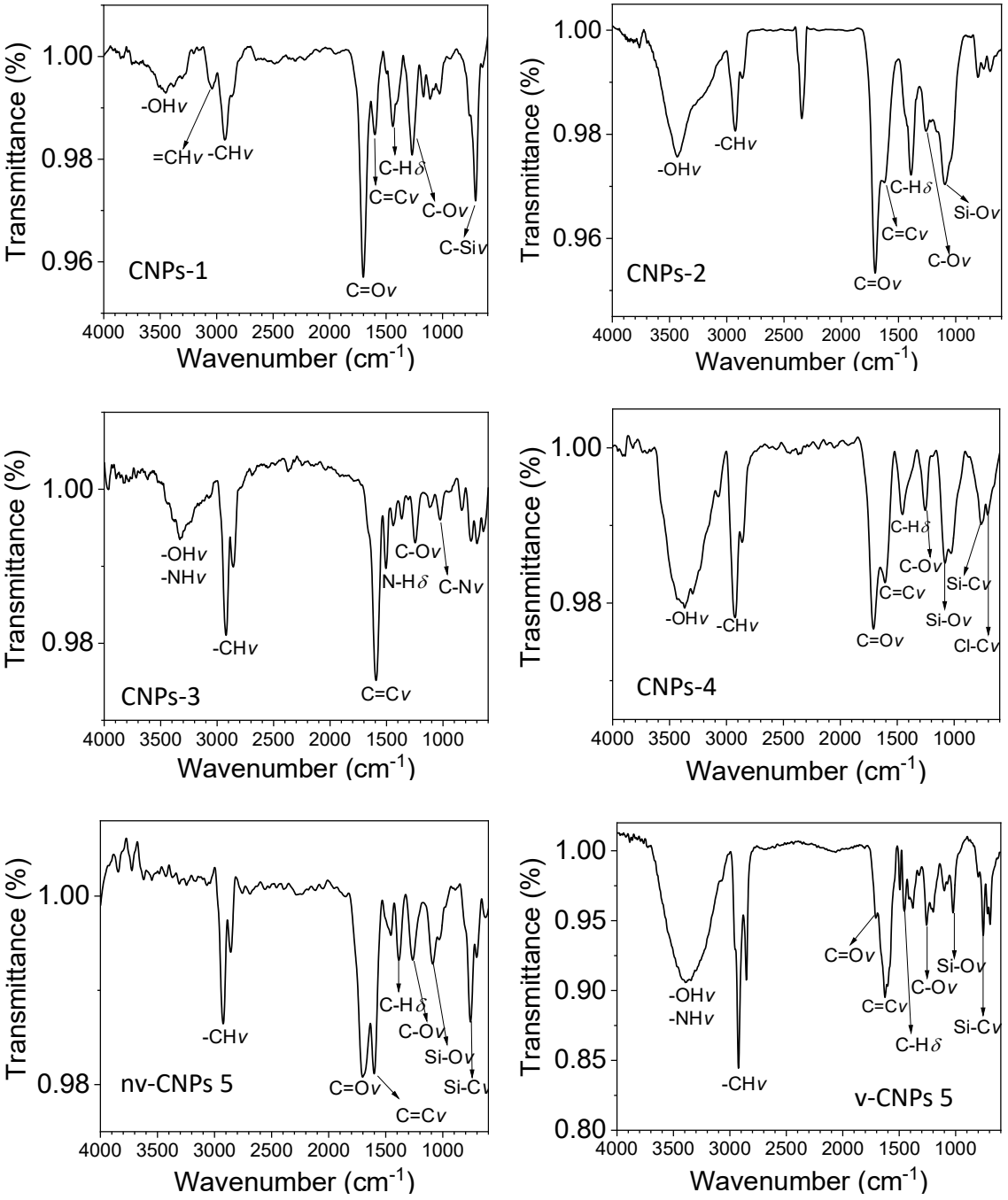

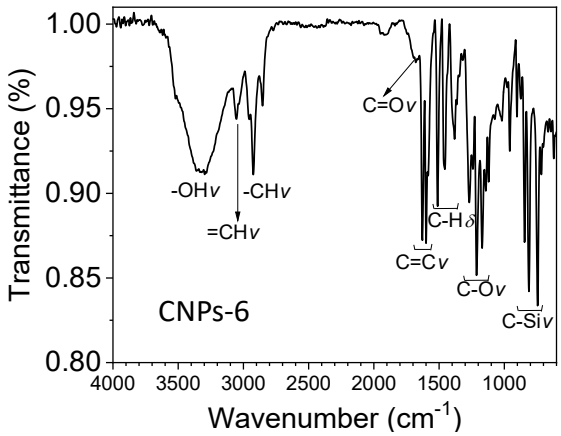

Figure 13. Fourier transform infrared spectroscopy (FTIR) spectra of different CNPs.

Photophysical properties of CNPs

In general, the CNPs studied show strong optical absorption in the UV region of the spectrum, a shoulder above 250 nm and a tail extending into the visible range as shown in Figure 14. Their corresponding peak/shoulder wavelengths and the wavelength they reach with a relative absorption of at least 1 % with respect to the absorption maximum are collected in Table 5. The molar absorption coefficients cannot be determined, as the molar concentration of the CNPs cannot be known.

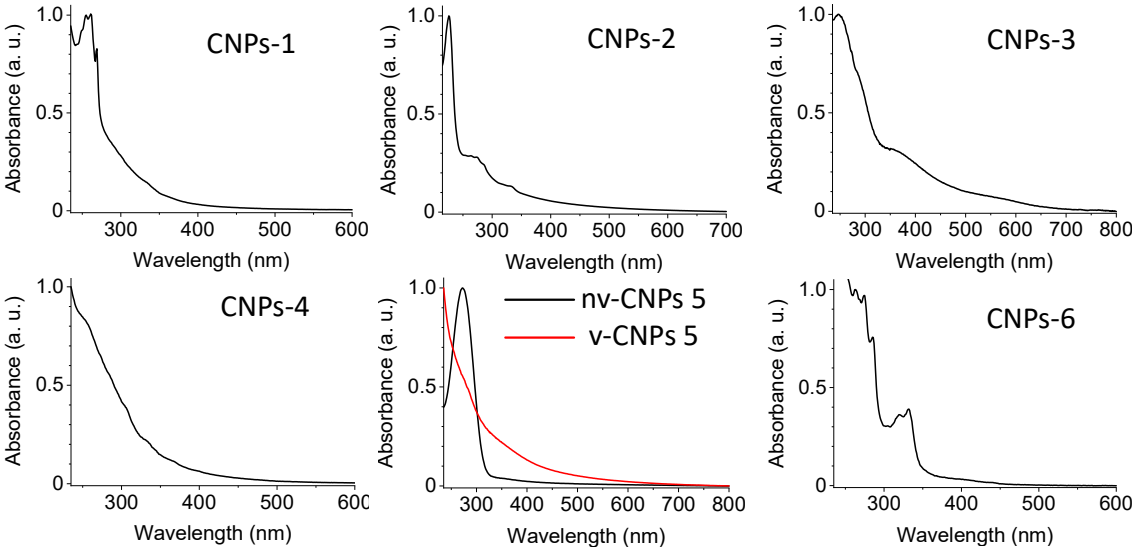

Figure 14. Absorption spectra of the different CNPs in 2-propanol.

Table 5. Position of the absorption maxima (± 2) of the different CNPs (* relative absorption of at least 1 % with respect to the maximum absorption up to this wavelength).

Sample	CNPs 1	CNPs 2	CNPs 3	CNPs 4	nv-CNPs 5	v-CNPs 5	CNPs 6
λ_{abs} (nm)	255 261 269 491*	226 594*	247 707*	525*	272 511*	642*	263 274 285 320 332 448*

The emission spectra of the CNPs show broad spectra (typically with FWHM values of more than 100 nm), and excitation wavelength-dependent spectra with emission peaks between the near-UV region and the blue region but in some cases may show significant emission in the red region, as shown in Figure 15. On the other hand, tables 6 and 7 show the maximum emission and excitation position, respectively, for the different CNPs when excited or detected at a specific wavelength.

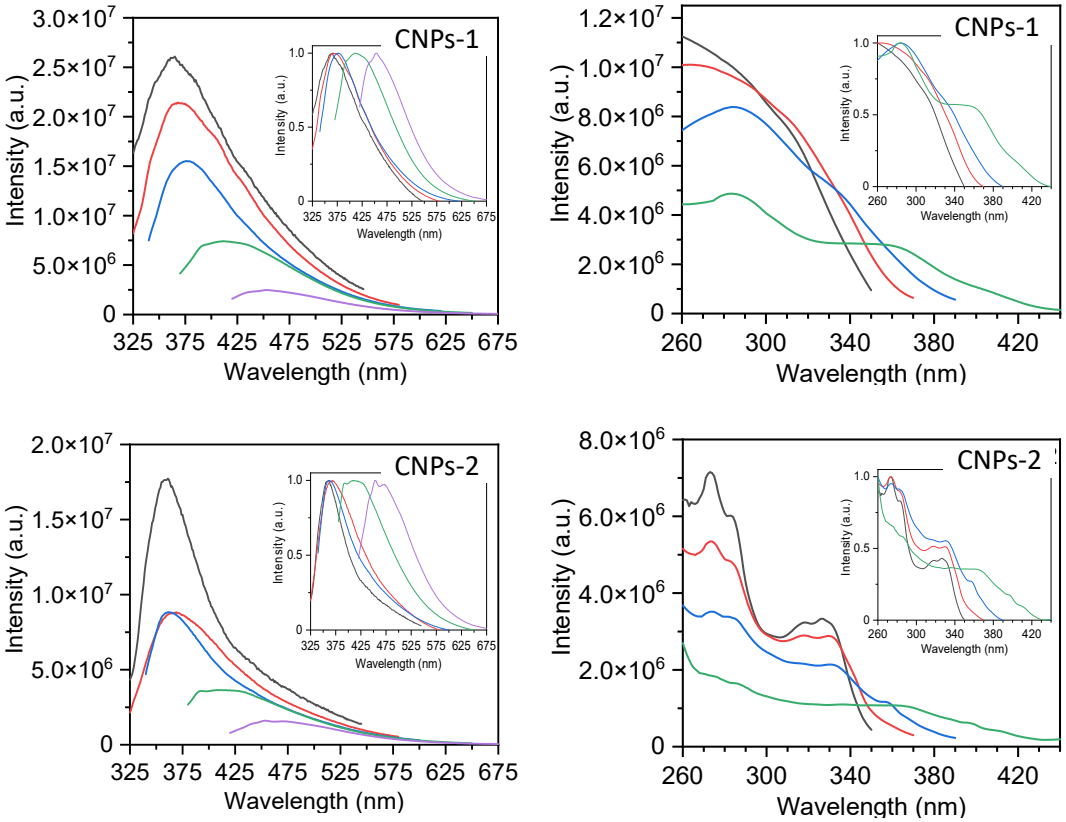

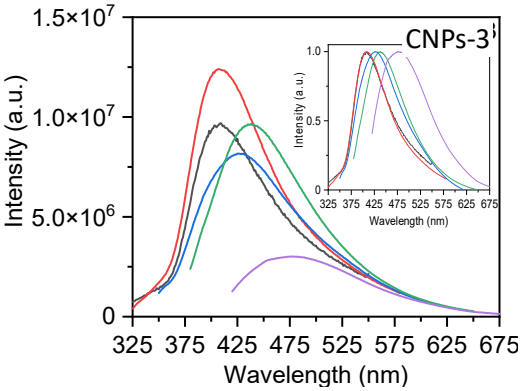
CNPs-3
Intensity (a.u.)
Wavelength (nm)

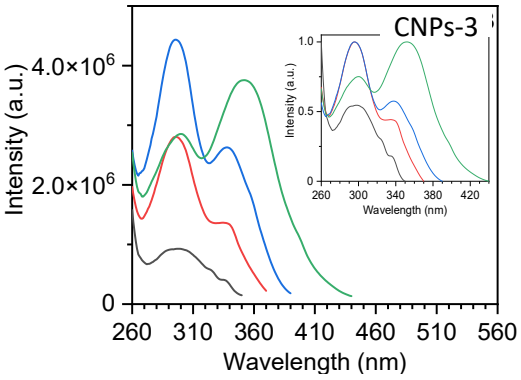
CNPs-3
Intensity (a.u.)
Wavelength (nm)

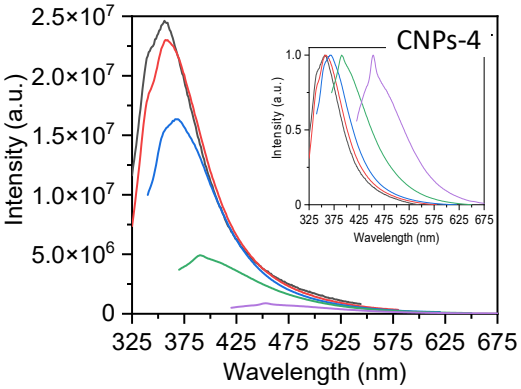
CNPs-4
Intensity (a.u.)
Wavelength (nm)

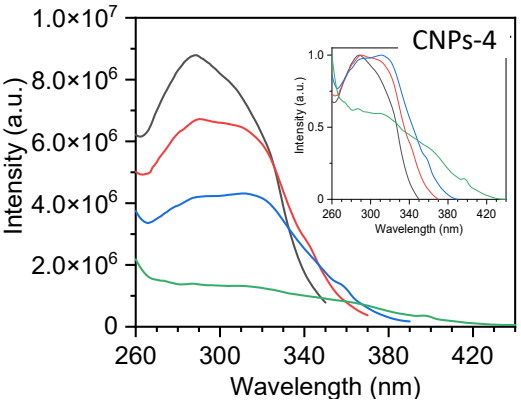
CNPs-4
Intensity (a.u.)
Wavelength (nm)

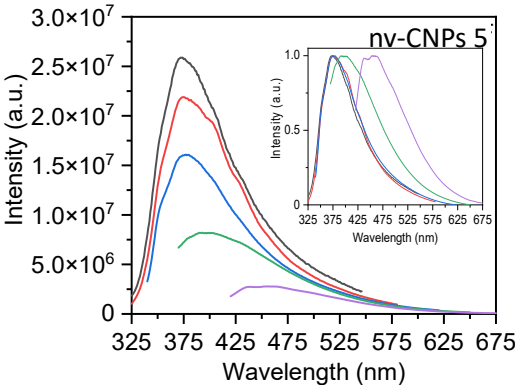
nv-CNPs 5
Intensity (a.u.)
Wavelength (nm)

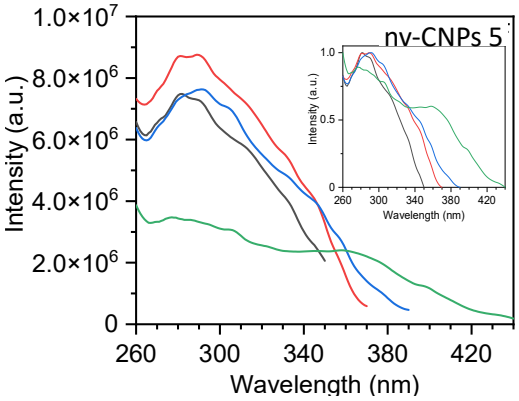
nv-CNPs 5
Intensity (a.u.)
Wavelength (nm)

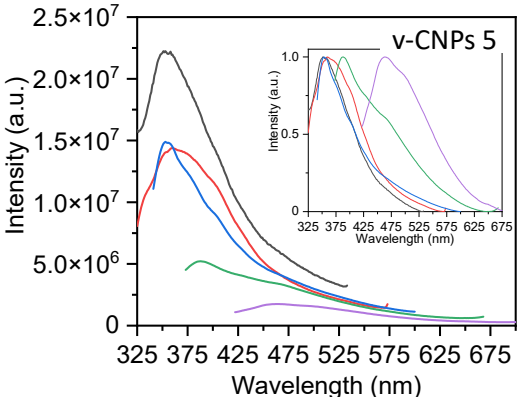
v-CNPs 5
Intensity (a.u.)
Wavelength (nm)

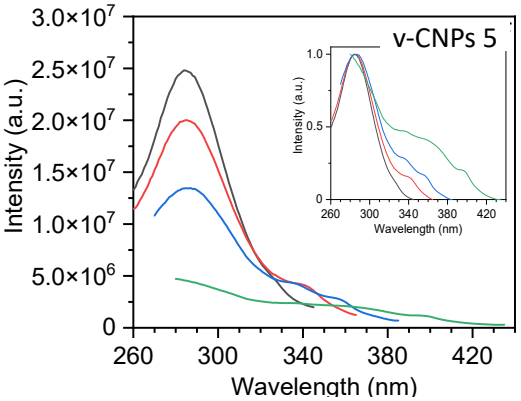
v-CNPs 5
Intensity (a.u.)
Wavelength (nm)

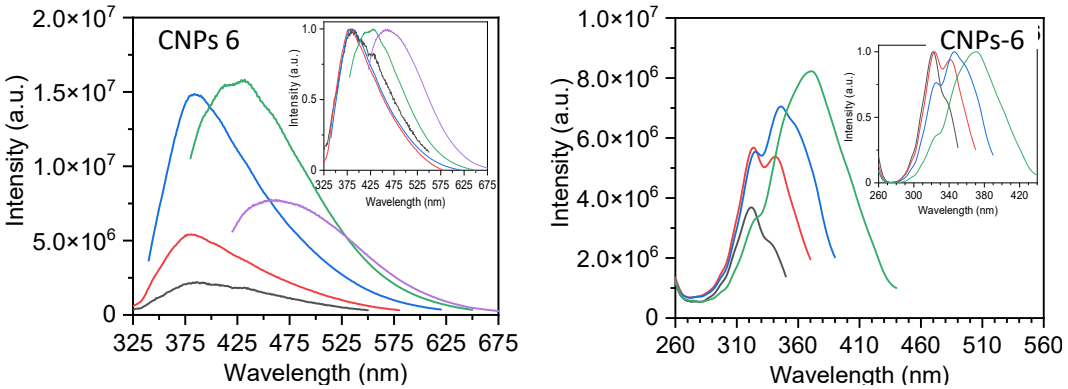

Figure 15. Emission spectra at 280 nm (grey), 300 nm (red), 320 nm (blue), 350 nm (green) and 400 nm (purple) (left column), and excitation spectra at 360 nm (grey), 380 nm (red), 400 nm (blue) and 450 nm (green) (right column) of the different CNPs in 2-propanol.

Table 6. Position of the emission maxima (± 2 nm) of the different CNPs at different excitation wavelength.

Sample	CNPs 1	CNPs 2	CNPs 3	CNPs 4	nv-CNPs 5	v-CNPs 5	CNPs 6
λ_{exc} 280 nm	365	361	409	356	374	353	386
λ_{exc} 300 nm	368	369	407	357	374	360	381
λ_{exc} 320 nm	376	361	427	369	377	353	384
λ_{exc} 350 nm	411	411	438	390	393	388	432
λ_{exc} 400 nm	453	453	477	453	457	463	457

Table 7. Position of the excitation maxima (± 2 nm) of the different CNPs at different emission wavelength.

Sample	CNPs 1	CNPs 2	CNPs 3	CNPs 4	nv- CNPs 5	v- CNPs 5	CNPs 6
λ_{em} 360 nm	<260	273 283 318 326	297 323* 335*	289	282 288*	284	322 336*
λ_{exc} 380 nm	<260	273 282 318 330	296 335*	290	289 281*	285 340*	324 341
λ_{exc} 400 nm	283	273 282 316* 330	296 338	312 293*	291 303*	287 336* 353*	325 346*
λ_{exc} 450 nm	284 339*	272* 285* 336 350 360 395* 407	300 352	287 299* 308* 396*	277 285* 303* 345 358 396*	337* 354* 394*	371 326*

*shoulder positions

Table 8 shows the quantum fluorescence yields of the different CNPs for both 375 and 457 nm excitation wavelengths. In general, low fluorescence yields ranging from 9 to 2 % are obtained for the different CNPs, with values that do not depend on the excitation wavelength used.

Table 8. Values of the quantum fluorescence yield for the different CNPs in 2-propanol (0.05 mg/mL) for λ_{exc} = 375 and 475 nm.

Sample	ϕ_f (λ =375 nm)	ϕ_f (λ =457 nm)
CNPs-1	0.09 ± 0.01	0.08 ± 0.01
CNPs-2	0.09 ± 0.01	0.08 ± 0.01
CNPs-3	0.03 ± 0.01	0.04 ± 0.01
CNPs-4	0.03 ± 0.01	0.02 ± 0.01
nv-CNPs 5	0.02 ± 0.01	0.03 ± 0.01
v-CNPs-5	0.004 ± 0.009	--
CNPs-6	0.05 ± 0.01	0.04 ± 0.01

When fluorescence decays were analyzed, it was observed that tri-exponential fits were usually required, except when using an excitation wavelength of 502 nm, where a biexponential fit was sufficient. Average amplitude lifetimes ranging from 3.4 to 1.5 ns and average intensity lifetimes ranging from 7.5 to 2.2 ns were obtained, which decreased with dependence on the redshift of the excitation wavelength (mainly

because the longest lifetime, τ_1, is visibly shortened as the excitation wavelength increases) (Fig. 16 and Table 9). This shortening of the half-life in intensity and τ_1 also occurs with increasing oxygen concentration, which acts as a photophysical intermolecular deactivation chemical species (Table 10 and 11). The fluorescence lifetime decay could not be obtained for the volatilized fraction of CNPs prepared from naphthalene, due to its low fluorescence yield.

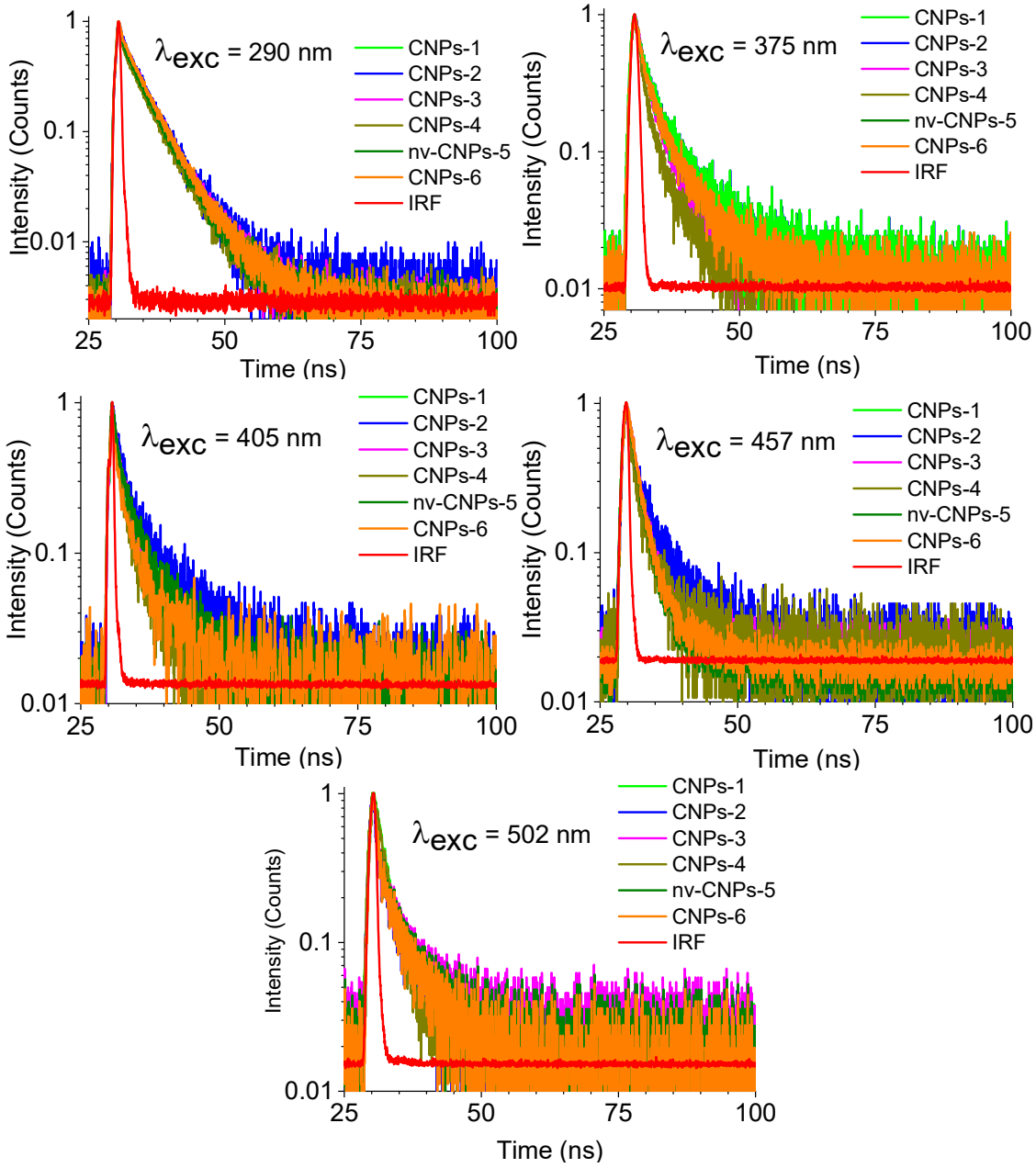

Figure 16. Fluorescence decays under air for the different CNPs (CNPs-1 green, CNPs-2 blue, CNPs-3 magenta, CNPs-4 dark yellow, nv-CNPs-5 Olive, CNPs-6 orange and IRF red) (λ_{exc} = 290, 375, 405, 457, 502 nm).

Table 9. Fluorescence the lifetimes and weighted amplitudes of the excited species, as well as the average lifetimes in intensity and amplitude for the different excitation wavelengths (λ_{exc} = 290, 375, 405, 457, 502 nm) under air for the different CNPs.

Sample	λ_{exc} (nm)	$\boldsymbol{\tau_1}$ (ns)	A_1	$\boldsymbol{\tau_2}$ (ns)	A_2	$\boldsymbol{\tau_3}$ (ns)	A_3	$\boldsymbol{\tau_I}$ (ns)	$\boldsymbol{\tau_A}$ (ns)
CNPs-1	290	15.8 ± 0.6	0.04	4.3 ± 0.1	0.26	1.00 ± 0.05	0.70	6.3	2.4
	375	14.4 ± 0.4	0.05	3.8 ± 0.1	0.28	0.91 ± 0.04	0.67	6.2	2.4
	405	12.5 ± 0.4	0.08	4.3 ± 0.1	0.32	1.30 ± 0.06	0.61	6.1	3.2
	457	10.0 ± 0.5	0.06	3.9 ± 0.2	0.22	1.57 ± 0.06	0.72	4.3	2.6
	502			3.5 ± 0.1	0.21	1.33 ± 0.05	0.79	2.2	1.8
CNPs-2	290	16.2 ± 0.7	0.05	4.1 ± 0.1	0.13	0.99 ± 0.03	0.82	7.5	2.4
	375	15.2 ± 0.5	0.06	3.9 ± 0.1	0.27	0.91 ± 0.05	0.67	7.2	2.6
	405	12.6 ± 0.3	0.09	4.2 ± 0.1	0.35	1.23 ± 0.08	0.56	6.5	3.3
	457	9.5 ± 0.4	0.13	3.6 ± 0.1	0.46	1.2 ± 0.1	0.41	5.4	3.4
	502			4.5 ± 0.4	0.49	1.2 ± 0.3	0.51	3.8	2.8
CNPs-3	290	15.5 ± 0.6	0.05	4.33 ± 0.09	0.48	1.21 ± 0.09	0.47	6.3	3.4
	375	12.2 ± 0.6	0.03	3.33 ± 0.07	0.32	0.84 ± 0.04	0.66	4.3	2.0
	405	10.3 ± 0.4	0.04	3.21 ± 0.05	0.40	1.11 ± 0.04	0.56	3.9	2.3
	457	8.5 ± 0.5	0.05	3.28 ± 0.08	0.42	1.19 ± 0.07	0.53	3.6	2.4
	502			4.3 ± 0.2	0.36	1.1 ± 0.1	0.64	3.3	2.2
CNPs-4	290	15.9 ± 0.7	0.02	4.2 ± 0.2	0.16	0.85 ± 0.02	0.82	5.0	1.7
	375	10.3 ± 0.4	0.04	2.48 ± 0.06	0.21	0.61 ± 0.02	0.75	4.0	1.5
	405	10.0 ± 0.4	0.04	2.93 ± 0.08	0.25	0.91 ± 0.03	0.71	3.8	1.8
	457	9.0 ± 0.6	0.05	3.1 ± 0.1	0.33	1.04 ± 0.07	0.62	3.7	2.1
	502			3.8 ± 0.5	0.33	0.8 ± 0.2	0.67	2.9	1.8
nv-CNPs 5	290	14.2 ± 0.4	0.04	4.31 ± 0.08	0.32	1.37 ± 0.04	0.64	5.4	2.8
	375	9.4 ± 0.3	0.07	2.79 ± 0.07	0.36	0.75 ± 0.04	0.57	4.4	2.1
	405	9.1 ± 0.2	0.09	3.48 ± 0.08	0.38	1.05 ± 0.06	0.53	4.7	2.7
	457	8.3 ± 0.2	0.14	3.6 ± 0.1	0.45	1.2 ± 0.1	0.41	4.9	3.3
	502	6.1 ± 0.2	0.40			1.5 ± 0.2	0.60	4.9	3.3
CNPs-6	290	15.0 ± 0.5	0.04	4.23 ± 0.08	0.37	1.19 ± 0.06	0.59	5.7	2.9
	375	9.4 ± 0.9	0.03	2.82 ± 0.03	0.68	0.66 ± 0.08	0.29	3.4	2.4
	405	9.6 ± 0.5	0.04	2.87 ± 0.07	0.38	0.92 ± 0.05	0.58	3.6	2.0
	457	7.9 ± 0.6	0.09	2.9 ± 0.1	0.38	0.9 ± 0.1	0.53	4.0	2.3
	502	8 ± 2	0.10			1.3 ± 0.4	0.90	4.3	2.0

Table 10. Fluorescence lifetimes and weighted amplitudes of species excited at 375 nm under argon, air and oxygen for the different CNPs.

Sample	$[O_2]$	τ_1 (ns)	A_1	τ_2 (ns)	A_2	τ_3 (ns)	A_3	τ_I (ns)	τ_A (ns)
CNPs-1	0	14.9 ± 0.8	0.05	3.74 ± 0.08	0.17	0.88 ± 0.02	0.78	6.8	2.1
	0.2098	14.4 ± 0.4	0.05	3.8 ± 0.1	0.28	0.91 ± 0.04	0.67	6.2	2.4
	1	13.7 ± 0.8	0.03	3.60 ± 0.08	0.24	0.89 ± 0.02	0.73	4.8	1.9
CNPs-2	0	16.8 ± 0.4	0.05	3.8 ± 0.1	0.18	0.84 ± 0.03	0.78	7.9	2.2
	0.2098	15.2 ± 0.5	0.06	3.9 ± 0.1	0.27	0.91 ± 0.05	0.67	7.2	2.6
	1	13.8 ± 0.8	0.04	3.6 ± 0.1	0.30	0.90 ± 0.02	0.65	5.4	2.2
CNPs-3	0	12.7 ± 0.4	0.04	3.08 ± 0.07	0.32	0.93 ± 0.04	0.64	4.8	2.1
	0.2098	12.2 ± 0.6	0.03	3.33 ± 0.07	0.32	0.84 ± 0.04	0.65	4.3	2.0
	1	11.7 ± 0.7	0.03	3.05 ± 0.07	0.31	0.96 ± 0.03	0.66	3.9	1.9
CNPs-4	0	10.7 ± 0.3	0.04	2.45 ± 0.06	0.16	0.50 ± 0.01	0.80	4.7	1.0
	0.2098	10.3 ± 0.4	0.04	2.48 ± 0.06	0.21	0.61 ± 0.02	0.75	4.2	1.4
	1	8.9 ± 0.5	0.06	2.77 ± 0.08	0.58	0.70 ± 0.02	0.36	3.9	2.4
nv-CNPs 5	0	10.1 ± 0.3	0.06	3.1 ± 0.1	0.19	0.92 ± 0.03	0.75	4.6	1.9
	0.2098	9.4 ± 0.3	0.07	2.79 ± 0.07	0.36	0.75 ± 0.04	0.57	4.4	2.1
	1	8,4 ± 0,5	0,07	3,21 ± 0,08	0,57	0,84 ± 0,02	0,36	4	2,7
CNPs-6	0	10,0 ± 0,3	0,04	3,1 ± 0,1	0,13	0,94 ± 0,03	0,82	3,8	1,6
	0.2098	9,4 ± 0,9	0,03	2,82 ± 0,03	0,68	0,66 ± 0,08	0,29	3,4	2,4
	1	8,7 ± 0,4	0,04	2,69 ± 0,07	0,18	0,95 ± 0,06	0,78	3,2	1,6

Table 11. Fluorescence lifetimes and weighted amplitudes of species excited at 457 nm under argon, air and oxygen for the different CNPs.

Sample	$[O_2]$	τ_1 (ns)	A_1	τ_2 (ns)	A_2	τ_3 (ns)	A_3	τ_I (ns)	τ_A (ns)
CNPs-1	0	11.3 ± 0.2	0.08	3.88 ± 0.08	0.39	1.07 ± 0.06	0.53	5.6	3.0
	0.2098	10.0 ± 0.5	0.06	3.9 ± 0.2	0.22	1.57 ± 0.06	0.72	4.3	2.6
	1	9.6 ± 0.3	0.02	3.85 ± 0.06	0.24	0.93 ± 0.02	0.73	3.4	1.8
CNPs-2	0	10.6 ± 0.2	0.10	3.43 ± 0.07	0.38	0.95 ± 0.05	0.52	5.7	2.9
	0.2098	9.5 ± 0.4	0.13	3.6 ± 0.1	0.46	1.2 ± 0.1	0.41	5.4	3.4
	1	9.0 ± 0.2	0.04	3.50 ± 0.05	0.30	0.96 ± 0.03	0.65	3.7	2.0
CNPs-3	0	9.1 ± 0.2	0.05	3.26 ± 0.06	0.33	0.82 ± 0.03	0.62	4.0	2.0
	0.2098	8.5 ± 0.5	0.05	3.28 ± 0.08	0.42	1.19 ± 0.07	0.53	3.6	2.4
	1	7.7 ± 0.2	0.03	3.03 ± 0.04	0.31	0.82 ± 0.02	0.66	3.0	1.7
CNPs-4	0	9.4 ± 0.6	0.05	3.2 ± 0.2	0.62	0.8 ± 0.2	0.33	4.0	2.7
	0.2098	9.0 ± 0.6	0.05	3.1 ± 0.1	0.62	1.04 ± 0.07	0.33	3.8	2.7
	1	8.0 ± 0.4	0.05	3.0 ± 0.1	0.58	0.9 ± 0.2	0.37	3.5	2.5
nv-CNPs 5	0	9.7 ± 0.3	0.17	4.6 ± 0.2	0.56	1.6 ± 0.4	0.27	6.1	4.7
	0.2098	8.3 ± 0.2	0.14	3.6 ± 0.1	0.45	1.2 ± 0.1	0.41	4.9	3.3
	1	7.2 ± 0.2	0.17	3.4 ± 0.1	0.57	1.1 ± 0.4	0.25	4.6	3.4
CNPs-6	0	8.3 ± 0.2	0.08	3.00 ± 0.08	0.21	0.81 ± 0.02	0.71	4.2	1.9
	0.2098	7.9 ± 0.6	0.09	2.9 ± 0.1	0.38	0.9 ± 0.1	0.53	4.0	2.3
	1	7.2 ± 0.2	0.04	2.60 ± 0.05	0.26	0.72 ± 0.02	0.70	2.9	1.5

The radiant constant of the excited singlet states can be determined according to equation 7 for samples for which the quantum fluorescence performance and the fluorescence lifetime have been determined using the same excitation wavelength.

$$\Phi_{em}^{s} = \boldsymbol{k_r^s}\, \boldsymbol{\tau_{em}^s} \quad \text{eq. 7}$$

Table 12. Values of the radiant constant of the excited singlet state for the different CNPs with excitation wavelengths of 375 and 457 nm.

Sample	$\boldsymbol{k_r^s}$ (s^{-1}) (λ =375 nm)	$\boldsymbol{k_r^s}$ (s^{-1}) (λ =457 nm)
CNPs-1	$1.45\ 10^7$	$1.16\ 10^7$
CNPs-2	$1.25\ 10^7$	$1.11\ 10^7$
CNPs-3	$6.98\ 10^6$	$1.11\ 10^7$
CNPs-4	$7.5\ 10^6$	$5.40\ 10^6$
nv-CNPs 5	$4.54\ 10^6$	$6.12\ 10^6$
CNPs-6	$1.47\ 10^7$	$1.0\ 10^7$

The oxygen deactivation constant of the excited singlet states can be determined from the Stern-Volmer equation by measuring fluorescence intensity (eq. 8) or fluorescence lifetime (eq. 9) at different oxygen concentrations (Table 13).

$$\frac{I_0}{I} = 1 + k_q\, I_0\, [Q] \quad \text{eq. 8} \qquad \frac{\tau_0}{\tau} = 1 + k_q\, \tau_0\, [Q] \quad \text{eq. 9}$$

Table 13. Values of the singlet deactivation constant when using an excitation wavelength of 375 and 457 nm from the longest lifetime (τ_1), from the average time in current (τ_I) and from the emission current (Int).

	λ_{exc} = 375 nm			λ_{exc} = 457 nm		
Sample	k_q^s (s^{-1}) As of τ_1	k_q^s (s^{-1}) As of τ_I	k_q^s (s^{-1}) As of Int	k_q^s (s^{-1}) As of τ_1	k_q^s (s^{-1}) As of τ_I	k_q^s (s^{-1}) As of Int
CNPs-1	$5.5\ 10^6$	$6.1\ 10^7$	$2.6\ 10^8$	$1.9\ 10^7$	$1.1\ 10^8$	$5.2\ 10^8$
CNPs-2	$1.4\ 10^7$	$5.9\ 10^7$	$2.4\ 10^8$	$1.6\ 10^7$	$9.8\ 10^7$	$5.2\ 10^8$
CNPs-3	$7.3\ 10^6$	$5.4\ 10^7$	$2.7\ 10^8$	$3.4\ 10^7$	$8.0\ 10^7$	$6.8\ 10^8$
CNPs-4	$1.9\ 10^7$	$4.2\ 10^7$	$2.7\ 10^8$	$1.8\ 10^7$	$3.4\ 10^7$	$9.9\ 10^7$
nv-CNPs 5	$1.9\ 10^7$	$3.1\ 10^7$	$2.3\ 10^8$	$3.4\ 10^7$	$5.9\ 10^7$	$1.1\ 10^8$
CNPs-6	$1.5\ 10^7$	$4.6\ 10^7$	$5.6\ 10^8$	$1.8\ 10^7$	$1.1\ 10^8$	$4.4\ 10^8$

For these CNPs, the quantum yield of singlet oxygen production was also determined. Figure 17, and Table 14 shows the lifetimes of singlet oxygen phosphorescence and the quantum yield of singlet oxygen production for the different CNPSs, both for an excitation wavelength of 355 and 473 nm. The luminescence observed is assigned to $^1O_2$ because the transient is completely quenched in presence of sodium azide (NaN_3, a well-known $^1O_2$ quencher; 25 mM).

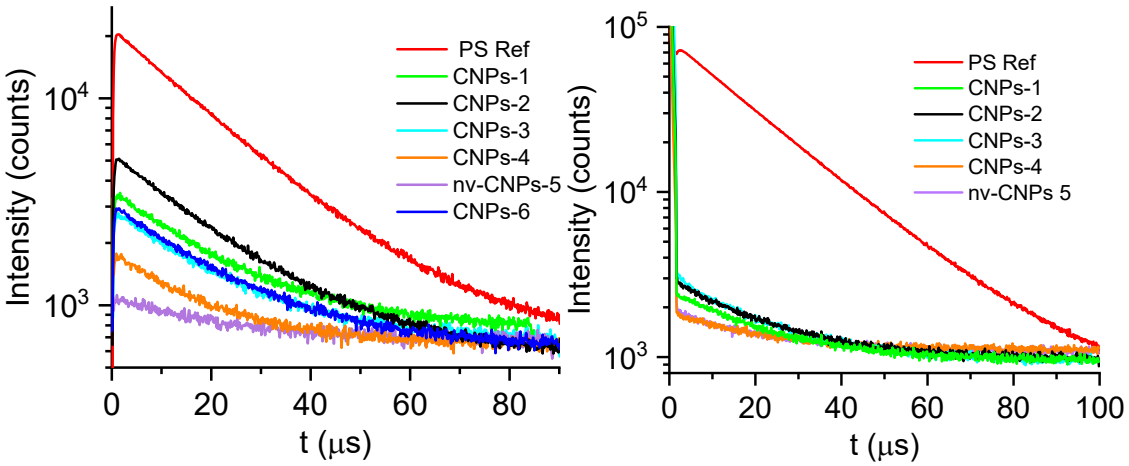

Figure 17. Singlet oxygen phosphorescence kinetics at 1275 nm in i-PrOH of CNPs and reference photosensitizers (PS Ref). Phenalen-1-one and Rose Bengal were used as references for excitation wavelength of 355 nm a), and 473 nm b), respectively.

Table 14. Values of lifetime values of singlet oxygen phosphorescence as well as quantum yields of singlet oxygen production for the different CNPs, both for an excitation wavelength of 355 and 473 nm.

	λ_{exc} = 355 nm		λ_{exc} = 473 nm	
Sample	τ_Δ (μs)	ϕ_Δ	τ_Δ (μs)	ϕ_Δ
CNPs-1	19.3	0.35	18.68	0.02
CNPs-2	19.6	0.37	20.14	0.04
CNPs-3	20.3	0.24	19.96	0.04
CNPs-4	19.7	0.09	8.77	0.01
nv-CNPs 5	~ 5	0.04	20.13	0.01
CNPs-6	17.1	0.28	---	---
Phenalen-1-one	19.93	1.00	---	---
Rose Bengal	---	---	20.41	0.75

To obtain the lifetime of the excited triplet state in the absence of oxygen, a flash photolysis experiment is required. These lifetimes of the excited triplet state are shown in Figure 18 and Table 15.

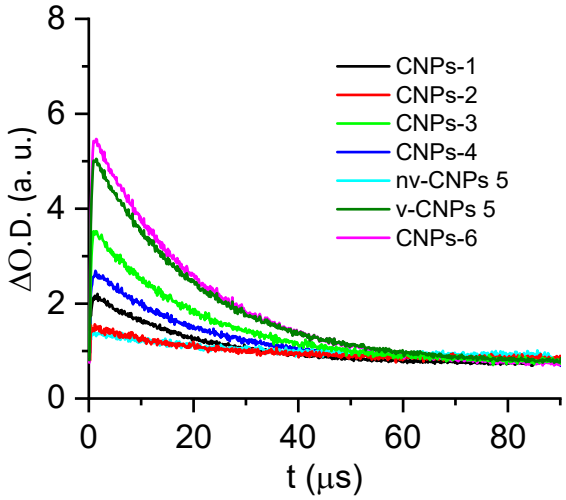

Figure 18. Transient absorption of the triplet excited-state of CNPs in Ar-purged deuterated PBS. (λ_{exc} = 355 nm, λ_{obs} = 600 nm).

Table 15. Lifetime values of the triplet state excited at 355 nm and a Xe lamp in right angle geometry, observing at 600 nm and under argon.

Sample	τ (μs)
CNPs-1	15.3 ± 0.5
CNPs-2	5.00 ± 0.05
CNPs-3	21.4 ± 0.8
CNPs-4	17.4 ± 0.3
nv-CNPs 5	3.8 ± 0.2
v-CNPs 5	29.4 ± 0.8
CNDs-6	30.6 ± 0.6

4.2.4. Conclusions

A novel method for the preparation of CNPs has been studied using a pulsed Nd-YAG laser and a bottom-up approach from different aromatic organic precursors. This method has shown great potential in terms of reproducibility of the products obtained and the great versatility of the precursors that can be used, as well as the modulable reaction conditions. In order to understand the mechanism of CNPs formation, a small-scale setup was used to obtain experimental evidence that the reaction follows a zero reaction order and that there is a possible catalytic role for the laser impact surface.

The batch of CNPs obtained was structurally characterized by a wide range of techniques; thanks to atomic force microscopy the CNPs could be observed in isolation and not forming aggregates, revealing average sizes between 1 and 11 nm. Electron microscopy has not been able to observe the CNPs in isolation, but it has been possible to observe that two different families of CNPs are formed, those with graphitic structures of the nano-onion like fragments type and those with amorphous structures. Interestingly, the characterization by EELS and Raman shows that, starting from

precursors with a majority, or even total, Csp^2 content, CNPs are formed with a Csp^3 content of between 30 - 60 %. It is also evident that the use of precursors with heteroatoms such as N and Cl can favour the production yield of CNPs, but no significant amount of these heteroatoms remains in the CNPs. Finally, at the structural level, infrared spectroscopy was also used to determine the functional groups present on the surface of these nanoparticles, where in general, methyl, -OH, -C=O groups are mainly observed.

Regarding the photophysical properties observed in the CNPs produced, it should be noted that they all show a very similar light absorption with a strong absorption of light in the UV region with a long tail extending towards the visible, even with remarkable absorptions in the red region of the visible spectrum. All CNPs also show broad excitation wavelength-dependent emission spectra that shift towards the red with increasing excitation wavelength. The fluorescence quantum yields were also determined to be always less than 10 %, which is in agreement with the low fluorescence quantum yields reported in the literature for these systems. It was also observed that all the CNPs produced are capable of producing singlet oxygen at room temperature, in solution with UV-Vis excitation with yields as high as 37%. The photophysical characterization was completed with the determination of the fluorescence lifetimes at room temperature under different excitation wavelengths and under different oxygen concentration, which allows estimating the different deactivation constants of the excited singlet state.

References

1. a) J. Ren, L. Stagi, P. Innocenzi, *Prog. Solid. State Ch*. **2021**, *62*, 100295; b) Z. Kang, S. T. Lee, *Nanoscale* **2019**, *11*, 19214; c) M. J. Molaei, *Talanta* **2019**, *196*, 456; d) T. J. Bandosz, C. O. Ania, *Adv. Sci.* **2018**, *5*, 1800293; e) R. Das, R. Bandyopadhyay, P. Pramanik, *Mater. Today Chem*. **2018**, *8*, 96; f) Z. Peng, X. Han, S. Li, A. O. Al-Youbi, A. S. Bashammakh, M. S. El-Shahawi, R. M. Leblanc, *Coord. Chem. Rev*. **2017**, *343*, 256; g) S. Y. Lim, W. Shen, Z. Gao, *Chem. Soc. Rev*. **2015**, *44*, 362; h) S. Zhu, Y. Song, X. Zhao, J. Shao, J. Zhang, B. Yang, *Nano Res*. **2015**, *8*, 355; i) Y. Wang, A. Hu, *J. Mater. Chem C* **2014**, *2*, 6921.

2. a) R. Garriga, T. Herrero-Continente, M. Palos, V. L. Cebolla, J. Osada, E. Muñoz, M. J. Rodríguez-Yoldi, *Nanomaterials* **2020**, *10*, 1617; b) D. Jović, V. Jaćević, K. Kuča, I. Borišev, J. Mrdjanovic, D. Petrovic, M. Seke, A. Djordjevic, *Nanomaterials* **2020**, *10*, 1508; c) K. S. Khashan, F. A. Abdulameer, M. S. Jabir, A. A. Hadi, G. M. Sulaiman, *Adv. Nat. Sci. Nanosci. Nanotechnol.* **2020**, *11*, 035010; d) P. Xie, S. T. Yang, Y. Huang, C. Zeng, Q. Xin, G. Zeng, S. Yang, P. Xia, X. Tang, K. Tang, *ACS Appl. Mater. Interfaces* **2020**, *12*, 29094; e) H. Pandey, S. Saini, S. P. Singh, N. K. Gautam, S. Singh, *Comp. Biochem. Physiol. C-Toxicol. Pharmacol.* **2020**, *228*, 108646; f) H. Belkahla, R. Boudjemaa, V. Caorsi, D. Pineau, A. Curcio, J. S. Lomas, P. Decorse, A. Chevillot-Biraud, T. Azaïs, C. Wilhelm, H. Randriamahazaka, M. Hémadi, *Nanoscale Adv*., **2019**, *1*, 2571; g) I. S. Raja, S. J. Song, M. S. Kang, Y. B. Lee, B. Kim, S. W. Hong, S. J. Jeong, J. C. Lee, D. W. Han, *Nanomaterials* **2019**, *9*, 1214; h) Y. Liu, H. Jiang, C. Liu, Y. Ge, L. Wang, B. Zhang, H. He, S. Liu, *Atmos. Chem. Phys.* **2019**, *19*, 8175; i) R. Madannejad, N. Shoaie, F. Jahanpeyma, M. H. Darvishi, M. Azimzadeh, H. Javadi, *Chem. Biol. Interact*. **2019**, *307*, 206; j) M. Havrdova, K. Hola, J. Skopalik, K. Tomankova, M. Petr, K. Cepe, K. Polakova, J. Tucek, A. B. Bourlinos, R. Zboril *Carbon* **2016**, *99*, 238, k) S. T. Yang, X. Wang, H. Wang, F. Lu, P. G. Luo, L. Cao, M. J. Meziani, Ji. H. Liu, Y. Liu, M. Chen, Y. Huang, Y. P. Sun, *J. Phys. Chem. C* **2009,** *113,* 18110.

3. a) R. Singh, S. Akhil, V. G. Vasavi Dutt, N. Mishra, *Nanoscale Adv*. **2021**, *3*, 6984; b) A. Molkenova, A. Toleshova, S. J. Song, M. S. Kang, A. Abduraimova, D. W. Han, T. Sh. Atabaev, *Mater. Lett*. **2020**, *261*, 127012; c) Y. Zheng, J. Zheng, J. Wang, Y. Yang, T. Lu, X. Liu, *Nanomaterials* **2020**, *10*, 303; d) Q. Zhang, S. Deng, J. Liu, X. Zhong, J. He, X. Chen, B. Feng, Y. Chen, K. Ostrikov, *Adv. Funct. Mater*. **2019**, *29*, 1805860; e) M. Sun, C. Liang, Z. Tian, E. V. Ushakova, D. Li, G. Xing, S. Qu, A. L. Rogach, *J. Phys. Chem. Lett*. **2019**, *10*, 3094; f) Z. Gan, L. Liu, L. Wang, G. Luo, C. Moc, C. Chang, *Phys. Chem. Chem. Phys*. **2018**, *20*, 18089; g) B. Ju, Y. Wang, Y. M. Zhang, T. Zhang, Z. Liu, M. Li, S. X. A. Zhang, *ACS Appl. Mater. Interfaces* **2018**, *10*, 13040; h) Z. Wang, F. Yuan, X. Li, Y. Li, H. Zhong, L. Fan, S. Yang, *Adv. Mater*. **2017**, *29*, 1702910; i) J. Shao, S. Zhu, H. Liu, Y. Song, S. Tao, B. Yang, *Adv. Sci.* **2017**, *4*, 1700395; j) K. Jiang, J. Wu, Q. Wu, X. Wang, C. Wang, Y. Li, *Part. Part. Syst. Charact*. **2017**, *34*, 1600197; k) J. Yang, G. Gao, X. Zhang, Y. H. Ma, H. R. Jia, Y. W. Jiang, Z. Wang, F. G. Wu, *Nanoscale*, **2017**, *9*, 15441; l) J. Zhao, C. Liu, Y. Li, J. Liang, J. Liu, T. Qian, J. Ding, Y. C. Cao, *Luminescence* **2017**, *32*, 625; m) R. Mahajan, A. S. Bhadwal, N. Kumar, M. Madhusudanan, R. Namdeo, P. R. M. Tripathi, *IET Nanobiotechnol*. **2017**, *11*, 360; n) W. Wang, C. Damm, J. Walter, T. J. Nacken, W. Peukert, *Phys. Chem. Chem. Phys*. **2016**, *18*, 466; o) B. Wang, W. Tang, H. Lu, Z. Huang, *J. Mater Sci*. **2015**, *50*, 5411; p) Z. Q. Xu, L. Y. Yang, X. Y. Fan, J. C. Jin, J. Mei, W. Peng, F. L. Jiang, Q. Xiao, Y. Liu, Carbon

2014, *66*, 351; q) Q. Liu, B. Guo, Z. Rao, B. Zhang, J. R. Gong, *Nano Lett*. **2013**, *13*, 2436; r) X. Yan, X. Cui, L. Li, *J. Am. Chem. Soc*. **2010**, *132*, 5944.

4. a) F. Arcudi, L. Đorđević, S. Rebeccani, M. Cacioppo, A. Zanut, G. Valenti, F. Paolucci, M. Prato, *Adv. Sci.* **2021**, *8*, 2100125; b) S. Nayak, P. Das, *ACS Omega* **2021**, *6*, 21425; c) Y. Ou, G. Zhu, F. Rao, J. Gao, J. Chang, X. Xie, W. Zhang, Y. Huang, M. Hojamberdiev, *ACS Appl. Nano Mater*. **2021**, *4*, 7330; d) X. Gu, Z. Chen, Y. Li, J. Wu, X. Wang, H. Huang, Y. Liu, B. Dong, M. Shao, Z. Kang, *ACS Appl. Mater. Interfaces* **2021**, *13*, 24814; e) C. Xu, W. Zhang, R. Wang, S. Tan, J. M. Holub, B. Tang, *Anal. Chem*. **2021**, *93*, 9111; f) J. Yu, C. Zhang, Y. Yang, T. Su, G. Yi, X. Zhang, *Appl .Surf. Sci*. **2021**, *551*, 149476; g) I. Martins, H. Tomás, F. Lahoz, J. Rodrigues, *Biomacromolecules* **2021**, *22*, 2436; h) A. Babusenan, B. Pandey, S. C. Roy, J. Bhattacharyya, *Carbon* **2020**, *161*, 535; i) A. Ferrer-Ruiz, T. Scharl, P. Haines, L. Rodríguez-Pérez, A. Cadranel, M. A. Herranz, D. M. Guldi, N. Martín, *Angew. Chem. Int. Ed*. **2018**, *57*, 1001; j) C. Rao, S. Khan, N. C. Verma, C. K. Nandi, *ChemBioChem* **2017**, *18*, 2385.

5. a) J. Bai, G. Yuan, X. Chen, L. Zhang, Y. Zhu, X. Wang, L. Ren, *Adv. Sci.*, DOI: 10.1002/advs.202104278; b) R. Jelinek, *Carbon Quantum Dots: Synthesis. Properties and Applications*, (Carbon Nanostructures, Series Ed: P. Araujo), Springer International Publishing, Cham, Switzerland **2017**; c) A. A. Kokorina, E. S. Prikhozhdenko, G. B. Sukhorukov, A. V. Sapelkin, I. Yu. Goryacheva, *Russ. Chem. Rev*. **2017**, *86*, 1157; d) Z. Jin, P. Owour, S. Lei, L. Ge, *Curr. Opin. Colloid Interface Sci*. **2015**, *20*, 439; e) L. Lin, M. Rong, F. Luo, D. Chen, Y. Wang, X. Chen, *Trends Anal. Chem*. **2014**, *54*, 83; f) L. Wang, S. J. Zhu, H. Y. Wang, Y. F. Wang, Y. W. Hao, J. H. Zhang, Q. D. Chen, Y. L. Zhang, W. Han, B. Yang, H. B. Sun*, Adv. Opt. Mater.* **2013**, *1*, 264.

6. a) K. J. Mintz, Y. Zhou, R. M. Leblanc, *Nanoscale* **2019**, *11*, 4634; b) S. Zhu, Y. Song, X. Zhao, J. Shao, J. Zhang, B. Yang, *Nano Res*. **2015**, *8*, 355.

7. a) T. E. Kim, H. J. Jang, S. W. Park, J. Wei, S. Cho, W. I. Park, B. R. Lee, C. D. Yang, Y. K. Jung, *ACS Appl. Bio Mater*. **2021**, *4*, 3453; b) C. L. Shen, Q. Lou, J. H. Zang, K. K. Liu, S. N. Qu, L. Dong, C. X. Shan, *Adv. Sci.* **2020**, *7*, 1903525; c) K. K. Liu, S. Y. Song, L. Z. Sui, S. X. Wu, P. T. Jing, R. Q. Wang, Q. Y. Li, G. R. Wu, Z. Z. Zhang, K. J. Yuan, C. X. Shan, *Adv. Sci.* **2019**, *6*, 1900766; d) S. Ghosh, K. Ghosal, S. A. Mohammad, K. Sarkar, *Chem. Eng. J*. **2019**, *373*, 468; e) M. Hassan, V. G. Gomes, A. Dehghani, S. M. Ardekani, *Nano Res*. **2018**, *11*, 1; f) H. Kim, Y. Park, S. Beack, S. Han, D. Jung, H. J. Cha, W. Kwon, S. K. Hahn, *Adv. Sci.* **2017**, *4*, 1700325; g) J. Zhou, W. Deng, Y. Wang, X. Cao, J. Chen, Q. Wang,W. Xu, Pan Du, Q. Yu, J. Chen, M. Spector, J. Yu, X. Xu, *Acta Biomater*. **2016**, *42*, 209; h) K. Hola, Y. Zhang, Y. Wang, E. P. Giannelis, R. Zboril, A. L. Rogach, *Nano Today* **2014**, *9*, 590.

8. a) P. C. Yeh, S. Yoon, D. Kurniawan, Y. G. Chung, W. H. Chiang, *ACS Appl. Nano Mater*. **2021**, *4*, 5636; b) E. Asadian, M. Ghalkhani, S. Shahrokhian, *Sens. Actuators B Chem*. **2019**, *293*, 183; c) M. Li, T. Chen, J. J. Gooding, J. Liu, *ACS Sens*. **2019**, *4*, 1732; d) X. Gao, C. Du, Z. Zhuang W. Chen, *J. Mater. Chem. C* **2016**, *4*, 6927; e) Y. Guo, L. Zhang, S. Zhang, Y. Yang, X. Chen, M. Zhang, *Biosens. Bioelectron*. **2015**, *63*, 61.

9. a) E. Zhang, X. Jia, B. Wang, J. Wang, X. Yu, B. Lu, *Adv. Sci.* **2020**, *7*, 2000470; b) M. J. Molaei, *Solar Energy* **2020**, *196*, 549; b) X. Xu, W. Tang, Y. Zhou, Z. Bao, Y. Su, J. Hu, H. Zeng, *Adv. Sci*. **2017**, *4*, 1700273; c) K. A. Shiral Fernando, S. Sahu, Y. Liu, W. K. Lewis,

E. A. Guliants, A. Jafariyan, P. Wang, C. E. Bunker, Y. P. Sun, *ACS Appl. Mater. Interfaces* **2015**, *7*, 8363.

10. a) B. Zhao, Z. Tan, *Adv. Sci.* **2021**, *8*, 2001977; b) H. Jia, Z. Wang, T. Yuan, F. Yuan, X. Li, Y. Li, Z. Tan, L. Fan, S. Yang, *Adv. Sci*. **2019**, *6*, 1900397; c) E. Liu, D. Li, X. Zhou, G. Zhou, H. Xiao, D. Zhou, P. Tian, R. Guo, S. Qu, *ACS Sustainable Chem. Eng*. **2019**, *7*, 9301; d) Y. Zhang, P. Zhuo, H. Yin, Y. Fan, J. Zhang, X. Liu, Z. Chen, *ACS Appl. Mater. Interfaces* **2019**, *11*, 24395; e) Z. Zhou, P. Tian, X. Liu, S. Mei, D. Zhou, D. Li, P. Jing, W. Zhang, R. Guo, S. Qu, A. L. Rogach, *Adv. Sci.* **2018**, *5*, 1800369.

11. a) H. He, L. Liu, X. Chen, Q. Wang, X. Wang, W. M. Nau, F. Huang, *Anal. Chem*. **2021**, *93*, 3968; b) Q. Wang, Z. Feng, H. He, X. Hu, J. Mao, X. Chen, L. Liu, X. Wei, D. Liu, S. Bi, X. Wang, B. Ge, D. Yua, F. Huang, *Chem. Commun*. **2021**, *57*, 5554.

12. a) J. Ahn, S. Pak, Y. Song, H. Kim, *Carbohydr. Polym*. **2021**, *255*, 117387; b) U. A. Rani, L. Y. Ng, C. Y. Ng, E. Mahmoudi, *Adv. Colloid. Interface Sci*. **2020**, *278*, 102124.

13. a) R. M. Yadav, Z. Li, T. Zhang, O. Sahin, S. Roy, G. Gao, H. Guo, R Vajtai, L. Wang, P. M. Ajayan, J. Wu, *Adv. Mater.*, DOI: 10.1002/adma.202105690; b) D. E. Lee, D. J. Kim, S. Moru, M. G. Kim, W. K. Jo, S. Tonda, *Appl. Surf. Sci*. **2021**, *563*, 150292.

14. a) C. Testa, A. Zammataro, A. Pappalardo, G. Trusso Sfrazzetto, *RSC Adv*. **2019**, *9*, 27659; b) R. Wang, K. Q. Lu, Z. R. Tang, Y. J. Xu, *J. Mater. Chem. A*, **2017**, *5*, 3717; c) C. Han, N. Zhang, Y. J. Xua, *Nano Today* **2016**, *11*, 351.

15. a) Y. Ding, X. Wang, M. Tang, H. Qiu, *Adv. Sci.*, DOI: 10.1002/advs.202103833; b) Y. C. Liang, K. K. Liu, X. Y. Wu, Q. Lou, L. Z. Sui, L. Dong, K.J. Yuan, C. X Shan, *Adv. Sci.* **2021**, *8*, 2003433; c) C. L. Shen, Q. Lou, C. F. Lv, J. H. Zang, S. N. Qu, L. Dong, C. X. Shan, *Adv. Sci.* **2019**, *6*, 1802331; d) Z. Tian, D. Li, E. V. Ushakova, V. G. Maslov, D. Zhou, P. Jing, D. Shen, S. Qu, A. L. Rogach, *Adv. Sci.* **2018**, *5*, 1800795.

16. a) J. H. Park, Y. J. Oh, D. Y. Park, J. Lee, J. S. Park, C. R. Park, J. H. Kim, T. Kim, S. J. Yang, *Adv. Sci.* **2021**, *8*, 2102718; b) Q. Li, Z. Zhang, L. Qi, Q. Liao, Z. Kang, Y. Zhang, *Adv. Sci.* **2019**, *6*, 1801057.

17. C. Xia, S. Zhu, T. Feng, M. Yang, B. Yang, *Adv. Sci.* **2019**, *6*, 1901316.

18. F. Niu, Y. Xu, M. Liu, J. Sun, P. Guo, J. Liu, *Nanoscale* **2016**, *8*, 5470.

19. a) Z. Qiu, A. Narita, K. Mullen, *Faraday Discuss*. **2021**, *227*, 8; b) X. Y. Wang, J. I. Urgel, G. Borin Barin, K. Eimre, M. Di Giovannantonio, A. Milani, M. Tommasini, C. A. Pignedoli, P. Ruffieux, X. Feng, R. Fasel, K. Müllen, A. Narita, *J. Am. Chem. Soc.* **2018**, 140, 9104; c) S. Wang, N. Kharche, E. Costa Girão, X. Feng, K. Müllen, V. Meunier, R. Fasel, P. Ruffieux, *Nano Lett*. **2017**, *17*, 4277; d) A. Narita, X. Feng, K. Müllen, *Chem. Rec*. **2015**, *15*, 295; e) S. Yang, R. E. Bachman, X. Feng, K. Müllen, *Acc. Chem. Res*. **2013**, *46*, 116; f) R. Liu, D. Wu, X. Feng, K. Müllen, *J. Am. Chem. Soc*. **2011**, *133*, 15221; g) S. Yang, X. Feng, L. Zhi, Q. Cao, J. Maier, K. Müllen, *Adv. Mater*. **2010**, *22*, 838; h) J. Cai, P. Ruffieux, R Jaafar, M. Bieri, T. Braun, S. Blankenburg, M. Muoth, A. P. Seitsonen, M. Saleh, X. Feng, K. Müllen, R. Fasel, *Nature* **2010**, *466*, 470; i) L. Zhi, K. Müllen, *J. Mater. Chem*. **2008**, *18*, 1472.

20. a) M.J. Yang, J. X. Shi, Y. Yin, C. G. Shi, *Phys. Status Solidi B* **2021**, *258*, 2100110; b) L. Zhi, C. Jimin, L. Dongfang, Z. Chenyu, *Infrared Laser Eng*. **2020**, *49*, 20200298; c) K. S. Khashan, F. A. Abdulameer, M. S. Jabir, A. A. Hadi, G. M. Sulaiman, *Adv. Nat. Sci.: Nanosci. Nanotechnol*. **2020**, *11*, 035010; d) A. I. Sidorov, V. F. Lebedev, A. A. Kobranova, A. V. Nashchekin, *Quantum Electron.* **2018**, *48*, 45; e) T. Okamoto, E. Miyasaka, K. Mitamura, K. Matsukawa, T. Yatsuhashi, *J. Photochem. Photobiol. A-Chem*. **2017**, *344*, 178; f) H. P. S. Castro, V. S. Souza, J. D. Scholten, J. H. Dias, J. A. Fernandes, F. S. Rodembusch, R. dos Reis, J. Dupont, S. R. Teixeira, R. R. B. Correia, *Chem. Eur. J.* **2016**, *22*, 138; g) X. Li, H. Wang, Y. Shimizu, A. Pyatenko, K. Kawaguchi, N. Koshizaki, *Chem. Commun*. **2011**, *47*, 932; h) S. L. Hu, K. Y. Niu, J. Sun, J. Yang, N. Q Zhao, X. W. Du, *J. Mater. Chem*. **2009**, *19*, 484; i) Y. P. Sun, X. Wang, F. Lu, L. Cao, M. J. Meziani, P. G. Luo, L. Gu, L. Monica Veca, *J. Phys. Chem. C* **2008***, 112,* 18295; j) Y. P Sun, B. Zhou, Y. Lin, W. Wang, K. A. Shiral Fernando, P. Pathak, M. J. Meziani, B. A. Harruff, X Wang, H Wang, P. G. Luo, H. Yang, M. E. Kose, B. Chen, L. Monica Veca, S. Y. Xie, *J. Am. Chem. Soc*. **2006**, *128*, 7756.

21. a) D. Zhang, B. Gökce, S. Barcikowski , *Chem. Rev*. **2017**, *117*, 3990; b) D. Tan, K. N. Sharafudeen, Y. Yue, J. Qiu, *Progr. Mater. Sci*. **2016**, *76*, 154; c) K. Habiba, V. I. Makarov, B. R. Weiner, G. Morell, in *Manufacturing Nanostructures* (Eds: A.Waqar, N. Ali), One Central Press, UK, Altrincham, **2015**, Ch. 10; d) V. Nguyen, L. Yan, J. Si, X. Hou, *J. Appl. Phys*. **2015**, *117*, 084304; e) D. Tana, S. Zhou, J. Qiu, N. Khusro, *J. Photochem. Photobiol. C-Photochem. Rev*. **2013**, *17*, 50; f) P. Liu, H. Cui, C. X. Wang, G. W. Yang, *Phys. Chem. Chem. Phys*. **2010**, *12*, 3942.

22. a) Z. Zhu, S. Wang, Y. Chang, D. Yu, Y. Jiang, *Carbon* **2016**, *105*, 416; b) R. Gokhale, P Singh, *Part. Part. Syst. Charact*. **2014**, *31*, 433; c) R. R. Gokhale, V. P. Thakare, S. Warule, B. Lefez, B. Hannoyer, J. P. Jog, S. B. Ogale, *AIP Adv*, **2012**, *2*, 022130.

23. a) M. Sajjad, V. Makarov, M. S. Sultan, W. M. Jadwisienczak, B. R. Weiner, G. Morell, *Adv. Mater. Sci. Eng*. **2018**, 3254081; b) K. Habiba, D. P. Bracho-Rincon, J. A.Gonzalez-Feliciano, J. C.Villalobos-Santos, V. I. Makarov, D. Ortiz, J. A. Avalos, C. I. Gonzalez, B. R.Weiner, G.Morell, *Appl. Mater. Today* **2015**, *1*, 80; c) K. Habiba, V. I. Makarov, J. Avalos, M. J. F. Guinel, B. R. Weiner, G. Morell, *Carbon* **2013**, *64*, 341; d) S. Yang, H. Zeng, H. Zhao, H. Zhang, W. Cai, *J. Mater. Chem*. **2011**, *21*, 4432.

24. a) T. Okamoto, E. Miyasaka, K. Mitamura, K. Matsukawa, T. Yatsuhashi, *J. Photochem. Photobiol. A-Chem*. **2017**, *344*, 178; b) T. Okamoto, K. Mitamura, T. Hamaguchi, K. Matsukawa, T. Yatsuhashi, *ChemPhysChem* **2017**, *18*, 1007; c) T. Hamaguchi, T. Okamoto, K. Mitamura, K. Matsukawa, T. Yatsuhashi, *Bull. Chem. Soc. Jpn*. **2015**, *88*, 251.

25. H. Yu, X. Li, X. Zeng. Y. Lu, *Chem. Commun*. **2016**, *52*, 819.

26. W. L. F. Armarego, C. L. L. Chai, Purification of Laboratory Chemicals, 5th Ed., Butterworth-Heinemann – Elsevier, Burlington (MA), **2003.**

27. "Scatter in UV-Vis absorption spectra", can be found under http://www.fluortools.com/software/ae/documentation/tools/scatter, **2020.**

28. D. F. Eaton. Reference materials for fluorescence measurement. *Pure Appl. Chem.* **1988**, 7, 1107.

29. J. Koziol. *Photochem. Photobiol.***1966**, *5*, 41.

30. "Refractive Index values for chemicals commonly used in the laboratory," can be found under http://home.miracosta.edu/dlr/info/refractive_index.htm, **2010.**

31. A. Jiménez-Banzo. X. Ragàs. P. Kapusta and S. Nonell. *Photochem. Photobiol. Sci.* **2008**, *7*, 1003.

32. F. Wilkinson, W. P. Helman, A. B. Ross. *J. Phys. Chem. Ref. Data,* **1993**, *22,* 113.

33. R. Schmidt, C. Tanielian, R. Dunsbach, C. Wolff, *J. Photochem. Photobiol. A-Chem.* **1994**, *79*, 11.

34. a) Org. Biomol. Chem. Vol 16, 4044-4060, **2018**. b) F. Wilkinson, W.P. Helman, A.B. Ross, Quantum yields for the photosensitized formation of the lowest electronically excited state of molecular oxygen in solution. J. Phys. Chem. Ref. Data **1993**. 22. 113.]

36. a) S. D. Berger, D. R. McKenzie & P. J. Martin, EELS analysis of vacuum arc-deposited diamond-like films, Philosophical Magazine *Letters*, **1988**, *57*:6, 285-290; b) J. Bruley, D. B. Williams, J. J. Cuomot & D. P. Pappas. *Journal of Microscopy*, Vol. *180*, Pt I, **1995**, pp. 22-32; *30*. c) D. Galvana,T., Y.T. Peia, J.Th.M. De Hossona, A. Cavaleiro. *Surface & Coatings Technology 200*, **2005**, 739–743; d) *Journal of Applied Physics,* **2005***, 97*, 074302, doi: 10.1063/1.1868054

Chapter 3:

Photocatalysis of Carbon Nanodot–TiO_2 Heterostructures Activated by Visible Light

Chapter 3: Photocatalysis of Carbon Nanodot–TiO_2 Heterostructures Activated by Visible Light

4.3.1. Introduction

The design of photocatalysts for the utilization of solar radiation is of strong interest for a more sustainable and green approach in applications such as water remediation, wastewater treatment, air cleaning and disinfection aimed at bacteria-free environments. These applications generally rely on the use of reactive oxygen species (ROS) generated in photocatalytic redox reactions to destroy organic matter. Metal oxides and particularly titanium dioxide (TiO_2) are the prime catalytic materials with strong photocatalytic oxidation power and concurrent degradation ability while at the same time exhibiting a robust photostability [1]. They are widely employed due to earth abundance and low cost, low toxicity and mild impact on the environment. However, because of the large bandgap of TiO_2, the optical absorption is limited to UV light [2] and consequently significant attention has been directed at increasing the visible light activity of TiO_2. This objective can be achieved by the sensitization of the semiconductor, by doping or by forming heterostructures of TiO_2 with other materials, which improves the light harvesting and expands the spectral range of absorption. At the same time electron–hole recombination can be reduced by doping via trapping of electrons before reaching the surface. Metals such as Au, Ag, Pt, V, Cr, or Fe as well as non-metals such as B, C, N, S have been utilized for this purpose [3]. Among these, carbon-TiO_2 heterostructures have gained widespread interest in photocatalytic applications, because these systems potentially harvest a broad spectrum of solar radiation and exhibit enhancement of the photocatalytic activity due to strong interfacial electronic effects of the carbon support [4, 5]. Carbon-based composites of TiO_2 have been reported using carbon of different type such as activated or graphitic carbon, carbon nanotubes [6, 7] and graphene [4]. However, these nanomaterials can make a poor surface contact with TiO_2 nanoparticles (NP), and as such the photoinduced charge transfer processes from the nanocarbon to TiO_2 may not be efficient [8]. More recently CND have emerged as a new zero-dimensional carbon material which has been reported to exhibit unique optical and electronic properties, such as excellent light-harvesting, broad excitation spectra, tunable photoluminescence and efficient photoinduced charge transfer ability in catalytic processes [9-16]. CND typically exhibit a size in the range of 3-5 nm and functional groups on their surface; these characteristics facilitate their self-assembly onto nanostructured materials such as nanoparticles or nanotubes, improve interfacial interaction and in some cases may help to improve the dispersion or stabilization of the nanomaterials [17]. Due to their unique characteristics, CND have been used to sensitize several semiconductor materials, and primarily TiO_2, to attain photocatalysis in the visible range [9-16, 18-21].

The process of hydrothermal synthesis of carbon dots, however, has been shown recently [22-29] to overwhelmingly produce small organic molecules, some of them fluorescent, like IPCA (imidazo[1,2, α]pyridine-7-carboxilic acid, 1,2,3,5-tetrahydro-5-oxo) or

IPCA-EDA (N-(2aminoethyl)-5-oxo-1,2,3,5 tetrahydroimidazol [1,2,α]pyridine-7-carboxamide). The UV-Vis and PL spectra are dominated by these small conjugated fluorophores and their photoproducts [23]. Graphitic cores, on the other hand, are formed in very low mass yields, typically below 1%. They are observable by techniques such as HR-TEM, GI-WAXS and SERS and are almost exclusively responsible for the formation of singlet oxygen [23]. The PL quantum yield of the CND, on the other hand, is very low, and is still dominated by the small chromophores, which remain attached to the CND even after prolonged dialysis. The question therefore arises whether any photocatalytic activity of heterostructures of this complex mixture with TiO_2 NP is due to the molecular components or due to the CND. This question appears especially relevant taking into account that in many studies of photocatalytic activity of such heterostructures no attempt is made to separate the majority molecular fraction from the CND.

The mechanism of enhancement of visible photocatalysis by CND has been frequently postulated to be based on the efficient light absorption by the CND resulting in the generation of charge carriers in the conduction band of the TiO_2 component, reducing at the same time recombination of the photoinduced electron–hole pairs. Frequently, however, the schemes reported to explain the charge transfer are merely qualitative and are not based on experimental determination of the work functions of the CND and TiO_2. Moreover, a significant number of publications have also tried to explain the mechanism of enhancement of visible photocatalysis based on photoluminescence up-conversion by the CND under continuous illumination [19-21, 30-31].

In the present study we investigate the photocatalytic activity of the CND@TiO_2 heterostructures using cw light-emitting diodes and clarify the relative participation of different reactive oxygen species in the photocatalytic process by employing appropriate scavengers. Using a tunable laser, we acquire photocatalytic action spectra in the visible range of wavelengths. Due to the scarcity of powerful narrow-band widely tunable light sources such action spectra have very rarely been reported (compare, e.g., [32] where a monochromator and very long exposure times were employed for this purpose). The mechanism for photocatalysis under irradiation by visible light is elucidated based on ultraviolet and x-ray photoemission spectra (UPS/XPS) to determine the relative position of energy levels. Moreover, the exploitation of visible light photocatalysis of CND@TiO_2 for the engineering of anti-bacterial polymer nanocomposite surfaces is demonstrated. Because of the importance of any possible super-efficient up-conversion process for photocatalytic activity of CND@TiO_2 heterostructures we have further revisited this process for the case of cw and nanosecond, as well as femtosecond pulsed excitation.

4.3.2. Experimental Section

Synthesis of CND

6.5 mmol of citric acid (Sigma Aldrich, 99 %) and 12 mmol of ethylenediamine (Fluka Analytical, 99,5 %) were dissolved in 30 mL of water in a Teflon liner. The Teflon liner was placed in a stainless-steel autoclave and held at 200 °C for 5 hours. After the autoclave was cooled to room temperature, the reaction products were subjected to dialysis for one week using a cellulose dialysis membrane of 14 kDa molecular weight cut-off (MWCO).

Synthesis of CND@TiO_2 photocatalysts

Heterostructures of TiO_2 coated with CND (CND@TiO_2) were prepared by mixing 5 mg of 10 nm TiO_2 NP of anatase crystal phase (Nanoamor) with 1 mL of a stable suspension of the synthesized CND. After stirring 24 hours at room temperature, the mixture was centrifuged several times at 10.000 rpm, removing the supernatant every time, until no absorption band at 350nm could be detected. The resultant filtered precipitate of CND@TiO_2 was used for the photocatalysis experiments.

Characterization of CND@TiO_2 photocatalysts

UV-Vis absorption spectra were recorded on a UV-Vis spectrophotometer (Varian Cary 50) using a 1 cm quartz cuvette (Suprasil). Room-temperature PL and PLE spectra were acquired on a spectrofluorimeter (Horiba FluoroLog 3) equipped with a high-pressure Xenon lamp and a Hamamatsu R928P photomultiplier; the PLE and PL spectra were corrected for the characteristics of the lamp source and of the detection system, respectively. Attenuated total internal reflection Fourier-transform infrared spectroscopy (ATR-FTIR) was carried out using a Bruker Alpha ATR-FTIR spectrometer

A field emission gun transmission electron microscope (FEG-STEM) (Talos F200X, FEI) integrating an energy dispersive spectrometry (EDS) chemical analysis system and a CMOS digital camera for image acquisition 4000x4000 pixels) was employed for high resolution electron microscopy. The equipment offers a point-to-point resolution ≤ 0.25 nm at 200 kV, information limit ≤ 0.12 nm at 200 kV, and a STEM-HAADF resolution at 200 kV ≤ 0.16 nm.

XPS (X ray Photoelectron Spectroscopy) measurements were carried out using the Al k-alpha monochromatic line (1486.7 eV) in a SPHERA U7 hemispherical analyzer mounted in a UHV (Ultra High Vacuum) chamber with a base pressure of 5 x 10^{-10} mbar. UPS (Ultraviolet photoelectron Spectroscopy) was performed in the same chamber by irradiating the samples with the He I line (21.2 eV) of a helium discharge lamp. The angle for the UPS measurements between the sample surface and the analyzer was 90 ^{o} and the pass energy was set to 3 eV. As the materials studied in this work were insulators, to prepare samples suitable for XPS and UPS analysis, a solution of the materials were drop-cast on thick Cu foils with a sputtered gold

layer to improve the electrical contact to ground. To compensate built-up charges, an electron gun was used (FG-500 Specs, 3 eV and 40 micro-Amperes) for the XPS measurements and in between the acquisition of UPS spectra. For binding energy correction in XPS, the Ti $2p_{3/2}$ was centered at 458.8 eV and for the CND, the Au $4f_{7/2}$ core level of the substrate at 84.0 eV was taken as binding energy reference. Work function measurements were done measuring the cut-off of the secondary electrons in the UPS spectra, applying a negative bias of – 5 V to the sample. In spite of the use of metallic substrates to deposit the samples and the metallic ground contact on the samples, the UPS spectra were shifted due to charging, as can be expected, but they reproduced well the main features observed in the XPS valence band (VB) spectra. We therefore took advantage of XPS measurements in the same UHV chamber with a charge compensation gun (so all the core levels are well positioned), to determine the position of the VB by XPS and use this spectrum to properly reposition the VB measured by UPS.

Photocatalysis studies

The following light emitting diodes (LEDs) were used for dye degradation experiments: (a) blue LED: matrix of 4 LEDs, LZ4-40B208-0000 (LedEngin Inc), 10 W, (b) green LED: matrix of 4 LEDs, ILH-OP04-TRGR-SC221-WIR200 (Intelligent LED Solutions), 7.6 W; red LED: M625D3 (Thorlabs), 920 mW; white LED: ILH-ON0-WMWH-SC211-WIR200 (Intelligent LED Solutions), 2.2 W. All LEDs were mounted on appropriate heat sinks and driven by double regulated power supplies. The power density at the sample was controlled by distance and measured with a Thorlabs PM100D power meter connected to a S302C thermal detector head. For laser degradation experiments, a tunable Continuum Sunlite optical parametric oscillator (OPO), pumped by a Powerlite DLS seeded, q-switched and frequency-tripled Nd:YAG laser, pulse width 5 ns, linewidth 0.075 cm^{-1} was employed. Output power was measured with a Gentec Maestro power and energy meter connected to a Gentec QE12LP-S-MB thermal head. In all cases the photocatalytic degradation of the dyes was determined by UV-Vis spectrometry by the value of absorption at the absorption maximum of the dye.

Bactericidal efficiency of CND@TiO_2 surface nanocomposite films

To prepare the CND@TiO_2 surface nanocomposite films, a solution of poly(methyl methacrylate (PMMA) in toluene (7.5 % wt.) was spin-coated onto a PET support substrate and subsequently soft-baked at 70^{o}C. A stable dispersion of CND@TiO_2 in methanol (0.1-1 % wt) was then deposited on the PMMA thin film by spin-coating. The sample was hot-pressed at a temperature of 170 ^{o}C and a pressure of 45 bars to embed and fix the nanoparticles within the softened PMMA surface.

Staphylococcus aureus (RN4220), *Escherichia coli* (CECT 516) and *P aeruginosa (CECT 4628) from the Spanish Type Culture Collection* (University of Valencia, Spain) were grown overnight on Luria Broth (LB) media at 37 ^{o}C shaking at 250 rpm; for S. aureus LB media was

supplemented with 1 µg/ml of erythromycin. The antibacterial function of the surfaces was evaluated according to the ISO standard no. 27447:2009, titled: "Fine ceramics (advanced ceramics, advanced technical ceramics) -- Test method for antibacterial activity of semiconducting photocatalytic materials." For this purpose, a bacterial suspension of $2 \cdot 10^5$ bacteria cell/ml is inoculated over the imprinted substrates and then exposed for 1 hour to visible light (white LED, at a fluence of 30 mW/cm^2). After the exposure time, the substrates were washed three times with Soya Casein Digest Lecithin Polysorbate (SCDLP) broth medium. Then subsequent 10-fold dilutions of the recovered volume were prepared until a dilution of 1:1000 was obtained, which placed on an agar Petri dish and incubated during 24 hours. After the incubation time the number of colonies were counted corresponding to the surviving bacteria. In addition to the PMMA/CND@TiO_2 samples control samples of pristine PMMA and PMMA/TiO_2 were tested.

Up-conversion experiments

Up-conversion studies were performed using a Clark-MXR CPA femtosecond regenerative amplifier (λ = 775 nm, Δt = 150 fs, pulse energy E = 0.8 mJ, pulse repetition rate 1 kHz, as well as the OPO laser mentioned above.

4.3.3. Results and discussion

Synthesis and characterization of CND

Nitrogen-doped CND were synthesized via a hydrothermal method (see the Chapter 1) using citric acid and ethylenediamine as starting materials and dialyzed for one week using a 14 kDa molecular weight cut-off (MWCO) membrane.

Figure 1a shows the suspension in water of the synthesized and purified CND under illumination by visible and ultraviolet light, respectively. The suspension exhibits strong blue photoluminescence which is due to the residual organic molecular components and its photoproducts [23]. An analysis of the absorption features by time-dependent density functional theory (TD-DFT) indicates that the absorption is dominated by the IPCA molecule as shown in Figs. 2 and 3.

Figure 1b exhibits the high-resolution TEM image of two CND resulting from the synthesis. The size of the CND is around 3-5 nm and it is possible to distinguish the crystalline planes. The inset figure in the lower right-hand corner displays the two-dimensional fast Fourier transform (2D-FFT) of the TEM image revealing the spatial frequencies which correspond to the different interplanar distances (see Fig. 4 and Table 1), confirming the crystalline structures of both the CND and the TiO_2 anatase crystal phase. The FTIR spectrum of the CND (Fig. 1c) exhibits a broad band at 3430 cm^{-1} corresponding to OH stretching vibrations. The shoulder between 3200-3300 cm^{-1} is related to NH stretching vibrations and the bands just below 3000 cm^{-1} correspond to CH stretching vibrations. The peak at 1654

cm^{-1} is related to the C=O carbonyl stretching vibration and the band at 1563 cm-1 corresponds to C=C stretching. In addition, the peak at 1395 cm^{-1} is related to NH, OH or CH bending vibrations. Asymmetric and symmetric stretching vibrations of C–O–C cause absorptions at about 1400 cm^{-1} and 1057 cm^{-1}. Photoluminescence studies were performed at different excitation wavelengths (Figure 1d). The maximum emission was obtained for excitation at 340 nm, coinciding with the maximum of the absorbance. It is worth noting that the wavelength of the maximum of the emission spectrum occurs around 430 nm and this maximum is redshifted to 550 nm for an excitation wavelength of 500 nm. In contrast to many previous reports, which associated such excitation-wavelength dependent shifts to quantum size effects, we ascribe this shift to the inhomogeneity of the local environments of the fluorescing molecules attached to the CND, as well as to the formation of photoproducts during dialysis [23].

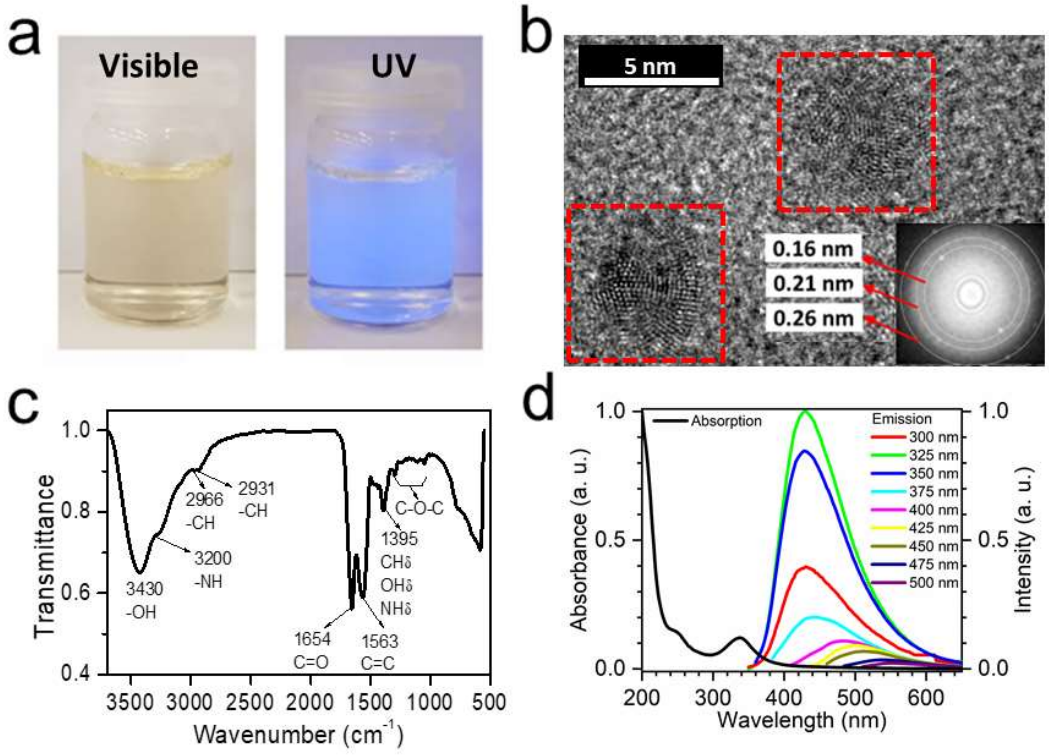

Figure 1. Characterization of synthesized CND: a) Aqueous solution under visible and UV light exposure, b) High resolution TEM image of two CND (marked by the red rectangles) and its Fourier transform indicating the corresponding interplanar distances. c) FTIR spectrum and d) Absorption and photoluminescence spectra obtained at different excitation wavelengths.

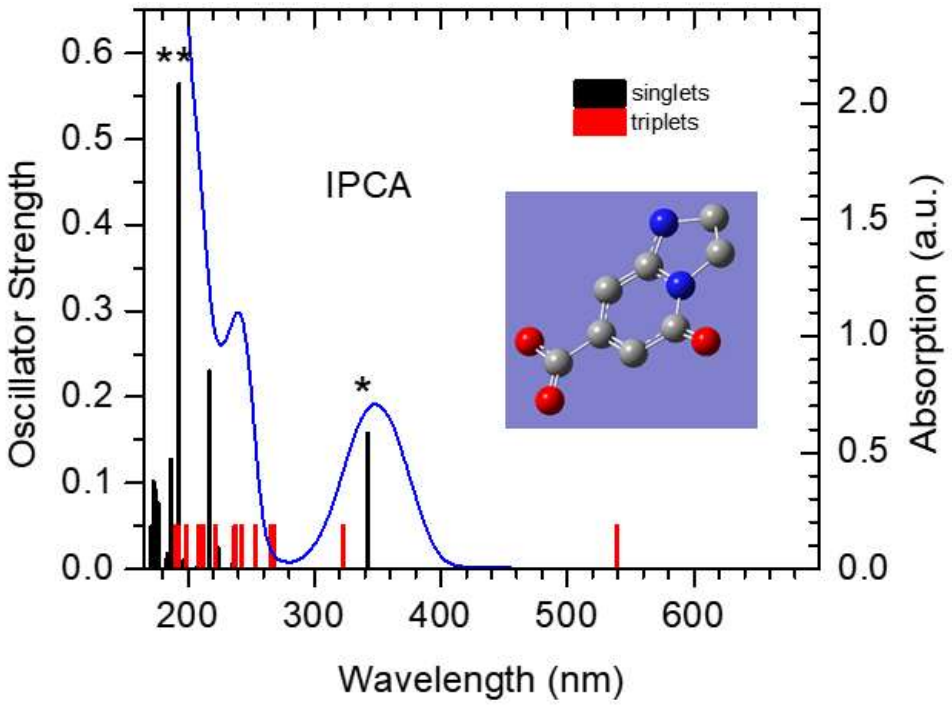

Figure 2. Quantum-chemical calculation of the UV-Vis spectrum and electronically excited states of the main conjugated product of hydrothermal synthesis of CND, the small molecule IPCA ((imidazo[1,2,α]pyridine-7-carboxilic acid, 1,2,3,5-tetrahydro-5-oxo)) in water. The blue curves indicates the measured absorption spectrum of the dialysate, black bars the vertical transitions from the ground state to the excited singlet states and red bars the calculated positions of the triplet excited states. Because spin-orbit coupling was not included in the calculation the red bars are given a constant (arbitrary) height. Calculation using Gaussian09, basis set 6-311++ G(d), CAM-B3LYP functional and polarizable continuum model for the solvent.

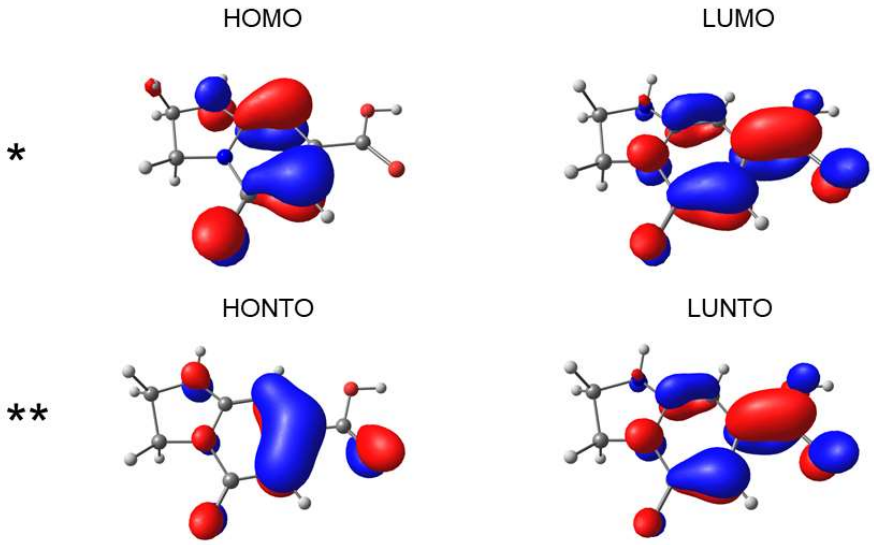

Figure 3. Frontier orbitals of IPCA ((imidazo[1,2,α]pyridine-7-carboxilic acid, 1,2,3,5-tetrahydro-5-oxo)) in water for the transitions indicated by (*) and (**) in Figure 2, respectively.

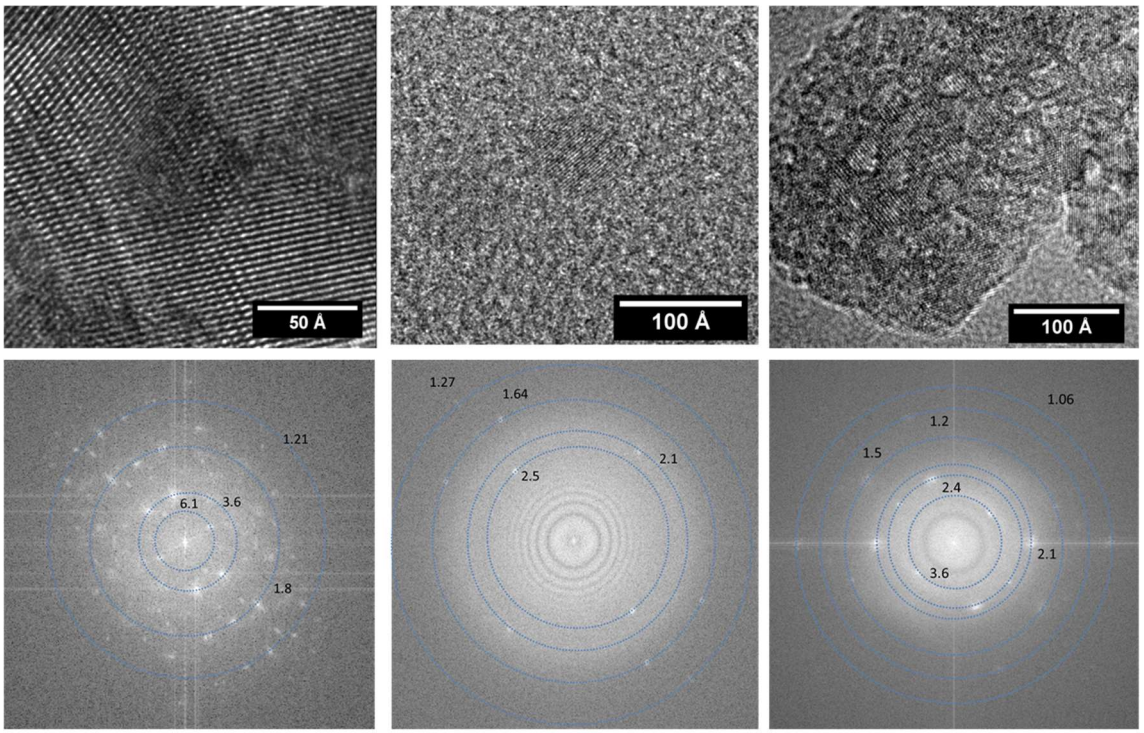

Figure 4. HRTEM images of CND@TiO_2 heterostructures and Fast Fourier transform (FTT) of the corresponding images.

Table 1. Identification of different lattice spacings observed in the TEM images. In the case of the CND the indices refer to graphite.

TiO_2 Anatase		CND	
hkl	d (Å)	hkl	d (Å)
101	3.52	002	3.35
103	2.43	100	2.13
004	2.38	101	2.03
112	2.33	102	1.80
200	1.89	004	1.68
105	1.70	103	1.54
211	1.67	110	1.23
213	1.49	112	1.16
204	1.48	105	1.14
		006	1.12

Synthesis and characterization of CND@TiO_2 heterostructures

The synthesized CND were mechanically mixed with TiO_2 NP to obtain a photocatalytic heterostructure active for visible light. After stirring the mixture for 24 h the suspension was centrifuged at 10.000 rpm for 15 min and the supernatant was removed thereafter. The procedure was repeated until the supernatant showed no measurable absorption at 350 nm. The interaction between the CND and the TiO_2 NP was assessed by HR-TEM. Fig. 5a reveals CND attached to TiO_2 NP (CND@TiO_2) by identification of the interplanar distances, 0.35 nm for TiO_2 and 0.21 nm for CND. Further analysis of the FFT of HRTEM images is presented in the Fig. 4 and Table 1. The FTIR spectra of TiO_2 (black solid line), CND (blue solid line) and the CND@TiO_2 nanocomposite (red solid line) are shown in Fig. 5b. The spectrum of TiO_2 shows strong bands around 1633 cm^{-1} and 3394 cm^{-1} due to the bending mode (ν_2) of surface-adsorbed water and the stretching mode of the hydroxyl groups on the TiO_2 surface. These peaks are also present in the nanocomposite (red spectrum). In the fingerprint region, several broad peaks appear at 610, 690, 773, 906 and 1048 cm^{-1}. These peaks are related to the O-Ti-O vibration modes [33]. The suppression of some of these peaks, as well as the appearance of new peaks located at 1155, 1216, and 1458 cm^{-1} in the composite suggests the creation of new bonds with the carbonaceous particles. FTIR spectra of TiO_2 NP incubated with the dialysate, on the other hand, yielded no evidence of the formation new bonds and resulted essentially in a superposition of the FTIR spectra of the two constituents (Fig. 6). The CND@TiO_2 heterostructures present a UV-Vis absorption spectrum (Fig. 5c) similar to that of pure TiO_2 NP, with an enhancement at the absorption at around 340 nm due to the CND, but, in addition to that, with an absorption tail extending much more towards the red up to 650 nm, which is evidence of a strong interaction between CND and TiO_2 [34-39]. Such an interaction is not apparent in the absorption spectra of the TiO_2 mixtures with the material outside of the dialysis bags collected during dialysis (dialysate, Fig. 5d) and with RhB (Fig. 7), where the absorption spectrum of the mixture results only from the combination of the individual spectra.

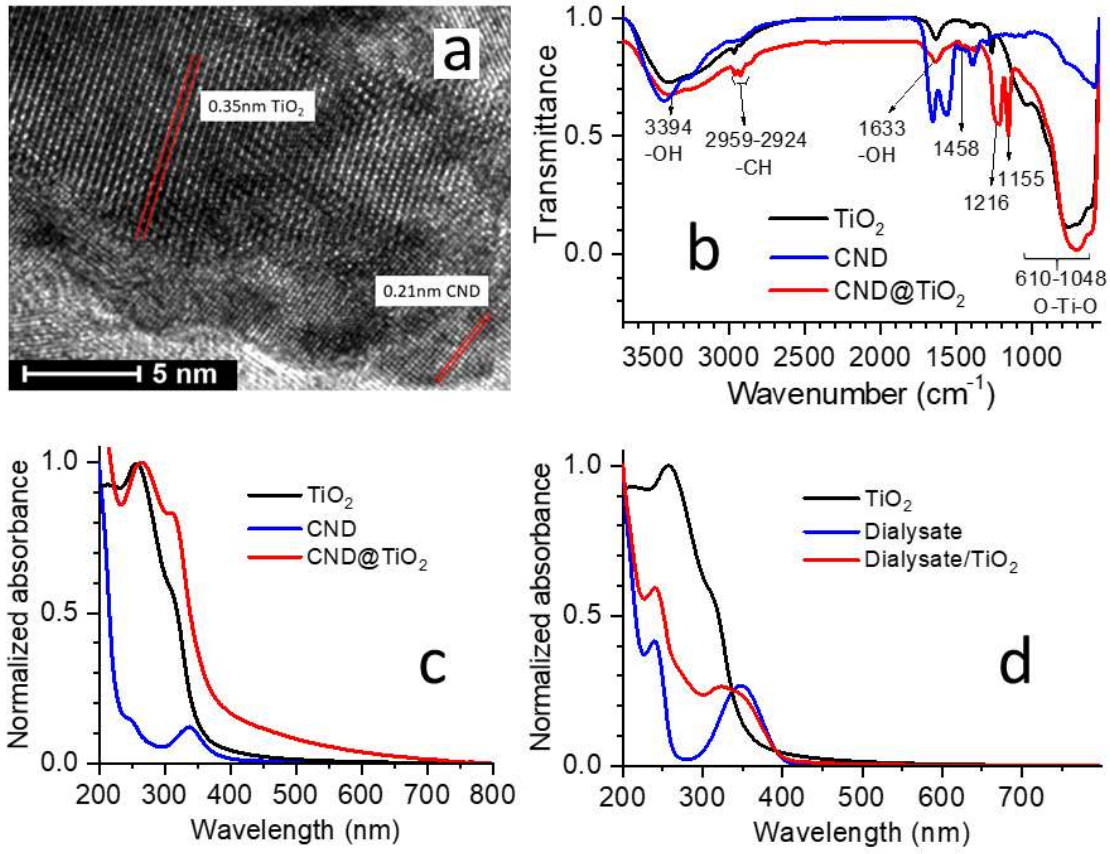

Figure 5. Characterization of CND@TiO_2 heterostructures: a) HR-TEM image, b) FTIR spectra of TiO_2 (black line), CND (blue line) and CND@TiO_2 (red line), c) Normalized absorption spectra of TiO_2 (black line), CND (blue line), and CND@TiO_2 (red line) in aqueous suspension, and d) Normalized absorption spectra of TiO_2 (black line), dialysate (blue line), and TiO_2/dialysate (red line) in aqueous suspension.

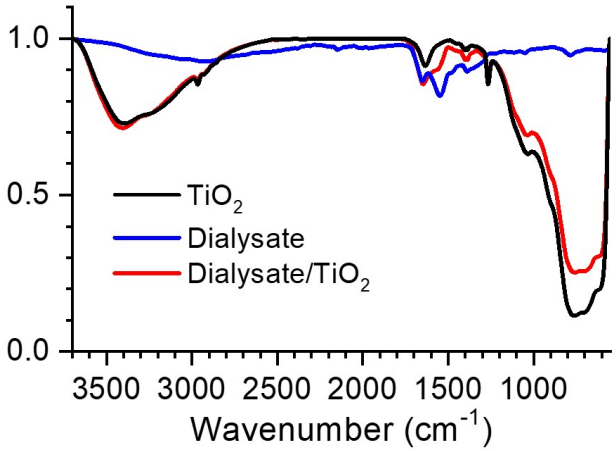

Figure 6. FTIR spectra of TiO_2 (black line), dialysate (blue line) and dialysate/TiO_2 (red line).

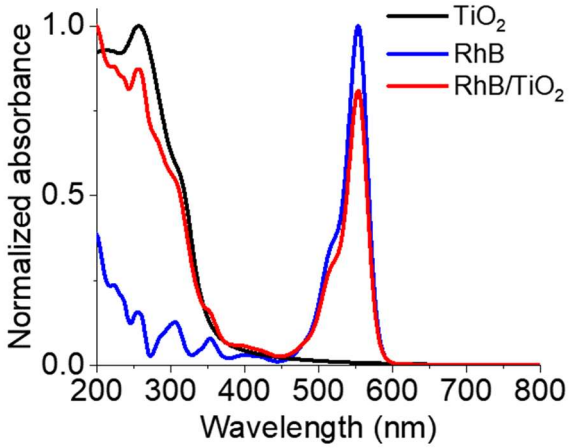

Figure 7. Normalized absorption spectra of TiO_2 (black line), RhB (blue line), and RhB/TiO_2 (red line) in water / aqueous suspension.

Photodegradation under visible light illumination

In order to assess the visible light photocatalytic efficiency of the CND@TiO_2 heterostructures, the degradation of the dye rhodamine B (RhB) in suspensions of CND@TiO_2 upon irradiation by different visible light sources was studied. Three light-emitting diodes (LEDs) with different emission wavelengths were selected for this purpose: blue (center wavelength λ_C = 456 nm), green (λ_C = 525 nm) and red (λ_C = 634 nm). The illumination intensity at the sample was set to the same value in these experiments (12.7 mW/cm^2). The spectra of the LEDs are shown in Fig. 8. As shown in Fig. 9, irradiation by the blue LED yielded the highest activity in the presence of the photocatalysts, followed by the green LED, whereas red light produced only a minor degradation. In all cases CND@TiO_2 produced a significantly stronger photodegradation at these irradiation wavelengths than pristine TiO_2.

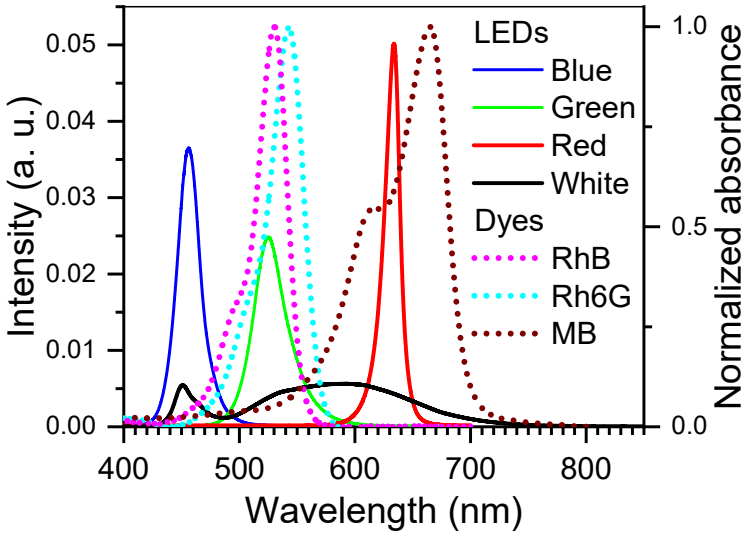

Figure 8. Emission spectra of the different LED sources (blue, green, red and white), normalized to the area under the spectrum, and normalized absorption spectra of the different dyes used in the degradation experiments.

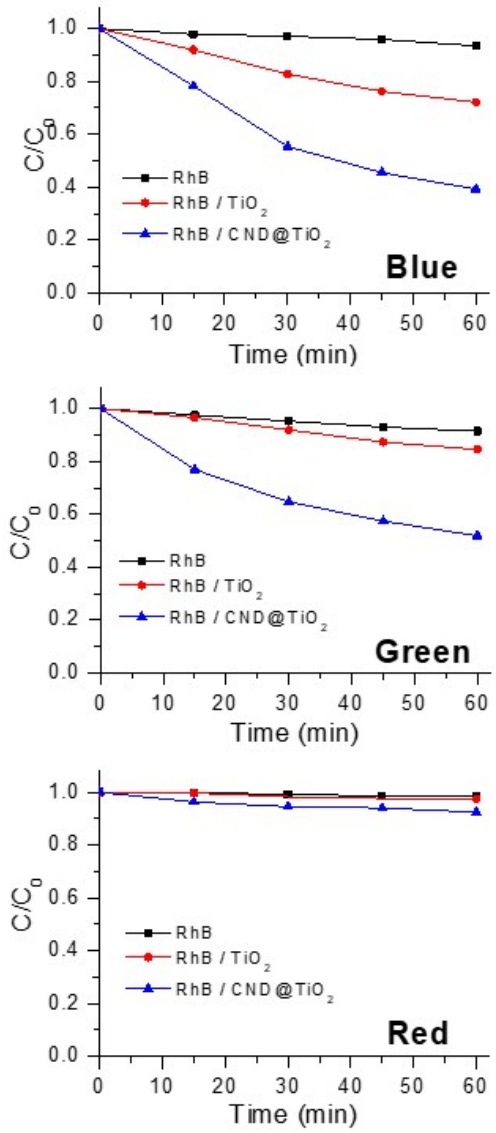

Figure 9. Photocatalytic activity of CND@TiO_2 heterostructures under illumination by different light sources at equal illumination intensity (12.7mW/cm^2), measured as the decrease of RhB concentration with exposure time. From top to bottom: Blue, Green and Red LED.

In order to obtain a more complete understanding of the wavelength dependence of the photocatalytic activity, the decomposition of two additional dyes with absorption maxima at different visible wavelengths was studied, i.e., rhodamine 6G (Rh6G) and methylene blue (MB). The percentages of dye degraded after 60 min of exposure are presented in Figure 10, whereas the photocatalytic activity shown as the decrease of dye concentration with exposure time is shown in Figs. 11 and 12.

As shown in Fig. 10, RhB is degraded under visible light illumination and the degradation is strongest for CND@TiO_2 when it is irradiated with blue light. Similar results are seen for Rh6G, with a generally reduced degradation of this dye compared to RhB. For both dyes there is only a minor degradation induced by the red light. MB behaved differently; this dye was slightly degraded by blue and green light. In contrast, degradation was significant under red light irradiation. Fig. 8 displays the emission of the different LEDs and the

absorbance spectra of the dyes and reveals a strong overlap between the red LED emission and the absorption of MB. The wavelength dependence of degradation of the dyes in the presence and absence of the photocatalysts will be discussed below in more detail. It is already evident, however, from the results shown in Figs. 9, 10, 11, 12 and Table 2 that in the presence of TiO_2 the photocatalytic degradation is significant for all dyes, but in particular with the blue LED and, in the case of MB also for the red LED. The CND@TiO_2 heterostructures enhance the photocatalytic degradation of all dyes and for each irradiation wavelength relative to pristine TiO_2.

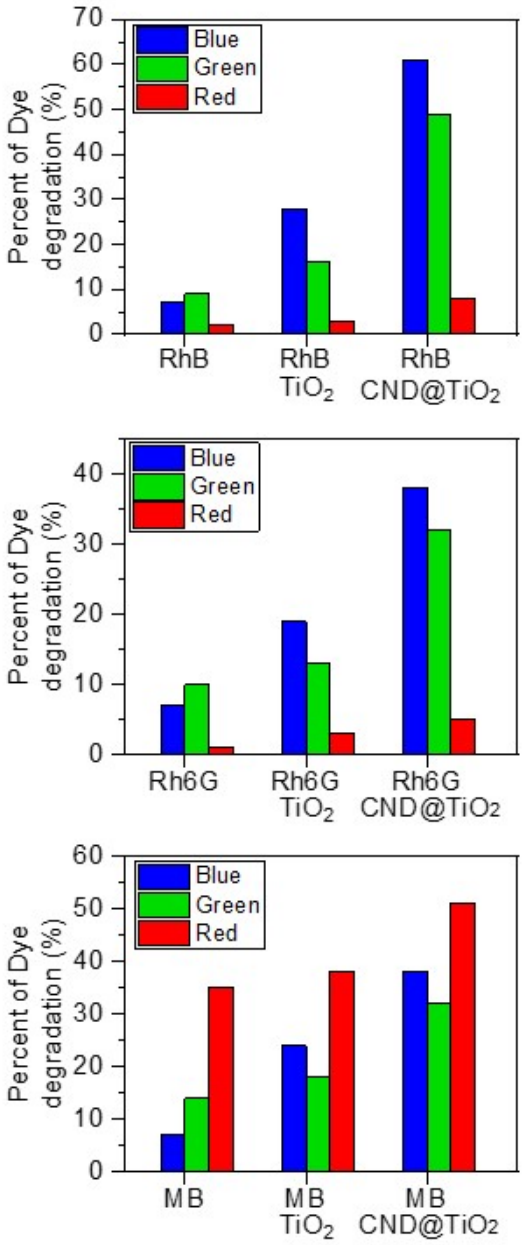

Figure 10. Degradation of the different dyes by irradiation with LEDs of different wavelengths after 60 min of exposure. From top to bottom: RhB, Rh6G and MB.

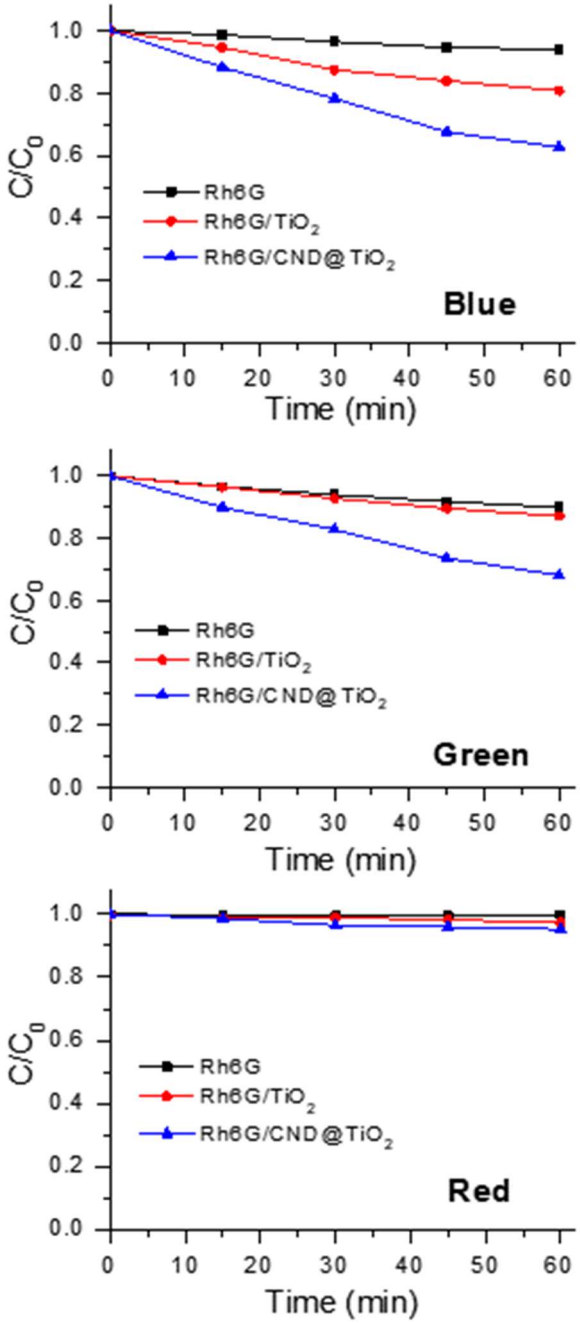

Figure 11. Photocatalytic degradation of Rhodamine 6G (Rh6G) by CND@TiO_2 heterostructures under illumination by different LED light sources. Power density = 12.7 W/cm^2.

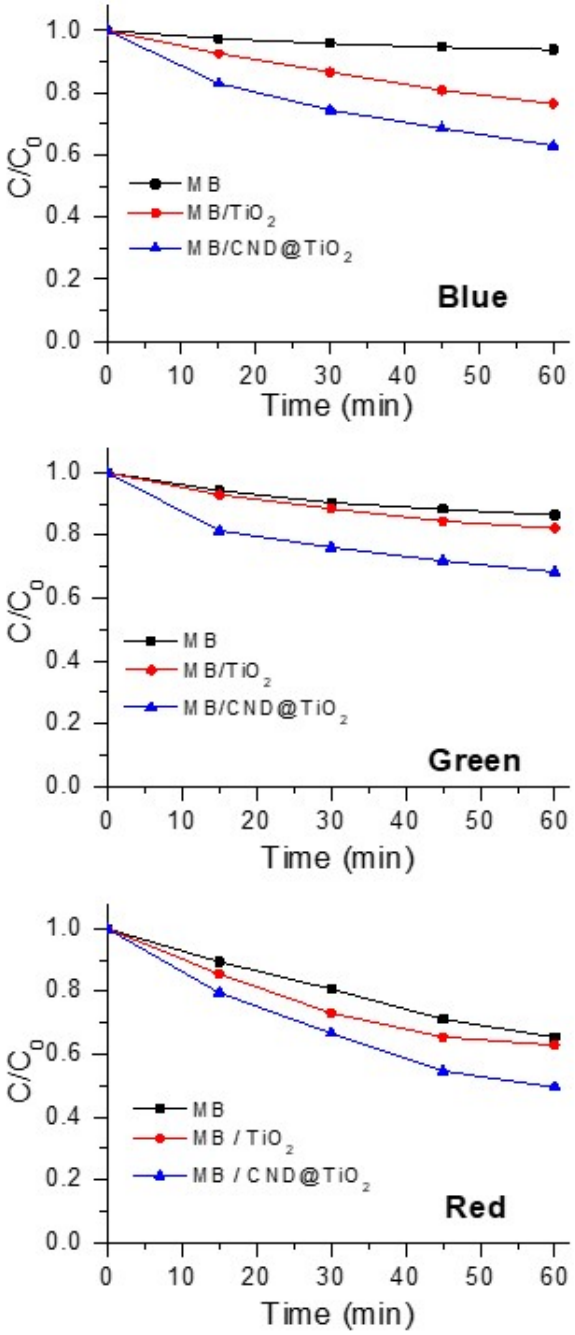

Figure 12. Photocatalytic degradation of Methylene Blue (MB) by CND@TiO_2 heterostructures under illumination by different LED light sources. Power density = 12.7 W/cm^2.

Table 2. Percentage of degradation of the different dyes under illumination by different LED sources after 60 min of exposure.

	Blue (%)	Green (%)	Red (%)
RhB	7	9	2
RhB and TiO_2	28	16	3
RhB and CND@ TiO_2	61	49	8
Rh6G	7	10	1
Rh6G and TiO_2	19	13	3
Rh6G and CND@ TiO_2	38	32	5
MB	7	14	35
MB and TiO_2	24	18	38
MB and CND@ TiO_2	38	32	51

The results obtained raised the question in how far there exists a correlation between the efficiency of the photocatalytic process and the absorbance spectra of the dyes. As only three wavelengths are insufficient for this purpose, degradation of the xanthene dyes RhB and Rh6G was studied as a function of the wavelength employing an optical parametric oscillator (OPO), pumped by a seeded Q-switched and frequency-tripled Nd-YAG laser as the excitation source which permits a wavelength tunability over the wavelength range of interest with a high pulse energy (>10 mJ) and a very small linewidth (0.075 cm^{-1}). Fig. 13 displays the normalized degradation of RhB and Rh6G as a function of the wavelength, after receiving a total fluence of 8.6 J of irradiation by the OPO laser at 12 mJ/pulse, with the absorption spectrum of the dye superimposed.

Due to the ≈10 times higher time-averaged intensity of the OPO laser compared to irradiation by the LEDs and the higher total fluence employed in this experiment the degradation of the dyes was stronger in this case (compare Figs. 14 and 15). Even in the absence of photocatalysts a significant degradation was already observed, decreasing towards the red part of the spectrum. The exact mechanism of this degradation is presently unknown, but also of minor interest for the present study. It could, for example, be related to a catalytic action of the walls of the quartz cuvette. In the presence of TiO_2 NP, a monotonic decrease of the photocatalytic activity with increasing wavelength is also observed, but the degradation is significantly enhanced relative to the dyes alone. The additional effect is most likely related to defects of TiO_2 NP with a decreasing density of states further into the band gap of TiO_2 (Urbach tail). Surprisingly, however, neither the rhodamine dyes alone nor in the presence of TiO_2 exhibit a maximum of degradation at the peak wavelength of the absorption of the dyes. Degradation mechanisms requiring optical excitation of the dyes are therefore irrelevant in these cases. Fig. 10, on the other hand, suggests that this is different for MB where maximum degradation is observed when the wavelength of irradiation coincides with that wavelength. This can be explained considering the relevant photophysical parameters of the dyes investigated (see Table 3 and Fig. 16). Whereas MB is characterized by a very high intersystem crossing probability (0.54), both rhodamines exhibit extremely low values (0.006

for RhB and 0.002 for Rh6G) for that parameter. Considering the degradation of methylene blue shown in Fig. 10 we can conclude that degradation via processes involving the triplet state and therefore requiring optical excitation of the dye, contribute significantly to degradation of MB. Part of this contribution consists in the sensitization of singlet oxygen via the triplet state of MB.

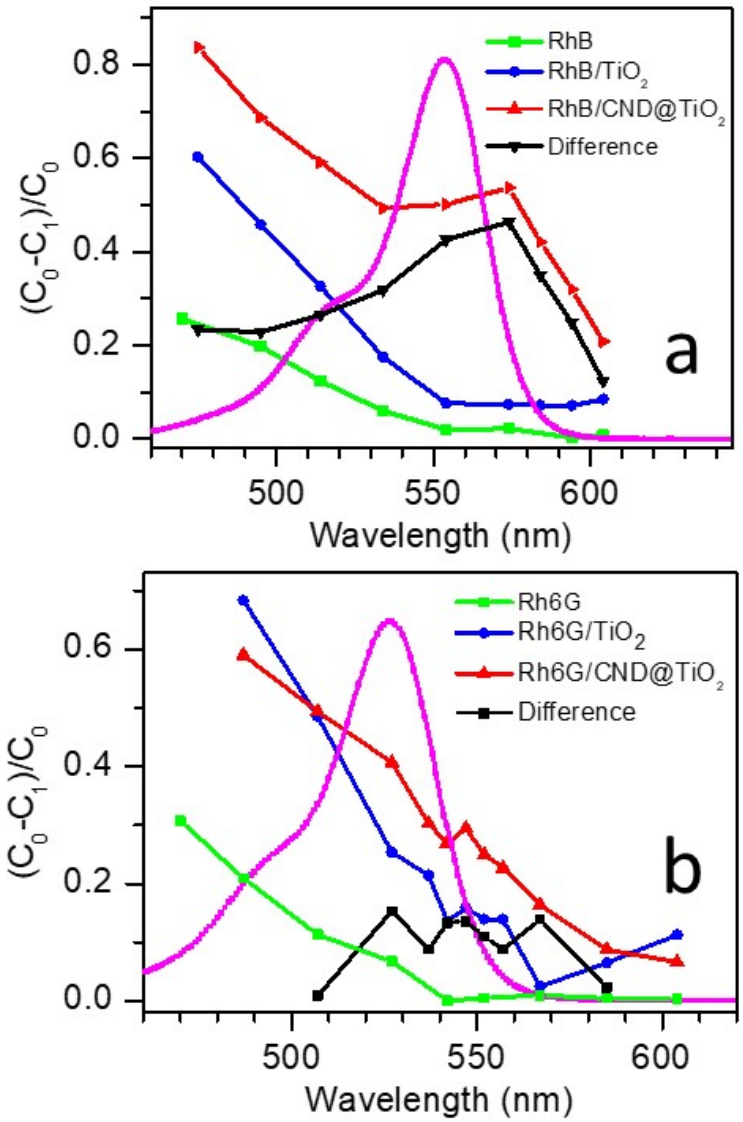

Figure 13. Wavelength-dependent degradation under laser irradiation of a) RhB and b) Rh6G in the absence and presence of the photocatalysts. Green curves: dye solutions alone. Blue curves: dye solutions incubated in colloidal suspensions of TiO_2 NP. Red curves: dye solutions in the presence of CND@TiO_2 heterostructures. Black curves: differential photocatalytic activity of dye/CND@TiO_2 and dye/TiO_2 mixtures, respectively The magenta curves indicate the absorbance of the xanthene dyes at a concentration of 0.01M.

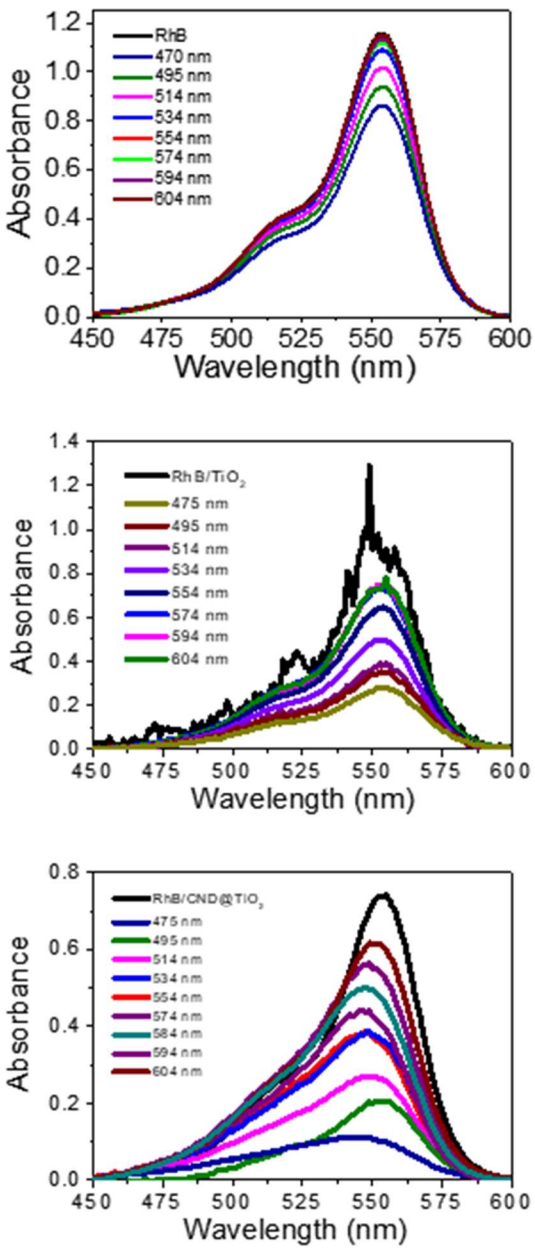

Figure 14. Degradation of RhB alone and in conjunction with the different nanoparticles using an OPO laser as visible light source. De-ethylation takes place in the case of the CND@TiO_2 heterostructures.

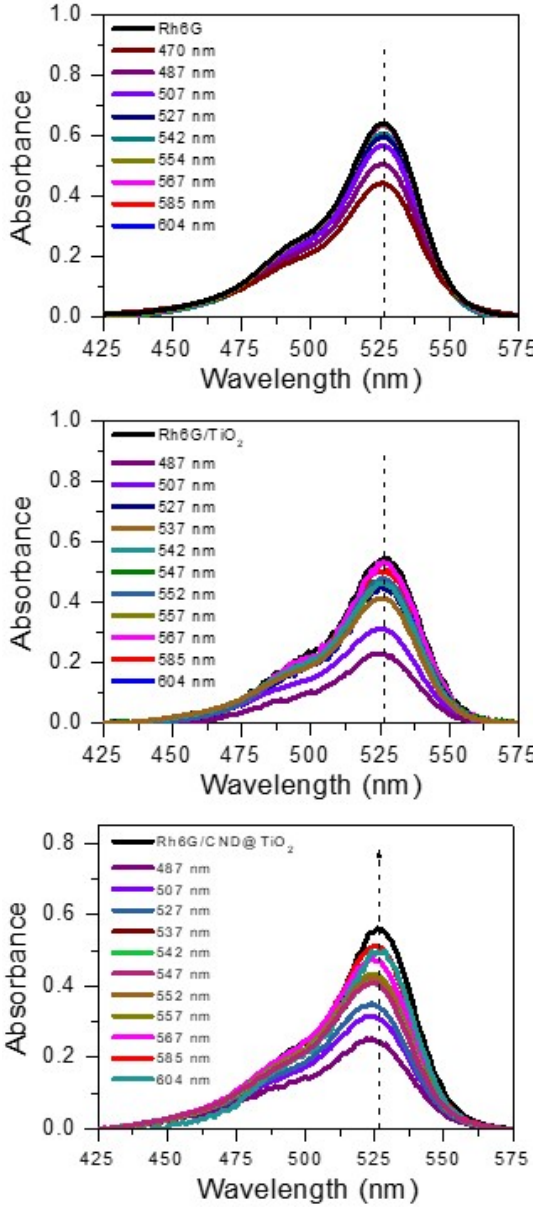

Figure 15. Degradation of Rh6G with the different nanoparticles using OPO laser as visible light source (small de-ethylation effect observed with Rh6G).

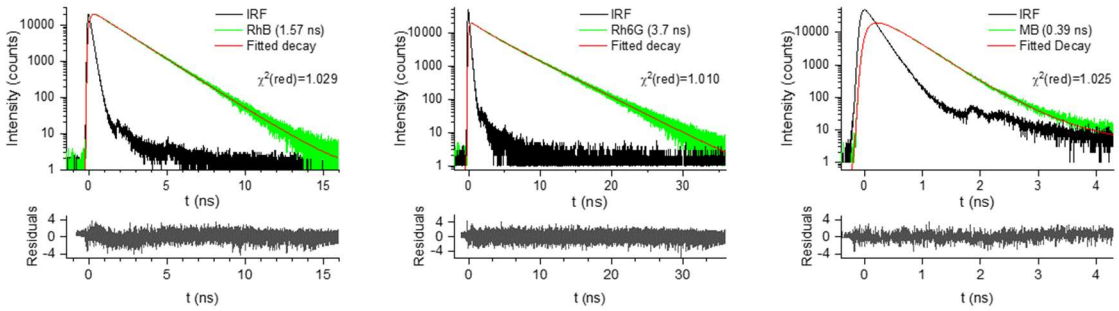

Figure 16. Fluorescence decay of the dyes in non-deoxygenated water. Numbers in brackets indicate the intensity-averaged lifetime in case of multi-exponential decays.

Table 3. Photophysical parameters of RhB, Rh6G and MB.

	RhB	**Rh6G**	**MB**
Singlet Lifetime (ns)	6.1[1], 1.57[a]	8.3[1], 3.67[a]	0.52[2], 0.37[a]
Triplet Lifetime (µs)	6[3]	-	2[4]
Intersystem Crossing Rate (s^{-1})	$5.3x10^5$ [3], $3x10^5$ [1]	$0.9x10^5$ [1]	$\approx 1x10^9$ [7]
Intersystem Crossing Probability	0.006[5]	0.002[5]	0.54[6]

[a]own measurement: dyes in non-deoxygenated water at 300 K (compare Figure 16)

[1]Yamashita, M., Kuniyasu, A., Kashiwagi, H., J. Chem. Phys., **1977**, 66, 986-988. (ethanol, 77K)

[2]Alarcon, E.I., González-Béjar, M., Montes-Navajas, P., Garcia, H., Lissi, E. A., Scaiano, J.C., *Photochem. Photobiol. Sci.*, **2012**, 11, 269-273. (MB monomer, H_2O, RT)

[3]Menzel, R., Thiel, E. ,*Chem. Phys. Lett.*, **1998**, 291, 1998 237–243. (ethylene glycol jet in air)

[4]Morgounova, E., Shao, Q., Hackel, B., Ashkenazi, S., Proc. SPIE, 2013, 8596, 85960O-1-85960O-9 (non-deoxygenated aqueous solution)

[5]Korobov, V. E., Shubin, V. V., Chibisov, A. K., Chem. Phys. Lett., **1977**, 45, 498-501. (H_2O)

[6]Nemoto, M., Kokubun, H., Koizumi, M., *Bull.Chem. Soc. Japan*, **1969**, 42, 1223, 2464 (ethanol),

[7]calculated from the singlet lifetime and the intersystem crossing probability.

The degradation of the rhodamine dyes by CND@TiO_2 exhibits a non-monotonic wavelength dependence, which is related to the dye absorption in both cases, but with a peak on the long wavelength side of the absorption. When subtracting the effect of the dye degradation in the presence of TiO_2 from the dye degradation by CND@TiO_2, this maximum is more clearly recognizable, which indicates an additional photocatalytic process due to the presence of the CND in the strongly interacting CND@TiO_2 (compare the discussion with respect to Fig. 5c). This additional process apparently requires photoexcitation of the dye and is most likely due to enhanced adsorption of the dyes to CND compared to TiO_2. Enhanced intersystem crossing for adsorbed molecules can also be expected based on the singlet oxygen generation capacity of CND [23], which also involves a spin-flip process. The red shift of the maximum of additional degradation relative to the absorption of the free dye most likely occurs due to the interaction with the CND.

Mechanism of enhancement of visible photocatalysis

The photocatalytic effect of CND@TiO_2 was further studied following the photodegradation of RhB under irradiation by a white light emitting diode (LED) (λ_C = 446 nm, compare Fig. 8) in the presence of several radical and $^1O_2$ scavengers. Before irradiation, the RhB solution (5 mL, 5 mg/L) and sodium azide [40] (3.25 mg, 0.05 mmol), (2R,3R,4R,5R)-Hexane-1,2,3,4,5,6-hexol (mannitol) [41] (9.1 mg, 0.05 mmol), disodium 4,5-dihydroxybenzene-1,3-disulfonate (tiron) [42] (15.7 mg, 0.05 mmol) or ethylenediamine tetraacetic acid (EDTA) [43] (14.6 mg, 0.05 mmol), respectively, were mixed to trap $^1O_2$, $OH^\bullet$ radicals, $O_2^{-\bullet}$ radicals and holes (h^+), respectively. Then, CND@TiO_2 (100 µL (5 mg/mL)) was added and the reaction was exposed to the light for 90 min. The illumination intensity at the sample was set to the same value (12.7 mW/cm^2) in these experiments as in previous experiments.

As can be seen in Fig. 17A, without catalysts, the photodegradation of RhB solution under irradiation by the white LED was almost undetectable. CND@TiO_2 produced a photocatalytic degradation of 77 % under white LED irradiation during 90 min. However, a dramatic suppression of photodegradation efficiency was observed after adding Tiron or NaN_3 scavengers, lowering the photocatalytic degradation efficiency of CND@TiO_2 to 33 % and 44 % respectively, which shows that $O_2^{-\bullet}$ and $^1O_2$ were mainly responsible for the photocatalytic degradation reactions. In contrast, the introduction of EDTA and mannitol had only a weak influence on the photodegradation rates, indicating that h^+ and $OH^\bullet$ played a relatively minor role in the degradation of the RhB solution. This is remarkably different from previous reports [44] of photocatalytic degradation reactions with CND@TiO_2 heterostructures including CND synthesized from β-cyclodextrin via calcination by P_2O_5, where a significant role of $OH^\bullet$ was reported, that was absent for the pristineTiO_2 NP.

Fig. 17B presents the photocatalytic reaction kinetics of CND@TiO_2 alone and in the presence of the different scavengers employed here, in which the experimental data can be described by a pseudo-first order model expressed by the formula $ln(C_0/C) = kt$, where C_0 and C are the RhB concentration in solution at time 0 and time t, respectively. The quantity *k* is the fitted kinetic rate constant. It can be seen that the plots of ln C_0/C against the irradiation time *t* are very nearly straight lines, which reveals that in all cases the photodegradation of the RhB solutions follows a pseudo-first order kinetics. The kinetic rate constant for CND@TiO_2 is 0.0163 min^{-1} and this is reduced to 0.0149, 0.0128, 0.0063 and 0.0043 min^{-1} in the presence of mannitol, EDTA, NaN_3 and Tiron, respectively.

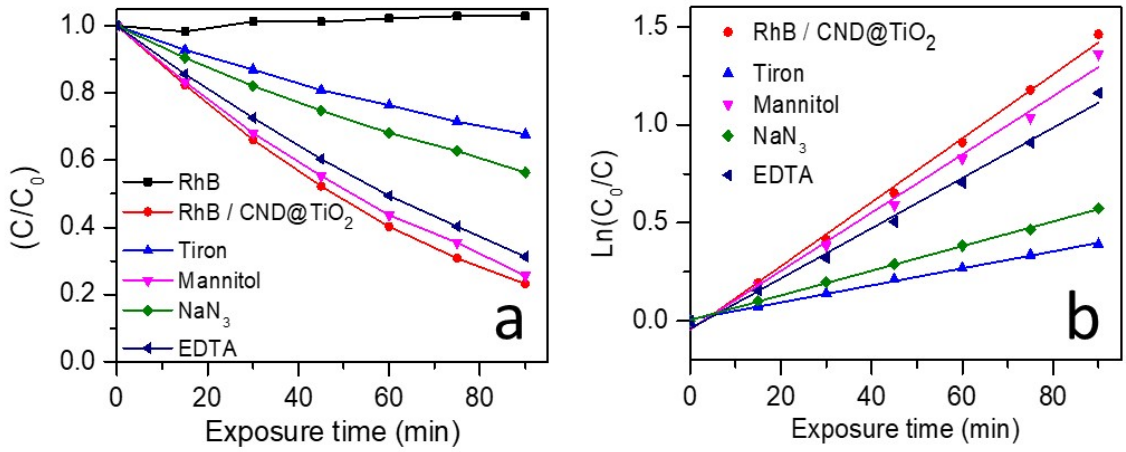

Figure 17. a) Photocatalytic degradation of RhB with CND@TiO_2 and different scavengers under irradiation by white LED. b) The pseudo-first order kinetic fitting of the photodegradation of RhB.

As reported previously [23] the production of singlet oxygen ($^1O_2$) by the CND, with a yield of 45%, could be directly detected via time-resolved phosphorescence [45]. The dialysate, on the other hand, generated a negligible amount of $^1O_2$ (yield 4%) under visible light irradiation, in reasonable agreement with the different photocatalytic degradation efficiencies of the heterostructures CND@TiO_2 and TiO_2/dialysate (see Fig. 18). The photocatalytic degradation efficiency for the TiO_2/dialysate must therefore be mostly limited to the production of the $O_2^{\bullet-}$ radical and possibly to holes and $OH^\bullet$ radicals, whereas in the case of the photocatalyst CND@TiO_2 the photocatalytic degradation efficiency arises mainly from the contribution of the $O_2^{\bullet-}$ radical and $^1O_2$. In any case the importance of the presence of atmospheric oxygen in the photodegradation process under visible light illumination is evident as shown in Fig. 19.

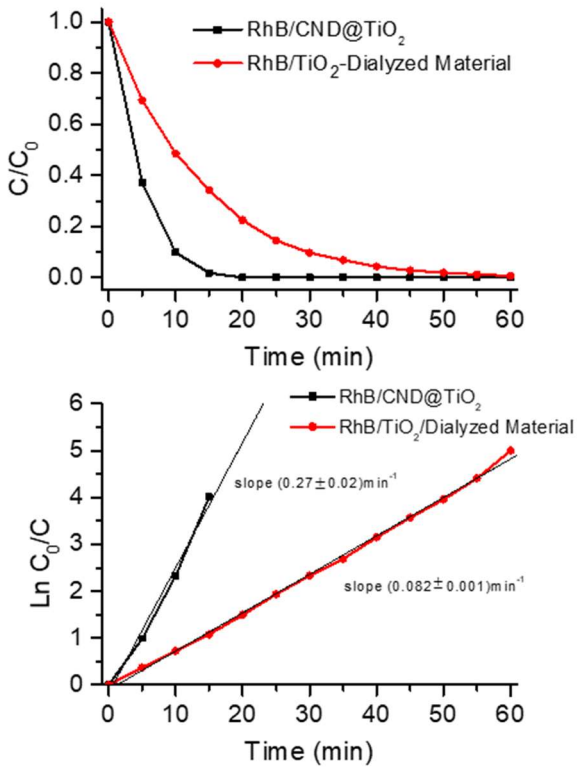

Figure 18. Photocatalytic degradation of RhB by CND@TiO_2 heterostructures and by TiO_2/dialyzed material under illumination by a white LED and the corresponding pseudo-first order kinetic fittings. Power density = 46.3 mW/cm^2.

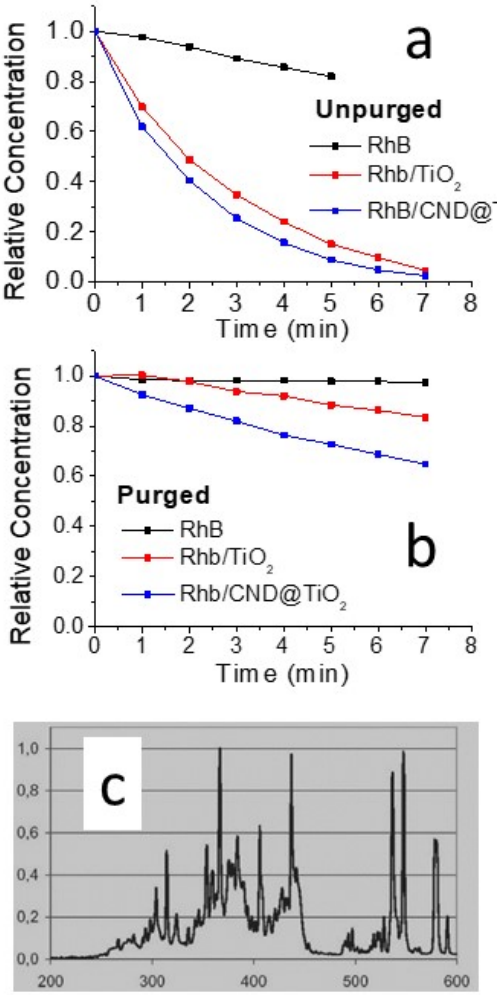

Figure 19. Photocatalytic degradation of RhB under irradiation by a UV lamp (Hoenle UVASPOT 400/T, 80 mWcm^{-2}, emission spectrum shown below) in the absence (a) and presence (b) of oxygen. (b) Purging by N_2 gas for 10 min. (c) Spectrum of the lamp.

The relevant optical band gaps were determined by UV-Vis spectroscopy as shown in the Tauc plot of Fig. 20a. The corresponding band gaps of pure TiO_2 NP and pure CND were 3.5 eV and 3.23 eV, respectively. For CND@TiO_2, on the other hand, no well-defined band gap is observed and the very broad absorption tail indicates a wide distribution of absorption edges for CND@TiO_2 (compare the discussion below). For the determination of work functions UPS spectra were acquired as described in the Experimental section (Fig. 20b). The UPS spectra are dominated by the O 2p VB of TiO_2 with maxima/shoulders at around 5.0(5.4) eV and 6.6 (7.2) eV below the Fermi level and a band edge of 1.99 eV (2.59 eV) below the Fermi level for TiO_2 and CND@TiO_2, respectively. The work functions determined are 5.04 eV (TiO_2), 6.50 eV (CND) and 5.44 eV (CND@TiO_2). This means that, upon formation of the CND@TiO_2 heterostructures the Fermi level moves towards the VB edge, compared to TiO_2 alone.

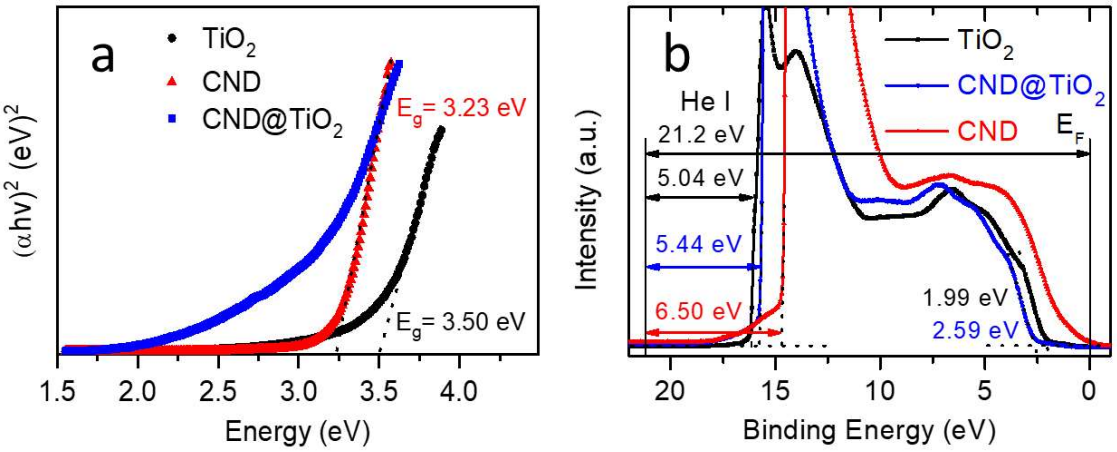

Figure 20. a) Tauc plot of $(\alpha hv)^2$ vs photon energy (hv) for the determination of the band gap energies for TiO_2, CND and CND@TiO_2 heterostructures. b) The ultraviolet photoelectron spectroscopy (UPS) spectra of CND, TiO_2 and CND@TiO_2 heterostructures used to calculate the work function. For TiO_2 NP and CND@TiO_2, the VB positions are also indicated (1.99 eV and 2.59 eV, respectively).

Based on the above analysis, the proposed photocatalytic mechanism of the CND@TiO_2 heterostructures is presented in Fig. 21. The energy levels of CND and TiO_2 before forming the heterostructure are shown in the box on the left-hand side of the figure. Whereas the Fermi level and the band gap of the present CND follow from the measurements shown in Fig. 20, the absolute position of the VB, i.e., the ionization energy has not been determined and the position shown represents a case where the Fermi level is close to the center of the band gap. Because of the intrinsic wide band gap of TiO_2, transitions localized at TiO_2 due to visible light can only occur due to defect levels within the bandgap. A similar situation occurs for CND where the absorption in the visible is also very weak. When the CND@TiO_2 heterostructures are formed (see the box on the right-hand side of the figure), the Fermi levels E_F align. Upon irradiation with visible light, because of the interaction between both constituents, transitions (shown in red in Fig. 21) are now possible from the HOMO of the CND towards the conduction band of the TiO_2. This is the origin of the long-wavelength tail of the absorption of CND@TiO_2 shown in Fig. 5c (red curve) and Fig. 20a (blue curve). The large width of this tail therefore seems to indicate a wide distribution of ionization energies of the CND. This may be related to a wide distribution of surface functional groups. The photo-induced electrons are able to stay in the CB of TiO_2 long enough to react with O_2 present in the suspension to produce $O_2^{\bullet-}$ radicals. Holes generated in the HOMO of CND can also transfer to the HOMO of RhB adsorbed to the hetero-structures favoring subsequent oxidation of the dye. According to the experiments with EDTA, scavenger of holes, however, this process appears to be of minor importance (compare Fig. 17). On the other hand, Fig. 21 also shows the existence of excited triplet states (or even higher spin states) of the CND, accessible under irradiation even by visible light, which are deactivated by collision with oxygen molecules, thus generating singlet oxygen [23], which further enhances the photo-degradation performance. All photo-catalytic processes discussed so far obviously

do not require optical excitation of the dye and cause the off-resonant part of the photo-catalytic degradation (Fig. 13).

In addition, photo-excitation of the dye (shown in blue in Fig. 21) produces electrons in the LUMO level of RhB (as well as Rh6G and MB), which are prone to transfer to the LUMO band of the CND and from there to the CB of TiO_2, further enhancing the photo-degradation performance by the formation of superoxide radicals. The remaining hole in the HOMO of RhB will again favor oxidation of the dye. This resonant process appears to be especially relevant for RhB (compare Fig. 13a) and implies the existence of a strong interaction of the dye with the CND@TiO_2 heterostructures, not present for TiO_2 alone, i.e., between the dye and the CND component. As stated above, the red shift of the resonant additional photo-degradation of the xanthene dyes shown in Fig. 13 is most likely due to this interaction. Concurrently, the absence of a resonant process in the case of the photocatalytic degradation by TiO_2 NP indicates that electrons in the LUMO of RhB cannot transfer to the CB of TiO_2, presumably because of a weak electronic interaction between the dye and TiO_2 NP. Finally, it should be remarked that enhanced intersystem crossing of the dyes adsorbed to CND can also be expected, because the CND are spin-active, as evidenced by their production of singlet oxygen. Enhanced intersystem crossing in turn enables another photo-catalytic degradation mechanism by the sensitization of singlet oxygen via the triplet state of the dyes.

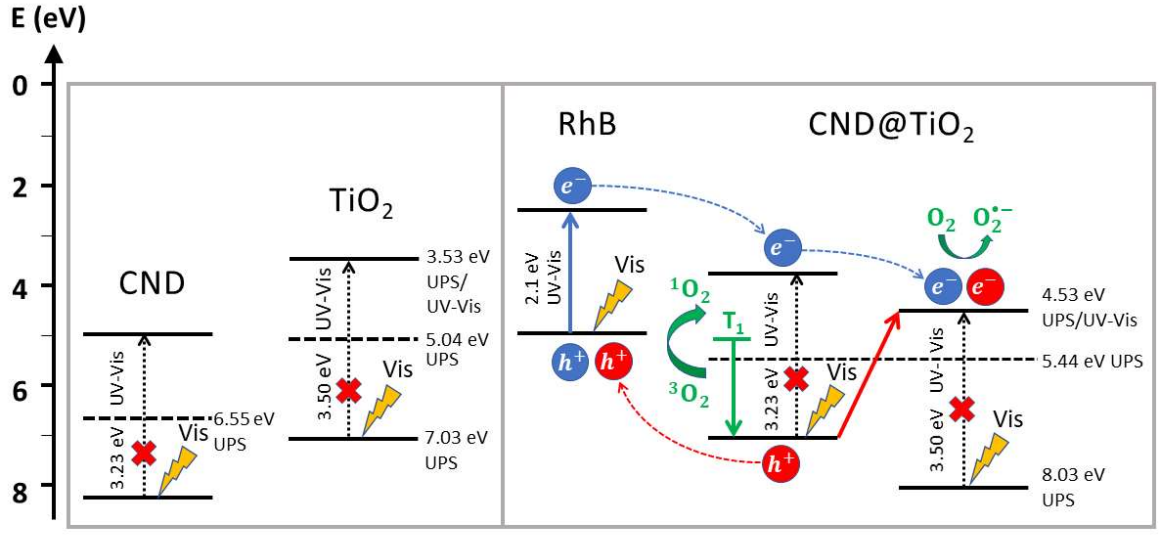

Figure 21. Schematic representation of the band alignments of CND and TiO_2 before (box on the left-hand side) and after (box on the right-hand side) forming the CND@TiO_2 heterostructure and adsorption of RhB. Two possible excitations by visible light are indicated in red and in blue including charge transfer processes after excitation (red and blue dashed lines, respectively). Fermi levels determined by UPS are shown as black dashed lines (compare Fig. 20b). Processes generating ROS are shown in green. (compare the main text).

Bactericidal activity of the CND@TiO_2 based surface nanocomposite films

CND and CND@TiO_2 heterostructures have been found to be efficient bactericidal materials in solution due to their photocatalytic properties upon visible light illumination causing oxidative damage to bacteria [46-47]. Here we designed a bactericidal PMMA surface nanocomposite film active under visible light by embedding and immobilizing the CND@TiO_2 heterostructures on the film surface. We assessed the bactericidal activity against *S. aureus*, as a model for Gram positive bacteria, and *E. coli* and *P. aeruginosa* as models for Gram negative bacteria. Following the ISO 22196 norm, we quantify the number of viable bacteria cells remaining on the surface of the nanocomposites as CFUs (Colony Forming Units) after 1 hour of visible light irradiation. Fig. 22 shows, in absolute numbers, the *S. aureus, P. aeruginosa* and *E. coli* live cells counted after irradiation of the bacteria on the samples and subsequent growth in the broth medium. The results indicate a clear bactericidal action of the PMMA-CND@TiO_2 nanocomposite films compared to the PMMA-TiO_2 and the pristine PMMA control surfaces. The number of *S. aureus* viable cells recovered from the PMMA-CND@TiO_2 surfaces decreased by 61% compared to PMMA and 29% compared to that of PMMA-TiO_2 control surfaces. The reduction obtained for other bacteria strains were, respectively 73% and 50%, for *P. aeruginosa* and 89% and 79% for *E. coli*. The enhanced bactericidal effect of the CND@TiO_2 nanocomposite under visible light compared to the TiO_2 nanocomposite films was thus particularly noteworthy for *E. coli*. The data presented in Figure 22 indicate that CND@TiO_2 nanocomposite has higher bactericidal efficacy toward both types of tested bacteria strains compared to the pristine control surfaces. This data is in agreement with previous studies where the bactericidal efficiency of CND@TiO_2 dispersions against Gram positive and Gram negative bacteria were investigated [48-49].

The bactericidal action of the PMMA- CND@TiO_2 surface nanocomposites arises from the oxidative stress to the bacteria induced by the reactive oxygen species (ROS) generated upon light exposure. Which ROS species are driving the bacterial damage to which degree is currently not known. According to the results presented in section 3.4, we can presume that the CND@TiO_2 surfaces exert their bactericidal action primarily through $O_2^{\bullet-}$ radicals and $^1O_2$

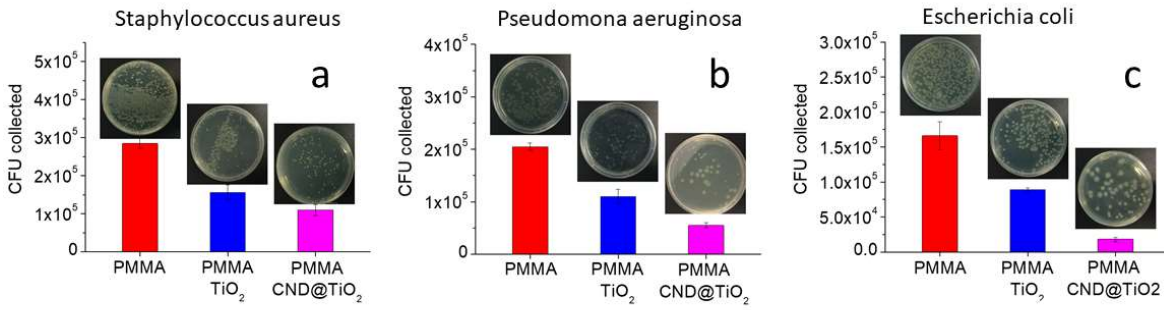

Figure 22. Bactericidal activity of PMMA-CND@TiO_2 surface nanocomposite and neat PMMA and PMMA-TiO_2 surface nanocomposite controls after exposure to visible light in CFU for a) S. aureus, (b) P. aeruginosa and (c) E. coli.

as these are the major ROS species detected. The level of ROS generated can cause irreversible damage to the bacteria membrane through oxidation of lipids and proteins which ultimately leads to bacterial death [50-51].

Up-conversion by CND

We have studied possible up-conversion by our CND, previously reported previously for similar samples even at excitation densities typical for fluorimeters. We have found no up-converted signals, neither in the fluorimeter nor with excitation by a high-power nanosecond optical parametric oscillator. Only in the case of focused excitation by a femtosecond regenerative amplifier we have indeed been able to observe up-conversion, presumably due to two-photon excitation, but not essentially different from up-conversion by a related conjugated small molecule, citrazinic acid, and only at excitation densities close to generation of a supercontinuum (see Fig. 23). This suggests that most reports of up-converted emission of CND are simply due to not blocking the second order of diffraction in the excitation monochromator of fluorimeters.

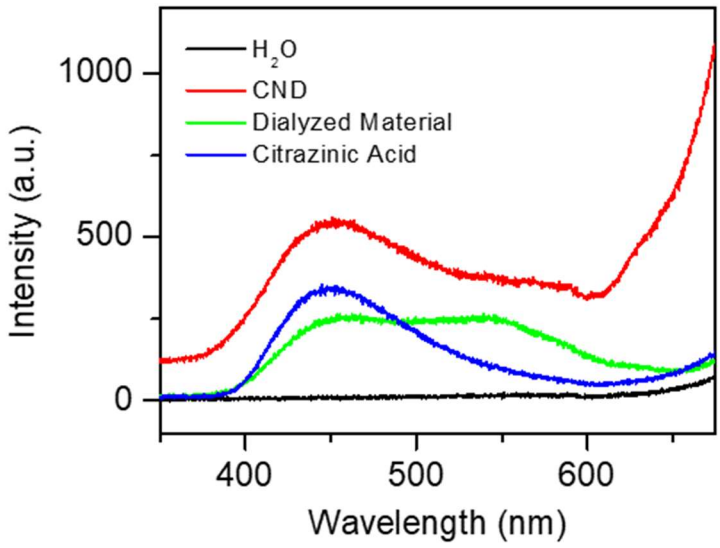

Figure 23. Up-conversion spectra of retentate and dialysate in aqueous solution, respectively. For comparison, the spectra obtained with citrazinic acid in aqueous solution and with distilled water alone are shown. Excitation by a regenerative amplifier, wavelength 775 nm, pulse width 150 fs, pulse energy 50 μJ, repetition rate 1 kHz, focused by a f=300 mm lens into the cuvette. The rise in intensity beyond λ≈600nm is due to scattered laser light.

4.3.4. Conclusions

Hydrothermal carbon dots have been prepared from citric acid and ethylene diamine and heterostructures with TiO_2 NP (CND@TiO_2) have been produced. Photodegradation of two xanthene dyes, RhB and Rh6G, as well as of MB in the presence and absence of the photocatalytically heterostructures CND@TiO_2 has been studied under illumination by different high-power visible light LED sources and compared with the degradation induced by TiO_2 alone. Photocatalytic action spectra of the xanthene dyes have also been obtained, with higher spectral resolution, employing a high-power tunable OPO laser. Different degradation pathways for the xanthene dyes and MB, respectively, are deduced from the different wavelength dependence of degradation. Whereas for MB a resonant contribution, i.e., enhanced photodegradation in the case of excitation in the absorption band, is observed already for the dye alone, this is not the case for RhB and Rh6G, not even in the presence of TiO_2. This is ascribed to a) different photophysics of the dyes, the reported intersystem crossing rate of MB exceeding the corresponding rates for RhB and Rh6G by two orders of magnitude and b) at least in the case of the xanthene dyes a relatively weak electronic interaction with the TiO_2 NP. Only in the presence of CND@TiO_2 a resonant contribution is also observed for RhB and Rh6G. This is ascribed to a strong interaction of the xanthene dyes with the CND component of the heterostructures. Photodegradation experiments of RhB with scavengers of $^1O_2$, $O_2^{-\bullet}$, $OH^\bullet$ and h^+ revealed that $^1O_2$ and $O_2^{-\bullet}$ are the dominant ROS species in the photodegradation, whereas $OH^\bullet$ and h^+ played only a minor role. On the other hand, the photocatalytic activity of the small molecule fraction produced in hydrothermal synthesis of the CND, which is always present even after prolonged dialysis, has been shown to be very low compared to that of CND@TiO_2 for equal absorption at 350 nm.

A remarkable bactericidal action of CND@TiO_2 nanocomposite surfaces under visible light against Gram-positive and Gram-negative bacteria has also been demonstrated. Hence, CND@TiO_2 nanocomposites may prove valuable to keep indoor surfaces germ-free without the need for application of hazardous biocides or ultraviolet light and in view of other potential applications in the biomedical field, food packing, building or furnishing industries. Finally, up-conversion processes have been revealed to be completely irrelevant for the photocatalytic activity of the present CND.

References

1. P. V. Kamat, TiO_2 Nanostructures: Recent Physical Chemistry Advances, J. Phys. Chem. C 116 (2012) 11849-11851, https://doi.org/10.1021/jp305026h.

2. H. Xu, S. Ouyang, L. Liu, P. Reunchan, N. Umezawa, J. Ye, Recent Advances in TiO_2-Based Photocatalysis. J. Mater. Chem. A 2 (2014) 12642-12661, https://doi.org/10.1039/C4TA00941J.

3. A. O. Ibhadon, P. Fitzpatrick, Heterogeneous Photocatalysis: Recent Advances and Applications, Catalysts 3 (2013) 189-218, https://doi.org/10.3390/catal3010189.

4. H. Zhang, X. Lv, Y. Li, Y. Wang, J. Li, P25-Graphene Composite as a High Performance Photocatalyst. ACS Nano 4 (2010) 380-386, https://doi.org/10.1021/nn901221k.

5. M. Haro, L. F. Velasco, C. O. Ania, Carbon-Mediated Photoinduced Reactions as a Key Factor in the Photocatalytic Performance of C/TiO_2. Catal. Sci. Technol. 2 (2012) 2264-2272, https://doi.org/10.1039/C2CY20270K.

6. K. Woan, G. Pyrgiotakis,W. Sigmund, Photocatalytic Carbon-Nanotube–TiO_2 Composites, Advanced Materials, 21 (2009) 2233-2239, https://doi.org/10.1002/adma.200802738.

7. A. Saha, A. Moya, A. Kahnt, D. Iglesias, S. Marchesan, R. Wannemacher, M. Prato, J. J. Vilatela, D. M. Guldi, Interfacial Charge Transfer in Functionalized Multi-Walled Carbon Nanotube@ TiO_2 Nanofibres. Nanoscale 9 (2017) 7911-7921, https://doi.org/10.1039/C7NR00759K.

8. G. Zhang, F. Teng, Y. Wang, P. Zhang, C. Gong, L. Chen, C. Zhao, E. Xie, Preparation of Carbon–TiO_2 Nanocomposites by a Hydrothermal Method and Their Enhanced Photocatalytic Activity. RSC Adv. 3 (2013) 24644-24649, https://doi.org/10.1039/C3RA44950E.

9. M. Han, S. Zhu, S. Lu, Y. Song, T. Feng, S. Tao, J. Liu, B. Yang, Recent Progress on the Photocatalysis of CNDs: Classification, Mechanism and Applications. Nano Today 19 (2018) 201-218, https://doi.org/10.1016/j.nantod.2018.02.008.

10. S. Young Park, H. Uk Lee, Y-C. Lee, S. Choi, D. Hyun Cho, H. Sik Kim, S. Bang, S. Seo, S. Chang Lee, J. Won, B-C. Son, M. Yang, J. Lee, Eco-Friendly Carbon-Nanodot-Based Fluorescent Paints for Advanced Photocatalytic Systems, Sci. Rep. 5 (2015) 12420-12427, https://doi.org/ 10.1038/srep12420.

11. Q. Wu, W. Li, P. Wu, J. Li, S. Liu, C. Jin, X. Zhan, Effect of Reaction Temperature on Properties of CNDs and their Visible-Light Photocatalytic Degradation of Tetracycline, RSC Adv. 5 (2015) 75711-75721, https://doi.org/10.1039/C5RA16080D.

12. D. Yan, Y. Liu, C-Y. Liu, Z-Y. Zhang, S-D. Nie, Multi-Component in situ and in-Step Formation of Visible-Light Response C-Dots Composite TiO_2 Mesocrystals, RSC Adv. 6 (2016) 14306-14313, https://doi.org/10.1039/C5RA24475G.

13. M. C. Ortega-Liebana, J. L. Hueso, S. Ferdousi, K. L. Yeung, J. Santamaria, Nitrogen-Doped Luminescent CNDs for Optimal Photo-Generation of Hydroxyl Radicals and Visible-Light Expanded Photo-Catalysis, Diamond & Related Materials 65 (2016) 176–182, https://doi.org/ 10.1016/j.diamond.2016.03.021.

14. G. B. Markad, S. Kapoor, S. K. Haram, P. Thakur, Metal Free, Carbon-TiO_2 Based Composites for the Visible Light Photocatalysis, Solar Energy 144 (2017) 127–133, https://doi.org/ 10.1016/j.solener.2016.12.025.

15. M. Sun, S. Qu, W. Ji, P. Jing, D. Li, L. Qin, J. Cao, H. Zhang, J. Zhao, D. Shen, Towards Efficient Photoinduced Charge Separation in CNDs and TiO_2 Composites in the Visible Region, Phys. Chem. Chem. Phys. 17 (2015) 7966-7971, https://doi.org/10.1039/C5CP00444F.

16. N. Mas, J. L. Hueso, G. Martinez, A. Madrid, R. Mallada, M. C. Ortega-Liebana, C. Bueno-Alejo, J. Santamaria, Laser-Driven Direct Synthesis of CNDs and Application as Sensitizers for Visible-Light Photocatalysis, Carbon, 156 (2020) 453-462, https://doi.org/10.1016/j.carbon.2019.09.073

17. V. Georgakilas, J. A. Perman, J. Tucek, R. Zboril, Broad Family of Carbon Nanoallotropes: Classification, Chemistry, and Applications of Fullerenes, CNDs, Nanotubes, Graphene, Nanodiamonds, and Combined Superstructures, Chem. Rev. 115 (2015) 4744-4822, https://doi.org/10.1021/cr500304f.

18. H. Li, X. He, Z. Kang, H. Huang, Y. Liu, J. Liu, S. Lian, A. T. Chi Him, X. Yang, S-T. Lee, Water-Soluble Fluorescent Carbon Quantum Dots and Photocatalyst Design, Angew. Chem. Int. Ed. Engl. 49 (2010) 4430-4434, https://doi.org/10.1002/anie.200906154.

19. J. Ke, X. Li, Q. Zhao, B. Liu, S. Liu, S. Wang, Upconversion Carbon Quantum Dots as Visible Light Responsive Component for Efficient Enhancement of Photocatalytic Performance, J. Colloid Interface Sci. 496 (2017) 425-433, https://doi.org/10.1016/j.jcis.2017.01.121

20. Y. Hu, X. Xie, X. Wang, Y. Wang, Y. Zeng, D. Y. H. Pui, J. Sun, Visible-Light Upconversion Carbon Quantum Dots Decorated TiO_2 for the Photodegradation of Flowing Gaseous Acetaldehyde, Applied Surface Science 440 (2018) 266-274, https://doi.org/10.1016/j.apsusc.2018.01.104.

21. Z. Gan, X. Wu, G. Zhou, J. Shen, P. K. Chu, Is There real Upconversion Photoluminescence from Graphene Quantum Dots? Advanced Optical Materials 1 (2013) 554-558, https://doi.org/10.1002/adom.201300152.

22. Y. Song, S. Zhu, S. Zhang, Y. Fu, L. Wang, X. Zhao, B. Yang, Investigation from Chemical Structure to Photoluminescent Mechanism: A Type of Carbon Dots from the Pyrolysis of Citric Acid and an Amine, J. Mater. Chem. C 3 (2015) 5976-5984, https://doi.org/10.1039/C5TC00813A.

23. S. Ramírez-Barroso, A. Jacobo- Martín, I. Navarro-Baena, J. J. Hernández, C. Navio, I. Rodríguez, R. Wannemacher, On the Nature of Solvothermally Sinthesized CNDs, J. Mat. Chem. C 9 (2021) 16935-16944, https://doi.org/10.1039/D1TC04255F.

24. J. B. Essner, J. A. Kist, L. Polo-Parda, G. A. Baker, Artifacts and Errors Associated with the Ubiquitous Presence of Fluorescent Impurities in CNDs, Chem. Mater 30 (2018) 1878-1887, https://doi.org/10.1021/acs.chemmater.7b04446

25. J. Schneider, C. J. Reckmeier, Y. Xiong, M. von Seckendorff, A. S. Susha, P. Kasák, A. L. Rogach, Molecular Fluorescence in Citric Acid-Based Carbon Dots, J. Phys. Chem. C 121 (2017) 2014-2022, https://doi.org/10.1021/acs.jpcc.6b12519.

26. L. Shi, J. H. Yang, H. B. Zeng, Y. M. Chen, S. C. Yang, C. Wu, H. Zeng, O. Yoshihito, Q. Zhang, Carbon Dots with High Fluorescence Quantum Yield: the Fluorescence Originates from Organic Fluorophores, Nanoscale 8 (2016) 14374-14378, https://doi.org/10.1039/C6NR00451B.

27. J. B. Essner, D. J. Boogaart, S. N. Baker, G. A. Baker, Effects of Carbon Nanodot Fraction on the Performance of Sensitized Mesoporous Titania Based Photovoltaic Devices, J. Mater. Chem. C 10 (2022) 8824-8833, https://doi.org/10.1039/D2TC00454B.

28. B. Bartolomei, A. Bogo, F. Amato, G. Ragazzon, M. Prato, Nuclear Magnetic Resonance Reveals Molecular Species in Carbon Nanodot Samples Disclosing Flaws, Ang. Chem. Int. Ed. 61 (2022) 1-6, https://doi.org/10.1002/ange.202200038.

29. G. Minervini, A. Panniello, A. Madonia, C. M. Carbonaro, F. Mocci, T. Sibillano, C. Gianini, R. Comparelli, C. Ingrosso, N. Depalo, E. Fanizza, M. L. Curri, M. Striccoli, Photostable Carbon Dots with Intense Green Emission in an Open Reactor Synthesis, Carbo n 198 (2022) 230-243, https://doi.org/10.1016/j.carbon.2022.07.034.

30. M. C. Ortega-Liebana, J. L. Hueso, S. Ferdousi, R. Arenal, S. Irusta, K. L. Yeung, J. Santamaria, Extraordinary Sensitizing Effect of Co-doped CNDs Derived from Mate Herb: Application to Enhanced Photocatalytic Degradation of Chlorinated Wastewater Compounds Under Visible Light, Applied. Catalysis B: Enviromental 218 (2017) 68-79, https://doi.org/10.1016/j.apcatb.2017.06.021.

31. X. Wen, P. Yu, Y-R. Toh, X. Ma, J. Tang, On the Upconversion Fluorescence in CNDs and Graphene Quantum Dots, Chem. Commun. 50 (2014) 4703-4706, https://doi.org/10.1039/C4CC01213E.

32. S. Ren, Y. Wang, G. Fan, R. Gao, W. Liu, Sandwiched ZnO@Au@CdS Nanorod Arrays with Enhanced Visible-Light-Driven Photocatalytical Performance, Nanotechnology 28 (2017) 465403-1-465403-9, https://doi.org/10.1088/1361-6528/aa8d43.

33. S. Bagheri, K. Shameli, S. B. Abd Hamid, Synthesis and Characterization of Titanium Dioxide Nanoparticles Using Egg White Solution via Sol-Gel Method, Journal of Chemistry 2013 (2012) 1-5, https://doi.org/10.1155/2013/848205.

34. C. Ronchi, F. A. Soria, L. Ferraro, S. Botti, C. Di Valentin, Absorption Mechanism of Dopamine/DOPAC-Modified TiO_2 Nanoparticles by Time-Dependent Density Functional Theory Calculations, Mater. Today Energy 19 (2021) 100571-100594, http://dx.doi.org/10.1016/j.mtener.2020.100571.

35. S. Ayissi, P. A. Charpentier, K. Palotás, N. Farhangi, F. Schwarz, W. A. Hofer, Preferential Adsorpion of TiO_2 Nanostructures on Functionalized Single-Walled Carbon Nanotubes: A DFT Study, J. Phys. Chem. C 119 (2015) 15085-15093, https://doi.org/10.1021/acs.jpcc.5b01406.

36. M. Pastore, E. Mosconi, S. Fantacci, F. De Angelis, Compuational Investigations on Organic Sensitized for Dye-Sensitized Solar Cells, Current Organic Synthesis 9 (2012) 215-232, https://doi.org/10.2174/157017912799828987

37. A. R. S. Kandada, S. Fantacci, S. Guarnera, D. Polli, G. Lanzani, F. De Angelis, A. Petrozza, Role of Hot Singlet Excited States in Charge Generation at the Black Dye/TiO_2 Interface, ACS Appl. Mater. Interfaces 5 (2013) 4334-4339, https://doi.org/10.1021/am400530v.

38. F. De Angelis, S. Fantacci, E. Mosconi, M. K. Nazeeruddin, M. Grätzel, Absorption Spectra and Excited State Energy Levles of the N719 Dye on TiO_2 in Dye-Sensitized Solar Cell Models, J. Phys. Chem. C 115 (2011) 8825-8831, https://doi.org/10.1021/jp111949a

39. C. Lin, Y. Liu, D. Shao, G. Wang, H. Xu, C. Shao, W. Zhang, Z. Yang, Density Functional Theory Design of Double Donor Dyes and Electron Transfer on Dye/TiO_2 (101) Composite Systems for Dye-Sensitized Solar Cells, RSC. Adv. 11 (2021) 3071-3078, https://doi.org/10.1039/D0RA08815C.

40. F. Rodrigo, I. P. Mihalis, A. C. John, Glutathione Depletion is Necessary for Apoptosis in Lymphid Cells Independent of Reactive Oxygen Species Formation, J. Biol. Chem. 282 (2007) 30452-30465, https://doi.org/10.1074/jbc.M703091200.

41. B. Shen, R. G. Jensen, H. J. Bohnert, Mannitol Protects against Oxidation by Hidroxyl Radials, Plant. Physiol. 115 (1997) 527-532, https://doi.org/10.1104/pp.115.2.527.

42. T. Bleeke, H. Zhang, N. Madamanchi, C. Patterson, J. E. Faber, Catecholamine-Induced Vascular Wall Growth is Dependent on Generation of Reactive Oxygen Species, Circ. Res. 94 (2004) 37-45, https://doi.org/10.1161/01.RES.0000109412.80157.7D.

43. T. Liu, L. Wang, X. Lu, J. Fan, X. Cai, B. Gao, R. Miao, J. Wang, Y. Lv, Comparative Study of the Photocatalytic Performance for the Degradation of Different Dyes by $ZnIn_2S_4$: Adsorption, Active Species, and Pathways, RSC. Adv. 7 (2017) 12292-12300, https://doi.org/10.1039/C7RA00199A.

44. M. M. Ali, J. S. Arya Nair, K. Y. Sandhya, Role of Reactive Oxygen Species in the Visible Light Photocatalytic Mineralization of Rhodamine B dye by P25–Carbon Dot Photocatalyst, Dyes and Pigments 163 (2019) 274–284, https://doi.org/S014372081831787X.

45. A. Jiménez-Banzo, X. Ragàs, P. Kapusta, S. Nonell, Time-Resolved Methods in Biophysics. Photon Counting vs. Analog Time-resolved Singlet Oxygen Phosphorescence Detection, Photochem. Photobiol. Sci. 7 (2008) 1003–1010, https://doi.org/10.1039/B804333G.

46. M. Varghese, M. Balachandran. Antibacterial efficiency of carbon dots against Gram-positive and Gram-negative bacteria: A review. J. Environ. Chem. Eng. 9 (2021) 106821. https://doi.org/10.106/j.jece.2021.106821

47. Y. Wu, C. Li, H.C. van der Mei, H.J. Busscher, Y. Ren, Carbon quantum dots derived from different carbon sources for antibacterial applications. Antibiotics 10 (2021) 623. https://doi.org/10.3390/antibiotics10060623

48. Q. Xu, H. Cai, W. Li, M. Wu, Y. Wu, X. Gong, Carbon dot/inorganic nanomaterial composites. J. Mater. Chem. A 10 (2022) 14709-14731. https://doi.org/10.1039/D2TA02628G

49. Y. Yan, W. Kuang, L. Shi, X. Ye, Y. Yang, X. Xie, Q. Shi, S. Tan, Carbon quantum dot-decorated TiO_2 for fast and sustainable antibacterial properties under visible-light. J. Alloys Compd. 777 (2019) 234-243. https://doi.org/10.1016/j.jallcom.2018.10.191

50. Y. Li, W. Zhang, J. Niu, Y. Chen, Mechanism of photogenerated reactive oxygen species and correlation with the antibacterial properties of engineered metal-oxide nanoparticles. ACS Nano 6 (2012) 5164-5173. https://pubs.acs.org/doi/abs/10.1021/nn300934k

51. A. Sirelkhatim, S. Mahmud, A. Seeni, N. H. M. Kaus, L. C. Ann, S. K. M. Bakhori, H. Hasan, D. Mohamed, Review on Zinc Oxide Nanoparticles: Antibacterial Activity and Toxicity Mechanism, Nano-Micro Lett. 7 (2015) 219–242, https://doi.org/10.1007/s40820-015-0040-x.

Chapter 4:

Photophysics of Curved Molecular Nanographenes

Chapter 4: Photophysics of Curved Molecular Nanographenes

4.4.1. Introduction

The synthesis and characterization of molecular nanographenes (NGs), doped or not with heteroatoms, has been intensively investigated in recent years in view of their wide range of applications, such as the development of self-assembled nanomaterials or in fields like photocatalysis, energy conversion and storage, optoelectronics, single-molecule electronics, spintronics and magnetoelectronics, molecular switches and sensors or in multiphotonic processes, nonlinear optics and bioimaging.[1] The structural features of molecular nanographenes include hydrogen-terminated or edge-functionalized polycyclic aromatic hydrocarbons (PAHs);[2] heteroatom-doped NGs having heterocyclic motifs;[1b,d,e,h] or topologically complex curved NGs containing helicene moieties plus combinations of eight-, seven- and/or five-membered rings into the hexagonal carbon lattice of graphene.[3] Compared to graphene, whose overlapping conduction and valence bands pose limits to the development of some applications, NGs exhibit a non-zero energy gap, thus broadening the scope of its potential uses.

The chemical induction of well-defined curvatures in molecular nanographenes (often with inherent chirality) leading to curved nanographenes (CNGs), as well as steric interactions, may allow the fine tuning of their excited-state energy levels and, therefore, of their photophysical properties. In fact, this can be a promising strategy to obtain organic materials with interesting features related to appropriate relative energy differences and distributions of the singlet and triplet excited states manifolds. Examples of appealing unimolecular photophysical properties of organic materials would be dual fluorescence, phosphorescence, and thermally activated delayed fluorescence (TADF).[4] Furthermore, the peculiar topology and hydrophobicity of CNGs may allow bimolecular pathways based on interactions with other molecular entities or surfaces, giving rise to energy or electron transfer photoprocesses (e.g., Förster resonance, type II or type I photosensitization, etc.) that may advantageously broaden the field of application of CNGs.[5] All these distinctive emissions or excited-state reaction paths are susceptible of application in diverse areas such as quenching-based sensing of chemical species, data encryption, 3D printing, as emitters in organic light emitting diodes (OLEDs), or in theranostics combining bioimaging (avoiding interference by the autofluorescence of biological samples) and photosensitization properties of reactive oxygen species (in photodynamic therapy treatments).[6] In particular, unimolecular deactivation pathways resulting in phosphorescence and TADF, when combined with chirality, are amenable for the smart development of high performance optoelectronic applications like data storage, security tags, chirality sensing, and next-generation displays.[7]

Phosphorescence is generated through two consecutive intersystem crossing (ISC) steps, the non-radiative $S_1 \rightarrow T_1$ ISC and the radiative $T_1 \rightarrow S_0$ transition, which are both spin-forbidden processes because of the different multiplicity of the initial and final states involved in the transition. Therefore, the rate constant of intersystem crossing (k_{ISC}) from singlet excited state to triplet excited state is small and the quantum yield of the intersystem crossing (Φ_{ISC})

is low, so the population of triplet excited state is not favored. However, even if the triplet excited state can be populated, due to the generally small rate constant of phosphorescence decay (k_P) and the relatively large rate constant of nonradiative deactivation (k_{nr}) and quenching process (k_q) of the excited triplet at room temperature, it is still challenging to obtain organic materials with high phosphorescence quantum yields (Φ_P) at room temperature. Several strategies have been developed to improve the quantum yields of ISC and of organic phosphorescence. For example, in organic systems with aldehyde or ketone functional groups, the presence of n→π* transitions has been reported to mediate the ISC process and significantly enhance k_{ISC} and increase Φ_{ISC}. Alternatively, by introducing heavy atom functional groups such as bromine and iodine substituents into organic molecules, the heavy atom effect (HAE) can enhance spin-orbit coupling (SOC), and thus facilitate the ISC process, promoting k_P and improving Φ_P.[8] However, HAE also shortens the phosphorescence lifetime (τ_P). On the other hand, rigid crystalline and glassy environments have been used to restrict intramolecular deactivation routes such as vibrational and rotational motions causing decay of the triplet excited states. These rigid environments inhibit non-radiative decay pathways, decrease k_{nr} and k_q of the triplet excited states and improve Φ_P of organic systems at room temperature. Moreover, modifying the molecular packing, or adding supramolecular interactions like inclusion complexation and hydrogen bonding can also contribute to suppress the molecular vibrations of the triplet excited states in order to increase Φ_P.[9]

Up-conversion between the lowest triplet and singlet excited states, through reverse intersystem crossing (RISC) gives rise to TADF, provided the energy barrier among both types of excited states is low enough and ambient thermal energy allows the radiative-forbidden triplets to be up-converted effectively to the radiative-allowed singlet state, thanks to a tiny singlet–triplet splitting energy ($\Delta E_{S\text{-}T}$), typically below 0.5 eV. Therefore, reducing the energy gap between the lowest excited singlet state and its nearest triplet state is of major importance in the case of TADF. This has been generally achieved by synthesizing organic dyes containing suitable combinations of electron-donor (D) and electron-acceptor (A) moieties connected together via different types of bridges, usually with high twists or nonconjugated connections to obtain reduced overlaps between the highest occupied molecular orbitals (HOMOs, ideally located in the donor part) and lowest unoccupied molecular orbitals (LUMOs, preferably located in the acceptor fragment). These molecular architectures provide smaller overlap integrals between the HOMO and the LUMO, resulting in tiny energy differences between the first singlet (S_1) and triplet (T_1) excited states, thus allowing high RISC. In these molecules, intramolecular charge-transfer (CT) between D and A moieties is the dominant transition, leading to a lowest singlet state with CT character. Appropriately designed TADF dyes often rely on one of the following strategies: i) inducing a large steric hindrance in D-A molecular systems to produce a twisted intramolecular charge transfer (TICT) state; ii) allowing a through-space charge transfer (TSCT) with nonconjugated linkers by controlling the distance between the D and A units and also their relative orientation; or iii) taking advantage of multiple resonance effects in heteroaromatic compounds (e.g., with trisubstituted sp^2 heteroatoms, such as boron or nitrogen with π-conjugated connections to either π-donor or

π-acceptor groups). Moreover, the so-designed dyes display restricted rotation and increase the molecular rigidity, which suppresses the nonradiative deactivation and can also help avoiding severe aggregation causing efficient excited state deactivation.[10] Interestingly, the presence of high-lying triplet states (T_n) can also help to promote TADF, and dyes taking advantage of reverse intersystem crossing from high-lying triplet state (hRISC) where energy up-conversion from a higher triplet state (T_n, $n \geq 2$) to the S_1 state occurs, have recently been described.[11]

Furthermore, it has to be noted that chiral dyes exhibiting TADF properties combined with circularly polarized (CP) luminescence can show great potential in empowered OLED systems applied to high quality 3D, augment-reality, and virtual reality displays.[12] In principle, CP-TADF systems would only require the addition of a chiral moiety (either a stereocentre, a chiral axis, or a planar chirality element) to the TADF dye. However, development of efficient CP-TADF dyes is a challenging issue since several problems beyond their complex synthesis can occur, such as a low luminescence dissymmetry factor (g_{lum}) value if the chiral moiety is not directly involved in the frontier molecular orbitals responsible for the lowest-lying electronic transition. Moreover, although reduced HOMO-LUMO overlap is required for low $\Delta E_{S\text{-}T}$ values and efficient TADF (usually at the expense of sacrificing color purity), large HOMO-LUMO overlaps would, in contrast, improve g_{lum} values by increasing the angle between the electric transition dipole moment and the magnetic transition dipole moment.[7,13]

Herein we report on the unusual photophysics of three different curved nanographenes (CNGs 6, 7 and 8) shown in Figure 1.[14] The studied CNGs are composed of a corannulene fragment of positive curvature and a modified hexabenzocoronene fragment that can impart negative curvature via a seven-membered ring connection between the terminal rings of a [6]helicene (Figure 1). Depending on the type of attachment between both fragments, by forming either a loose-helicene (CNG 6), a cycloheptatrienically constrained helicene (CNG 8) or a cycloheptatrienically and sterically constrained helicene (CNG 7), distinct and valuable photophysical properties can be observed. Additionally, it must be mentioned that all the CNGs under study are inherently chiral and have been synthesized as racemic mixtures.[14,15]

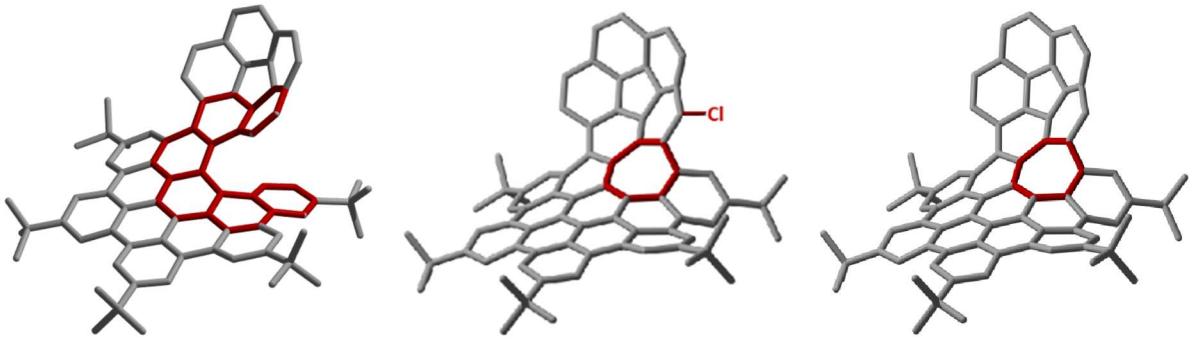

Figure 1. Curved nanographenes (CNGs) 6, 7 and 8 (only one enantiomer shown). The loose [6]helicene of 6, the chlorine atom of 7 and the cycloheptatrienically-constrained [6]helicene of 7 and 8 (due to the presence of the seven-membered ring) are highlighted in red.

The presence of curvature and torsion in the studied CNGs can significantly modify the energy levels of their electronic excited states, the vibronic coupling among them, and even give rise to distinct and dissimilarly populated excited state minima. In this way, the lower energy gaps between excited states, and also the accessible positions and energy barriers of their conical intersections can modulate the quantum efficiency of the relaxation processes from higher energy singlet excited states to the lowest energy singlet (S_1) and even from there to the ground state (S_0), allowing competitive processes that may involve decoupling of upper singlet excited states and population of a local minimum of S_1 (leading to dual fluorescence emission as clearly observed in CNG 7), or to coupled singlet and triplet excited states (allowing phosphorescence and/or TADF emissions in certain temperature ranges for all the CNGs).

Therefore, these novel chiral molecular nanographene architectures pave the way for a new series of non-metal, non-D/A-type TADF dyes, displaying relatively narrow-band TADF emission via hRISC from high-lying triplet states, where concurrent TADF + CPL may be exploited for the future development of high performance optoelectronic devices.

4.4.2. Experimental Section

UV-VIS absorption spectra were recorded in a Varian Cary 5000 UV-VIS-NIR spectrophotometer. Emission spectra were acquired in a Fluoromax-4 Horiba spectrofluorometer. PL lifetime (τ_F) experiments were performed by the time-correlated single photon counting (TCSPC) technique with an Acton SP2500 spectrometer (PicoQuant) equipped with a PicoHarp300 TCSPC board (PicoQuant) and a PMA 06 photomultiplier (PicoQuant). A HydraHarp-400 TCSPC event timer with 1 ps time resolution was used to measure the PL decays. The excitation source was a 405 nm picosecond pulsed diode laser (LDH-D-C-405, PicoQuant) driven by a PDL828 driver (PicoQuant) with FWHM < 70ps. Decays were analyzed using PicoQuant Fluofit v4.6.5 data analysis software. The deactivation of the excited state is adjusted by equation (1).

$$I(t) = \int_{-\infty}^{t} IRF(t') \sum_{i=1}^{n} A_i \, e^{-\frac{t-t'}{\tau_i}} \, dt' \quad \text{eq. 1}$$

Concerning the emission quantum yields determined for CNGs **6**, **7** and **8** were determined at room temperature, using N_2 purged solutions with optical densities < 0.1 at 300 and 470 nm, by comparison with the corresponding emission spectrum of quinine sulfate in H_2SO_4 0.05 M ($\phi_{fluorescence}$ = 0.55 ± 0.03) and fluorescein in NaOH 0.1 M ($\phi_{fluorescence}$ = 0.91 ± 0.05), respectively. Identical emission wavelength ranges were used for all the samples in order to determine the areas under the spectral curves (for the λ_{exc} = 300 nm the λ_{em} = 410-600 nm and for the λ_{exc} = 470 nm the λ_{em} = 480-700 nm) . The optical density of each solution was checked before and after collection of the corresponding emission spectrum. In these conditions, the unknown Φ_{fluo} values were calculated as follows:

$$\Phi_{fl} = \Phi_{fl\,Ref} \frac{I}{I_{Ref}} \frac{A_{Ref}}{A} \frac{n^2}{n_{Ref^2}} \quad \text{eq. 2}$$

where, Φ_{fluo} is the fluorescence quantum yield of the sample, I is the integrated area of the emission intensity under the spectral curve, A is the absorbance at the excitation wavelength, and n is the refractive index of the solvent (1.332988 for water, 1.361 for ethanol and 1.4459 for chloroform).

The 1,3-Diphenylisobenzofuran was used to evaluate the singlet oxygen production of the CNGs. A blue light emitting diode (LED) was used as the light source (λ_C = 446 nm). The illumination intensity at the sample was set to the same value in these experiments (12,9 W/cm^2). (17 V, 1 A, 15 cm). To ensure that an equal number of photons were absorbed per unit time in all experiments, the concentration for each dye was adjusted at an absorbance value of ~0.10 at the λ_{exc} = 446 nm. Bleaching of DPBF by singlet oxygen can be monitored by its absorbance at ~410 nm and/or its fluorescence at 457 nm. The observed rate constants (k_{obs}) were obtained by a linear least-squares fit of the plot of Abs or Em versus time. The values of singlet oxygen quantum yields (Φ_Δ) were calculated with respect to phenalenone used as references (Φ_Δ = 1.0 ± 0.5).

$$\Phi_\Delta^{PS} = \frac{\Phi_\Delta^{Ref} k_{obs}^{PS} Abs_0^{Ref}}{k_{obs}^{Ref} Abs_0^{PS}} \frac{n^2}{n_{Ref^2}} \quad \text{eq. 3}$$

where Φ_Δ is the quantum yield singlet oxygen production of the sample, k_{obs} and $is$the rate constanst observed in a linear least-squares fit of the plot of Em vs time, Abs_0 is the initial absorbance of each photosensitizer at maximum absorption wavelengths, and and n is the refractive index of the solvent (1.332988 for water and 1.4459 for chloroform).

4.4.3. Results and discussion

Absorption and fluorescence excitation and emission spectra at room temperature

The UV–vis absorption spectra of CNGs 6, 7 and 8, and of their structural precursors corannulene (Cor) and terc-butylated hexabenzocoronene (HBC-tBu) in $CHCl_3$ are shown in Figure 2. Table 1 collects the spectral data of CNGs 6, 7, 8, Cor and HBC-tBu. The absorption spectra of the CNGs resembles that of their structural precursors, however, the vibronic fine structure of HBC-tBu in the UV–vis spectrum is missing in the CNGs. In turn, the molecular nanographenes show broad absorption bands with sparse peaks and shoulders due to strong overlap of vibronic modes. In addition, CNGs have a relatively intense absorption band in the visible region compared to their structural precursors, evidencing the occurrence of allowed electronic transitions in the low-energy spectral interval, conversely to structurally rigid HBC-tBu. All this is a direct consequence of the extended π-conjugated domain in the non-symmetrical curved nanographenes showing conformational pseudorotations. Furthermore, the presence of a cycloheptatrienic connection within the [6]helicene moiety causes a red shift of about 20 nm of the visible absorption band when comparing CNGs 7 and 8 with CNG 6 (ca.

+ 60 nm vs HBC-tBu) which is an interesting feature for devising optoelectronic applications deployed with visible light excitation.

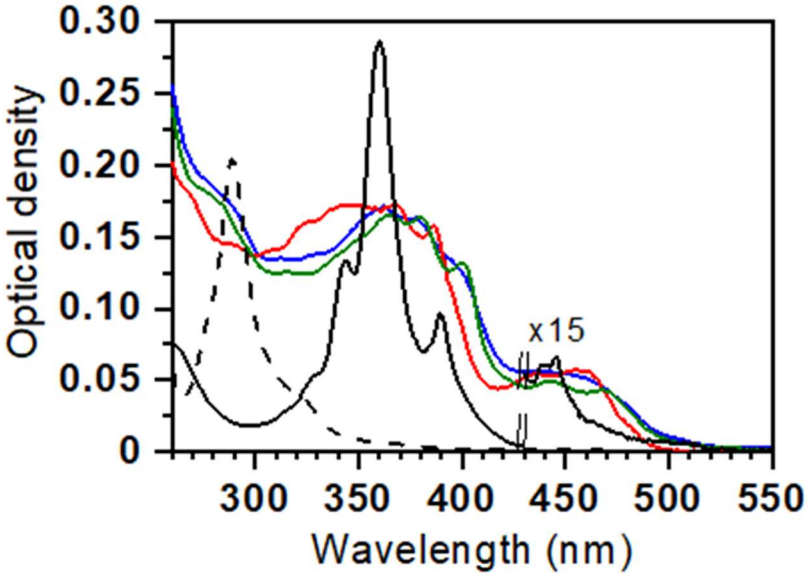

Figure 2. Absorption spectra in chloroform at room temperature of CNGs 6 (red), 7 (green) and 8 (blue) and of their structural precursors Cor (black dash) and HBC-tBu (black). The visible portion of the HBC-tBu absorption spectrum (≥ 430 nm) has been magnified (×15).

Table 1. Spectral data of the investigated compounds and of their structural precursors at room temperature.

CNG	λ_{abs}^{max} [nm][a)]	ε [mol^{-1} dm^3 cm^{-1}]	λ_{fluo}^{max} (FWHM) [nm][b)] ([eV, nm])
Cor	289, 318 sh	31000, 6600	**420**, 440[c)]
HBC-*t*Bu	344, 360, 390, 445	64000, 142000, 46000, 1800	474, **483**, 492, 517[d)]
6	346, 367, 386, 436, 456	73000, 72000, 65000, 21000, 22000	**490**, 519 (0.30, 62)
7	367, 380, 401, 443, 467	77000, 76000, 62000, 23000, 20000	430, **507**, 530 (0.25, 56)
8	362, 378, 441	68000, 64000, 20000	493, **523**, 557 sh (0.32, 75)

[a)]Absorption peaks and shoulders (sh) in chloroform; [b)]Emission peaks in chloroform with the fluorescence maxima highlighted in bold numbers; [c)]In dichloromethane;[16] [d)]In tetrahydrofurane.[17]

Regarding the green fluorescence of CNGs at room temperature, their excitation-emission maps are shown in Figure 3, and their corresponding fluorescence maxima from spectra acquired with excitation at the absorption maximum in the visible are gathered in Table 1. Individual excitation and emission spectra at selected wavelengths show, however, remarkable differences despite the apparent structural similarity of the molecular nanographenes (Figure 4).

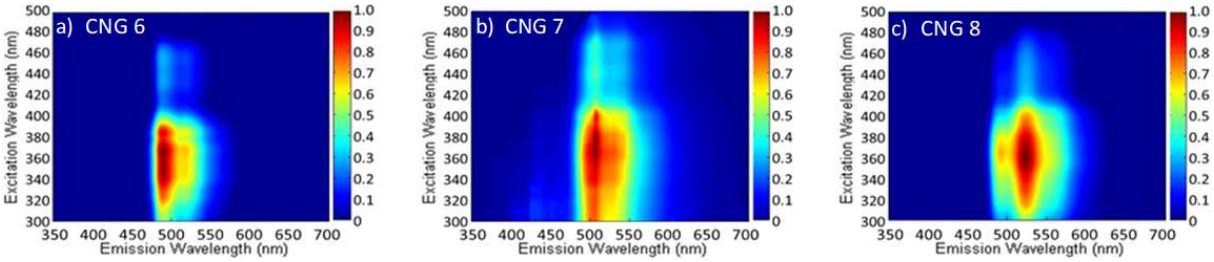

Figure 3. Excitation-emission maps of CNGs 6, 7 and 8 in $CHCl_3$ at room temperature.

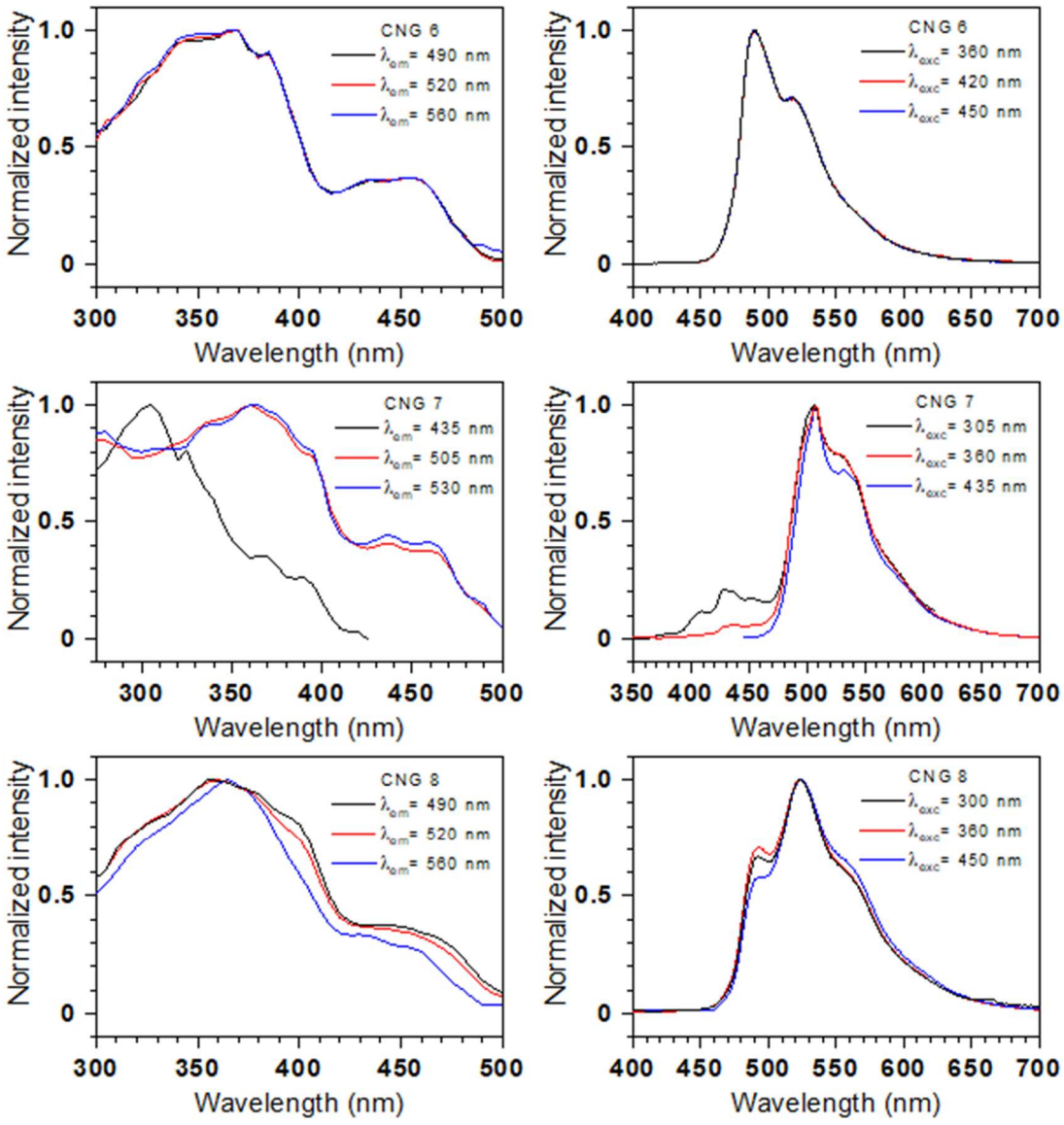

Figure 4. Fluorescence excitation spectra (left) and emission spectra (right) of CNGs 6 (top), 7 (middle) and 8 (bottom) in chloroform at room temperature, collected at different emission and excitation wavelengths, respectively.

The excitation and emission spectra of CNG 6 show homogeneous behavior regardless of the selected measurement wavelength, and perfect agreement between the UV–vis absorption and excitation spectra has been observed. Similarly, no changes with excitation wavelength have been observed in the emission spectra of CNG 6 that shows a maximum at 490 nm and a red-shifted secondary peak at 519 nm. On the other hand, this homogeneity is not observed in the excitation and emission spectra of CNGs 7 and 8.

In the case of CNG 8, a slight broadening of the emission spectrum and a noticeable narrowing of the excitation spectrum can be observed with the increasing excitation and emission wavelengths, respectively. 8 has an emission maximum at 523 nm, a shoulder at 557 nm, and a secondary emission peak at 493 nm (with varying intensity ratios with respect to the primary peak), however, only the excitation spectrum collected at 520 nm accurately reproduces the absorption spectrum, while the excitation spectrum collected at 560 nm is 15-20 nm blue-shifted. Furthermore, the intensity ratio between the emission maximum at 523 nm and the secondary peak at 493 nm changes with the excitation wavelength (relative intensity at 493 nm of 0.59 for λ_{exc} = 450 nm, but 0.72 for λ_{exc} = 360 nm). Compared to CNG 6, these spectral differences observed in the cycloheptatrienically constrained helicene CNG 8 could be relating the important changes regarding the molecular structure to changes affecting not only the sublevels of the vibrational and pseudorotational modes but also the electronic energy levels of its singlet excited states.

Concerning the excitation spectra of CNG 7, a very strong shift of ca. 80 nm can be observed depending on the selected emission wavelength. In this sense, while excitation spectra like the absorption spectrum of CNG 7 can be recorded at 505 or 530 nm, a blue-shifted excitation spectrum (resembling the absorption spectrum of corannulene) is acquired when the emission monochromator is set at 435 nm or below. On the other hand, the intensity ratio between the emission maximum at 507 nm and the shoulder at 530 nm changes with the excitation wavelength (relative intensity at 530 nm of 0.72 for λ_{exc} = 435 nm and 0.79 for λ_{exc} = 305 nm). Remarkably, a new emission band centered at 430 nm, which can represent up to 25% of the area under the emission spectrum, also changes its relative intensity with excitation wavelength (relative intensity at 430 nm of 0.06 for λ_{exc} = 360 nm and 0.21 for λ_{exc} = 305 nm).

Fluorescence quantum yields, emission lifetimes and S_1 quenching by molecular oxygen at room temperature

The fluorescence quantum yields and emission lifetimes in the ns range of the CNGs are collected in Table 2 and Table 3. The emission quantum yields of CNG 6 and 8 were determined by excitation at their absorption maxima and are in excellent agreement with previously reported data.[14] On the other hand, due to its dual emission at short excitation wavelengths and the associated variability of its excitation spectrum (Figure 3), CNG 7 shows Φ_{fluo} 0.17 when excited above 400 nm but increasing values up to 0.21 when excited at 305 nm. Regarding the emission lifetimes of CNGs, all the molecular nanographenes under study

present multiexponential decays at room temperature, and no dependence with concentration has been found in the tested 10^{-5}–10^{-7} M concentration range; however, dissimilar behaviours are shown when comparing CNG 6 and CNGs 7 and 8 decay fittings (Table 3). CNG 6 requires biexponential fits and, irrespective of the selected detection wavelength (emission peak or shoulder), shows the same lifetime components and preexponential factors, within experimental uncertainty, resulting in the same average lifetimes regardless of the intensity weighted ($<\tau>_{Int} = \Sigma[I_i\tau_i^2]/\Sigma[I_i\tau_i]$, where I_i and τ_i are the discrete preexponential intensity factors and lifetimes, respectively) or amplitude weighted ($<\tau>_{Ampl} = \Sigma[A_i\tau_i]/\Sigma[A_i]$, where A_i and τ_i are the discrete preexponential amplitude factors and lifetimes, respectively) mean lifetime choice.[18] However, CNGs 7 and 8 not only require biexponential or triexponential functions to fit the experimental decays, respectively, but both of them show different decay fitting parameters depending on the selected detection wavelength (emission peak, shoulder or tail), evidencing the complex nature of the emitting singlet excited state, as already seen in the fluorescence excitation and emission spectra of these two CNGs (Figure 3). Nevertheless, the radiative (k_r) and overall nonradiative ($k_{nr\ total}$) deactivation rate constants of S_1 could be estimated (Table 2) from the values of the fluorescence quantum yield and mean emission lifetimes, and the obtained values are in good agreement, within experimental error, independently of the intensity weighted or amplitude weighted average lifetime used. We report also in Table 2 the upper limit of the intersystem crossing quantum yield (Φ_{ISC}) of the CNGs.

Table 2. Fluorescence quantum yield, emission lifetimes, radiative and nonradiative deactivation rate constants of the singlet excited state, and upper limit of the intersystem crossing quantum yield of the investigated compounds in chloroform at room temperature under inert atmosphere unless otherwise indicated. Experimental uncertainty ±10%.

CNG	Φ_{fluo}	$<\tau_{fluo_0}>_{Int}$ [ns][a]	$<\tau_{fluo_{air}}>_{Int}$ [ns][a]	k_r [s^{-1}][b]	$k_{nr\ total}$ [s^{-1}][c]	Φ_{ISC}[d]
6	0.50	11.2	8.9	4.5×10^7	4.5×10^7	0.50
7	0.17,[e] 0.21[f]	11.6	8.3	1.5×10^7	7.2×10^7	0.83
8	0.25	5.3	4.8	4.7×10^7	1.4×10^8	0.75

[a]Intensity weighted average lifetime, determined at the wavelength of the emission maximum; [b]Unimolecular radiative deactivation rate constant from S_1 to S_0, calculated from $\Phi_{fluo}/<\tau_{fluo0}>_{Int}$;[18b] [c]Overall unimolecular nonradiative deactivation rate constant from S_1, calculated from $(1-\Phi_{fluo})/<\tau_{fluo0}>_{Int}$; [d]Upper limit of the intersystem crossing quantum yield, calculated from $1-\Phi_{fluo}$; [e]Unimolecular internal conversion deactivation rate constant from S_1 to S_0; [f]Unimolecular intersystem crossing deactivation rate constant from S_1 to the triplet excited state manifold; [g]Excitation at 435 nm; [h]Excitation at 305 nm.

Table 3. Emission decays of the CNGs in chloroform at room temperature under air-equilibrated conditions unless otherwise indicated.

CNG	λ_{det} [nm][a)]	τ_1 [ns][b)]	A_1	I_1	τ_2 [ns][b)]	A_2	I_2	τ_3 [ns][b)]	A_3	I_3	$<\tau_{fluo}>_{Int}$ [ns][b)]	$<\tau_{fluo}>_{Ampl}$ [ns][b)]	χ^2
6	490[c)]	5.4	0.10	0.05	11.5	0.90	0.95	-	-	-	11.2	10.9	0.996
	490	6.2	0.21	0.15	9.4	0.79	0.85	-	-	-	8.9	8.7	0.954
	520	5.3	0.21	0.13	9.3	0.79	0.87	-	-	-	8.7	8.4	0.989
7	507[c)]	3.4	0.86	0.56	22	0.14	0.44	-	-	-	11.6	5.9	0.999
	507	3.2	0.87	0.58	15.4	0.13	0.42	-	-	-	8.3	4.8	1.001
	540	3.2	0.88	0.60	15.1	0.12	0.40	-	-	-	8.1	4.7	1.003
	600	3.2	0.91	0.69	14.8	0.09	0.31	-	-	-	6.8	4.3	1.000
8	527[c)]	3.4	0.73	0.55	7.1	0.26	0.42	16	0.01	0.02	5.3	4.5	0.952
	527	3.2	0.72	0.56	6.3	0.27	0.41	15.8	0.01	0.03	4.8	4.1	1.003
	495	2.8	0.22	0.11	6.5	0.77	0.86	15.2	0.01	0.03	6.4	5.8	0.954
	560	3.2	0.80	0.66	6.3	0.19	0.31	16.8	0.01	0.03	4.5	3.9	0.924

[a)]Detection wavelength for the acquisition of the emission decay; [b)]Experimental uncertainty, ±10%; [c)]Nitrogen-purged solution.

Fluorescence, phosphorescence and thermally activated fluorescence at low temperature

Figure 5 shows the temperature-dependent fluorescence spectra of CNGs 6, 7 and 8, and of their structural precursors Cor and HBC-tBu in chloroform. Spectra acquired at 65 K generally exhibit some blue shift and narrowing upon cooling, and the emission maxima of the CNGs and their structural precursors present noticeable hypsochromic shifts as the medium rigidity increases (rigidochromism). At 65 K some overlap between the fluorescence and phosphorescence bands has been detected for the three CNGs as well as for Cor and HBC-tBu (Figure 5). The wavelengths of the emission peaks (fluorescence and phosphorescence) and the fluorescence, phosphorescence and TADF lifetimes at 65 K are collected in Table 4, 5, 6, 7 and 8. It should be noted that CNG 7, the sterically and cycloheptatrienically constrained curved nanographene, exhibits a fine-structure low-temperature fluorescence spectrum with several peaks compared to its less constrained 7-membered ring partner, CNG 8, and to the loose [6]helicene analogue, CNG 6. Regarding the emission decays, in all cases (CNGs 6, 7 and 8 and their structural precursors Cor and HBC-tBu) at least biexponential functions are required to fit the experimental decays acquired at low temperatures. Figure 6 shows the fluorescence decays of CNGs 6, 7 and 8 at 298 K and 65 K, evidencing that emission

wavelength-dependent decays are observed except for CNG 6 at room temperature. Figure 7 shows the phosphorescence decays of CNGs 6, 7 and 8 at 65 K, again evidencing that emission wavelength-dependent decays are observed, except for CNG 6, the curved nanographene with simpler photophysics. In the case of CNG 8, it has to be noted that phosphorescence decays acquired at 125 K and 725 and 800 nm, respectively, show equilibrated populations. Concerning the structural precursors Cor and HBC-tBu, while Cor shows rather homogeneous decays irrespective of the emission wavelength selected for the acquisition of the fluorescence and phosphorescence decays, HBC-tBu shows a similar behaviour to that displayed by the CNGs, i.e., emission wavelength-dependent decays (Figure 8).

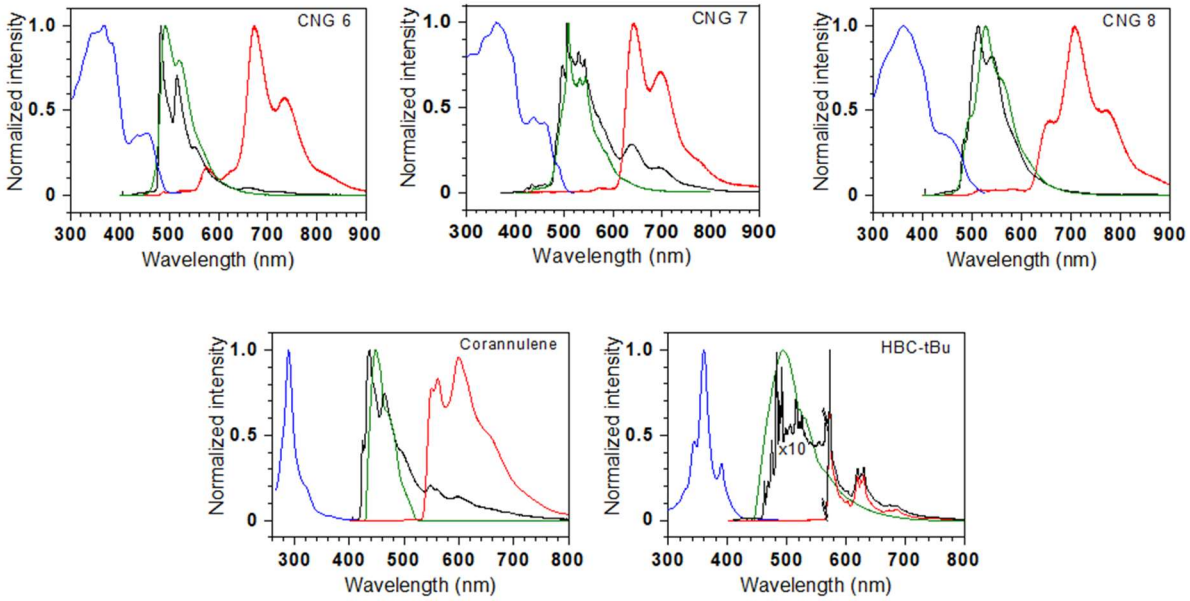

Figure 5. Fluorescence excitation (blue) and emission (green) spectra at 298 K, and fluorescence (black) and phosphorescence (red) spectra at 65 K of CNGs 6, 7, 8 and of their structural precursors Cor and HBC-tBu in chloroform. λ_{em} = 500 nm for the excitation spectra, λ_{exc} = 405 nm for the emission spectra. Fluorescence spectrum of HBC-tBu at 65 K ×10 at wavelengths below 566 nm.

Table 4. Fluorescence and phosphorescence spectral maxima and emission lifetimes of the investigated compounds and of their structural precursors in chloroform at 65 K.

CNG	λ_{fluo}^{max} [nm (eV)][a)]	$<\tau_{fluo}>_{Int}$ [ns]	λ_{phos}^{max} [nm (eV)][b)]	$<\tau_{phos}>_{Int}$ [s]	$<\tau_{TADF}>_{Int}$ [ms][c)]
6	483 (2.57)	26.5	673 (1.84)	0.67	67.0
7	506 (2.45)	30.0	640 (1.94)	1.0	13.0
8	511 (2.42)	6.7	707 (1.75)	0.9	15.0
Cor	437 (2.84)	11.4	600 (2.07)	0.16	-
HBC-*t*Bu	482 (2.57)	53.1	573 (2.16)	1.0	-

[a)]Fluorescence peaks and shoulders with the fluorescence maxima highlighted in bold numbers; [b)]Phosphorescence peaks and shoulders with the phosphorescence maxima highlighted in bold numbers; [c)]Thermally activated delayed fluorescence intensity weighted mean lifetime determined at 125 K with detection at 510–520 nm.

Table 5. Fluorescence and phosphorescence spectral maxima of the investigated compounds and of their structural precursors in chloroform at 65 K.

CNG	λ_{fluo}^{max} [nm (eV)][b)]	λ_{phos}^{max} [nm (eV)][b)]
6	**483** (2.57), 516 (2.40), 552 (2.25)	576 (2.15), **673** (1.84), 733 (1.69)
7	424 (2.92), 433 (2.86), 449 (2.76), 460 (2.70), 496 (2.50), **506** (2.45), 513 (2.42), 530 (2.34), 542 (2.29)	571 (2.17), **640** (1.94), 697 (1.78), 777 (1.60)
8	482 (2.57), **511** (2.42), 538 (2.30)	656 (1.89), **707** (1.75), 770 (1.61)
Cor	**437** (2.84), 463 (2.68), 494 (2.51)	549 (2.26), 561 (2.21), **600** (2.07), 660 (1.88), 730 (1.70)
HBC-*t*Bu	462 (2.68), 475 (2.61), **482** (2.57), 488 (2.54), 492 (2.52), 515 (2.41), 526 (2.36)	**573** (2.16), 619 (2.00), 630 (1.97), 683 (1.82)

[a)]Fluorescence peaks and shoulders with the fluorescence maxima highlighted in bold numbers; [b)]Phosphorescence peaks and shoulders with the phosphorescence maxima highlighted in bold numbers

Table 6. Fluorescence lifetimes of the CNGs and of their structural precursors in chloroform at 65 K.

CNG	λ_{det} [nm][a]	τ_1 [ns][b]	A_1	I_1	τ_2 [ns][b]	A_2	I_2	τ_3 [ns][b]	A_3	I_3	τ_4 [ns][b]	$<\tau_{fluo}>_{Int}$ [ns][b]	$<\tau_{fluo}>_{Ampl}$ [ns][b]	χ^2
6	*482*	*10.8*	*0.38*	*0.18*	*29.9*	*0.62*	*0.82*	-	-	-	-	*8.7*	*8.4*	*0.989*
	515	9.8	0.46	0.22	29.8	0.54	0.78	-	-	-	-	26.5	22.7	1.071
7	*505*	*3.2*	*0.57*	*0.19*	*8.6*	*0.33*	*0.29*	*52*	*0.10*	*0.52*	-	*30*	*9.7*	*0.999*
	540	3.3	0.61	0.19	9.8	0.29	0.28	53	0.10	0.53	-	31	10.3	0.986
	570	1.7	0.65	0.29	6.1	0.34	0.58	38.8	0.01	0.13	-	9.2	3.6	0.940
8	*482*	-	-	-	*4.6*	*0.44*	*0.19*	*15.9*	*0.56*	*0.81*	-	*14.1*	*10.8*	*1.004*
	510	3.1	0.52	0.28	6.2	0.44	0.60	18.0	0.04	0.12	-	6.7	5.1	1.010
	540	2.8	0.35	0.23	6.0	0.61	0.63	16.9	0.04	0.14	-	6.8	5.3	0.805
Cor	*437*	*2.4*	*0.19*	*0.05*	*8.2*	*0.50*	*0.44*	*15.1*	*0.32*	*0.51*	-	*11.4*	*9.3*	*0.886*
	494	2.5	0.19	0.05	8.3	0.47	0.41	15.5	0.34	0.54	-	11.9	9.6	0.862
HBC-*t*Bu	463	4.3	0.31	0.06	19.8	0.11	0.11	64.4	0.26	0.81	1.3[c]	54.4	20.3	0.995
	475	3.1	0.45	0.15	17.2	0.08	0.15	62.9	0.10	0.66	0.9[c]	44.6	9.3	0.990
	482	*3.4*	*0.31*	*0.07*	*18.0*	*0.12*	*0.13*	*64.7*	*0.19*	*0.78*	*1.0*[c]	*53.1*	*16.2*	*1.011*
	488	4.2	0.27	0.07	19.7	0.11	0.14	66.9	0.17	0.75	1.3[c]	53.3	15.3	0.989
	492	4.1	0.30	0.09	18.9	0.11	0.14	66.2	0.15	0.73	1.3[c]	51.3	14.0	0.993
	515	4.0	0.31	0.14	16.4	0.11	0.20	68.4	0.08	0.60	1.2[c]	45.0	9.2	0.989
	526	4.4	0.35	0.16	16.6	0.10	0.19	68.6	0.08	0.58	1.3[c]	43.7	9.3	0.990

[a]Detection wavelength for the acquisition of the emission decay, data acquired at the fluorescence maximum in italics; [b]Experimental uncertainty, ±10%; [c]Preexponential factors can be calculated from $1-\Sigma A_i$ or $1-\Sigma I_i$, taking into account the discrete components included in the corresponding cells in the same row.

Table 7. Phosphorescence lifetimes of the CNGs and of their structural precursors in chloroform at 65 K unless stated otherwise.

CNG	λ_{det} [nm][a]	τ_1 [s][b]	A_1	I_1	τ_2 [s][b]	A_2	I_2	τ_3 [s][b]	A_3	I_3	$<\tau_{phos}>_{Int}$ [s][b]	$<\tau_{phos}>_{Ampl}$ [s][b]	χ^2
6	*668*	*0.11*	*0.12*	*0.02*	*0.69*	*0.88*	*0.98*	-	-	-	*0.67*	*0.62*	*1.143*
	730	0.18	0.20	0.06	0.71	0.80	0.94	-	-	-	0.67	0.60	1.000
	806	0.10	0.24	0.04	0.68	0.76	0.96	-	-	-	0.65	0.54	0.907
7	*660*	-	-	-	*0.12*	*0.29*	*0.05*	*1.15*	*0.71*	*0.95*	*1.1*	*0.85*	*0.985*
	700	0.03	0.03	0.08	0.18	0.49	0.14	1.10	0.58	0.78	0.9	0.73	1.085
	770	0.08	0.01	0.04	0.18	0.50	0.30	0.98	0.49	0.66	0.71	0.57	1.007
8	640	-	-	-	0.26	0.32	0.08	1.08	0.68	0.92	1.00	0.82	1.142
	710	*0.03*	*0.08*	*0.13*	*0.22*	*0.80*	*0.26*	*1.36*	*0.12*	*0.62*	*0.90*	*0.34*	*1.139*
	780	0.08	0.14	0.23	0.20	0.76	0.41	0.95	0.10	0.36	0.44	0.26	1.139
	640[c]	0.04	0.06	0.04	0.23	0.31	0.17	1.1	0.63	0.79	0.91	0.77	1.111
	710[c]	0.06	0.15	0.44	0.15	0.74	0.29	0.59	0.11	0.27	0.23	0.18	1.089
	780[c]	0.04	0.15	0.45	0.12	0.73	0.29	0.64	0.12	0.26	0.22	0.17	1.058
Cor	550	0.13	0.76	0.64	0.23	0.24	0.36	-	-	-	0.16	0.15	0.904
	600	*0.12*	*0.72*	*0.59*	*0.22*	*0.28*	*0.41*	-	-	-	*0.16*	*0.15*	*0.994*
	730	0.11	0.62	0.46	0.20	0.38	0.54	-	-	-	0.16	0.14	1.000
HBC-*t*Bu	575	-	-	-	0.63	0.58	0.41	1.3	0.42	0.59	1.0	0.9	1.035
	625	*0.16*	*0.22*	*0.04*	*0.71*	*0.62*	*0.55*	*2.0*	*0.16*	*0.41*	*1.2*	*0.8*	*1.057*
	690	0.10	0.28	0.04	0.59	0.52	0.44	1.8	0.20	0.52	1.2	0.7	1.099

[a]Detection wavelength for the acquisition of the emission decay, data acquired at the phosphorescence maximum in italics; [b]Experimental uncertainty, ±10%; [c]125 K.

Table 8. Thermally activated delayed fluorescence lifetimes of the CNGs in chloroform at 125 K.

CNG	λ_{det} [nm][a]	τ_1 [ms][b]	A_1	I_1	τ_2 [ms][b]	A_2	I_2	τ_3 [ms][b]	A_3	I_3	τ_4 [ms][b]	$\langle\tau_{fluo}\rangle_{Int}$ [ms][b]	$\langle\tau_{fluo}\rangle_{Ampl}$ [ms][b]	χ^2
6	520	9.3	0.88	0.39	104	0.12	0.61					67	20.8	1.092
7	510	2.2	0.45	0.15	7.1	0.43	0.48	18.6	0.12	0.35	200[c]	13	6.4	0.977
8	520	2.1	0.43	0.14	7.2	0.45	0.49	19.2	0.12	0.35	220[c]	15	6.6	1.024

[a]Detection wavelength for the acquisition of the emission decay; [b]Experimental uncertainty, ±10%; [c]Preexponential factors can be calculated from $1-\Sigma A_i$ or $1-\Sigma I_i$, taking into account the discrete components included in the corresponding cells in the same row.

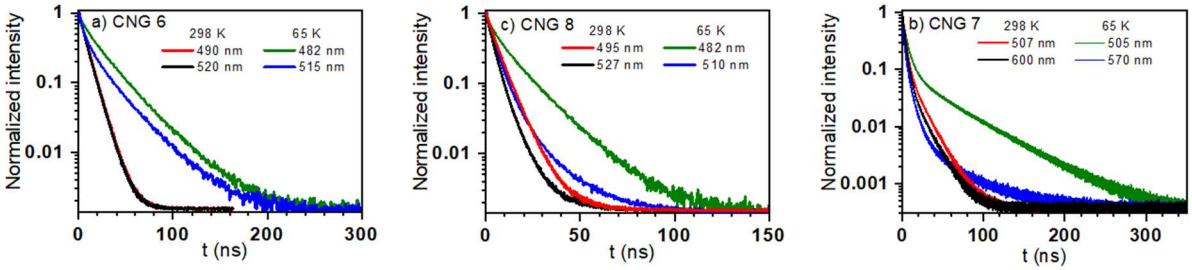

Figure 6. Fluorescence decays of CNGs 6, 7 and 8 at 298 K and 65 K in chloroform (λ_{exc} = 405 nm).

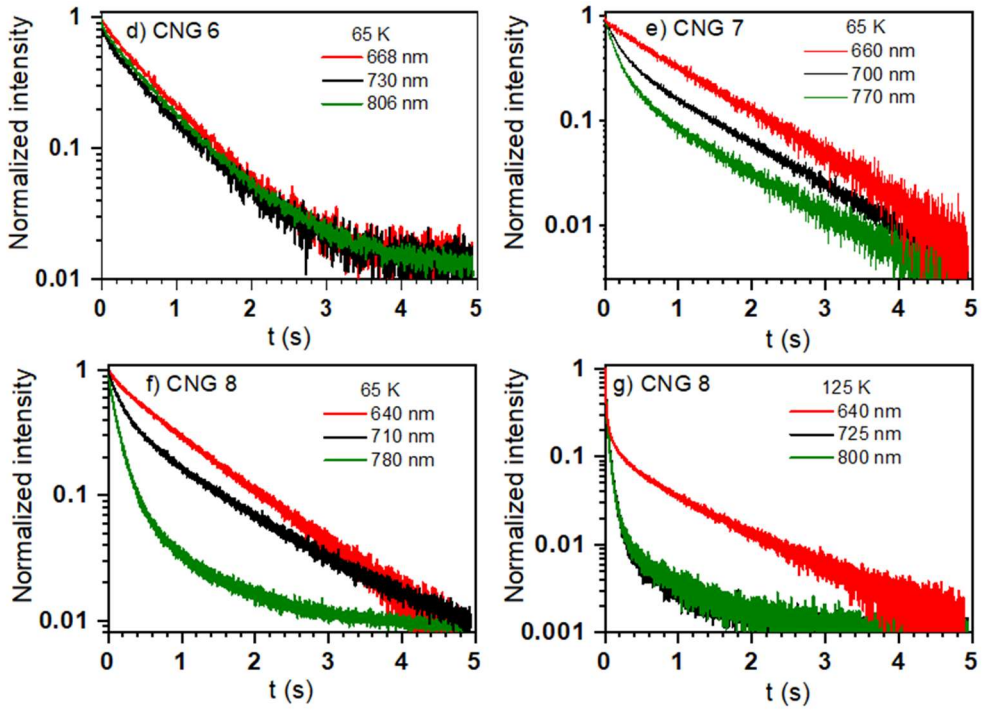

Figure 7. Phosphorescence decays of CNGs 6, 7 and 8 at 65 K or 125 K in chloroform (λ_{exc} = 405 nm).

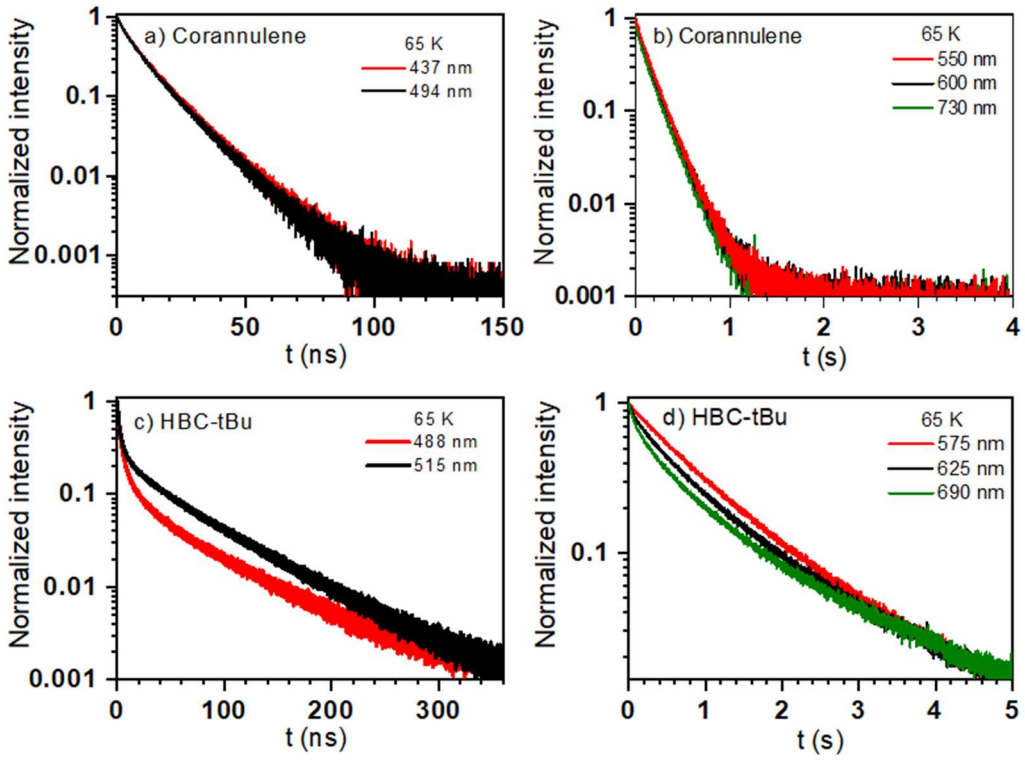

Figure 8. Fluorescence and phosphorescence decays of Cor and HBC-tBu at 65 K in chloroform (λ_{exc} = 405 nm).

Figure 9 shows the changes in phosphorescence intensity with temperature, giving rise to thermally activated delayed fluorescence occurring in the timescale of milliseconds (Figure 10) which is particularly relevant in the 100–140 K range. Changes in the position of the phosphorescence maxima of the CNGs with temperature, linked to occurrence and disappearance of the TADF phenomenon are shown in Figure 11. Phosphorescence peak shifts about 10 nm for CNG 6, around 20 nm for CNG 8 and >70 nm in the case of CNG 7 and, generally, TADF seems to be best tuned at temperatures in the 115–135 K range. On the other hand, the activation energy of TADF can be deduced by means of the Arrhenius equation applied to the temperature dependence of the phosphorescence intensity (Equation 4) or lifetime (Equation 5), using data from different phosphorescence maxima as the determination wavelengths (Figure 12 and 13).

$$\ln\left(I_{Phosph}\right) = \ln(A) - \frac{E_a}{R}\left(\frac{1}{T}\right) \quad \text{eq. 4}$$

$$\ln\left(\tau_{Phosph}\right) = \ln(A) - \frac{E_a}{R}\left(\frac{1}{T}\right) \quad \text{eq. 5}$$

where, I_{Phosph} and τ_{Phosph} are the emission intensity and average lifetime at the phosphorescence maximum selected, respectively, A is a pre-exponential factor, E_a is the activation energy, R is the gas constant and T is the absolute temperature. The thermal activation energies for the triplet excited state deactivation of CNGs 6, 7 and 8 are about 0.09, 0.11 and 0.07 eV (728, 884 and 575 cm^{-1}) respectively, from phosphorescence intensity measurements, and show excellent agreement when compared with results from

phosphorescence lifetime measurements 0.10, 0.11 and 0.08 eV (826, 898 and 613 cm^{-1}) for CNGs 6, 7 and 8, respectively. If the energy levels of S_1 and T_1 collected in Table 4 corresponding to the fluorescence and phosphorescence maxima at 65 K are considered, Δ_{S1-T1} values of 0.73, 0.51 and 0.67 for CNGs 6, 7 and 8, respectively, can be calculated. These relatively big energy differences do not match with the tiny activation barriers of the curved nanographenes (about 0.10 eV) for TADF to occur, therefore, TADF must be enabled from a high-lying dark triplet excited state above T_1 that facilitates the RISC process from the triplet to the singlet manifold.

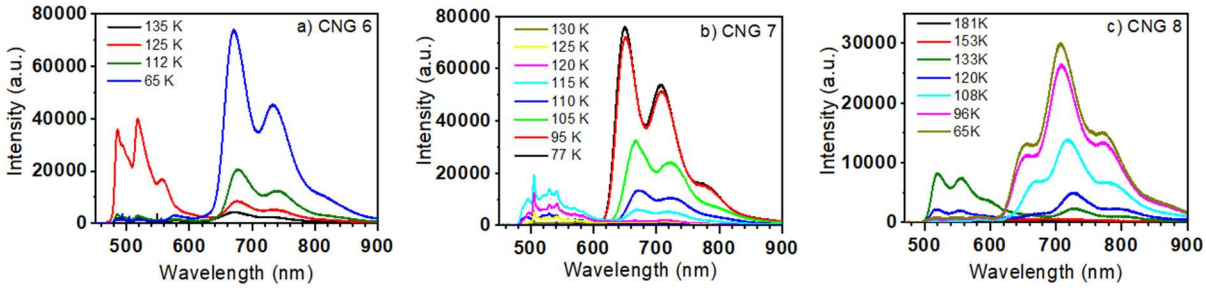

Figure 9. Thermally activated delayed fluorescence and phosphorescence spectra at low temperature of CNGs 6, 7, 8 in chloroform (λ_{exc} = 405 nm).

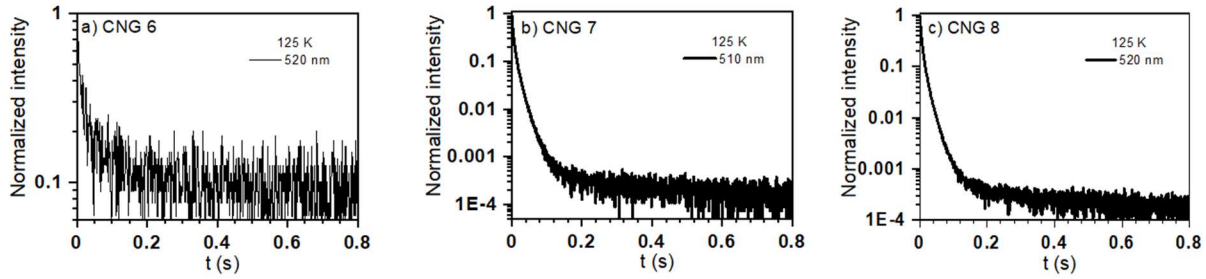

Figure 10. Thermally activated delayed fluorescence decays at 125 K of CNGs 6, 7, 8 in chloroform (λ_{exc} = 405 nm).

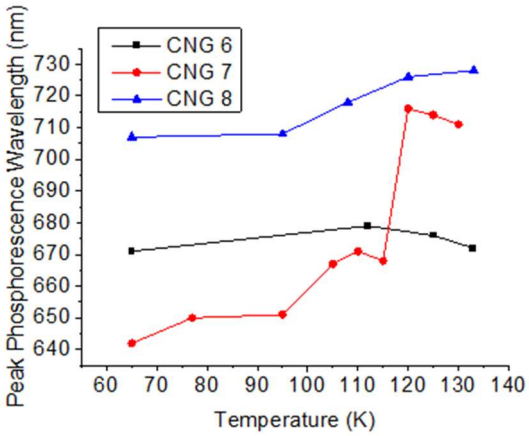

Figure 11. Changes with temperature in the position of the phosphorescence maxima of CNGs 6, 7 and 8 in chloroform.

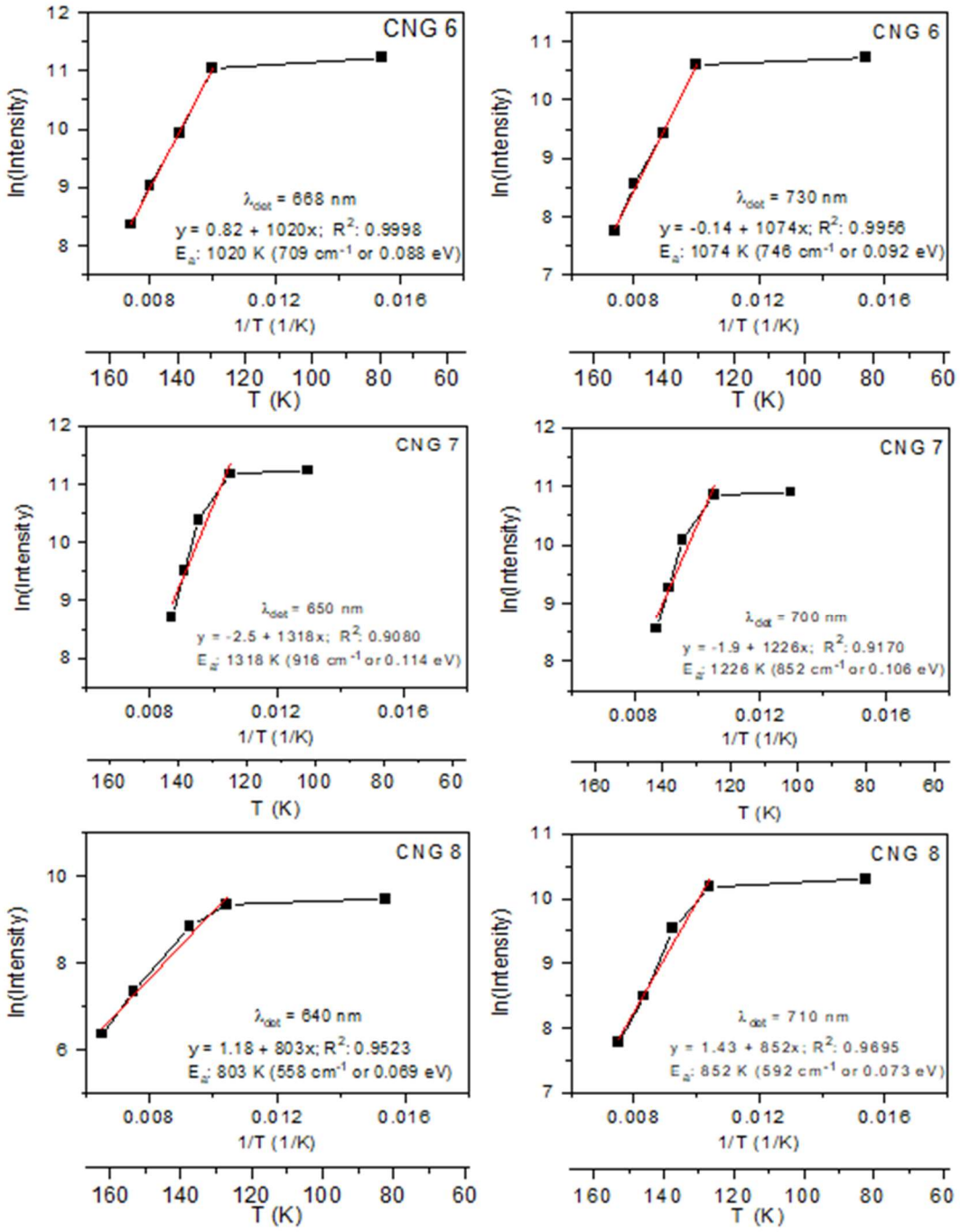

Figure 12. Arrhenius plots from phosphorescence intensities at different emission maxima of CNGs 6, 7 and 8 in chloroform at low temperatures.

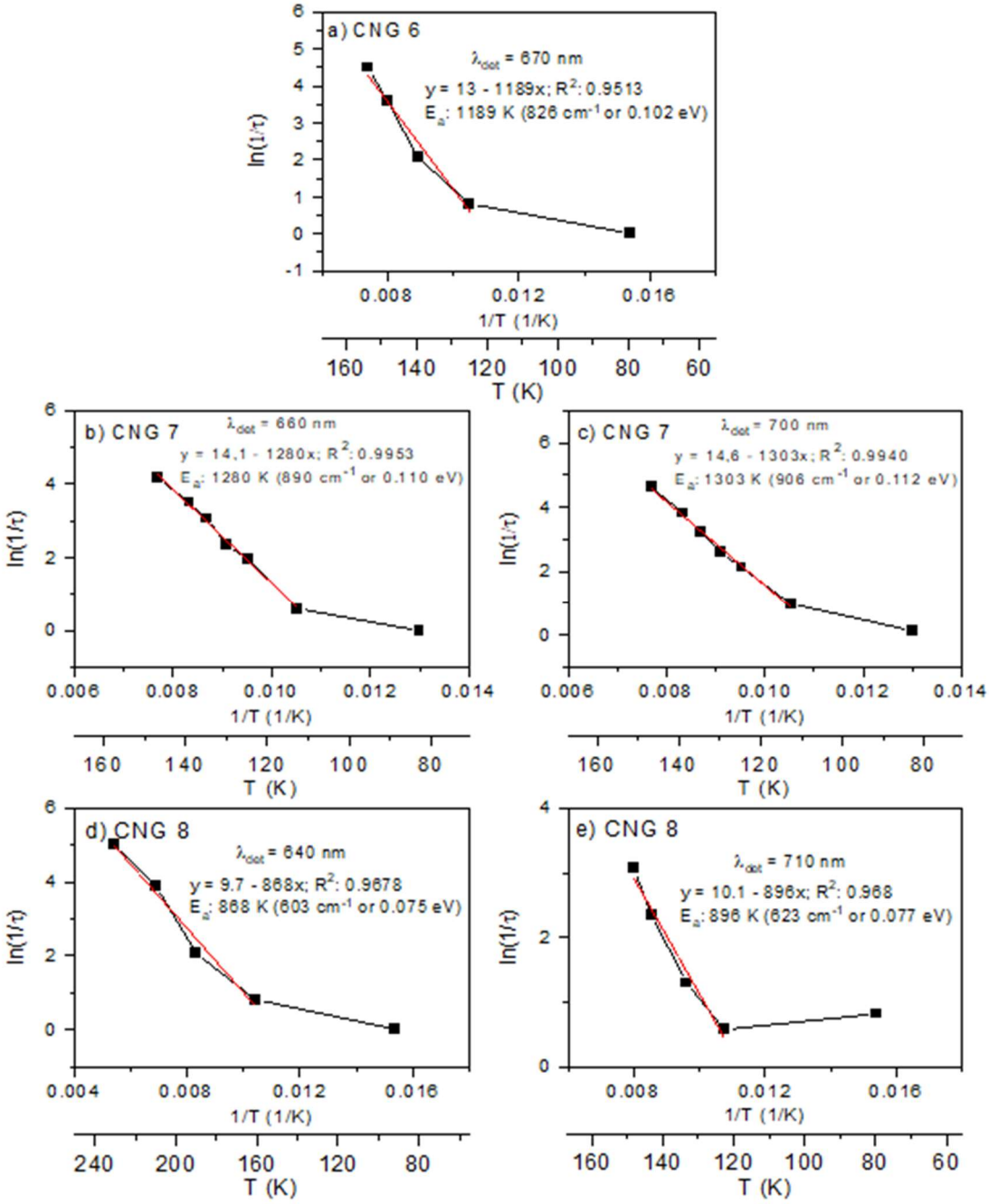

Figure 13. Arrhenius plots from phosphorescence lifetimes at different emission maxima of CNGs 6, 7 and 8 in chloroform at low temperatures.

Excited states quenching by molecular oxygen and singlet oxygen production quantum yield

Steady-state and time-resolved quenching experiments by molecular oxygen allowed to gain insights on the CNGs evolution from the singlet to the triplet excited state. Stern-Volmer equation and the intensity weighted average lifetimes ($<\tau>_{Int}$) were used to calculate the quenching parameters since, overall, better agreement between intensity and lifetime results was obtained when $<\tau>_{Int}$ was used, in particular, in case of the quite complex CNG 7 system.[18b] Quenching of the S_1 excited state by molecular oxygen was evidenced by the

changes in the mean lifetimes of the air-equilibrated solutions compared to the N_2-purged samples. Bimolecular quenching rate constants by O_2 are diffusion-controlled as shown by the k_{qS}^{O2} values $\approx 10^{10}$ mol^{-1} dm^3 s^{-1} (Table 9), whether they are calculated from emission intensity measurements or emission lifetime experiments. The probability of singlet excited state quenching by O_2 (P_S^{O2}) agrees, within experimental error, in the case of CNG 7 and 8, irrespective of the experimental technique used, and type of average lifetime selected for time-resolved measurements, however, a marked difference was surprisingly obtained for CNG 6, where $P_S^{O2}{}_I = 0.29$ from steady-state intensity measurements, but $P_S^{O2}{}_\tau = 0.21$ from time-resolved lifetime measurements (Table 9), which implies 10% static quenching (f_{static}) by molecular oxygen in the case of CNG 6.

On the other hand, the curved nanographenes can produce singlet oxygen, $^1O_2(^1\Delta_g)$, not only by quenching of their triplet excited states by ground-state molecular oxygen but, due to its long-lived nature, after singlet excited state quenching by O_2, following the so-called O_2-induced enhanced intersystem crossing (EISC) process. Therefore, the CNGs may be classified as TC photosensitizers where quenching of S_1 by O_2 catalyzes production of T_1, although singlet oxygen cannot be directly generated from S_1 (because $E_{S1}–E_{T1} < E_\Delta$, being E_Δ the energy difference between singlet oxygen and ground-state triplet oxygen) as can be deduced from the energy values collected in Table 4.[19] Singlet oxygen production quantum yields (Φ_Δ) were determined by chemical scavenging of $^1O_2$ with 1,3-diphenylisobenzofurane (Figure 14 and Figure 15). The obtained results are collected in Table 9 and are significantly lower than the upper limit of Φ_{ISC}.

Table 9. Bimolecular quenching rate constants of the investigated compounds by molecular oxygen, proportion of singlet excited states quenched, fraction of singlet excited states statically quenched, singlet oxygen production quantum yield and lower limit of the fraction of triplet states quenched by ground-state molecular oxygen leading to singlet oxygen production in chloroform at room temperature under inert atmosphere unless otherwise indicated. Experimental uncertainty, ±10%.

CNG	$k_{qS}^{O2_I}$ [mol^{-1} dm^3 s^{-1}][a)]	$k_{qS}^{O2_\tau}$ [mol^{-1} dm^3 s^{-1}][b)]	$P_S^{O2_I}$[c)]	$P_S^{O2_\tau}$[d)]	f_{static}[e)]	Φ_Δ[f)]
6	1.3×10^{10}	9.6×10^{9}	0.29	0.21	0.10	0.36
7	1.7×10^{10}	1.4×10^{10}	0.32	0.28	-	0.47
8	9.8×10^{9}	8.1×10^{9}	0.095	0.094	-	0.40

[a)]Bimolecular quenching rate constants by O_2 obtained after Stern-Volmer analysis from fluorescence intensity measurements; [b)]Bimolecular quenching rate constants by O_2 obtained after Stern-Volmer analysis from fluorescence average lifetimes, where intensity weighted or amplitude weighted mean lifetimes give equivalent values, within experimental error; [c)]Probability of singlet excited state quenching by O_2, determined from fluorescence intensity measurements; [d)]Probability of singlet excited state quenching by O_2, determined from fluorescence average lifetimes; [e)]Fraction of singlet excited states statically quenched by molecular oxygen; [f)]Singlet oxygen production quantum yields; [g)]Fraction of triplet excited states quenched by molecular oxygen leading to singlet oxygen production.

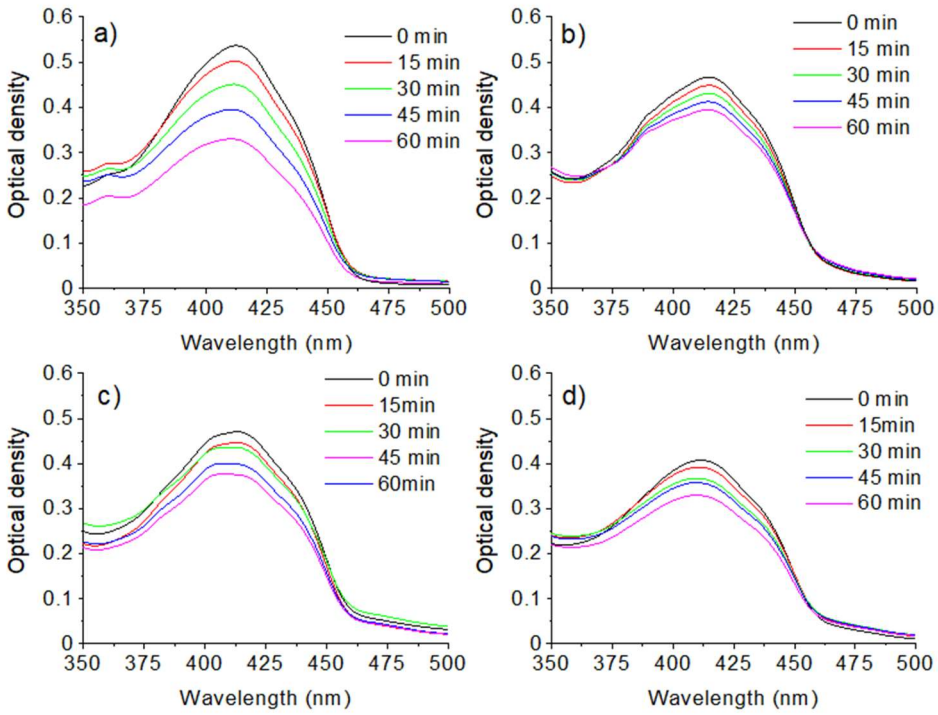

Figure 14. Evolution of 1,3-diphenylisobenzofuran absorption spectra in the presence of phenalen-1-one as the singlet oxygen production standard (Φ_Δ= 0.97) a), CNG 6 b), CNG 7 c) and CNG 8 d) in chloroform under UV-LED excitation at 365 nm.

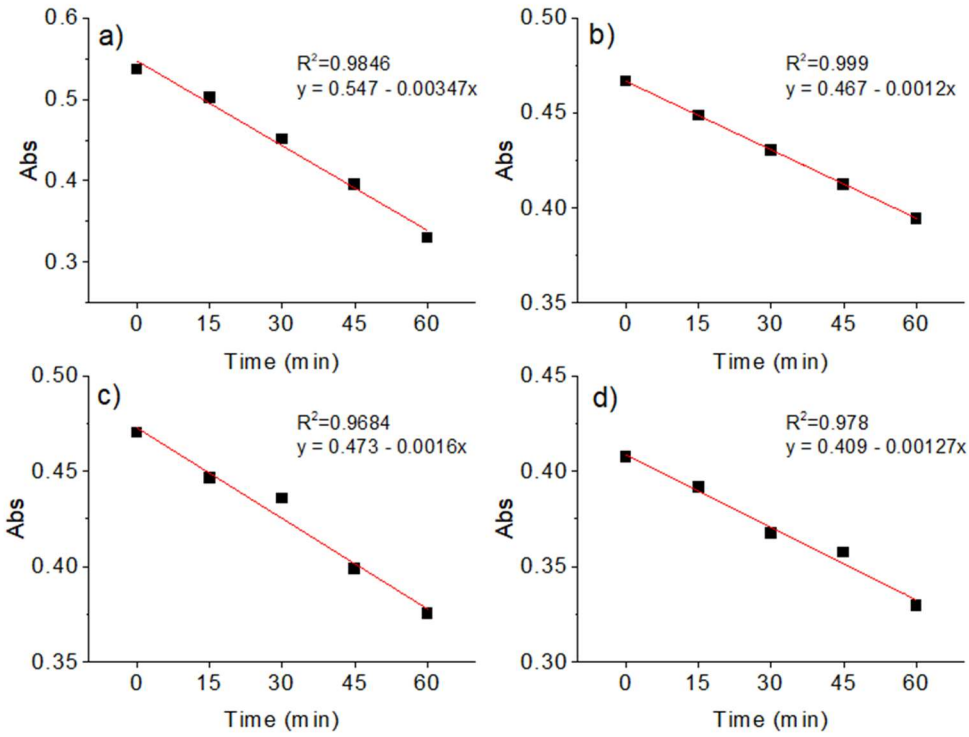

Figure 15. Absorbance changes in the photodegradation tests of 1,3-piphenylisobenzofuran by singlet oxygen in the presence of phenalene-1-one a), CNG 6 b), CNG 7 c) and CNG 8 d) in chloroform under UV-LED excitation at 365 nm.

Excited state properties in the solid state: fluorescence spectra, emission decays and quenching by molecular oxygen

Figure 16 shows the fluorescence spectra of the CNGs powders and the emission decays under nitrogen and in air-equilibrated conditions. Table 10 collects the results of the triexponential analysis of the emission decays under nitrogen and for air-equilibrated samples. Negligible quenching by molecular oxygen has been observed in the solid state in the case of CNG 6, while weak deactivation is noted for CNG 8 ($P_S^{O2}{}_\tau$ 0.09) which is equivalent to that observed in chloroform solution (Table 9); however, a surprisingly efficient quenching of the singlet excited state of CNG 7 has been observed ($P_S^{O2}{}_\tau$ 0.75), that exceeds the values observed in solution ($P_S^{O2}{}_I$ 0.32, $P_S^{O2}{}_\tau$ 0.28).

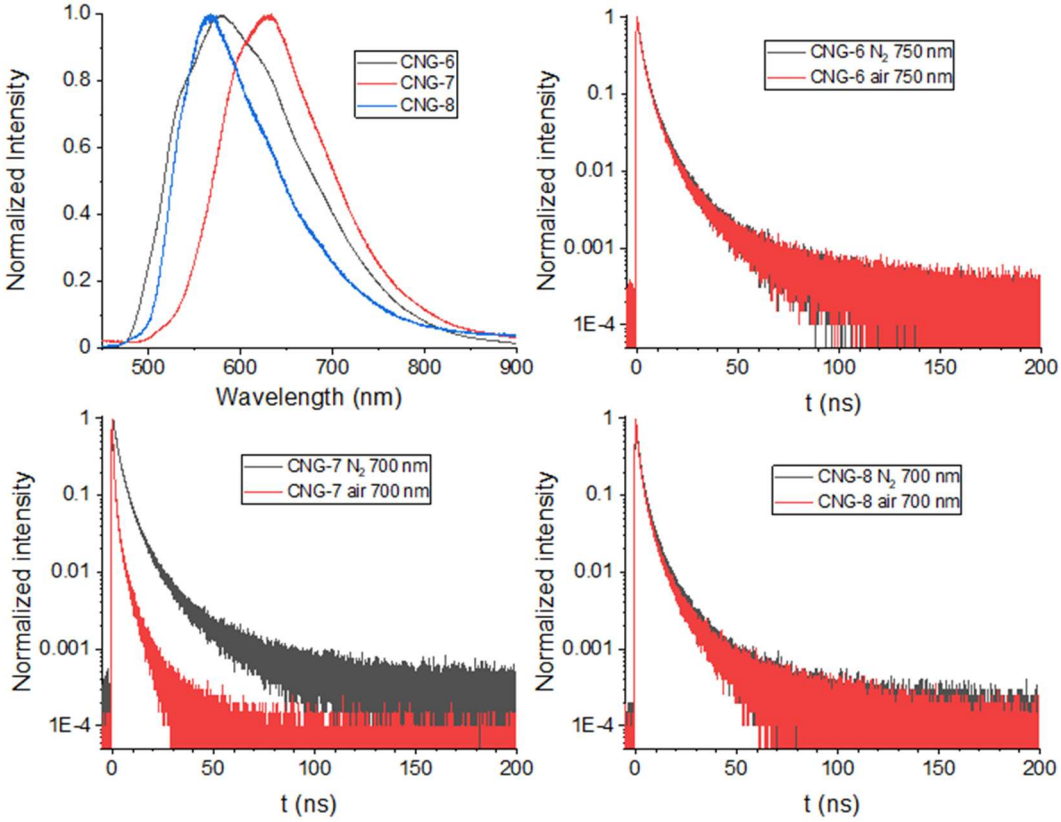

Figure 16. Emission spectra of CNGs in solid state and emission decays under N_2-purged and air-equilibrated atmosphere.

Table 10. Emission lifetimes of the CNGs in solid state under N_2-purged and air-equilibrated atmosphere.

CNG	λ_{det} [nm][a)]	τ_1 [ns][b)]	A_1	I_1	τ_2 [ns][b)]	A_2	I_2	τ_3 [ns][b)]	A_3	I_3	$<\tau_{fluo}>_{Int}$ [ns][b)]	$<\tau_{fluo}>_{Ampl}$ [ns][b)]	χ^2
6	580	1.7	0.70	0.39	5.4	0.29	0.52	20.6	0.01	0.09	5.3	3.0	1.135
	580 [c)]	1.6	0.71	0.39	5.2	0.28	0.52	20.6	0.01	0.09	5.1	2.8	1.105
7	632	0.40	0.87	0.57	1.6	0.12	0.30	5.7	0.01	0.13	1.4	0.61	0.983
	632 [c)]	2.0	0.73	0.45	5.9	0.26	0.47	24.9	0.01	0.08	5.6	3.2	1.101
8	568	0.94	0.72	0.39	3.3	0.26	0.50	12.4	0.02	0.11	3.5	1.7	1.088
	568 [c)]	1.0	0.72	0.38	3.7	0.26	0.50	13.1	0.02	0.12	3.8	1.9	1.076

[a)]Detection wavelength for the acquisition of the emission decay; [b)]Experimental uncertainty, ±10%; [c)] Nitrogen-purged solution.

4.4.4. Conclusions

The detailed study of the intriguing photophysics of a series of three closely related curved molecular nanographenes has been carried out, especially in the case of the two CNGs with positive and negative curvature (CNG **7** and CNG **8**), while for the structure with a [6]helicene (CNG **6**), a more conventional behaviour has been observed. The room temperature fluorescence spectra of CNG **8** and, especially, CNG **7**, show strong changes depending on the excitation wavelength used; this fact is also evident when quantifying the fluorescence quantum yield of CNG **7**, which ranges from 17% to 21% when changing the excitation wavelength form the visible to the UV. On the other hand, when analyzing the fluorescence decays of both CNG **7** and CNG **8** at room temperature, different multiexponential lifetimes are observed depending on the emission wavelength selected for decay acquisition. This behaviour is more pronounced at low temperature. It has been observed that these three nanographenes show phosphorescence and TADF at low temperatures, and again when analyzing the phosphorescence decay, both CNG **7** and CNG **8** show different lifetimes when varying the emission wavelength for signal detection. From the estimated energy levels of S_1 and T_1, with $\Delta E_{S1\text{-}T1} \geq 0.5$ eV, and the energy barrier for TADF ($\Delta E_a \leq 0.1$ eV), the TADF process cannot occur directly from T_1 to S_1 but a high-lying dark triplet excited state above T_1 must be involved. Knowing the quantum yields of singlet oxygen production (36%, 47% and 40% for CNG **6**, **7** and **8**, respectively), and fluorescence quantum yields (50%, 17%–21% and 25% for CNG **6**, **7** and **8**), it can be stated that CNG **7** and CNG **8** have a larger S1→T1 intersystem crossing rate; and having calculated the radiative and non-radiative deactivation rate constants of these three CNGs, it can also be affirmed that, once again, CNG **7** and **8** exhibit higher non-radiative deactivation rate constants.

References

1. a) Y. Gu, Z. Qiu, K. Müllen, *J. Am. Chem. Soc.* **2022**, *144*, 11499-11524; b) A. Borissov, Y. K. Maurya, L. Moshniaha, W. S. Wong, M. Żyła-Karwowska, M. Stępień, *Chem. Rev*. **2022**, *122*, 565-788; c) Z. Liu, S. Fu, X. Liu, A. Narita, P. Samorì, M. Bonn, H. I. Wang, *Adv. Sci*. **2022**, *9*, 2106055; d) R. S. Jassas, E. U Mughal, A. Sadiq, R. I. Alsantali, M. M. Al-Rooqi, N. Naeem, Z. Moussa, S. A. Ahmed, *RSC Adv*. **2021**, *11*, 32158; e) S. M. Suresh, D. Hall, D. Beljonne, Y. Olivier, E. Zysman-Colman, *Adv. Funct. Mater.* **2020**, *30*, 1908677; f) X. Y. Wang, X. Yao, A. Narita, K. Müllen, *Acc. Chem. Res*. **2019**, *52*, 2491-2505; g) I. Pozo, E. Guitián, D. Pérez, D. Peña, *Acc. Chem. Res*. **2019**, *52*, 2472-2481; h) M. Grzybowski, B. Sadowski, H. Butenschön, D. T. Gryko, *Angew. Chem. Int. Ed*. **2020**, *59*, 2998-3027; i) M. Stępien, E. Gonka, M. Zyła, N. Sprutta, *Chem. Rev*. **2017**, *117*, 3479-3716; j) H. Ito, K. Ozaki, K. Itami, *Angew. Chem. Int. Ed*. **2017**, *56*, 11144-11164; k) J. Siegel, Y. T. Wu (Eds), *Polyarenes I*. *Topics in Current Chemistry*, Vol 349. Springer, Berlin, Heidelberg, Germany **2014**; l) C. Zhang, Y. Liu, X. Q. Xiong, L. H. Peng, L. Gan, C. F. Chen, H. B. Xu, *Org. Lett*. **2012**, *14*, 5912-5915; m) K. Müllen, J. P. Rabe, *Acc. Chem. Res.* **2008**, *41*, 511-520.

2. a) R. Sekiya, T. Haino, *Chem. Eur. J*. **2021**, *27*, 187-199; b) B. P. Mathew, M. R. Kuram, *Inorg. Chim. Acta* **2019**, *490*, 112-129.

3. a) Y. Fei, J. Liu, *Adv. Sci*. **2022**, *9*, 2201000; b) E. M. Muzammil, D. Halilovic, M. C. Stuparu, *Commun. Chem.* **2019**, *2*, 58; c) I. R. Márquez, S. Castro-Fernández, A. Millán, A. G. Campaña, *Chem. Commun*. **2018**, *54*, 6705-6718.

4. a) S. K. Behera, S. Y. Park, J. Gierschner, *Angew. Chem. Int. Ed.,* **2021**, 60, 2-16; b) J. M. Teng, Y. F. Wang, C. F. Chen, *J. Mater. Chem. C* **2020**, *8*, 11340-11353; c) F. M. Xie, J. X. Zhou, Y. Q. Li, J. X. Tang, *J. Mater. Chem. C* **2020**, *8*, 9476-9494; d) Z. Yang, Z. Mao, Z. Xie, Y. Zhang, S. Liu, J. Zhao, J. Xu, Z. Chi, M. P. Aldred, *Chem. Soc. Rev.,* **2017**, 46, 915-1016; e) L. Bergmann, D. M. Zink, S. Bräse, T. Baumann, D. Volz, *Top. Curr. Chem.* **2016**, *374*, 22; f) S. Mukherjee, P. Thilagar, *Chem. Commun.,* **2015**, 51, 10988-11003; g) Z. Chi, X. Zhang, B. Xu, X. Zhou, C. Ma, Y. Zhang, S. Liu, J. Xu, *Chem. Soc. Rev.* **2012**, 41, 3878-3896.

5. a) S. Zank, J. M. Fernández-García, A. J. Stasyuk, A. A. Voityuk, M. Krug, M. Solà, D. M. Guldi, N. Martín, *Angew. Chem. Int. Ed*. **2022**, *61*, e202112834; b) J. I. Urgel, M. Di Giovannantonio, Y. Segawa, P. Ruffieux, L. T. Scott, C. A. Pignedoli, K. Itami, R. Fasel, *J. Am. Chem. Soc.* **2019**, *141*, 13158-13164; c) Q. Huang, G. Zhuang, H. Jia, M. Qian, S. Cui, S. Yang, P. Du, *Angew. Chem. Int. Ed.* **2019**, *58*, 6244-6249; d) H. A. Lin, Y. Sato, Y. Segawa, T. Nishihara, N. Sugimoto, L. T. Scott, T. Higashiyama, K. Itami, *Angew. Chem. Int. Ed.* **2018**, *57*, 2874-2878; e) Y. Dai, Z. Li, J Yang, *Carbon* **2016**, *100*, 428-434.

6. a) Q. Dang, Y. Jiang, J. Wang, J. Wang, Q. Zhang, M. Zhang, S. Luo, Y. Xie, K. Pu, Q. Li, Z. Li, *Adv. Mater.* **2020**, *32*, 2006752; b) X. Huang, J. Song, B. C. Yung, X. Huang, Y. Xiong, X. Chen, *Chem. Soc. Rev.* **2018***,* 47, 2873-2920; c) S. Xu, R.Chen, C. Zheng, W. Huang, *Adv. Mater.* **2016**, *45*, 9920-9940; d) M. A. Haidekker, E. A. Theodorakis, *J. Mater. Chem. C.* **2016***, 4*, 2707-2718; e) J. Zhang, Q. Zou, H. Tian, *Adv. Mater.* **2013**, *3*, 378-399.

7. X. Wu, J. W. Huang, B. K. Su, S. Wang, L. Yuan, W. Q. Zheng, H. Zhang, Y. X. Zheng, W. Zhu, P. T. Chou, *Adv. Mater*. **2022**, *34*, 2105080.

8. a) Q. Liao, Q. Li, Z. Li, *Chem. Photo Chem*., **2021**, *5*, 694-701; b) K. Schmidt, S. Brovelli, V. Coropceanu, D. Beljonne, J. Cornil, C. Bazzini, T. Caronna, R. Tubino, F. Meinardi, Z. Shuai, J. L. Brédas, *J. Phys. Chem. A,* **2007**, *42*, 10490-10499.

9. a) X. Wang, Y. Sun, G. Wang, J. Li, X. Li, K. Zhang, *Angew. Chem. Int. Ed*. **2021**, *60*, 17138-17147; b) K. Narushima, Y. Kiyota, T. Mori, S. Hirata, M. Vacha, *Adv. Mater.* **2019**, *10*, 1807268; c) D. Li, F. Lu, J. Wang, W. Hu, X. M. Cao, X. Ma, Tian, *J. Am. Chem. Soc.* **2018**, *140*, 1916-1923; d) T. Ogoshi, H. Tsuchida, T. Kakuta, T. A.Yamagishi, A. Taema, T. Ono, M. Sugimoto, M. Mizuno, *Adv. Funct. Mater.* **2018**, *28*, 1707369; e) S. Cai, H. Shi, J. Li, L. Gu, Y. Ni, Z. Cheng, S. Wang, W. W. Xiong, L. Li, Z. An, W. Huang, *Adv. Mater.* **2017**, *29*, 1701244.

10. a) H. Liu, Z. Liu, G. Li, H. Huang, C. Zhou, Z. Wang, C. Yang, *Angew. Chem. Int. Ed*. **2021**, *60*, 12376-12380; b) P. Rajamalli, F. Rizzi, W. Li, M. A. Jinks, A. K. Gupta, B. A. Laidlaw, I. D. W. Samuel, T. J. Penfold, S. M. Goldup, E. Zysman-Colman, *Angew. Chem. Int. Ed*. **2021**, *60*, 12066-12073; c) L. Frédéric, A. Desmarchelier, L. Favereau, G. Pieters, *Adv. Funct. Mater*. **2021**, *31*, 2010281; d) R. Ansari, W. Shao, S. J. Yoon, J. Kim, J. Kieffer, *ACS Appl. Mater. Interfaces* **2021**, *13*, 28529-28537; e) G. Dai, M. Zhang, K. Wang, X. Fan, Y. Shi, D. Sun, W. Liu, J. Chen, J. Yu, X. Ou, S. Xiong, C. Zheng, X. Zhang, *ACS Appl. Mater. Interfaces* **2021**, *13*, 25193-25201; f) F. Fang, L. Zhu, M. Li, Y. Song, M. Sun, D. Zhao, J. Zhang, *Adv. Sci.* **2021**, 24, 2102970; g) H. Abroshan, Y. Zhang, X. Zhang, C. Fuentes-Hernandez, S. Barlow, V. Coropceanu, S. R. Marder, B. Kippelen, J. L. Brédas, *Adv. Funct. Mater.* **2020**, *30*, 2005898; h) M. Hasan, A. Shukla, V. Ahmad, J. Sobus, F. Bencheikh, S. K. M. McGregor, M. Mamada, C. Adachi, S. C. Lo, E. B. Namdas, *Adv. Funct. Mater*. **2020**, *30*, 2000580; i) J. Liu, Z. Li, T. Hu, X. Wei, R. Wang, X. Hu, Y. Liu, Y. Yi, Y. Yamada-Takamura, Y. Wang, P. Wang, *Adv. Optical Mater.* **2019**, *7*, 1801190; j) Y. Liu, C. Li, Z. Ren, S. Yan, M. R. Bryce, *Nat. Rev. Mater.* **2018**, 3, 18020-18039; k) M. Y. Wong, E. Zysman-Colman, *Adv. Mater.* **2017**, *29*, 1605444.

11. a) H. Lim, S. J. Woo, Y. H. Ha, Y. H. Kim, J. J. Kim, *Adv. Mater.* **2022**, *34*, 2100161; b) X. Cai, Z. Qiao, M. Li, X. Wu, Y. He, X. Jiang, Y. Cao, S. J. Su, *Angew. Chem. Int. Ed*. **2019**, *58*, 13522-13531.

12. L. Zhou, G. Xie, F. Ni, C. Yang, *Appl. Phys. Lett*. **2020**, *117*, 130502.

13. Y. Xu, Q. Wang, X. Cai, C. Li, Y. Wang, *Adv. Mater*. **2021**, 2100652.

14. J. M. Fernández-García, P. J. Evans, S. Rivero Medina, I. Fernández, D. García-Fresnadillo, J. Perles, J. Casado, N. Martín, *J. Am. Chem. Soc*. **2018**, *140*, 17188-17196.

15. J. M. Fernández-García, P. J. Evans, S. Filippone, M. A. Herranz, N. Martín, *Acc. Chem. Res.*, **2019**, *52*, 1565-1574.

16. J. Mack, P. Vogel, D. Jones, N. Kavala, A. Sutton, *Org. Biomol. Chem*. **2007**, *5*, 2448-2452; and references therein.

17. D. Lungerich, J. F. Hitzenberger, M. Marcia, F. Hampel, T. Drewello, N. Jux, *Angew. Chem. Int. Ed*. **2014**, *53*, 12231-12235.

18. a) Y. Li, S. Natakorn, Y. Chen, M. Safar, M. Cunningham, J. Tian, D. D. U. Li, *Front. Phys*. **2020**, *8*, 576862; b) E. Fišerová, M. Kubala, *J. Luminescence* **2012**, *132*, 2059-2064; c) A. Sillen, Y. Engelborghs, *Photochem. Photobiol.* **1998**, *67*, 475-486; d) E. R. Carraway, J. N. Demas, B. A. DeGraff, J. R. Bacon, *Anal. Chem*. **1991**, *63*, 337-342; e) E. R. Carraway, J. N. Demas, B. A. DeGraff, *Anal. Chem*. **1991**, *63*, 332-336.

19. a) D. García-Fresnadillo, S. Lacombe in *Singlet Oxygen. Applications in Biosciences and Nanosciences*, Vol. 1 (Eds. S. Nonell, C. Flors), Royal Society of Chemistry, Cambridge, UK **2016**, Ch. 6, pp. 105-143; b) C. Schweitzer, R. Schmidt, *Chem. Rev*. **2003**, *103*, 1685-1758; c) F. Wilkinson, W. P. Helman, A. B. Ross, *J. Phys. Chem. Ref. Data* **1993**, *22*, 113-262; d) A. J. McLean, D. J. McGarvey, T. G. Truscott, C. R. Lambert, E. J. Land, *J. Chem. Soc. Faraday Trans*. **1990**, *86*, 3075-308

5

Conclusions

5. CONCLUSIONS

Chapter 1: Solvothermally Synthesized Carbon Nanodots

- Hydrothermal synthesis is the most common process for producing CNDs because of its advantages such as environmental friendliness, simplicity and versatility.
- The major product in hydrothermal synthesis consists in small conjugated organic molecules and mainly non-conjugated oligomers, but graphitic cores are produced in a very small proportion. This fact highlights the necessity and importance of the isolation and purification process. Practically all previous reports in the literature did not compare the properties of interest of the CNDs with those of the small molecule fraction and the latter was simply discarded, if purification capable of separating those fractions was carried out at all. For example, these problems have been demonstrated recently in the case of supposedly “chiral CNDs,” where the chirality was later shown to be exclusively due to the small molecule fractions. Similarly, there has been an increasing number of recent reports on photoluminescence from supposedly non-conjugated polymer dots, where the purification and separation of small molecule by-products is questionable.
- Mass spectrometry proves to be an essential technique to identify and elucidate the presence of molecules that can be produced in the synthesis of CNDs
- The comparison and careful analysis of the structural and optical properties of the molecular products, and of the CNDs (in which the molecular products are always incorporated) allows us to affirm that, in contrast to many previous publications, the quantum yield of the solvothermal CNDs investigated is extremely low and that the UV-Vis, PL and PLE spectra are dominated by the molecular products and their photoproducts.
- Although the "soft synthesis conditions" produce graphitic cores in very low yield but we have been able to observe them by HR-TEM, GI-WAXS, and SERS.
- The ability to produce singlet oxygen is attributed exclusively to the graphitic cores, and the dependence of the emission on excitation, which is obviously not observed in the isolated molecular products, is due both to the formation of the molecular photoproducts, and to the fact that these graphitic cores offer different environments to the molecular products attached to them.
- The conclusions drawn from this work, on the need and importance of purification, as well as the relevance of an exhaustive characterization, are extrapolated and applicable to a large number of works on the production, characterization and applicability of CNDs; this is evident from the successive works that have been supported by this research: “The role of molecular fluorophores in the photoluminescence of carbon dots derived from citric acid: current state-of-the-art and future perspectives” Nanoscale, 2022, Advance Article; “Effects of carbon nanodot fractionation of the performance of sensitized mesoporous titania based photovoltaic devices” J. Mater. Chem. C.,

2022, 10, 8824-8833; “Deep eutectic solvents-derivated carbon dots-decorated silica stationary phase with enhanced separation selectivity in reserved-phase liquid chromatography” J. Chromatogr. A, 2022, 1681, 463425; “Nuclear magnetic resonance reveals molecular species in carbon nanodot samples disclosing flaws” Angew. Chem. Int. Ed., 2022, 61; and “Photostable carbon dots with intense green emission in an open reactor synthesis” Carbon, 2022, 198, 230-243.

Chapter 2: Carbon Nanoparticles by Pulsed Laser Synthesis

- A novel method for the preparation of CNPs has been studied using a pulsed Nd-YAG laser and a bottom-up approach starting from different organic aromatic precursors. The potential interest of this technique has been demonstrated in terms of homogeneity of the products obtained, good availability of the reagents and the versatility of both the technique itself and the precursors.
- The kinetic formation of CNPs has been studied, and experimental evidence has been obtained pointing to zero-order kinetics, as well as a possible catalytic role of the laser beam impact surface.
- The production yields of CNPs are favoured in molten media (such as naphthalene).
- The pulsed laser causes a change of carbon hybridization from precursors, almost exclusively formed by Csp^2, to CNPs with Csp^3 presence between 30 and 60 %, which is mainly on the surface as can be observed thanks to FTIR. Moreover, the presence of the heteroatoms available in some precursors is not observed in the CNPs, which shows that the laser beam causes the C-X bond to be broken before the C-C bond because of its higher lability.
- CNPs are observed by AFM, STEM and Raman spectroscopy, and we can state that CNPs are nanoparticles of sizes between 1 and 10 nm height and 5-20 nm width that can have either amorphous or graphitic nano-onion-like structures depending on the precursor used.
- CNPs exhibit excitation wavelength-dependent fluorescence with relatively low fluorescence yields (<10 %) and can photosensitize singlet oxygen production with quantum yields of up to 37%.
- This research paves the way for further investigation of many other organic precursors, and other microparticles that can catalyze the reaction or be incorporated into the CNPs produced and confer new and interesting properties to them.

Chapter 3: Photocatalysis of Carbon Nanodot–TiO_2 Heterostructures Activated by Visible Light

- Photocatalytic activity of heterostructures of hydrothermal carbon nanodots and TiO_2 nanoparticles (CND@TiO_2) under visible light illumination is investigated via degradation of rhodamine B, rhodamine 6G and methylene blue dyes.
- Photocatalytic action spectra are acquired in the visible spectral range employing a widely tunable high-power laser (optical parametric oscillator).
- Different photocatalytic processes in the cases of pristine TiO_2 nanoparticles and CND@TiO_2 photocatalysts are identified based on the photocatalytic action spectra.
- A model of the relevant photocatalytic processes is established based on the photocatalytic action spectra, experiments with scavengers, UPS/XPS spectra, UV-Vis and FTIR spectra.
- Photocatalytic action of CND@TiO_2 is compared to the one of mixtures of the small molecule fraction from hydrothermal synthesis with TiO_2 nanoparticles.
- Up-conversion of CND does not exist, even at intensities close to the supercontinuum threshold. Measurable up-conversion results only from the small molecule fraction produced in the hydrothermal synthesis and only at intensities close to the supercontinuum threshold. This makes up-conversion processes completely irrelevant for visible light photocatalysis, again in contrast to many previous reports.
- Bactericidal CND@TiO_2 polymer surface nanocomposites are fabricated active against Gram positive and Gram negative bacteria. Significantly enhanced bactericidal activity is found under visible light illumination compared to TiO_2 polymer surface nanocomposites.

Chapter 4: Photophysics of Curved Molecular Nanographenes

- The photophysics of a series of three closely related curved molecular nanographenes has been studied in detail.
- When studying their fluorescence at room temperature, in the case of the two CNGs that present positive and negative curvature (CNG **7** and CNG **8**), changes in the fluorescence spectrum are observed when varying the excitation wavelength. This is supported by computational modelling of the potential energy surface and can be justified by the coexistence of two minima of the S_1 excited state potential energy surface. Depending on the excitation wavelength, certain higher excited levels can be reached, which preferentially tend to relax to one of the two minima of the potential energy surface of the excited state S_1. This is also consistent with the fluorescence quantum yield of CNG **7**, where depending on the excitation wavelength used, yields between 17% and 21% are obtained, which again depends on the excitation wavelength allowing certain higher excited levels to be reached that can be deactivated by

two minima of the potential energy surface of the S_1 excited state. In the case of CNG with a helicene in its structure (CNG **6**), no change in its fluorescence spectrum is observed when the excitation wavelength is varied.

- Again, when analysing the fluorescence lifetimes at low temperature (at RT the decays are similar) of CNG **7** and CNG **8**, depending on the spectral region in which the detection is performed, different lifetimes derived from each of the two minima of the excited state S_1 are observed. In the case of CNG **6**, no different lifetimes are observed when varying the emission wavelength.
- The three CNGs studied show phosphorescence at low temperature (observed between 65 and 140 K), and, equivalent to what was observed in the case of fluorescence, when the phosphorescence lifetimes of CNG **7** and CNG **8** are analysed, different lifetimes are observed depending on the spectral region where the detection is performed. Again, supported by the computational modelling of the potential energy surface, we can affirm the coexistence of at least two minima of the excited state T_1.
- The three CNGs studied show thermally activated delayed fluorescence (TADF) in a very narrow range of temperatures (110 - 140 K). The activation of TADF cannot occur directly from the T_1 triplet excited state causing the phosphorescence, due to the large S_1-T_1 energy gap compared to the thermal energy in this temperature range. The computational modelling of the potential energy surface reveals the existence of a T_3 triplet excited state with an intermediate energy between T_1 and S_1 that acts as a "springboard" and activates the TADF.
- The three CNGs studied show singlet oxygen photosensitization ability and can be classified as TC-type (where an O_2-induced enhanced intersystem crossing, EISC, process takes place resulting in oxygen-catalyzed production of the triplet state of the $^1O_2$ photosensitizer), with production yields of 36%, 47% and 40% for CNG **6**, **7** and **8**, respectively. These values, coupled with those of fluorescence yields which are 50%, 17%-21% and 25% for CNG **6**, **7** and **8**, respectively, also allow us to conclude that the presence of the closed [6]helicene and double curvature of CNG **7** and **8** (due to the 7-membered ring) favour the intersystem crossing from S_1 to T_1.
- Finally, by estimating the radiative and non-radiative deactivation constants, we can conclude that the presence of the cycloheptatriene ring, causing double curvature of CNG **7** and **8,** favours non-radiative deactivation of the singlet excited state.